PATTERNED NANOARRAY SERS SUBSTRATES FOR PATHOGEN DETECTION

A Thesis
Presented to
The Academic Faculty

by

Nicole Ella Marotta

In Partial Fulfillment
of the Requirements for the Degree
Doctor of Philosophy in the
School of Chemistry and Biochemistry

Georgia Institute of Technology
August 2010

PATTERNED NANOARRAY SERS SUBSTRATES FOR PATHOGEN DETECTION

Approved by:

Dr. Lawrence Bottomley, Advisor
School of Chemistry and Biochemistry
Georgia Institute of Technology

Dr. Mostafa El-Sayed
School of Chemistry and Biochemistry
Georgia Institute of Technology

Dr. L. Andrew Lyon
School of Chemistry and Biochemistry
Georgia Institute of Technology

Dr. Julia Kubanek
School of Biology
Georgia Institute of Technology

Dr. Loren Williams
School of Chemistry and Biochemistry
Georgia Institute of Technology

Date Approved: August 12, 2010

To Mom and Dad. I love you.

ACKNOWLEDGMENTS

I want to first and foremost thank my parents who have always encouraged me to do my best. Whether it was playing a sport, performing in a musical or doing well in school you were always there to cheer me on. You sat on the sidelines when I was playing field hockey, sat in the front row when I was singing, and traveled down the east coast for my defense. I am so happy to know you will always be there, even when I am in a different state. Without your constant love and support, I would not be where I am today, and I honestly cannot thank you enough.

I want to thank my advisor, Prof. Larry Bottomley, or Dr. B as I call him, for helping me become a better scientist. I remember when I was struggling with the this project and debating whether or not to complete the PhD. program. I had a meeting with you and you told me to trust you, it was going to work out. I did and I could not be happier. Thank you for believing that I could do it and helping me see that. I would also like to thank the rest of my thesis committee, Professors Andrew Lyon, Julia Kubanek, Nick Hud, and Mostafa El-Sayed for their words of wisdom and encouragement over the past few years.

In addition to my family, advisor, and committee, I want to thank the friends I have made here in Atlanta and at Tech. I love all of you but a few deserve acknowledgment. Laura,

thanks for being such an awesome friend. You are always there to talk if I need to, or just sit by the pool and hang out. Susan, thanks for being a great carpool partner and an even better date on Thursday nights. Meg, you lived with me for three of the most stressful years of my life and have become one of my closest friends. Thanks for helping me realize I didn't have to look up what a plasmon was again before my OP.

I would also like to thank all of the individuals that have helped me with my research. Thank you to current group members Megan Damm, Kelsey Beavers and David Futur and to past group members Jabulani Barber and Kane Barker for their thought provoking discussions and suggestions. I would like to thank past undergraduate researchers Katherine Siemens, Morgan Nunn, and Kit Ledford for helping me acquire and analyze data, Prof. Mohan Srinivasarao for allowing extended use of his Raman spectrometer and Dr. Matija Crne and Minsang Park for their help in keeping the spectrometer in working order. I also want to thank Charlie Suh, Mikkel Thomas, Janet Cobb-Sulivan and Gary Spinner of the Georgia Tech MiRC Cleanroom for all of their suggestions and guidance concerning clearnroom tools and processes. I want to acknowledge Profs. R. A. Dluhy, R. A. Tripp, and Y. Zhao and Drs. Jeremy Driskell and Vivien Chu from University of Georgia for their fruitful discussions regarding the fabrication and characterization of substrates.

Lastly, I graciously acknowledge Georgia Tech/UGA Biomedical Research program, Georgia Research Alliance VentureLab, Argent Diagnostics and SensorTech Inc. for providing the necessary funding.

TABLE OF CONTENTS

LIST OF TABLES

LIST OF FIGURES

LIST OF SYMBOLS AND ABBREVIATIONS

1kb	one kilobase DNA ladder
100bp	one hundred base DNA ladder
α	GLAD flux angle
Å	angstrom
a	average size of the field enhancing feature
A. histinolovorans	*Arthrobacter histinolovorans*
AmAc	ammonium acetate buffer
AFM	atomic force microscopy
Ag	silver
AgCl	silver chloride
AgFON	silver film over nanosphere
AgNP	silver nanoparticle
AgNR	silver nanorod
ALD	atomic layer deposition
Al_2O_3	aluminum dioxide
A_M	surface area of the metallic surface
Ar^+	argon laser source
β	GLAD growth angle
B. cereus	*Bacillus cereus*
bp	DNA base pair
BPE	trans-1,2-bis(4-pyridyl)-ethene
BSA	bovine serum albumin
c_{RS}	concentration of the solution used

CeO_2	cesium oxide
cfu	cell forming unit
CIP	alkaline phosphatase, calf intestinal phosphatase
CM	BBL^{TM} Cooked Meat Medium
cm	centimeter
cm^3	cubic centimeters
cm^{-1}	wavenumber
CO	carbon monoxide
CT	BBL^{TM} Campylobacter Thioglycollate Medium
°	degree
°C	degrees Celsius
DC	direct current
dia.	diameter
DLS	dynamic light scattering
DMSO	dimethyl sulfoxide
DNA	deoxyribonucleic acid
dsDNA	double stranded DNA
DSSC	dye-sensitized solar cell
$\varepsilon_{induced}$	induced electric field
$\varepsilon_1(\omega)$	dielectric constant of a metal
ε_2	relative permittivity of the environment
ε_{laser}	applied external field from the laser
e^-	electron
e-beam	electron beam
E. coil	*Escherichia coli*

EDTA	ethylenediaminetetraacetic acid
EF	enhancement factor
ELISA	enzyme-linked immunosorbent assay
C_3H_6	ethane
EtBr	ethidium bromide
eV	electron volt
FIB	focused ion beam
FON	film over nanosphere
GLAD	glancing angle deposition
GN	BBL™ GN (Gram Negative) Broth
h	Plancks constant, 6.62606 x 10^{-34} m^2 kg sec^{-1}
H_{eff}	effective height of the scattering volume
He-Ne	helium-neon laser source
hr	hour
HPLC	high performance liquid chromatography
Hz	hertz, number of cycles per second
I	intensity of the Raman mode
I_{RS}	intensity of normal Raman band
I_{SERS}	intensity of SERS band
kcal	kilocalorie
kg	kilogram
Kr^+	krypton laser source
kV	kilovolt
LB	Difco™ Luria Broth
LBB	BBL™ LB Broth

LPS	lipopolysaccharide
LSPR	localized surface plasmon resonance
μ_M	surface density of individual nanostructures
μ_S	surface density of molecules on a substrate surface
M	molar
m	meter
m^2	square meter
MFDS	multidimensional force spectroscopy
$MgCl_2$	magnesium chloride
MH	Difco™ Meuller-Hinton Broth
min	minute
mL	milliliter
mm	millimeter
MM	BBL™ Motility Test Medium
mM	millimolar
mol	mole
ms	millisecond
msec	millisecond
mV	millivolt
mW	milliwatt
µg	microgram
µL	microliter
µm	micrometer
μm^2	square microns
v	energy level

v_s	Stokes shift
v_a	anti-Stokes shift
NH_2	amine
nA	nanoamp
NIR	near infra-red
nm	nanometer
NB	Difco™ Nutrient Broth
Ω	ohm
OAD	oblique angle deposition
oligo	oligonucleotide
OD	optical density
%	percentage
pA	picoamp
PCR	polymerase chain reaction
PEG	polyethylene glycol
PDMS	polydimethylsiloxane
φ	GLAD azimuthal angle
C_3H_8	propane
PW	BBL™ Peptone Water
PVD	physical vapor deposition
QCM	quartz crystal microbalance
r	distance from the surface to the adsorbate
R6G	rhodamine-6G
RF	radio frequency
RSV	Respiratory Syncytial Virus

RU	BBL™ Rapid Urea Broth
s	second
SAM	self-assembled monolayer
SBD	single bi-deposition
SCE	saturated calomel electrode
sec	second
sec^{-1}	inverse seconds
SERS	surface enhanced Raman spectroscopy
SEM	scanning electron microscope
SF	BBL™ Selenite-F Broth
SiO	silicon monoxide
SL	BBL™ Sabouraud Liquid Broth
SM	BBL™ Standard Methods Agar
SMSERS	single molecule SERS
SSC	saline-sodium citrate buffer
ssDNA	single stranded DNA
SSEF	SERS surface enhancement factor
T_m	melting temperature
T_1	transition temperature 1
T_2	transition temperature 2
T_s	substrate temperature
TAE	Tris-acetate-EDTA buffer
TB	Turbo Broth™
TCEP	Tris((2-carboxyethyl)phosphine)
TEM	transmission electron microscopy

TiO_2	titanium dioxide
UHV	ultra high vacuum
UV	ultraviolet
V	volt
v/v	volume per volume
w/v	weight per volume
XRD	x-ray diffraction

SUMMARY

The objectives of the work presented were to 1) fabricate reproducible nanorod array SERS substrates, 2) detection of bacteria using nanorod substrates, 3) detection of DNA hybridization using nanorod substrates and 4) critically evaluate the sensing method.

A novel method for batch fabrication of substrates for surface enhanced Raman scattering (SERS) has been developed using a modified platen machined to fit in a commercial electron beam evaporator. The use of this holder enables simultaneous deposition of silver nanorod (AgNR) arrays onto six microscope slide substrates utilizing glancing angle deposition. In addition to multiple substrate fabrication, patterning of the AgNR substrates with 36 wells allows for physical isolation of low volume samples. The well-to-well, slide-to-slide, and batch-to-batch variability in both physical characteristics and SERS response of substrates prepared via this method was nominal. A critical issue in the continued development of AgNR substrates is their stability over time, and the potential impact on the SERS response. The thermal stability of the arrays was investigated and changes in surface morphology were evaluated using scanning electron microscopy and x-ray diffraction and correlated with changes in SERS enhancement. The findings suggest that the shelf-life of AgNR arrays is limited by migration of silver on the surface. Continued characterization of the AgNR arrays was carried out using fluorescent polystyrene microspheres of two different sizes. Theory suggests that enhancement between nanorods would be significantly greater than at the tops due to contributing electromagnetic fields from each nanostructure. In contrast to the theory,

SERS response of microspheres confined to the tops of the AgNR array was significantly greater than that for beads located within the array. The location of the microspheres was established using optical fluorescence and scanning electron microscopy.

The application of SERS to characterizing pathogens such as bacteria and viruses is an active area of investigation. AgNR array-based SERS substrates have enabled detection of pathogens present in biofluids. Specifically, several publications have focused on determining the spectral bands characteristic of bacteria from different species and cell lines. Studies were carried out on three strains of bacteria as well as the medium in which the bacteria were grown. The spectra of the bacteria and medium were surprisingly similar, so additional spectra were acquired for commonly used bacterial growth media. In many instances, these spectra were similar to published spectra purportedly characteristic of specific bacterial species.

In addition to bacterial samples, nucleic acid hybridization assays were investigated. Oligonucleotide pairs specifically designed to detect Respiratory Syncytial Virus (RSV) in nasal fluids were prepared and evaluated. SERS spectra acquired on oligos, alone or in combination, contain the known spectral signatures of the nucleosides that comprise the oligo. However, spectra acquired on an oligo with a 5'- or 3' thiol were distinctly different from that acquired on the identical oligo without a thiol pendant group suggesting some control over the orientation of the oligo on the nanorod surface. The signal enhancement in SERS depends markedly upon the location of the probe relative to

the substrate surface. By systematic placement of nucleotide markers along the oligo chain, the point at which the nucleotide disappears from the spectrum was identified.

The overall findings for AgNR SERS substrates suggest that the applicability of SERS for detecting nucleic acid hybridization is limited. The strong distance dependence coupled with the lack of substrate stability at temperatures required for annealing oligos during hybridization suggest that AgNRs are not the platform to use for hybridization assays.

CHAPTER 1

INTRODUCTION TO SURFACE ENHANCED RAMAN SCATTERING

The purpose of this chapter is to introduce the reader to surface enhanced Raman spectroscopy, the major technique used to sense biomolecules throughout this work. The details in how Raman works as well as the mechanisms responsible for the SERS phenomenon are described in detail. Also included is a review of the common substrates and applications currently in use.

1.1. History of Raman

In February of 1928, Chandrasekhara Venkata Raman and Kariamanickam Srinivasa Krishnan were performing studies on the scattering of light and discovered what is now referred to as the Raman effect. Raman earned the Nobel Prize in Physics for his discovery and contribution to the scattering of light in 1930.[21] The Raman effect was designated an American Chemical Society National Historical Chemical Landmark in 1998, demonstrating the significance the discovery.[12]

1.1.1. Raman Scattering

The Raman effect is an inelastic scattering caused by rotational and vibrational transitions in molecules.[13] When light is scattered from a molecule or atom, most of the photons are scattered at the same energy and wavelength of the incident photons. This is deemed an elastic or Rayleigh scattering event. Sir Raman and Sir Krishan discovered that about

one in a million photons is scattered at a different frequency that the incident photons. This difference can be higher or lower frequency than the Rayleigh line.

Figure 1.1 presents the energy level diagram for Raman and Rayleigh scattering. When a photon is scattered off a molecule in a ground vibrational state, $v = 0$, there is a momentary change in the energy state of the molecule corresponding to the virtual state designated as *j*. Molecules in the ground state can absorb a photon corresponding to an energy of hv_{ex} and emit a photon with a change in energy represented by $h(v_{ex} - v_v)$. This is referred to as a Stokes shift and written as v_s. Molecules in an already vibrationally excited state, $v = 1$, scatter and return to their ground state and produce a photon with energy corresponding to $h(v_{ex} + v_v)$. This is referred to as the anti-Stokes shift and written as v_a.[13] The absorption of energy (Stokes) results in a red shift in the Raman spectrum, whereas a loss in energy (anti-Stokes) results in a blue shift. The red shifted Stokes lines are much higher in intensity than the blue shifted anti-Stokes lines when the system is at thermal equilibrium. The intensity of anti-Stokes shifts increase when the system is at an elevated temperature, increasing the vibrationally excited molecules in the system.[10, 22-23]

Raman scattering is representative of the vibrational, rotational, or electronic energy of the molecule. Figure 1.2 presents the full spectrum of scattered light for cyclohexane. The most intense peak at zero corresponds to the Rayleigh scattering. The peaks present at higher (Stokes) and lower (anti-Stokes) frequencies correspond to the Raman shifts for cyclohexane. The Raman shift is a value associated with the bonds in the system and is

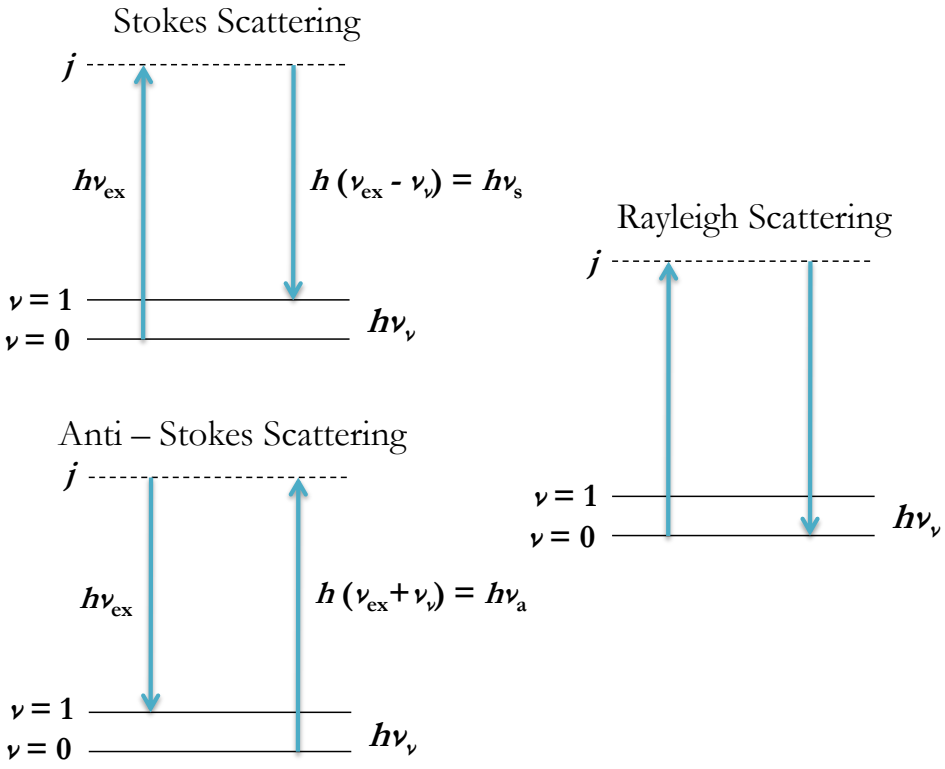

Figure 1.1. Energy level diagram for Raman and Rayleigh scattering. Image adapted from Ingle, 1988.[13]

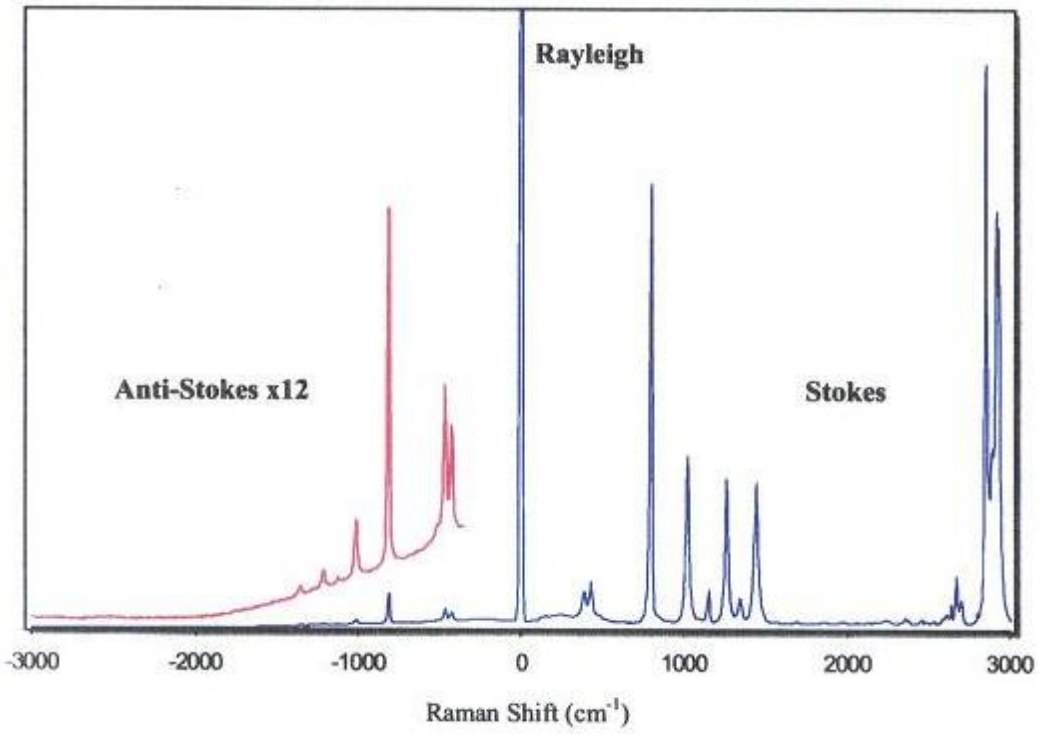

Figure 1.2. Presented is the full spectrum acquired for a solution of cyclohexane, a commonly used Raman standard. The red shifted Stokes lines are much higher in intensity than the blue shifted anti-Stokes lines since the system is at thermal equilibrium. The bands for Stokes and anti-Stokes are located at the same wavenumber, just representative of a gain or loss of energy.

written in cm^{-1}, referred to as wavenumbers. These values are used to account for any variation in the shift with a change in excitation wavelength.

1.1.2. Polarizability

The fundamental selection rule for Raman spectroscopy is that the polarizability of the molecule must change during the course of the vibration of the bonds. (In contrast, the fundamental selection rule for infrared spectroscopy is a net change in the dipole moment during the course of the vibration).[24] Polarizability is the ability of a charge distribution, such as electron cloud of an atom or molecule, to be distorted from its normal shape by an external electric field.[10, 23] The vibrational Raman cross section is determined by its degree of polarizability. The cross section of a molecule is representative of the area available for interaction of a beam particle, or in this case the incident monochromatic light. The larger the Raman cross section, the more likely the molecule will produce a Raman spectrum.

1.2. Instrumentation

Typically, a normal Raman spectrometer consists of a laser source, a cell to hold the sample, a wavelength selector, a radiation transducer and the appropriate signal processor and read-out device. Figure 1.3 presents these components in schematic form. A detailed description of each follows.

1.2.1. Laser Source

The laser source is generally He-Ne, Ar^+, or Kr^+ corresponding to different wavelengths. He-Ne lasers emit a highly collimated beam of lights at a wavelength of 632.8 nm; Ar^+ lasers emit at 488.0 and 514.5 nm, and Kr^+ lasers emit a wavelength of 530.9 and 647.1

nm.[13] The incident wavelength must be chosen carefully, as many samples undergo photodecomposition at shorter wavelengths. Also, some samples fluoresce and others absorb the incident radiation or the Raman scattered radiation. The optimum wavelength for a system would result in high intensities, low photodecomposition, low fluorescence, low and absorbance.[13] Pulsed lasers have also been implemented to optimize the excitation wavelength; short pulses also allow for time-resolution techniques to reject background fluorescence.

1.2.2. Sample Cells

Raman may be acquired on gas, liquid, and solid samples. Since both the exciting and scattered radiation is in the visible region, both glass and quartz may be used as sample chambers. Commonly, capillaries are used for liquid analytes. Since water is a weak Raman scatterer, the solutions may be in an aqueous environment. This is advantageous for both inorganic and biological samples. For gaseous samples, a higher powered laser is needed and a specially designed sample cell is often used. For solids, very little sample preparation is needed. The solid can be mounted within the laser beam and does not need to be in a special sample holder.[13]

1.2.3. Wavelength Selector

The use of a wavelength selection device is very important with Raman spectroscopy. Raman spectra require a high degree of resolution (less than 5 cm^{-1}) in order to separate the weaker Raman lines from the intense Rayleigh scattering. To improve upon this resolution, multiple monochromators may be utilized. Presently, holographic gratings are used to improve the resolution in comparison to the ruled gratings used previously.[13]

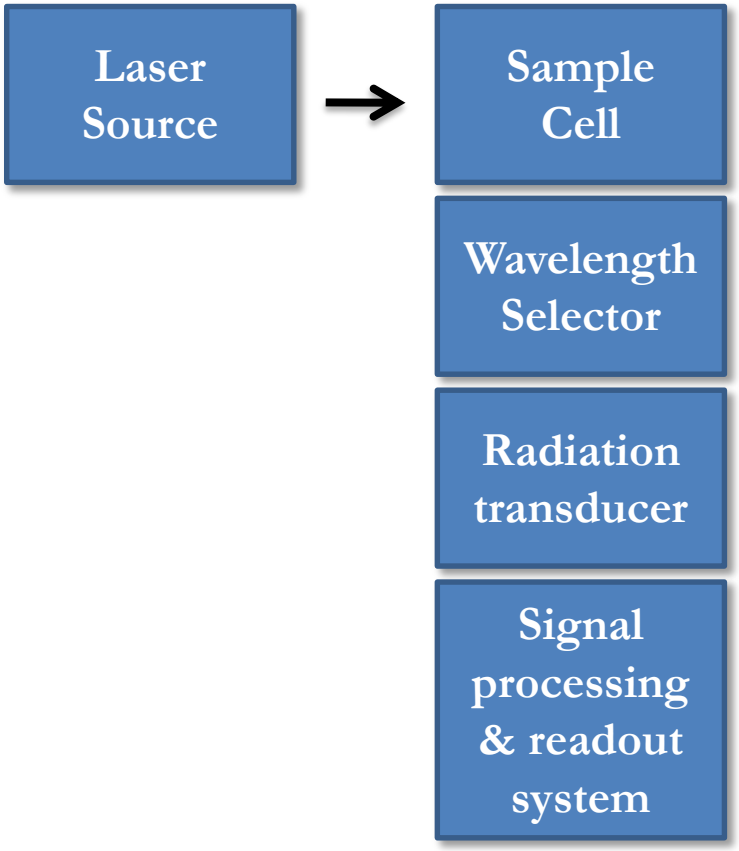

Figure 1.3. A schematic representative of the components composing a normal Raman spectrometer are presented. Components include a laser source, a sample cell, a wavelength selector, a radiation transducer and the appropriate signal processor and read-out device.

1.2.4. Transducer and Readout System

Historically, Raman spectrometers used photomultiplier tubes as detectors. More recently, photon counting systems replaced photomultiplier tubes because of the improved signal to noise ratios for the weak Raman signals and their residual background noise. Additionally, photon counting provides accurate results at high intensities, allowing for its use for a variety of Raman intensities.[13] Today, linear diode arrays and CCD detectors are routinely used to acquire a complete Raman spectrum in a decreased amount of time.

1.3. Early Raman Studies

Systems studied in the gas phase are limited due to experimental limitations. A variety of analytes in the gaseous phase were studied using Raman in the early to mid 1900's.[25-33] A few examples are methane,[34] inorganic halogenides,[35] oxygen,[36] carbon disulphide,[37] carbon dioxide,[38] and methylamine.[39] Most gaseous state studies were also compared to the liquid state. In the case of methylamine, spectral bands varied in both intensity and shift in wavelength. For example, the magnitude of an N-H shift due to hydrogen bonding between NH_2 groups in the liquid would not occur to an appreciable extent in the gas phase at the lower pressure experiments were carried out.[39] Typically, analysis of gaseous samples required large scattering columns, a powerful light source, and a fast spectrograph. Stray light must be eliminated in these studies, and some columnation of the scattering beam is required to avoid scattering by the glass chamber holding the gas itself.[39]

For early Raman studies of molecules such as DNA, bulk samples were required, typically in solid form or concentrated aqueous solutions. Otto *et al.* studied aqueous solutions of individual DNA bases (no phosphate backbone or sugar moiety were included) to establish the spectral bands associated with each base.[8] Other studies have been carried out on DNA oligonucleotides, where the structural changes in DNA were monitored. Characteristics of B-type conformations of DNA were investigated based upon the Raman band intensities.[40-47] One study looked into eight DNAs where four had varying GC content and four were periodic DNA polymers. Bands in the region of 800 - 850 cm^{-1} showed some dependence on the GC content as well as the base pair sequence. Additionally, bands attributed to A-family and B-family at 809 and 835 cm^{-1}, respectively, were observed indicating that DNA was in both conformations in solution.

Receptor binding induced conformational changes have been studied as well.[48-54] One study looked into the secondary structure of the cAMP receptor protein, referred to as CRP.[49] CRP in solution and CRP cAMP cocrystals were compared. The amide regions of the spectra, Amide I 1630-1700 cm^{-1} and Amide III 1220 - 1300 cm^{-1}, were compared for varying concentrations of CRP in solution and the distribution of conformations appeared to be the same for all solutions despite buffer and CRP concentration. In contrast, comparison of the spectra acquired on the CRP-cAMP cocrystals to spectra of CRP alone showed spectral differences in the two amide regions, suggesting conformational changes in the secondary structure upon cAMP binding to CRP. These initial DNA and protein based studies paved the way for future work in the field.

1.4. Discovery of Surface Enhanced Raman Scattering

In 1974 Fleishmann *et al.* employed Raman spectroscopy to study adsorption of molecules at an electrode surface. Specifically, pyridine at a silver electrode surface was investigated.[55] Pyridine was chosen due to its strong Raman scattering and its ability to absorb at the solid-gas interface.[56-57] This was the first time Raman was used to investigate monolayer adsorption at electrode surfaces. The electrode was subjected to cyclic linear potential sweeping in the electrochemical cell for 15 minutes at 0.5 V sec^{-1} between + 200 and – 300 mV in preparation for studies. The formation and reduction of silver chloride during each cycle resulted in substantial etching of the silver surface; resulting in approximately a tenfold increase in surface area.

Spectra acquired on pyridine adsorbed to the electrode surface diffuses considerably in comparison to that acquired using acidic oxide surfaces as the substrate.[56-57] Aqueous pyridine showed peaks at 1037 and 1005 cm^{-1} whereas at the electrode, pyridine showed peaks at 1036, 1025, and 1008 cm^{-1}. Interestingly, the band at 1025 cm^{-1} decreased with potential in the cathodic direction indicative of pyridine coordinating to the metal surface through the nitrogen atom.

Raman spectroscopy provides information regarding structural components of molecules of a system. Unfortunately, this technique is limited by the low signal intensity due to the small number of photons Raman scattered.[10] At first it was thought the enhancement was due to the increased number of molecules able to exist on the roughened surface, however two research groups determined the enhancement to be an intrinsic surface

enhancement.[11, 58-59] The enhancements observed were in the magnitude of $10^5 – 10^6$ in comparison to bulk material marking the beginning of what is now known as surface enhanced Raman spectroscopy (SERS).[11]

Albrecht and Creighton expanded on Fleishmann's studies in 1977.[58] In their early study, spectra for pyridine adsorbed to a silver electrode were acquired before and after a single oxidation-reduction cycle and compared. A single voltage sweep was applied and after the cycle, the spectral bands were almost five times more intense for the ring breathing modes and compared to the spectrum acquired before the sweep.

The Raman spectrum acquired for the bulk pyridine solution after removal of the electrode was devoid of the band at 1025 cm^{-1} verifying that this band was due to pyridine adsorbed at the electrode surface.[55] Other bands at 1000, 1036, 1218, and 1605 cm^{-1} showed an increase in intensity as well but not to the extent of the 1025 cm^{-1} band. The increase in surface area due to electrochemical roughening[60] was determined to be 10 – 20 %, improving upon previous studies.[55]

Based on calculations performed by Fleishmann, the increase in pyridine adsorbed at the electrode surface could not account for the increase in intensity. Albrecht and Creighton suggested that a surface effect increasing the molecular Raman scattering cross sections may be accountable. Previously, Philpott suggested that at roughened metal surfaces a broadening of electronic energy levels for bound molecules existed.[56-57, 61] Based on this observation, an interaction with the surface plasmons at the roughened metal surface

was proposed to be responsible for the intensity increase in the Raman spectra. Resonance Raman had been previously reported for conjugated chromophores[62] leading to a possible explanation for the enhanced signal at the roughened electrode surface for pyridine.

In addition to Albrecht and Creighton, Jeanmaire and Van Duyne independently investigated pyridine on a roughened silver electrode.[59] They set out to validate and expand on the use of Raman to investigate species adsorbed on electrode surfaces.[55, 63-64] An increase in Raman intensity was also seen using their system, prompting a systematic investigation to determine the parameters influencing the intensity using pyridine as the probe molecule.

Spectra were also acquired on adsorbed pyridine at a silver electrode surface and bands were observed at 1008 and 1036 cm^{-1} at a higher intensity than the aqueous solution. An additional band at 3067 cm^{-1} was observed corresponding to a C-H stretch that was obstructed in aqueous solution.[59]

In previous studies, the Raman intensity was dependent upon the method of preparation of the electrode.[59] When the pyridine solution was held at a potential of – 0.6 V in relation to the SCE the signal was roughly 10 times higher than pyridine in solution. If anodization was carried out in the presence of pyridine the signal increased up to a factor of 50. Addition of pyridine post anodization provided similar results. Through continued experimentation, Jeanmaire and Van Duyne concluded that an increase in signal only

occurred when the AgCl at the electrode surface was indeed reduced, creating a roughened or etched surface.[59]

Jeanmaire and Van Duyne attempted to correlate the increased response with the number of molecules that could occupy the surface of the electrode. A pyridine molecule occupies 38 $Å^2$ when in a flat configuration[65] and 25 $Å^2$ in a standing orientation. Based on the latter dimension, as well as the parameters of the Raman experiment, the number of molecules sampled on the electrode surface was ~3 x 10^{13}. The normal Raman spectra of the electrode compared to the solution was 5 to 6 orders of magnitude greater than expected, suggesting that the electrode surface was indeed acting to enhance the signal. Studies at various excitation wavelengths showed that the response was not due to a coupling of the scattering process with an electronic transition in the adsorbed molecule. This is seen with molecules such as crystal violet and methyl orange where the analyte is resonant at a specific wavelength, leading to an enhanced Raman signal.[59]

Upon further investigation, it was determined that etching the surface did not create a large enough surface area increase to give rise to the observed enhancement. Hendra *et al.*[63] determined the surface area increase to be approximately a factor of ten post electrochemical roughening. Since the signal increase was 50 fold, it cannot be accounted for by the surface area increase alone. Jeanmaire and Van Duyne suggested the formation of active sites at the surface as a possible explanation in addition to the surface area.

1.4. Surface Enhancement Mechanisms

Albrecht and Creighton as well as Jeanmaire and Van Duyne hinted that the enhancement they observed could not be strictly due to the increased surface area. Instead they suggested that the enhancement was due to something at the surface where the scatterer was adsorbed. Albrecht and Creighton[58] proposed a resonance from electronic states whereas Jeanmaire and Van Duyne[59] proposed an electric field enhancement. Parts of each proposed mechanism, were in fact, correct. Over the years, the surface enhancement has been attributed to two different mechanisms.

1.5.1. Electromagnetic Enhancement

Enhanced electromagnetic fields are supported by metal surfaces with the appropriate morphologies.[9] The overall excitation of conduction electrons within a material, such as a metal, is referred to as a plasmon; when confined to a surface it is deemed a surface plasmon. Figure 1.4 depicts a schematic representation of a surface plasmon confined to a spherical metal particle (represented by the blue sphere). An external electric field (represented by the blue arrow) provides an excitation causing the conduction electrons in the metal surface to oscillate collectively; leading to a surface plasmon resonance (represented by the orange sphere). Metals commonly employed are silver, gold, and copper because of their ability to support a surface plasmon.[66-69] The interaction of the incident laser with the surface plasmon on these metal surfaces makes up the electromagnetic enhancement mechanism for SERS.[9-11]

Early studies focused on electromagnetic enhancement resulting from interactions between adsorbed molecules and flat metal surfaces. A popular model presented by

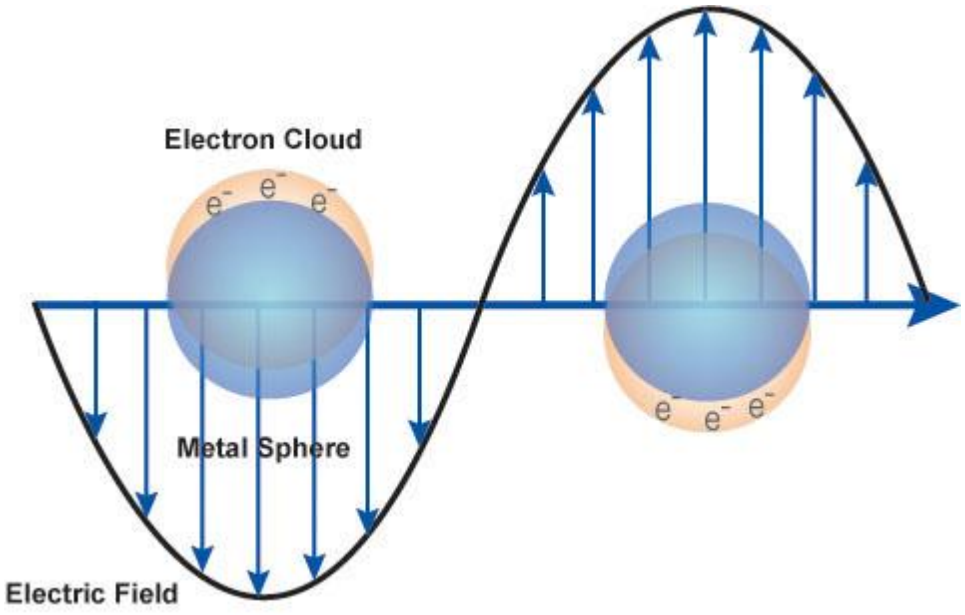

Figure 1.4. A schematic representation of surface plasmons confined to a spherical metal surface is presented. Upon excitation from an external electric field, the conduction electrons in the metal surface collectively oscillate leading to a surface plasmon resonance. The interaction of the incident laser with the surface plasmon on these metal surfaces is responsible for the electromagnetic enhancement mechanism for SERS.[9-11]

King, Van Duyne, and Schatz[70] was deemed the "image field model" and attributes the enhancement to a large change in polarizability, calculated using the chosen parameters and treating the Raman emitting system as a combination of the Raman scatterer and its conjugate-charge image at the metal. A dipole moment is induced on the molecule by the incident field as well as its image field. This is expressed as $\mu = \alpha(E + E_{im})$, where E and E_{im} are the incident and image fields and α is the molecular polarizability. The term E_{im} can be described as $E_{im} = [\varepsilon - \varepsilon_0/\varepsilon + \varepsilon_0]\mu/(4r^3)$ where r is the distance between the point dipole and the metal surface. Combining these two equations results in the overall expression, $\mu = \alpha_{eff}[1 - (\alpha_{eff} - 4r^3)(\varepsilon - \varepsilon_0/\varepsilon + \varepsilon_0)]^{-1}E$ where α_{eff} is the effective polarizability defined as $\alpha_{eff} = \alpha/[1 - (\alpha - 4r^3)(\varepsilon - \varepsilon_0/\varepsilon + \varepsilon_0)]$. Using this set of expressions, King *et al.* demonstrated on a flat silver surface that at a distance less than r = 1.65 Å the Raman enhancement was in an excess of 10^6 however when r = 2.00 Å the enhancement fell to 10^2. This model was refined by Weber and Ford[71-73] using the expression presented by Kliewer and Fuchs[74] to account for the metals dielectric response, essentially removing the local assumption made by King *et al.* They also used a spherical particle removing the point dipole restriction. In doing so, the image effect decreases by ~10^3 at comparable r values, showing the image-field enhancement is not an important contributor to SERS.

Using the spherical particle model,[71-75] molecules located within the external electric field experience an induced electric field, $E_{induced} = [\varepsilon_1(\omega) - \varepsilon_2/\varepsilon_1(\omega) + 2\varepsilon_2]E_{laser}$ where $\varepsilon_1(\omega)$ is the dielectric function of the metal, ε_2 is the relative permittivity of the environment, and E_{laser} is the applied external field from the laser. Excitation of the

surface plasmon significantly increases the local electric field experienced by the molecule on the surface. With a small increase in the local field, the Raman scattering is greatly enhanced. The overall enhancement provided by this mechanism scales with E^4.

1.5.2. Chemical Enhancement

The electromagnetic mechanism alone is not enough to account for the magnitude of enhancement. Since various molecules observed under the same experimental conditions gave different SERS intensities, another enhancement must exist independent of the electromagnetic enhancement. Specifically, spectra acquired on CO and N_2 differ in intensity by a factor of 200 even though the polarizabilities are comparable and the experimental conditions were held constant.[9] This is difficult to explain with strictly an electromagnetic enhancement. A logical explanation lies in a resonance Raman mechanism where new electronic states arise from chemisorption of the scatterer at the metal surface serving as intermediate states in Raman scattering. Specifically, the highest occupied molecular orbital (HOMO) and the lowest unoccupied molecular orbital (LUMO) of the adsorbed scatterer are symmetrically placed in energy in relation to the Fermi level of the metal.[9] When this is the case, charge transfer reactions, either the molecule to metal or metal to the molecule, may occur at half the energy of the molecular vibrations intrinsic to the adsorbate.

Chemical enhancement requires chemisorption of the Raman scatterer directly on the surface.[10-11, 76] Evidence of this has been reported where metal-molecule stretching modes are observed in the spectrum.[77] Additionally, when pyridine is adsorbed on different metal surfaces, specific spectral bands change in intensity.[78] A change in the

polarizability of the scatterer due to charge-transfer or chemical bond formation between the metal surface and the molecule contributes to this mechanism. The enhancement requires that an overlap between the adsorbate and the metal substrate exist and scales at approximately E^2.[10-11, 59]

In systems where both a chemical and electromagnetic aspect come into play, the mechanisms are multiplicative.[9] Estimates of the overall enhancement per molecule for the contribution of both chemical and electromagnetic enhancement mechanisms, scales on the order of $10^5 - 10^6$.[11, 58-59] The enhancement factor for a given substrate and molecule may be calculated using,[24]

$$EF = \frac{\frac{SERS\ Intensity}{\#\ of\ molecules}}{\frac{Raman\ Intensity}{\#\ of\ molecules}}$$

The signal intensities used must take into consideration the integration time used in the measurements.[24] Additionally, incident surface power and beam dimensions must be considered in determining the number of molecules excited when comparing SERS and normal Raman intensities.[79] Taking these additional parameters into consideration, one calculates the SERS surface enhancement factor (SSEF),[79]

$$SSEF = \frac{\frac{I_{SERS}}{\mu_M \mu_S A_M}}{\frac{I_{RS}}{C_{RS} H_{eff}}}$$

where I_{SERS} and I_{RS} are the SERS and normal Raman intensities, respectively, μ_M is the surface density of the individual nanostructures, μ_S is the surface density of the molecules on the substrate surface, A_M is the surface area of the metallic surface, c_{RS} is the

concentration of the solution used, and H_{eff} is the effective height of the scattering volume. Enhancement factors up to 10^{14} have been reported for single molecule detection.[80-81]

1.5.3. Distance Dependence

Electromagnetic enhancement is a long range effect that does not require the adsorbate be in direct contact with but within a few nanometers of the metal surface.[10, 23, 76] In contrast, the chemical enhancement is short-ranged and requires the adsorbate to be chemisorbed directly to the surface.[11, 82]

Gersten and Nitzan[83] investigated the distance dependence of hemispheroids with varying dimensions. See Figure 1.5 for schematic drawings of the hemispheroid shapes investigated. The enhancement ratio was plotted as a function of distance from the surface for the particles and it was observed that the enhancement was greatest at the surface and fell off with increasing distance. The hemispheroid shape played a role in the severity of the intensity fall off where a less eccentric particle had a more gradual fall-off of intensity with "significant" enhancement factors out to a larger distance than more eccentric spheroids. Essentially, a more spherical particle will have less severe distance dependence, whereas an ellipsoidal particle will have more significant distance dependence. Gersten proposed that this effect was due to the image enhancement effect previously discusses, a contributing factor to the overall electromagnetic enhancement mechanism.[83]

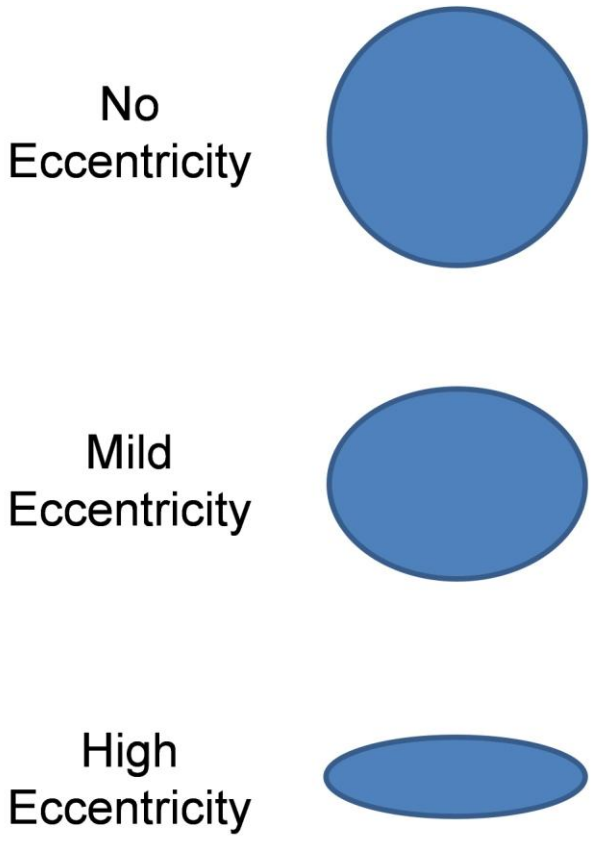

Figure 1.5. Presented are drawings representing different hemispheroid shapes. The top image is a perfect circle, and is the least eccentric particle of the three shown. The bottom image is the most eccentric particle, having a more ellipsoidal shape.

Recently, Dieringer *et al.* studied the effect distance had on SERS enhancement. They employed atomic layer deposition (ALD) to fabricate a spacer of a controlled distance from the roughened metal surface.[82] ALD was used to deposit uniform layers of aluminum oxide (Al_2O_3)[84-85] at thicknesses ranging from 0.0 nm to 4.8 nm. Ag film over nanosphere (AgFON) (a detailed description of these substrates is provided in section 1.6.3 of this chapter) were used as the base substrate for SERS studies. Previously, Equation 3, explained by the dipole decay law,[9] had been used to correlate the fall-off of SERS intensity with distance from the surface for a monolayer of molecules.[86] I represents the intensity of the Raman mode, r is the distance from the surface to the adsorbate, and a is the average size of the field enhancing feature.

$$I = \left(1 + \frac{r}{a}\right)^{-10} \tag{3}$$

For larger areas of curvature, this response can appear long-ranges, however for smaller radii id may appear to be closer to a surface effect.[9] Studies of pyridine on AgFON with increasing Al_2O_3 spacer distance showed that 2.8 nm from the substrate surface, the enhancement decreased by tenfold. The acquired data was plotted and compared to Equation 3 and was almost a perfect fit showing little to no enhancement at a distance of 4.8 nm from the surface.[82] Other studies have shown that the large electromagnetic field produced by the plasmon(s) at the surface of a nanoparticle is at most 10 nm.[87]

1.6. SERS Substrates

The strongest SERS enhancements are seen with coinage metals (silver, gold, and copper) due to their ability to support a surface plasmon; however the effect is expected for all metals with outer shells of $(n\text{-}1)d^{10}ns^1$.[59, 75, 88-90] In addition to substrate

composition, the shape of the substrate plays a crucial factor in the surface enhancement. For example, the electromagnetic field is at a maximum for regions with high curvature, ultimately resulting in greater SERS enhancement.[91] Evidence of this has been reported by Murphy and co-workers on isolated silver and gold nanoparticles of various aspect ratios.[92]

1.6.1. Nanoparticles

Silver and gold nanoparticles are the most frequently used SERS substrates due to the ease of preparation and well characterized SERS properties. [9, 11, 93-99] Silver nanoparticles are produced by the reduction of a silver salt (typically silver nitrate) by reducing agents such as sodium citrate,[100] EDTA, or sodium borohydride.[101] Nanoparticles produced from citrate or EDTA reduction tend to be more stable over time and are thus the preferred method of preparation.[102]

Gold nanoparticles are made in a similar fashion as silver, where chloroauric acid is reduced using reducing agents such as sodium citrate,[103] tetraoctylammonium bromide (in an organic layer such as toluene),[104] or hydroquinone.[105] For the same reason as silver, the citrate reduction is the most common and stable method. With both silver and gold, the size may be controlled based on the amount of reducing agent used in comparison to the metal.

1.6.1.1. Nanoparticle Aggregation

Junctions between nanoparticles where electromagnetic fields may overlap will generate large field enhancements and may even allow for single molecule detection.[80, 93] These fields are generated by the localized surface plasmon resonance of the

nanoparticles and may be tuned based on the size, shape, and degree of aggregation of the nanoparticles.[106] Through controlled aggregation, the "hot-spots" created by the electromagnetic field overlap may be taken advantage of.[24, 107-108] Additionally, nanoparticles may be used in combination with other metal surfaces where both metal surfaces contribute to the SERS enhancement.[2, 109-110] See Figure 1.6a for a schematic of these SERS substrates.

1.6.2. Nanoshells

Metal nanoshells typically consist of a dielectric core with a metallic shell of nanometer thickness, whose optical resonance can be "designed" in a controlled manner. By varying the dimensions of the core and shell material in relation to one another, the optical resonance of these nanoparticles can be varied over hundreds of nanometers in wavelength, across the visible and into the infrared region of the spectrum.[111-114] Halas and co-workers use these metallic nanospheres as SERS substrates for various biomolecular detection.[1, 113-117] Specifically, a silica core was used as a base and a gold shell was deposited around the outside serving as the SERS active portion. See Figure 1.6b for a schematic of these SERS substrates. Strongest Raman enhancements were reported when enough gold was deposited on the silica cores to form a nearly complete metal shell, creating a consistent electromagnetic enhancement throughout the surface of the particle.[114]

1.6.3. Film over Nanosphere

A monodispersed population of nanoparticles may be fabricated and confined to a surface using nanosphere lithography.[118-120] Specifically, a suspension of nanospheres are coated onto a base substrate and allowed to self-assemble into a hexagonally closed-

packed colloidal crystal serving as a deposition mask. Once the colloidal crystal deposition mask is formed, Ag films of various thicknesses are deposited over the nanosphere mask. Van Duyne and coworkers deemed these structures film over nanosphere (FON) substrates. Specifically, they employed silver over silica nanospheres (AgFON) for studies. See Figure 1.6c for a schematic of these SERS substrates. These substrates proved to be thermally stable, SERS-active, and suitable for use in ultrahigh vacuum (UHV) conditions.[120] AgFON have been used to study the localized surface plasmon properties of nanostructures,[87, 119, 121-122] distance dependence of the SERS electromagnetic enhancement mechanism[82, 84] detect single molecules,[123-124] and detect biomolecules.[125-129]

1.6.4. Nanorods

Enhancements associated with high curvature regions have been deemed the "lightening rod effect" and can contribute to 10^6 or greater enhancements for molecules at the tips of these needles or in pores.[83] Additionally, oscillations of the localized surface plasmon will take place along both the width (transverse plasmon band) and the length (longitudinal plasmon band) of the nanorod.[92, 130-131] The two waves can be tuned based on the aspect ratio of the particle. The overlap of both the longitudinal and lateral plasmon bands produces a strong electromagnetic enhancement at the rod ends.[92] Based on these effects, nanorod arrays should provide great enhancement between the nanorods in the array as well as the ends.

Nanorods have been fabricated in an array structure[132-141] as well as in solution in a similar manner to nanoparticles with the addition of a surfactant to control the direction

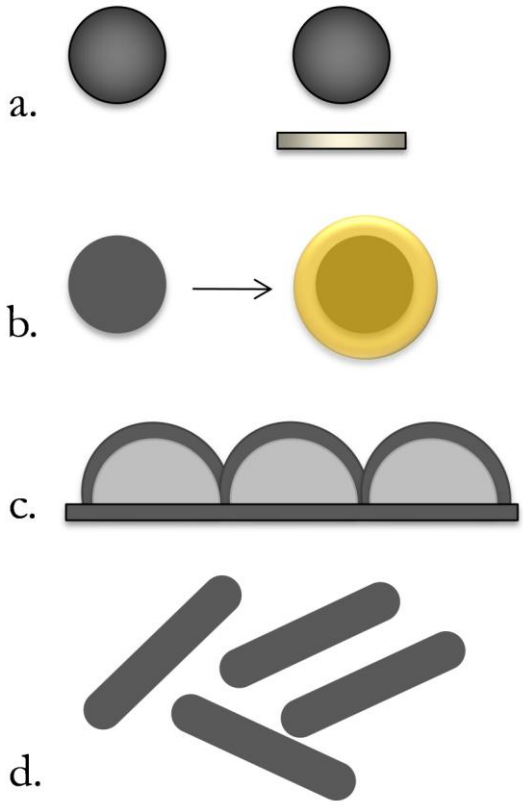

Figure 1.6. Presented are drawings representing different SERS substrates. a.) represents a single nanoparticle as well as a nanoparticle in a "sandwich" assembly where an additional metal surface is employed to create a "hot-spot," b.) depicts a nanoshell substrate where a nanoparticle core coated with a metal shell, encompassing the entire core particle, c.) presents a film over nanosphere schematic where lithography is used to create a base (dark grey structure) and a metal is deposited on top (light grey structure), and d.) depicts a nanorod shaped substrate able to move freely.

of axial growth.[92, 142] See Figure 1.6d for a schematic of the latter nanorod SERS substrates (for an image of the former nanorod substrate see Figure 2.11 in the next chapter). SERS substrates comprised of silver nanorod arrays have been shown to be highly uniform in structure, easy to fabricate, and provide high signal enhancements.[133-134, 136-137, 139-141, 143-148] These substrates show promise as solutions to the existing impediment to biosensor applications.[1, 125, 149-152]

1.7. Applications of SERS

1.7.1. Single Molecule Surface Enhanced Raman Scattering (SMSERS)

Kniepp and co-workers report NIR-SERS based single molecule detection of crystal violet in a solution of silver colloids.[80] A water immersion lens was used so that direct contact could be made with the solution while spectra were acquired. The ratio of molecules to colloids in solution was calculated to be 0.6, less than one molecule per colloid, in order to limit the number of molecules able to exist on a single colloid. Experimentally, spectra were acquired every second and plotted for comparison as molecules were likely to come in and out of the volume of solution interrogated by the laser. Single molecule detection was claimed based on the fact that a majority of the spectra were void of spectral bands associated with crystal violet. A few spectra, however, did contain peaks correspondingto crystal violet. Kneipp and co-workers concluded this was due to the detection of single molecules at the silver colloid surface.[80]

Nie and co-workers also investigated single molecule SERS around the same time as Kniepp.[81] Spectra on both single molecules and single nanoparticles were achieved at

room temperature. Individual silver colloidal nanoparticles were used to amplify the spectroscopic signatures of adsorbed rhodamine-6G (R6G) molecules. Raman enhancement factors were reported on the order of 10^{14} to 10^{15}, much larger than the ensemble-averaged values derived from conventional measurements. This enormous enhancement leads to vibrational Raman signals that are more intense and more stable than single-molecule fluorescence. Van Duyne and co-workers have also reported detection of single R6G molecules on silver nanoaggregates.[123]

1.7.2. Biomolecular Sensing

Nanoparticles coupled with SERS have been used to detect a variety of biomolecules. Specific examples include but not limited to proteins,[153-157] wholes cells,[5, 151, 157-160] bacteria,[161-183] and oligonucleotides.[1-4, 6-7, 109, 115, 152, 154, 184-186] Nanoparticle aggregation has also been employed to study biomolecules and biomolecular interactions. A few examples include antibody/antigen, [116, 155Bardhan, 2009 #1596, 187-188] and streptavidin/biotin[187, 189-190] binding interactions. Additionally, adenosine,[185, 191] glucose,[192] and toxic ions such as lead[191, 193] mercury and cadmium, [193] and lithium[24] have been studied using ligand based aggregation of nanoparticles.

1.7.2.1. Pathogen Detection

1.7.2.1.1. Viruses

Recently, there have been several reports for the use of SERS for virus detection. Direct spectroscopic detection of an intact virus has been reported.[139, 194-196] Specifically, virus specimens have been identified using very small volumes without manipulation of

the virus itself[139] and enveloped versus non-enveloped viruses are spectrally distinguishable.[194] Indirect detection using virus biomarkers[197] or a "sandwich" assembly using more than one metal surface[198-200] has also been reported.

1.7.2.1.2. Bacteria Cells

Distinguishing characteristics between different cell lines lie in the protein coat along the outside of the cell where the protein make-up is distinct for different bacterial cells. This change in protein composition had been studied using SERS, in turn identifying the bacterium present in a sample. A number of studies have been performed utilizing SERS with a variety of substrates: *in situ* silver[181-183] or gold[177] colloids, silver [163, 165-166, 168-174, 179-180, 201] or gold colloids[163] added post cell growth, silver nanorod arrays,[162, 176] silver coatings,[181] silver nanoparticles with antibodies,[202] and biofilms.[203] Methods have also been employed using Raman with optically trapped bacteria,[161] optically trapped bacteria coupled with confocal Raman[204] as well as studies performed using confocal Raman alone.[165-167, 178, 205]

1.7.2.1.3. Nucleotides

One of the first studies focusing on nucleotides was performed by Otto and co-workers in 1986 on a silver electrode surface.[8] Spectra were acquired for single nucleotide bases using both normal Raman and SERS and the spectral band locations were compared. The normal Raman spectra were also acquired on these nucleotides. Comparison of the spectra revealed a significant shift in spectral lines as well as new lines between the normal Raman and SERS.

Mirkin and co-workers have used nucleotide induced aggregation of gold nanoparticles for detection of DNA hybridization. Nanoparticles functionalized with a probe oligonucleotide were forced to aggregate upon addition of nanoparticles functionalized with the complementary DNA strand. The spectral signatures for the DNA were enhanced due to the spatial location of the oligonucleotides between two particles.[7, 187, 206]

Halas and co-workers[1, 111-117, 156, 207-210] have employed gold nanoshell structures to detect DNA hybridization. In a similar fashion to Mirkin and coworkers, one nanoshell solution was functionalized with a probe oligonucleotide and another with the strand complementary to the probe. Upon combining the two nanosphere solutions, hybridization was monitored using SERS. Hybridization of DNA located within the nanometer-sized gap between the two nanospheres, i.e. within the "hot-spot," was suggest as the basis for enhancement of the spectral bands for the nucleotide bases.[1, 115]

Also reported was the use of a thermal cycle prior to deposition of the DNA onto the gold nanoshell surface. Using this thermal pretreatment seemed to allow for the DNA to pack more tightly at the surface, ultimately leading to better signal to noise ratios as well as improved variability from substrate to substrate. Additionally, hybridization appeared to be more efficient when the thermal pre-treatment was employed.[1] It is important to note, however, that no distance dependence was observed or reported for DNA ranging from 20 - 70 bases in any of the studies. Adenine peaks were visible in the spectrum regardless of concentration or distance the base was located from the surface.[1]

Green and co-workers have developed a silver toroid SERS substrate for DNA detection.[6] Spectra were acquired on oligonucleotides 18 bases long in combination and alone. The relative intensity change with composition was noted and a ratio was used to compare the different sequences to one another. DNA hybridization was investigated as well and single base mismatches were identified with no distance dependence reported.

Graham and co-workers[3-5, 184, 211-212] have performed numerous studies using nanoparticle aggregations and assemblies for detection of oligonucleotides. Specifically, they employed a Raman label as well as nucleotides for detection of DNA hybridization. Since changes in nucleotides sequence is often difficult to distinguish, a Raman reporter is used to verify that hybridization has taken place. Specifically, silver nanoparticles were functionalized with single stranded DNA, complementary to an fluorescently tagged oligonucleotide in solution. Upon successful hybridization, the fluorescent label was enhanced by the silver surface and provided ample signal in the resulting SERS spectrum.

An crucial aspect of DNA hybridization assays is the orientation of the DNA on the substrate surface. X-ray photoelectron spectroscopy (XPS) has been employed to investigate the conformation of thiolated and nonthiolated DNA at a gold surface.[213-214] The XPS spectra were monitored for the response associated with the nitrogen atoms in the base for both thiolated and nonthiolated oligonucleotides consisting of only thymine bases. Additionally, the formation of a complete monolayer was monitored

based on the nitrogen response and correlated to the surface coverage. Results from the study suggested that thiolated DNA, when allowed to form a complete monolayer, was standing up off the surface. The contribution from the nitrogen in the ring of the thymine base was no longer present in the XPS spectra upon monolayer formation.

In addition to XPS, electrochemical methods have been employed to investigate the conformation of DNA on electrode surfaces.[215-219] One such study looked into the surface density of DNA at a gold electrode surface to evaluate hybridization efficiency as function of monolayer coverage. Specifically, the number of nucleotide phosphate residues were calculated using the amount of cationic redox marker measured at the electrode surface. Based on the electrode response observed, monolayer coverage of thiolated DNA was achieved however it was not the condition where hybridization was most efficient. Hybridization was the most successful when a spacer was implemented to allow room for the complementary strand of DNA to bind to the probe for *in situ* studies.

Overall, SERS is a sensitive and viable means for detecting analytes at the surface of a roughened metal surface. The coupling of both a chemical and electromagnetic enhancement mechanism can produce enhancement factors up to 10^{14} relative to normal Raman allowing for single molecule detection. Additionally, SERS may be utilized for biomolecule detection since the resulting SERS spectrum contains spectral bands unique to the molecule being investigated.

CHAPTER 2

INTRODUCTION TO GLANCING ANGLE DEPOSITION

The purpose of this chapter is to introduce the reader to the method in which silver nanorod array SERS substrates were fabricated in this work. A broad background is provided as well as details leading up to the use of glancing angle deposition to fabricate the arrays.

2.1. Physical Vapor Deposition

Physical vapor deposition (PVD) is a coating technique involving transfer of material on an atomic level; typically metals, where a thin film is deposited onto a surface at nanometer to micrometer thicknesses. PVD processes are carried out under vacuum and typically involve four steps; 1) evaporation, 2) transportation, 3) reaction and 4) deposition.[19, 220-223] Figure 2.1 shows this process schematically.

During evaporation, the source metal is bombarded with a beam of electrons or ions using a high energy source (Step 1 Figure 2.1). With this bombardment, atoms at the surface of the target metal are dislodged, as single atoms or clusters of them. Some source materials require a high degree of heating, which in turn, requires a lengthy cool down period upon completion of the run.[19, 222]

Following evaporation, atoms move from the target to the substrate in a transport step (Step 2 Figure 2.1). The substrate is typically oriented close the source metal, and the path for the atoms is linear in nature. During atom transport, a reaction step may occur

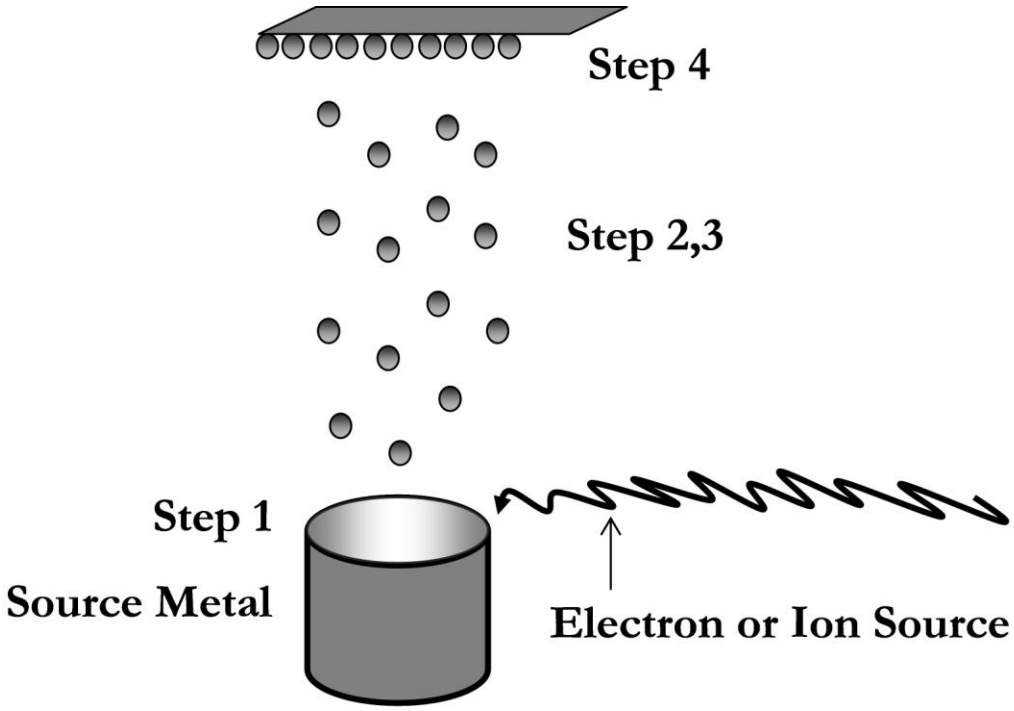

Figure 2.1. Schematic of physical vapor deposition (PVD). A source material is bombarded with an electron or ion source and atoms are dislodged (Step 1) and transported (Step 2) towards the substrate surface. During transport, the atoms may react with the gas used in the chamber (Step 3) prior to depositing on the substrate surface (Step 4). In some instances, the reaction step does not occur.

depending upon the identity and partial pressure of a gas during the process. Commonly used gases are nitrogen, methane, and oxygen (Step 3 Figure 2.1). The evaporated material may undergo a chemical reaction prior to the atoms depositing at the substrate surface. This is typically the case when depositing metal oxides, nitrides, carbides and other such materials. In processes where the source metal alone is the desired material, this step does not take place.[19, 221-222]

The final step is the deposition itself (Step 4 Figure 2.1). During this stage, the material coats the substrate surface and builds up to the desired thickness. Deposition rates are typically slow to ensure even distribution of material as well as lower temperatures at the substrate surface.[12, 19, 220, 222] A more detailed description of the effect substrate temperature has on the deposition is provided in section 2.2.1.3 of this chapter.

2.1.1. Sputter Deposition

Sputtering is a form of PVD for depositing thin films onto a substrate surface. Under vacuum, gaseous plasma is produced to accelerate ions from the plasma into the source metal (Figure 2.2). Coating material is passed into the vapor phase, primarily in atomic form, through ion bombardment of the source electrode (target) composed of the coating material.[18-19, 224] For sputtering to take place, an energy source (RF, DC, mW) is required to sustain the gaseous plasma. This energy source maintains the plasma state since throughout deposition as the plasma is losing energy to its surroundings. Upon collision with the target, material is eroded away and atoms of a neutral charge are ejected towards the substrate resulting in deposition of the source material. By manipulating the applied power and target source size, the deposition rate may be

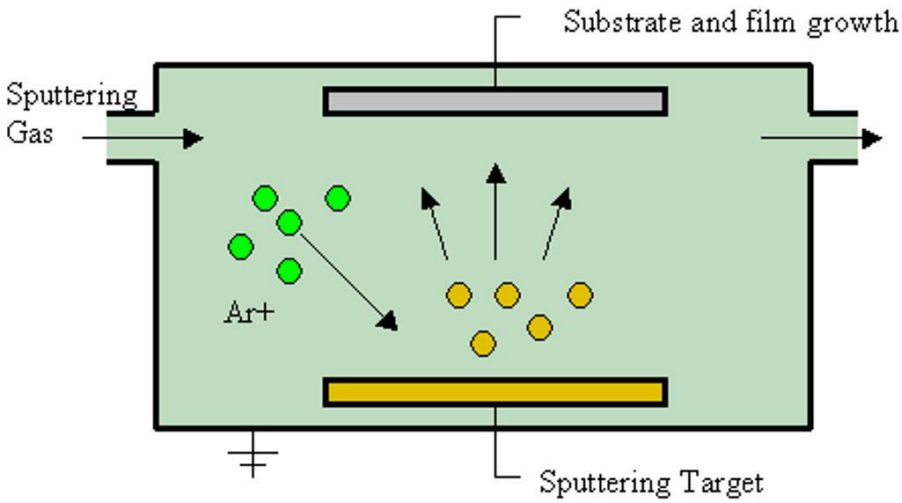

Figure 2.2. Schematic of sputtering deposition. The target is shown at the bottom where argon gas ions (green circle) are causing atoms (gold circle) to dislodge and evaporate towards the substrate surface. In this image, there is both an inlet and outlet for gas to keep gas the system at a low pressure.

controlled. During sputtering the pressure within the chamber is typically maintained at 0.1 Torr. An advantage to sputtering deposition in comparison to filament evaporation (described in section 2.1.2.1 below) is high melting point materials are easily sputtered without the concern of system heating. This method is commonly used to deposit metal oxides.[12, 225]

2.1.2. Thermal Evaporation

2.1.2.1. Resistive Evaporation

Sputtering deposition differs from resistive evaporation in that a heating element is the energy source responsible for vaporizing the source material as opposed to an ion source. When a high current is passed through a resistive element, heat is produced. The most common form of source material are small metal pellets. These pellets are typically heated within an aluminum oxide basket or a specially designed metal "boat" where the metal vaporizes and ultimately condenses on the substrate surface.[12, 221] Figure 2.3 presents a schematic of the evaporation process.

Low pressures, typically 10^{-6} or 10^{-5} Torr, are used during evaporation to avoid collisions between the vapor atoms within the plume.[12] To aid in maintaining vacuum, liquid nitrogen may be used to cool the chamber and reduce the vapor pressure of water within the chamber.[12] Atoms strike the sample surface in a linear fashion to form a thin film of the desired thickness, dependent upon the rate and duration of deposition. However, unlike sputtering, a high degree of heat is required to melt the metal pellets, causing the chamber to reach a high temperature.

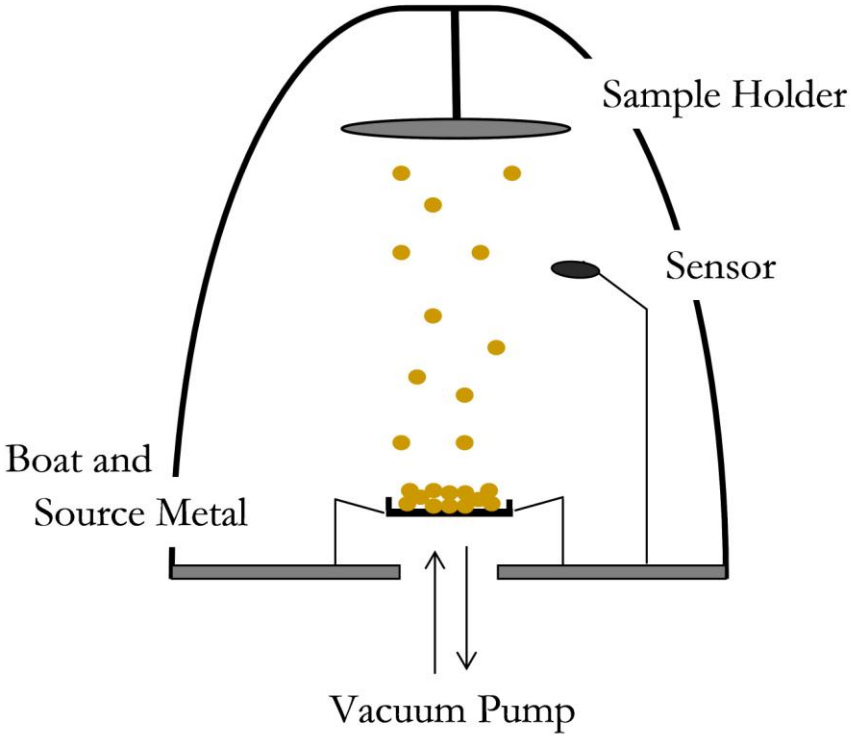

Figure 2.3. Schematic representation of filament evaporation. Source metal is contained in an evaporation boat and heated until evaporation begins. The sensor monitors the rate of deposition as well as the film thickness.

2.1.2.2. Electron Beam Evaporation

The electron beam (e-beam) evaporation system is the most common method for PVD of metals. In this method, the source metal is heated to a high temperature through electron bombardment in a high vacuum environment as opposed to direct heating.[19] Figure 2.4 displays a schematic of this type of deposition.

The quality of the deposited film depends upon the quality of the vacuum within the chamber. For higher quality films, ultra high vacuum (UHV) is optimal. Evaporation is normally conducted at pressures sufficiently low (10^{-6} to 10^{-9} Torr) so that the flux undergoes an essentially collisionless (line-of-sight) transport to the substrate.[19, 222-223] At very low pressures, the mean free path of vapor atoms equals or exceeds the vacuum chamber dimensions, so these particles travel in straight lines from the evaporation source towards the substrate.[12, 221]

The tool itself consists of a few key components. A hearth holds the source metal in a crucible so that the electron beam is focused in a small region. The hearth is typically water cooled to reduce the amount of heat given off upon melting the ingot.[12] A rotating hearth is commonly used with multiple pockets for source metals allowing for sequential depositions with a single pump-down.[220] This is an additional advantage over resistive evaporation. Because the evaporation rate is dependent upon the temperature of the source metal, a mechanical shutter is employed to prevent flux from reaching the substrate during initial stages, since heating the source metal is not a rapid process.

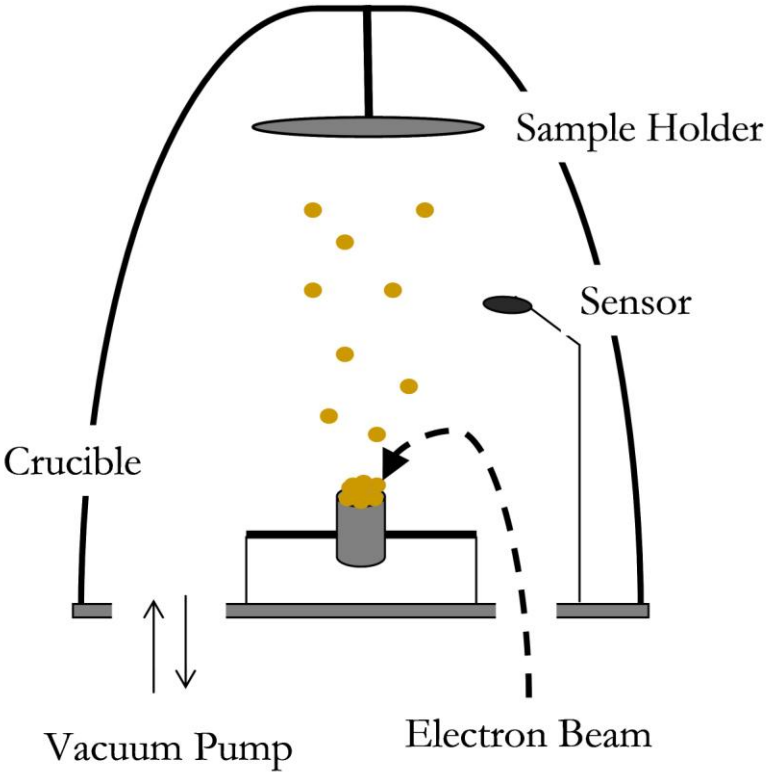

Figure 2.4. Schematic of an electron beam evaporator. In this particular image, the electron beam is drawn in the 270° conformation.

Typically 1-10 kW of electrical power is used during deposition to create the electron beam. During the ramping step, a higher power is used to initially melt the metal and during deposition, a slightly lower power is maintained. The beam is focused and positioned using a magnetic field during the evaporation. The preferred orientation of the electron beam is 270° as shown in Figure 2.4. In this set-up, the filament itself is out of the way of the evaporating material.

2.1.3. Plume Characteristics

During evaporation, atoms form a plume within the evaporation chamber.[15] Figure 2.5 shows a schematic of the distribution of particle density within the plume during deposition. The inner regions are dark blue and representative of denser regions and the lighter shades are representative of lower particle densities. Depending upon substrate placement within the plume, the substrate temperature as well as the deposition rate may be controlled. There exists a higher density of particles directly above the source metal (dark blue regions) and the particles decrease with distance from the source in both a vertical and horizontal direction (light blue regions).

The angle particles strike the surface also changes with distance because of the dimensions and trajectory of atoms in the plume. Upon movement of the substrate horizontally from the center of the source metal, atoms still follow a linear path and hit the surface at a non-normal incidence. This is shown schematically in Figure 2.6. Although the angle change is slight, the features at the surface will be directly affected. Based on vapor plume characteristics, a longer throw distance is desired for some processes. With a decreased particle density, a more consistent film will result.

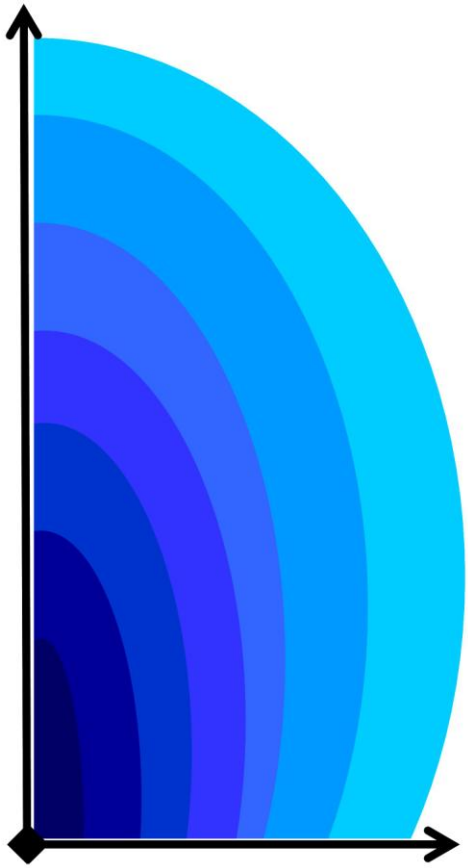

Figure 2.5. Schematic representative of the particle density within the evaporation plume during deposition. The darker blue depicts regions with higher particle density and the lighter blue represents regions with lower particle density. Arrows indicate the increasing distance from the source metal. Typical ranges for high to low particle density (particles/cm^3) are 10^{14} to 10^{10}.[15]

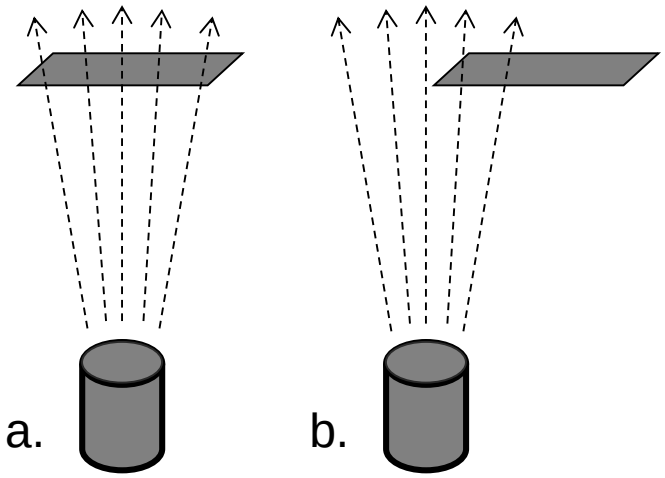

Figure 2.6. Schematic of the linear trajectory atoms take during evaporation. With substrates directly above the source (a.) the atoms strike the surface a slightly different angles than when the substrate is off-center (b.). The angles at which the atoms hit the surface changes due to the plume characteristics and can affect the overall structure of the thin film. Note, the atoms do not travel past the substrate, the lines are just extended to emphasize the difference in angles.

Additionally, the deposition rate decreases with distance and a slower deposition will contribute to the uniformity of the film.

2.2. Glancing Angle Deposition (GLAD)

It is well known that PVD results in films possessing a column like structure. Typically during thermal evaporation, the substrate is oriented in such as way that the flux material strikes the surface at an angle of incidence of 0°. However, upon positioning the substrate at an angle during deposition, thin films can be engineered to consist of unique structures.[226] Earlier studies[227-231] were carried out where metals were deposited onto static substrates at non-normal, or oblique, angles. A critical conclusion from these studies was that the grains grew towards the source metal, a detail later confirmed by Nieuwenhuizen and Haanstra.[232] More specifically, Konig and Helwig[233] recognized an increase in the atomic-scale shadowing, now referred to as "self- or ballistic shadowing," during deposition at these oblique angles.

Glancing angle deposition (GLAD) is a form of PVD that is used to fabricate porous thin films with engineered microstructures. An important feature of GLAD is that the incident flux material is not parallel to the substrate normal but rather at an oblique angle. PVD of oblique incident flux coupled with limited adatom diffusion at the substrate surface results in a film with columnar microstructures oriented towards the source metal. Rotation during this evaporation along the azimuthal axis may be used to sculpt columns of various shapes.[234] The traditional set-up for GLAD is depicted in Figure 2.7. The following paragraphs describe the mechanisms behind film growth and the factors that affect the structures.

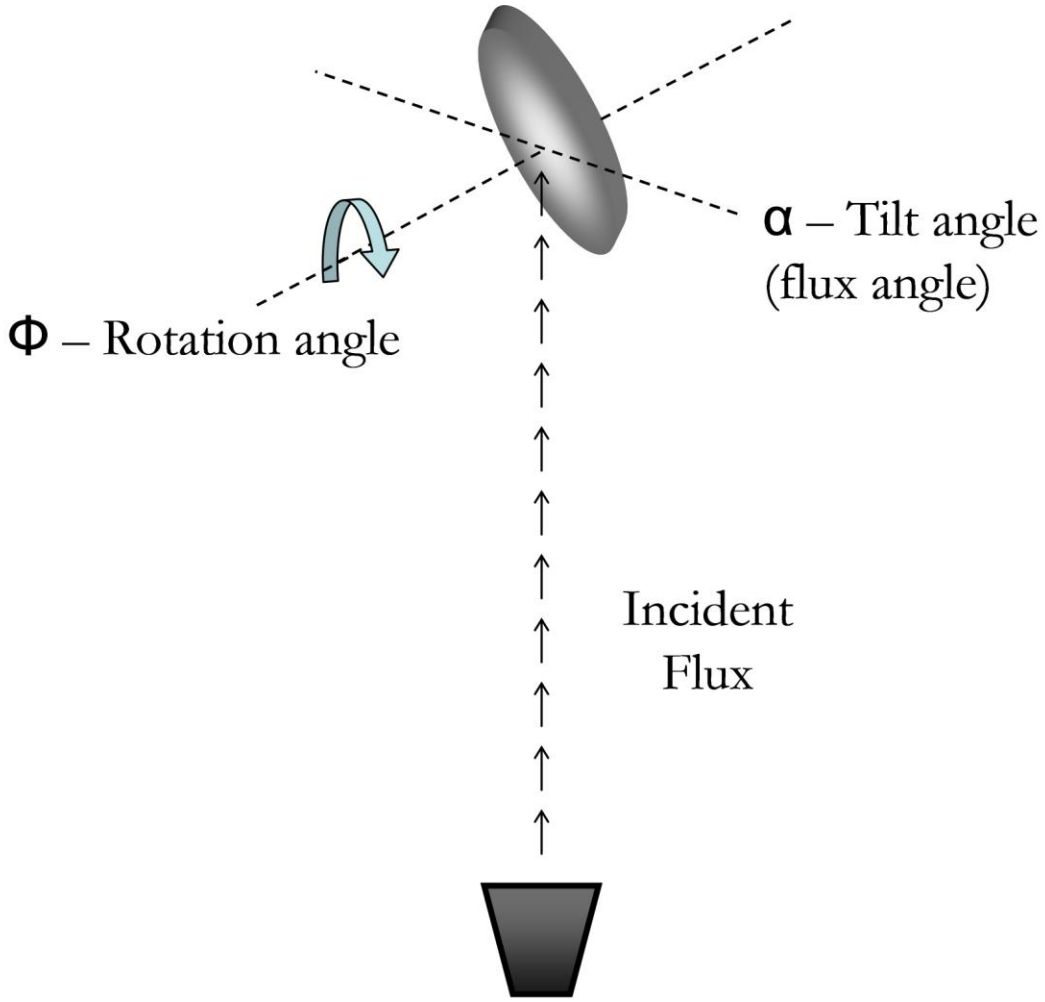

Figure 2.7. Schematic of GLAD. A motor may be employed to rotate the substrate (line labeled as φ rotation). The tilt angle (line labeled as α, flux angle) is presented as well. This parameter directly affects the overall structure of the columnar microstructures in the thin film. Image adapted from (Robbie 1998)[17].

2.2.1. Columnar Structure Formation

2.2.1.1. Nucleation

Thin film deposition results from a material going through a phase transition from vapor to a solid at the substrate surface.[222] Nucleation results when growth regions begin to form upon condensation of this flux material.[235-237] The vapor provides constant flux of atoms incident on the substrate surface where once adsorbed, the atoms may diffuse. These adsorbed atoms, or adatoms, can either re-evaporate off the surface (or detach from existing nucleates) or join other adatoms and form nuclei. The latter is favored once large nucleates form and it is no longer energetically favorable for an adatom to detach.[226] Figure 2.8 presents a scanning electron micrograph (SEM) of nucleate formation at the start of deposition. It is evident from the image that some nucleates are larger than others, and this will determine some of the thin film characteristics with continued deposition (described in more detail in section 2.2.2 in this Chapter). It should also be noted that nucleation is random in nature.

During nucleate formation, adatoms bound more strongly to the substrate surface grow in a monolayer type manner, referred to as Frank-van der Merwe growth.[238-239] In contrast, if binding is stronger between the adatoms themselves, three dimensional structures result referred to as island or Volmer-Weber growth.[239] A combination of these two growth mechanisms may occur as well and are deemed layer plus island or Stranski-Krastanov growth.[238-241] These nuclei form regardless of the angle of incident flux, however with GLAD, the Volmer-Weber growth mechanism is the most significant.[240-241]

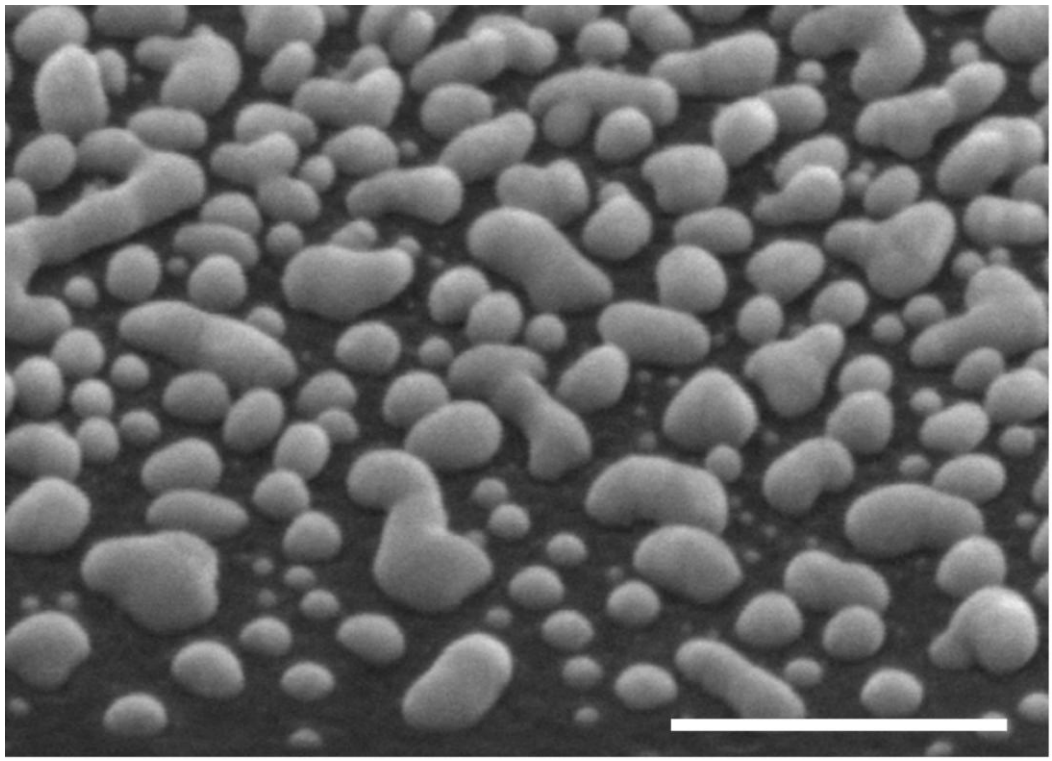

Figure 2.8. SEM image depicting nucleation on the substrate surface at the beginning of a silver deposition. In this particular image, the incident flux angle was 86°. Scale bar denotes 200 nm.

2.2.1.2. Ballistic Shadowing

Ballistic shadowing corresponds to the act of one particle blocking the region directly behind it from a second particle. The principle behind ballistic shadowing in GLAD lies in the evaporated material nucleating on the surface at the beginning of deposition. During deposition, the non-planar surface (see Figure 2.8) exhibits line of sight, or ballistic shadowing, becoming a dominant factor as the film continues to grow. Eventually, regions directly behind these nucleation points are blocked from the incident vapor. Upon further evaporation, material deposits onto the nucleus resulting in growth of a columnar-like structures.[226] With continued deposition, material builds up resulting in micro-column structures. Additionally, since atoms favorably deposit onto these nucleates, columnar structures form in the direction of the flux material.

The basis of shadowing lies heavily on the linear vapor trajectories of the incident flux. For improved shadowing, a longer throw distance is desired because collimation of the vapor material is improved with distance. This distance is not indefinite though, it does reach a point where the particles begin to lose energy and collide with one another. Upon collision, particles do not travel towards the substrate along the original linear path and may deposit in regions shadowed to begin with. This effectively decreases the particle columniation at the substrate surface as well as formation of columnar structures. E-beams and sputterers are the preferred tools for GLAD where the low operating pressures and large working distances are advantageous.[17, 226] Resistive evaporators are not commonly used due to excessive heating of the system that degrades the nanostructured surface.

2.2.1.3. Surface Temperature and Diffusion

Diffusion of the flux material at the substrate surface is significant during initial nucleation and continued deposition. As growth continues, vapor species deposit onto the substrate.[226] The movement of adatoms during diffusion at the surface goes against the shadowing mechanism allowing adatoms to deposit in the shadowed regions. Factors influencing diffusion at the surface include the incident energy of the particles, the energy required for diffusion to take place, and the thermal energy provided by the environment.[240-241] Part of the thermal energy comes from the temperature of the substrate, T_s, which will have an effect on the overall structure of the thin film.

Early experiments concerning film growth as a function of T_s were carried out by Movchan and Demchishin.[14] Regions of a substrate were held at various temperatures during deposition with a normal incident flux angle. Results indicated a three zone model where distinct structural zones were observed at certain temperatures, deemed zones 1, 2, and 3. These zones are presented and labeled in Figure 2.9. The work looked into temperature transitions as a ratio in relation to the melting temperature of the source material, T_m. Transitions were observed in between each zone and designated as T_1 and T_2. Regardless of the material evaporated, the ratios of T_1 and T_2 to T_m values were consistent, $T_1 / T_m \approx 0.3$ and $T_2 / T_m \approx 0.5$. These boundaries are indicated by the dashed lines in Figure 3.9.

In zone 1 ($T_1 < T_s$) the temperature is not high enough for significant diffusion and the observed thin film consists of tapered columns with voids between. With an increase in

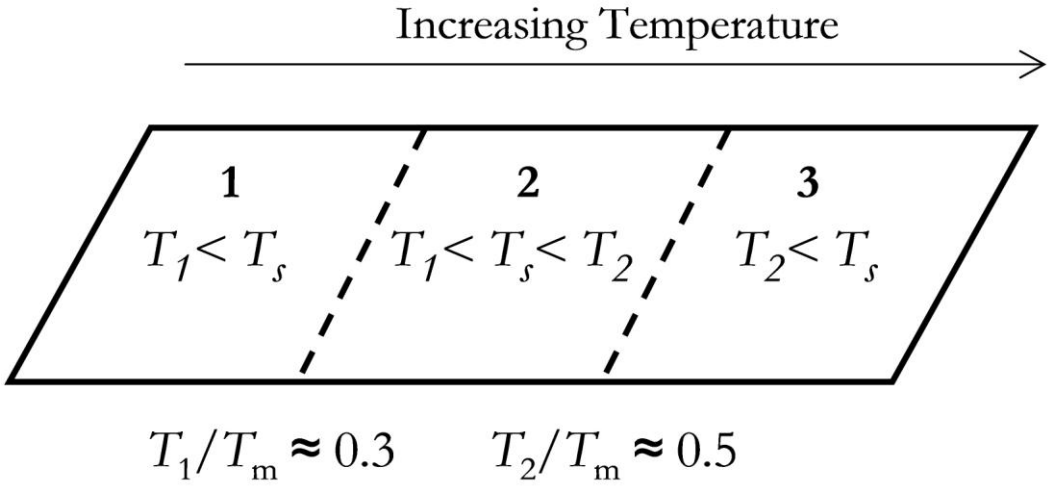

Figure 2.9. Schematic representation of the three zone temperature model. With increasing temperature, transition temperatures are reached where a structural change is observed.[14] Image adapted from Thornton.[18-19]

temperature, the first transition temperature is reached and results in zone 2 ($T_1 < T_s < T_2$). With this transition, the tapered columns in zone 1 begin to form a denser more defined structure with an increasing diameter. Past the second transition temperature ($T_2 < T_s$), a sufficient amount of thermal energy exists. Due to this increase in thermal energy, recrystallization of the thin film occurs upon continued deposition in zone 3. Because of these models, the structure of the thin film may be controlled or manipulated through substrate temperature and deposition rate. With an increased temperature and flux rate, diffusion across the surface is higher whereas with a lower temperature and rate of deposition diffusion is limited. Adatom diffusion at the substrate surface can alter the shape, size, and orientation of the growing microstructures.[19, 242-244]

2.2.2. Column Development

During initial growth, micro-columns are symmetrical about the growth axis. Upon further deposition atoms deposit in such a way that they begin to fan out from the center and symmetry is lost. Continued growth is an anisotropic process where growth is parallel to the incident flux;[20] there is no restriction on the lateral growth of the structure. Columns will continue to broaden until they become wide enough to merge with neighboring structures.[245] Column growth is an overall competitive process, and due to ballistic shadowing, smaller micro-columns may exist in the shadowed region behind a larger structure.[246] Growth of these shadowed columns ceases and the larger columns dominate the thin film. The dominating columns will grow in diameter in order to maintain the density of the thin film. With increased deposition the columns become larger and decrease in number. This development process is a distinguishing factor in the GLAD process.

2.2.2.1. Structure Control - Seeding

An additional aspect that may be controlled is the periodicity of the structures at the surface. The initial nucleation is a random event so structures are typically aperiodic.[247-248] Figure 2.10a demonstrates this schematically. The side view shows that not only are different sized nucleates possible, but they are not ordered and the spacing is inconsistent. A great deal of overlap may occur as well, negatively impacting these substrates for some applications. The top view further demonstrates the randomness of this phenomenon. Ideally, nucleates would form uniformly with periodic spacing.

Control of these structures can be accomplished in a couple different ways. A post-fabrication step can be used to etch away regions in which undesired growth has occurred or to create new structures within the thin film.[249-254] This effectively changes the width and height of the structures but will not change the spacing or location. If controlled spacing is desired, an additional step may be employed prior to GLAD deposition. To control the nucleation at the sample surface, and in turn the shadowing mechanism, the substrate can be pre-patterned in order to dictate where the columns grow. This is shown schematically in Figure 2.10b. With this pre-patterning, the nucleation at the beginning of deposition is mimicked resulting in a periodic structure consisting of single, evenly spaced columns.[255]

Patterning may be carried out using electron beam lithography of photoresist,[256-260] embossing,[261] optical lithography, [259, 262, 263 Ye, 2005 #954, 264] laser-direct

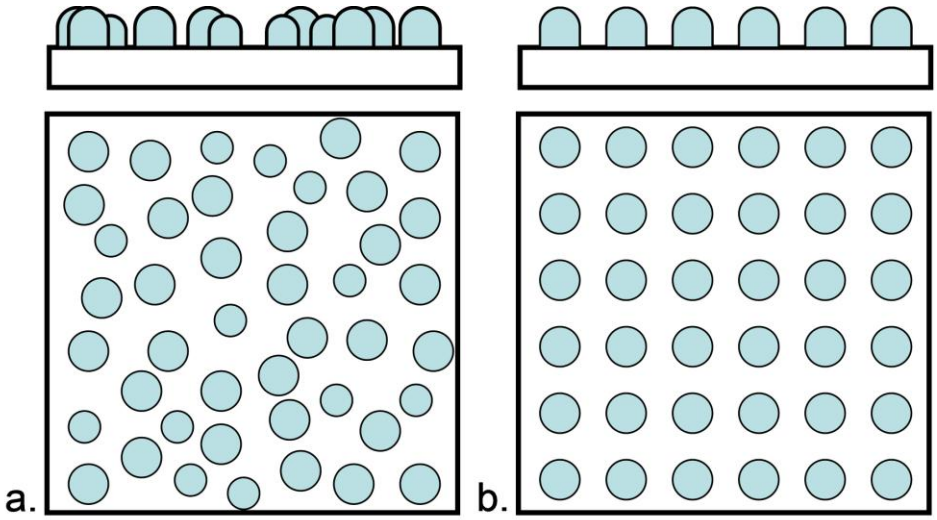

Figure 2.10. Schematic showing nucleates at the start of deposition. Both a side and top view is shown. a.) depicts the random nature of nucleation without seeding the surface before deposition. b.) depicts a seeded array where the nucleates are pre-patterned prior to deposition. By seeding the surface, the spacing and overall structure of the thin film can be controlled.

write lithography,[255, 265] and monolayers of self-assembled nanospheres.[266-267] In designing the seed layer the flux angle, seed width, seed planar height as well as the lattice spacing must be taken into consideration.[255] It is clear in Figure 2.10 that a thin film would have a structural difference when seeding is employed prior to GLAD deposition. Uniform and periodic columns would result, ideal for some sensing applications (GLAD applications are described in detail in section 2.3 of this chapter)

2.2.2.2. Structure Control – Angles and Rotation

A relationship has been established between the incident flux angle, α, and the columnar growth angle, β, of the microstructures comprising the thin film. Tait *et al.* studied the effects that changing α had on β.[20] Figure 2.11 shows the relationship between α and β. Also included is the Tait equation. Based on this relationship, the desired growth angle may be achieved through deposition at the corresponding flux angle. With a flux angle of 0°, a dense array results whereas a large, or oblique, flux angle around 80° results in a more porous array as seen in Figure 2.12.[17]

Since the density varies with flux angle, the range of microstructures attainable is limited using a conventional single source deposition. By implementing multiple sources and changing the amount of flux material coming from different angles simultaneously, the porosity may be held constant and the growth angle altered.[17] By varying the location of the source metal relative to the substrate, it is possible to control and maintain the growth angle.

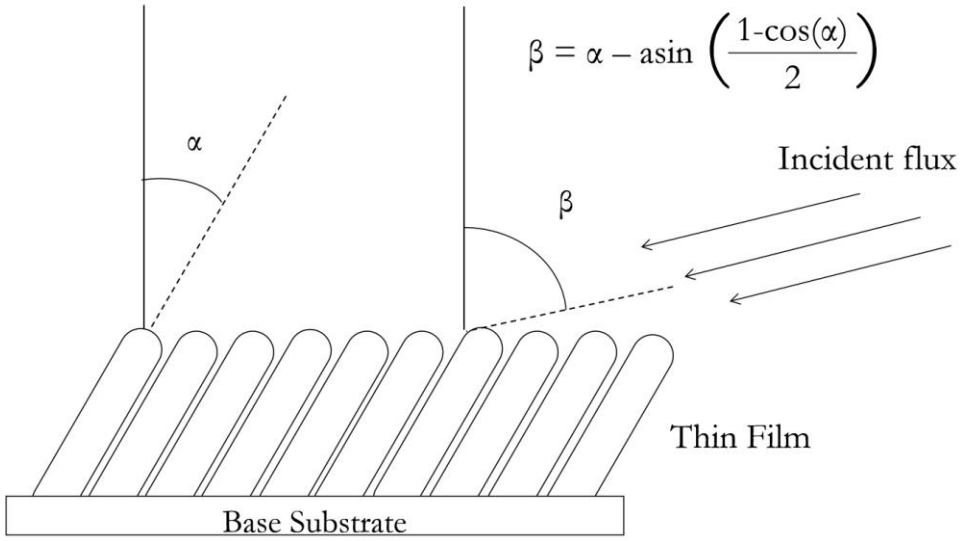

Figure 2.11. Schematic of the flux angle, α, and the growth angle, β, for GLAD. Because of self shadowing during deposition, the flux angle determines the growth angle. Both angles are measured from the substrate normal. Image was adapted from [17]. Also included is the Tait equation demonstrating the fixed relationship between α and β.[20]

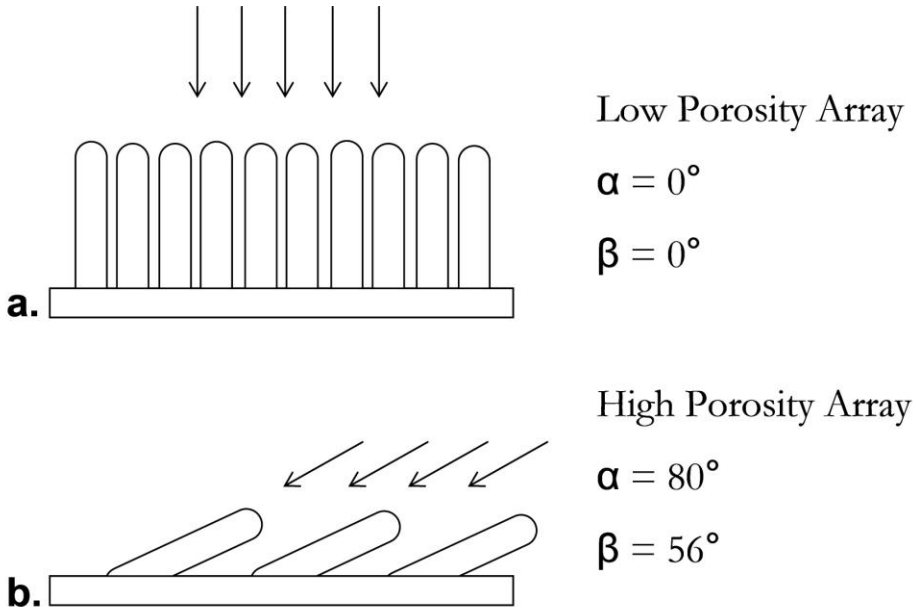

Figure 2.12. Schematic depicting the range of porosities when the flux angle is varied. Two extremes are represented. (a.) no tilting of the substrate results in vertical pillars and (b.) oblique angle of deposition results in slanted and porous arrays. Intermediate thin films are possible as well. Image adapted from [17].

In addition to porosity, the physical nature of the structures within the array may be controlled. Column broadening due to atomic shadowing was previously described in section 2.2.2 of this chapter. Rotating the substrate during deposition reduces this phenomenon. Rotation about an axis perpendicular to the substrate, φ rotation, allows for flux to arrive equally from all azimuthal directions and keep α constant (refer to Figure 2.7).[234] Rotation using an angle of 0.2° may be utilized to account for slight movement of the sample holder during deposition and hold the substrate at the same position throughout evaporation.[268]

Additionally, a variation of φ rotation (refer to Figure 2.7) was studied by Jensen and Brett[269] and referred to as PhiSweep. The basis behind this technique involved additional parameters such as sweep angle and sweep pitch. Sweep angle refers to the angle the substrate is rotated during deposition and the sweep pitch designates the thickness of deposition in between rotations. Essentially, a small amount of material is deposited before and after rotation in a repeating pattern, maintaining symmetry and hindering column broadening.[264] In addition to controlling the broadening, the structure itself may be influenced. If the sweep angle is large enough, growth takes on two different directions; towards the source at each substrate position. The sweep angle may also be altered to effect the tilt angle of the columns at the substrate surface.[270]

Other shapes such as “zig-zags”[17, 271] and coils have been fabricated by holding the flux angle constant, and rotating the substrate about its normal during deposition.[16] These two structures are presented in Figure 2.13. To create zig-zag structures (black

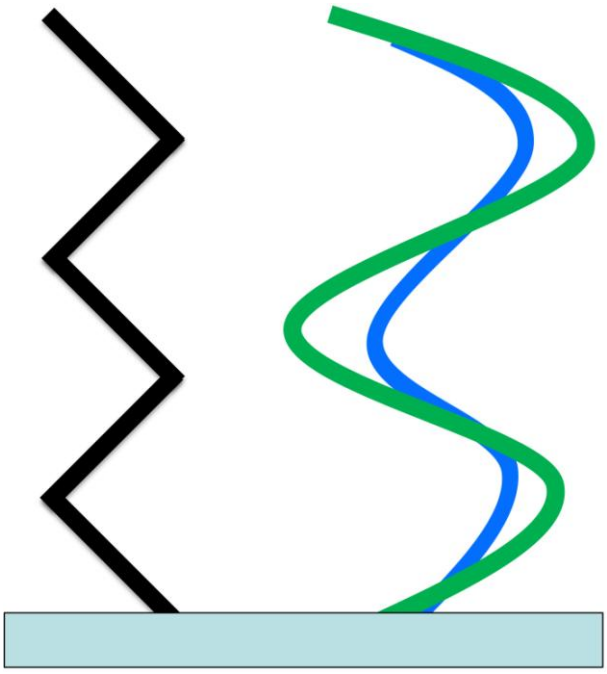

Figure 2.13. Drawing depicting zig-zag (black) and coil (green and blue) shapes fabricated by holding the flux angle constant and rotating the substrate about its normal during GLAD deposition.[16] The black zig-zag is the result of deposition moving the substrate 180°. The coils result from rotating the substrate at a constant rate relative to the deposition rate. Both the pitch of a coil and the growth angle can be controlled. Specifically, the pitch can be held constant while β changes. The green coil has a smaller β then the blue coil.[17]

structure), deposition was carried out at one angle and then the substrates were rotated about φ 180°. Effectively, columns grow towards the source in two different directions resulting in zag-zags. To create a coil-like structure (blue and green structures), rotation is carried out at a constant rate relative to the deposition rate. The resulting microstructures consist of helices with a constant pitch.[16] Using multiple rotations during deposition, the pitch of a coil can be held constant and the growth angle can be controlled to create the desired structure. Robbie *et al.* demonstrated the pitch could be held constant and β changes.[16] They showed this with two helices where one helix was deposited using conventional deposition with a single source and a single rotation point. A second helix was deposited with adding additional points of rotation and the structure was controlled where the pitch of the helix was maintained and β varied (green versus blue structure).

An additional technique developed to control the structures at the surface became known as serial bideposition (SBD).[272] During deposition, material is deposited at oblique angles and then abruptly rotated 180° every few nanometers. Typically, competitions of the column broadening and tilting mechanisms during growth reduce the overall anisotropy of the thin film. However, using SBD where the average deposition angle is normal to the substrate surface, vertical and highly pronounced anisotropic structures result.

2.3. Applications of Substrates Fabricated Using GLAD

Overall, GLAD can be used to produce a wide variety of substrates with a high degree of anisotropy dependent upon the deposition parameters. Based on the desired use for these

substrates, the differing properties of thin films consisting of columns, coils or zig-zags may be advantageous. The following is an overview of applications using GLAD substrates.

2.3.1. Optical Sensors

Typically optical interference coatings are created with materials of differing refractive indices resulting in coatings with specific transmission and reflection properties.[273] Using GLAD, the refractive index can be manipulated using a single source material in a controlled fashion by adjusting the vapor flux angle throughout deposition. Tailoring the porosity also affects the refractive index. Because of the small structure sizes, the arrays seem homogenous to light when the structures themselves are uniform in nature.[274] Upon manipulating the structural elements, the refractive index changes appropriately. This control allows for fabrication of structures with refractive index profiles desirable for optical interference filters, broadband anti-reflection coatings and birefringent omnidirectional reflectors.[244, 275-279]

Additionally, sensitivity to environmental changes typical of optical coatings can be improved using GLAD structures.[280] Functionalization of hydrophilic GLAD-based fibers with hydrophobic self-assembled monolayers (SAMs) results in optical filters insensitive to ambient water pressure.[281] Furthermore, when used as humidity sensors, GLAD substrates can be fabricated to incorporate defects in the film resulting in narrow bandpasses whose spectral location as a function of humidity is easily tracked. With increasing humidity, the peak shifts to longer wavelengths within the stop band.[274, 280]

2.3.2. Increased Surface Area

Based on the columnar structure making up GLAD thin films, a drastic increase in surface area is achieved. This increase relies heavily on the material and deposition conditions. It has been reported that the maximum surface enhancement in relation to a flat surface is achieved with a flux angle of 70°.[282] An increase in column size coupled with a decrease in columns with an increased spacing account for the higher surface area.

2.3.2.1. Electrode Systems

With the increased surface area described above, an increased number of analyte molecules may bind the metal surface. An example of this is with titanium dioxide (TiO_2), commonly used for dye sensitized solar cells (DSSC's). Essentially, the greater number of dye molecules bound directly to the metal electrode increases the efficiency.[283] This has been performed by Kiema *et al.* specifically using GLAD to fabricate their TiO_2 structures.[237] Solid oxide fuel cells have also been constructed using GLAD.[284] Yitria-stabilized zirconium columns were back-filled with cerium oxide (CeO_2) using a sol-gel, making a high interface density electrode structure. This technique enhances the conduction efficiency of the reaction.

2.3.2.2. Sensors Systems

Since GLAD structures are porous, gaseous analyte may be introduced easily. With the diffusion of gasses through the column structures, a change in the dielectric constant may be observed. Thin films made of oxides, specifically silicon monoxide (SiO), TiO_2, and aluminum oxide (Al_2O_3), are hydrophilic in nature. This attribute causes capillary condensation of water vapor within the array.[250] Because of the free flowing nature of

the gas, molecules are able to adsorb and desorb rapidly. The response time is an improvement compared to other techniques. Currently, a response time of 42 ms has been reported.[285] A more porous array will result in a lower sensitivity to humidity changes than those with a denser array because of the decreased pore size. With this detail, sensors may be optimized for a specific process.

2.3.2.3. Chemical Processes

GLAD substrates have been used to monitor chemical reactions at the surface of the microstructures. Specifically, platinum helical columns have been used to detect the catalysis of oxidation for automobile exhaust species such as CO, C_3H_6, and C_3H_8.[251] The conversion was not as efficient as other methods but is still promising in terms of future applications. Another use of TiO_2 films has been shown in monitoring the photo catalysis of the degradation of organic compounds bound to the surface. The GLAD structures were analyzed by changing the flux angle and monitoring photobleaching of methylene blue dye.[286] The response was optimal at a flux angle of 75°, close to the angle at which the surface area is the greatest. Functionalization of metal oxide GLAD thin films has also been studied.[287-288] Through hydroxyl functionalization, the columns become targets for siloxane-based chemical reactions. Based on the treatment method, vapor or solution based, the wettability of the surface can be controlled creating an interesting approach for chemically tuning a surface.[226]

2.3.3. Multifunctional Patchy Particles

Pawar and Kretzschmar used GLAD to create multifunctional patchy particles with varying dimensions of “patchiness”, “branching”, and “chemical ordering”. GLAD was coupled with a stamping technique to isolate particles and allow access to the entire

particle surface during deposition.[289-290] The patch size on each particles was controlled by changing the angle of vapor deposition. GLAD was carried out on a close-packed colloidal monolayers and the substrate was tilted during deposition within an evaporator. The monolayer was removed from the evaporator and repositioned with the opposite side of the nanoparticles facing the incident flux so that varying degrees of anisotropy were achieved on the same particle, producing "patches". This technique allows for the production of particles with varying dimensions of anisotropy. One such use for these particles is as colloidal motors due to the electrical contacts resulting from metal overlap on the particle surface.[291]

2.3.4. Silver Nanorod Arrays

Recently, GLAD has been used to fabricate silver nanorod arrays. The specific technique has become known as oblique angle deposition (OAD), a variation of GLAD. Figure 2.14 displays a scanning electron micrograph of a silver nanorod array. These arrays have proven to be excellent substrates for use with surface enhanced Raman scattering (SERS). These arrays have been shown to be highly uniform in structure, easy to fabricate, and provide strong, highly reproducible, SERS signal enhancements.[132-141, 143-148, 162] Through the shadowing and limited surface adatom diffusion, the array forms at a tilt off the surface. Variation in the deposition parameters will result in nanorods of different aspect ratios. The high SERS signal enhancement seen with silver nanorods results from the chemical and/or electromagnetic enhancement mechanisms described previously in Chapter 1.[58-59] The electromagnetic field contributing to the electromagnetic enhancement is theorized to be at a maximum for points with high

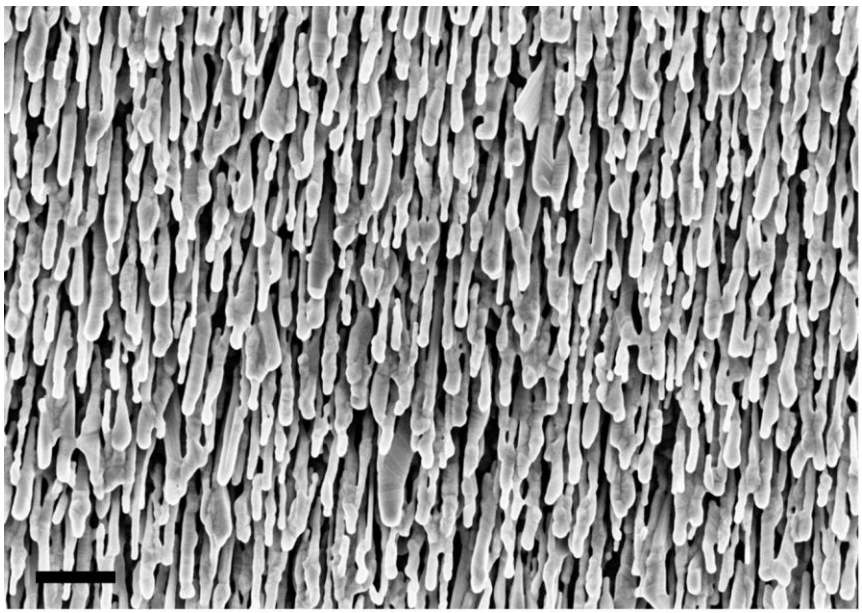

Figure 2.14. SEM micrograph depicting silver nanorod array substrates fabricated using oblique angle deposition.

curvature,[91] further supporting the use of nanorod arrays fabricated using OAD as SERS substrates.

Length studies were carried out at a flux angle of 86° to determine the optimal aspect ratio to provide the greatest enhancement for trans-1,2-bis(4-pyridyl)ethane (BPE), a Raman active probe molecule.[134] The SERS enhancement factors reached a maximum of 5×10^8 as the nanorod length approached 868 nm and then decreased to 3×10^6 as the nanorod length increased further to 1900 nm. Although the enhancement was seen to be greatest for rods 900 nm long, significant enhancement is seen with slightly shorter rods as well.[292]

CHAPTER 3

PATTERNED SILVER NANOROD ARRAY SUBSTRATES FOR SURFACE ENHANCED RAMAN SPECTROSCOPY

3.1. Introduction

Recently, substrates comprised of silver nanorod arrays have been shown to be highly uniform in structure, easy to fabricate, and provide unprecedented signal enhancements. [134-141, 143-145, 147] For silver nanorod (AgNR) arrays, a flux angle of 86° has been shown to be optimum for SERS applications.[134, 136-138, 226, 265, 274, 293] Variation in the levels of this and other empirical parameters negatively impacts the consistency of the physical characteristics and SERS performance of substrates fabricated by physical vapor deposition. One solution to this problem is to prepare multiple substrates per batch and to pattern each substrate enabling multiple analyses per substrate.

Presented in this chapter is an improved method for batch fabrication and patterning of SERS substrates. A modified platen for a commercial electron beam evaporator was designed to enable the simultaneous deposition of AgNR arrays onto six microscope slide substrates. Following removal of slides from the evaporator, wells were patterned by contact printing of a polymer onto the nanorod array surface. Well dimensions are defined by penetration of the polymer into the AgNR array and subsequent photocuring.

Inherent advantages of this method include: 1) simultaneous production of several nanorod array substrates with high structural uniformity, 2) physical isolation of AgNR arrays from one another to minimize cross contamination during sample loading, 3) dimensional compatibility of the patterned array with existing SERS microscope, 4) large SERS enhancement afforded by the nanorod array format, 5) small fluid volumes, and 6) ease of use for manual delivery of fluids to each element in the patterned array. In this chapter, the well-to-well, slide-to-slide, and batch-to-batch variability in physical characteristics and SERS response are critically examined.

3.2. Methods and Materials

3.2.1. Substrate Fabrication

SERS substrates were fabricated from standard 25 x 75 mm glass microscope slides. The process began by immersing each slide in "piranha" solution for 30 min, copious rinsing with deionized water, and drying under a flowing nitrogen gas stream. (Note: "Piranha" solution must be handled with care; it is extremely oxidizing, reacts violently with organics, and should only be stored in loosely tightened containers to avoid pressure buildup.) Next, slides were placed in a CVC-601 DC Sputtering tool (Consolidated Vacuum Corp., Rochester, NY) and thin films of titanium (50 nm) followed by silver (500 nm) were deposited onto one side of the slide normal to the surface. The titanium under-layer promotes adhesion of the silver to the glass surface.[292]

The substrates were then positioned on the specially designed sample stage in a CVC-SC5000 electron beam evaporator (Consolidated Vacuum Corp., Rochester, NY). Silver (99.99% from Kurt J. Lesker, Clairton, PA) was deposited onto the slides at a deposition

rate of 3 Å/sec, a starting pressure of 1 x 10^{-6} Torr, and at a flux angle of 86° from normal until the deposition thickness on the quartz crystal monitor (QCM) reached a reading of 1.5 μm. Since the monitor is located closer to the source metal, this value is not representative of nanorod length or average film thickness (Figure 2.4). The substrates were allowed to cool under vacuum for at least 10 min prior to backfilling the chamber with nitrogen and removal from the tool. Substrates were packaged in UniMailer™ slide holders (VWR Scientific Inc., West Chester, PA) and stored in a desiccator until use.[292]

3.2.2. Substrate Patterning

Each slide was mounted in a specially designed base (Figure 3.6a) with the nanorod array surface facing upward and in a fixed orientation with respect to nanorod growth direction. Next, a stamp comprised of aluminum round tubing (TTRA-05-12, Small Parts Inc, Miramar, FL) press fit into an aluminum plate was brought into contact with a thin film of UV curable epoxy (OG142, EPO-TEK, Billerica, MA) previously spread onto a clean microscope slide. Then, the stamp was brought into momentary contact with the Ag nanorod array with a vertical load sufficient to transfer the polymer to the Ag substrate. The pattern transferred to the substrate consisted of 36 rings and a solid circular marking indicating nanorod growth direction as shown in Figure 3.6b. The slide was removed from the base and exposed to UV light for 10 min (UltraLum Model EA40 UV Transilluminator, Claremont, CA) to cure the polymer. Following patterning, slides were returned to the holder and stored as above.[292]

3.2.3. Substrate Characterization

Substrates were characterized by scanning electron microscopy (SEM) using a Zeiss SEM Ultra60 scanning electron microscope (Carl Zeiss SMT Inc., Peabody, MA). Images were acquired with an accelerating voltage of 5 eV and at an incident angle of 52° relative to the surface normal. To minimize charging artifacts, slides were attached to the holder using double-sided copper tape. Images were collected in a minimum of five locations on each substrate for comparison purposes. Analysis of image features was performed using SmartTiff^{TM}, a software tool made available by Zeiss.

Ion milling of the AgNR surface was performed using a FEI Nova NanoLab 200 dual ion/electron beam microscope (FEI Corp., Hillsboro, OR). The substrate was imaged using the electron beam with a 10 kV operating voltage and a beam current of 0.54 nA. The ion beam uses a gallium ion source with beam current of 30 pA and an operating voltage of 30 kV. To prevent beam induced damage of the surface, the ion beam was not used to image the surface. Analysis of image features was performed using SmartTiff^{TM} as well.

SERS spectra were obtained with a Kaiser Optical Systems' Holoprobe 785 spectrometer (Kaiser Optical Systems, Inc., Ann Arbor, MI) using an excitation wavelength of 785 nm, a 10x objective, an integration time of 10 sec and a surface power of 4.5 mW. Rhodamine 6G (R6G) was used as the SERS probe. This analyte was used as received from Tokyo Kasei Kogyo Co. Ltd., (Toshima, Japan). Stock solutions of 1.0 mM R6G were prepared in deionized water and in saline-sodium citrate buffer (1X SSC, pH=7.4).

This buffer is prepared in 150 mM trisodium citrate and 15 mM sodium chloride and pH was adjusted to 7.4 using hydrochloric acid (Thermo-Fischer Scientific, Inc., Waltham MA). Test solutions were prepared by serial dilution of each stock. To characterize the SERS performance of each substrate, 5.0 μL aliquots of the test solution were applied to the desired well and allowed to dry in a desiccator. A minimum of five spectra were recorded per well at random locations. In some cases, spectra were acquired across an entire well at 25 μm intervals. Spectra were collected using GRAMS/32 (Galactic Industries Corporation), processed in Excel (Microsoft, Redmond WA), and background corrected using a program written in MatLab (The MathWorks, Inc., Novi, MI). Spectra were not rescaled or normalized unless otherwise noted. Figure 3.1 presents example spectra acquired for both R6G and DNA solutions. The full spectrum (0 – 2000 cm^{-1}), truncated spectrum (300 – 1800 cm^{-1}), background corrected spectrum, and normalized spectrum are included to demonstrate that no spectral bands were shifted or lost during processing.

3.3 Results and Discussion

In conventional GLAD fabrication, a single substrate is positioned directly above the source material (see Figure 2.7).[234] This ensures minimal variability in the flux angle[20] and maximal metal plume density[15, 294-298] during evaporation from one batch to another, assuming all other empirical parameters, including substrate location within the vapor plume, remain constant. When additional substrates are positioned above or below this one, the nanorod array on each substrate will be of differing length and porosity.[143] Substrates closer to the heated metal source will have longer nanorods; substrates further away from the heated metal source will have shorter

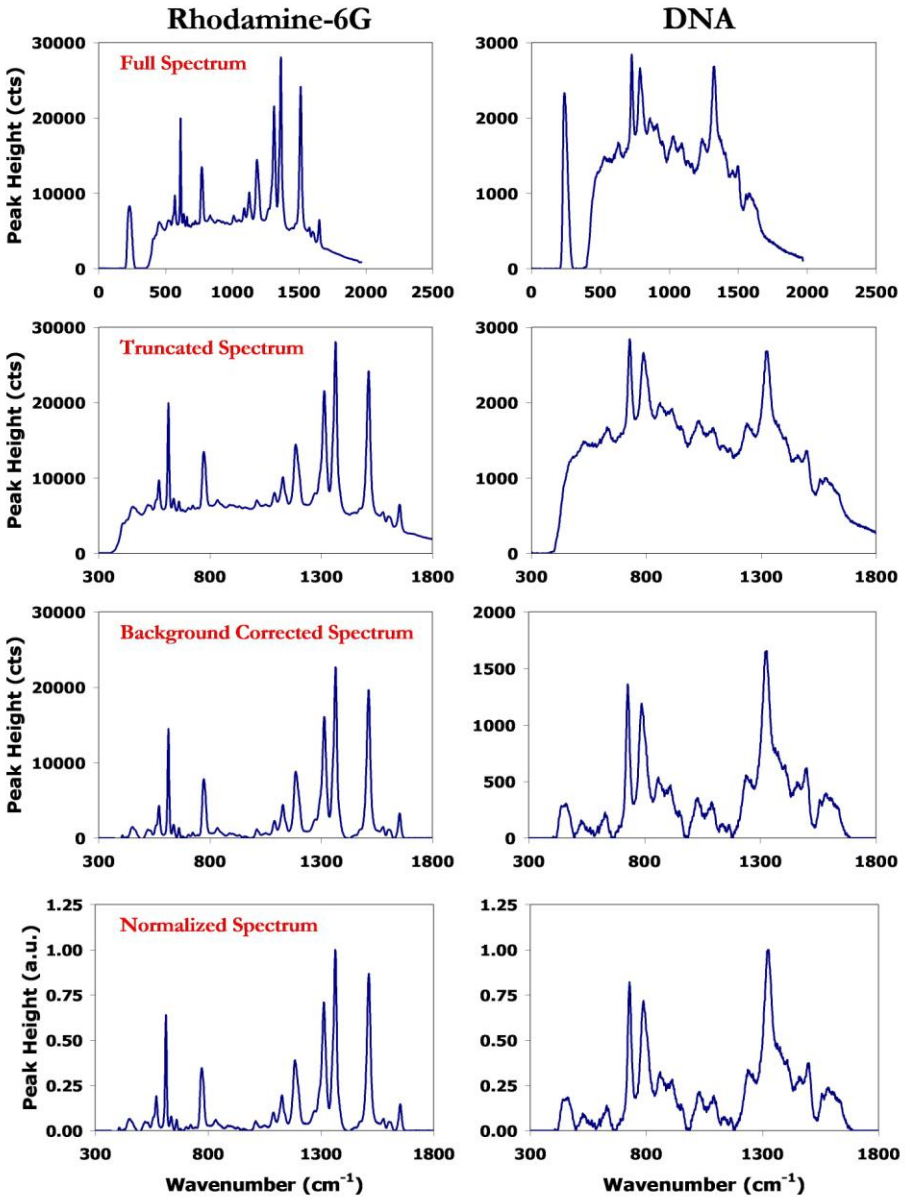

Figure 3.1 Data processing used in comparing spectra to one another. Spectra on the left represent a high enhancement factor probe molecule, rhodamine-6G, and the left are spectra representative of a lower enhancement scattered, DNA. The peak at around 250 cm^{-1} in the full spectrum for both molecules is attributed to the Raman instrument itself and is not from contamination on the surface.

nanorods. The growth angle will also vary with distance since vertical stacking requires that each successive substrate be slightly offset from the one below to avoid shadowing effects.[17] This offset changes the flux angle and atomic vapor density. In this context, we designed a holder that places each substrate at the same distance and fixed angle from the source, thereby minimizing the metal vapor flux angle and density variability. This is shown schematically in Figure 3.2.

A custom multi-substrate stage was designed specifically for use in a CVC electron beam evaporator; a photograph of the stage and all of its components is presented in Figure 3.3. The stage consists of a circular aluminum platen with four aluminum rod stand-offs machined to enable rapid and reliable placement into the multi-user evaporator (Figure 3.3a.). A square opening (17.0 cm per side) was cut into the platen to allow the metal plume to pass (figure 3.3b.). Because the specific tool is equipped with multiple crucibles that can be rotated into position during an evaporation, the center of the square was located above the source position rather than at the center of the platen. A hexagonal opening was cut into the center of a square aluminum plate with two aluminum positioning pegs extending below the plate for ease of placement into opening of the circular standoff plate. To the square plate, six angled slide holders were mounted flush with the edge of the hexagonal opening and held rigidly in place by two screws (Figure 3.3c.). Standard 25 x 75 mm glass microscope slides were mounted onto each holder by placement of the long edge of the slide onto a 1.0 mm deep ledge that was cut into each holder; double-sided adhesive tap ensured that the slide would not move during transfer or metal deposition. The center of each slide was rigidly held at a horizontal distance of

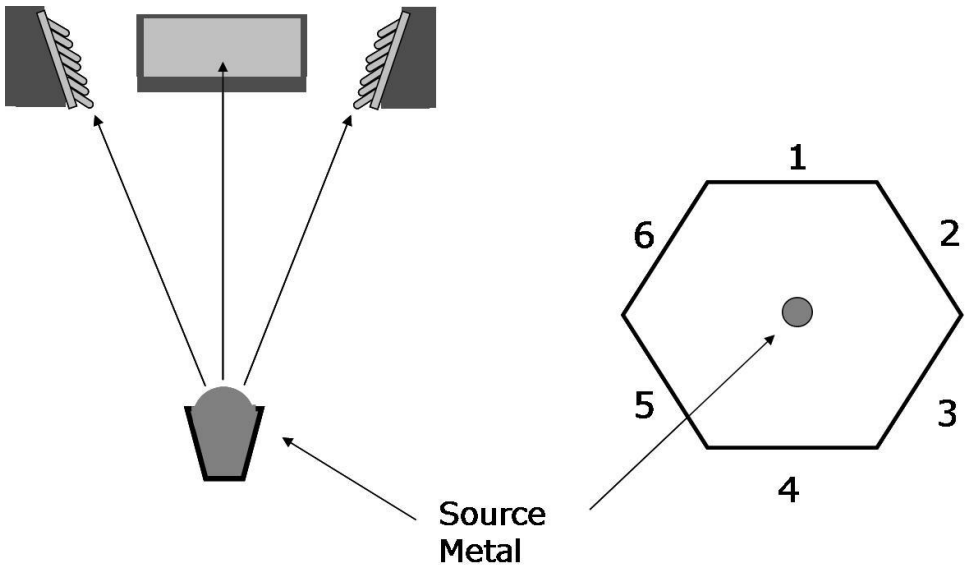

Figure 3.2. This figure presents a schematic of nanorod fabrication using the custom built multi-substrate holder. Positions of each of the glass microscope slide substrates in relation to the source metal are indicated by the numbers on the rightmost image.

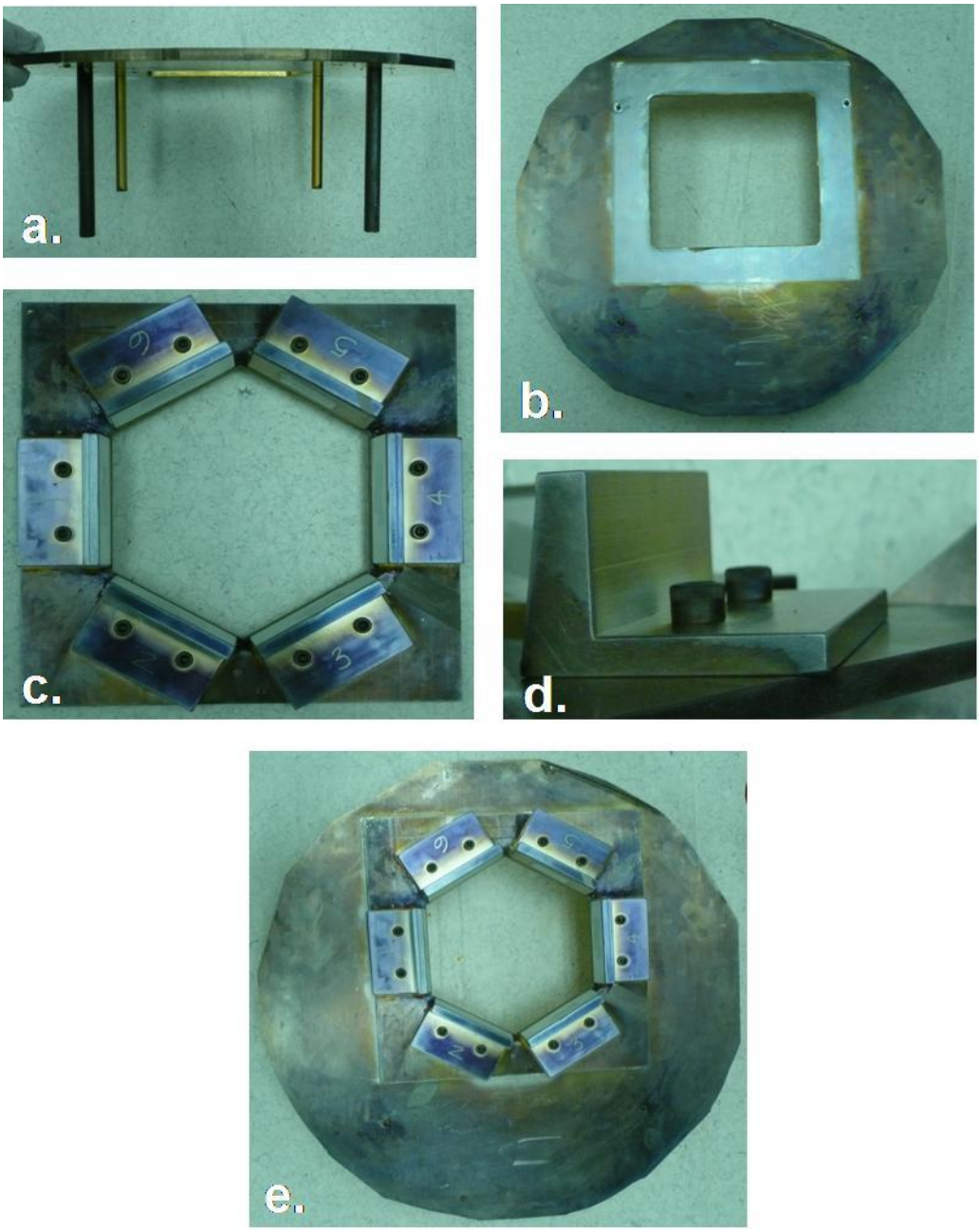

Figure 3.3. Photographs of the components of the multi-substrate holder: A) side view of the circular aluminum platen showing the four aluminum rod standoffs; B) topview of the platen showing the square opening allowing plume to pass; C) topview of the square aluminum plate to which six angled substrate holders are attached; D) sideview of a single substrate holder; E) topview of the assembled apparatus.

8.5 cm and a vertical distance of 42.1 cm from the source and at a fixed angle of 80.9°. This angle provides a flux angle of 86° during metal deposition. An individual slide holder is presented in Figure 3.3d. The entire apparatus is shown assembled in Figure 3.3e.

An SEM micrograph of the Ag nanorod array is presented in Figure 3.4a and is typical of those obtained for all six substrates in each batch. Images acquired in this fashion illustrate the consistency of nanorod thickness and spatial distribution; measurement of nanorod growth angle and length required FIB milling of a portion of the array to enable edge-on viewing (Figure 3.4b). Analysis of images acquired following focused ion beam (FIB) milling of each substrate indicated that a consistent growth angle of 57 ± 0.5° and a flux angle of 86 ± 0.5° were achieved with our custom slide holder. Nanorod lengths were 450 ± 15 nm across a single slide, 450 ± 20 nm across a batch, and 450 ± 15 nm between substrates from different batches. If the substrate holder was not centered above the source metal during deposition, the resulting array was unusable. The change in particle density within the plume and incident flux angle creates arrays of varying porosities and aspect ratios. This is demonstrated in Figure 3.5.

To maximize the number of samples analyzed per substrate, polymer wells were patterned onto the substrates through contact printing using the stamp depicted in Figure 3.6. The stamp assembly consists of a slide holder and stamp. A rectangular slot was cut into an aluminum plate to rigidly hold the slide in fixed position during stamping. Four guideposts were attached to the corners of the holder plate; compression springs were

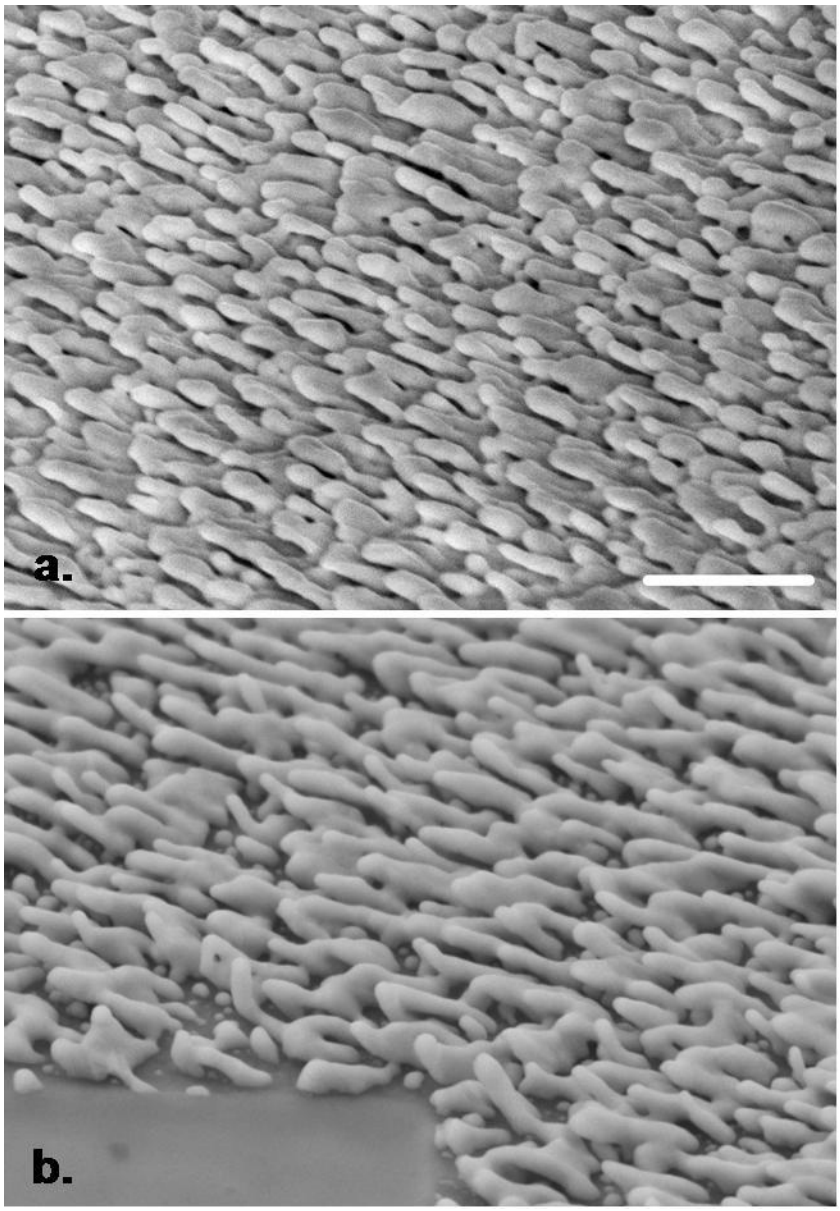

Figure 3.4. a.) Typical SEM micrograph following deposition of Ag nanorod arrays. Image was obtained at an angle of 52° relative to the surface normal; b.) SEM micrograph following FIB milling of a portion of rods. The scale bar denotes 1 μm and is applicable to both images. Note that the two images were acquired using different SEM tools.

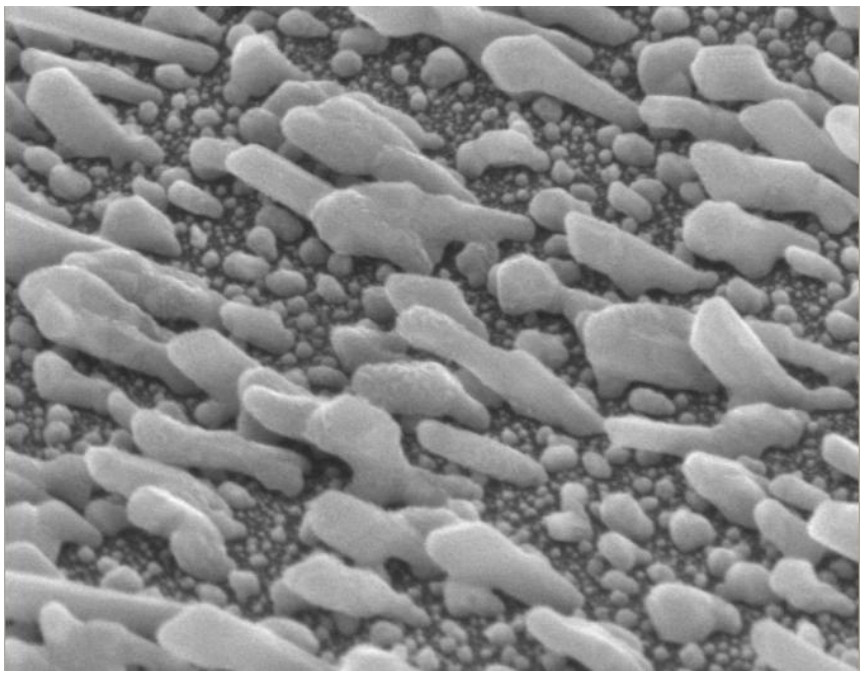

Figure 3.5. Ag nanorod arrays resulting from uneven centering of the substrate holder within the evaporator. The porosity and lengths are different from the nanorods shown in Figure 3.4 where the appropriate flux angle and placement within the plume were accomplished.

placed onto these guideposts to mediate the pressure applied to the substrate during stamping. The stamp consisted of thirty-six aluminum tubes (0.18 mm outer diameter) positioned in three rows of twelve with 1 mm spacing which were press fit into second aluminum plate. To mark the growth orientation of the nanorods, a closed end aluminum rod was press fit into the aluminum plate adjacent to one of the tubes. In Figure 3.6a, this rod is located below the tube on the lower right side of the stamp.

Circular wells were patterned onto the slide by momentary contact of the stamp, pre-loaded with UV curable epoxy, onto the nanorod array. This particular epoxy was chosen because: 1) walls can be created in a single application, 2) it has an indefinite handling time, 3) there is no out-gassing during curing, and 4) UV exposure did not diminish the SERS performance of the nanorods (see below). Figure 3.6b shows a photograph of a patterned substrate. The filled circle in the bottom left corner indicates that the direction of nanorod growth is up. Each well holds up to 20 μL of sample solution. The number of wells per substrate can be readily increased and the volume of sample reduced by using tubing of smaller diameter. From our experience, the spacing on the existing stamp of 1 mm between individual wells is optimal for preventing wicking of solution from neighboring wells.

The SERS performance of each substrate was determined using R6G. A 5 μL aliquot of an aqueous solution of R6G (10^{-5}M), with or without buffer, was placed into the wells and allowed to evaporate. Figure 3.7 presents a spectrum typical of those obtained for aqueous solutions without buffer.[123, 299-300] Also included is the background

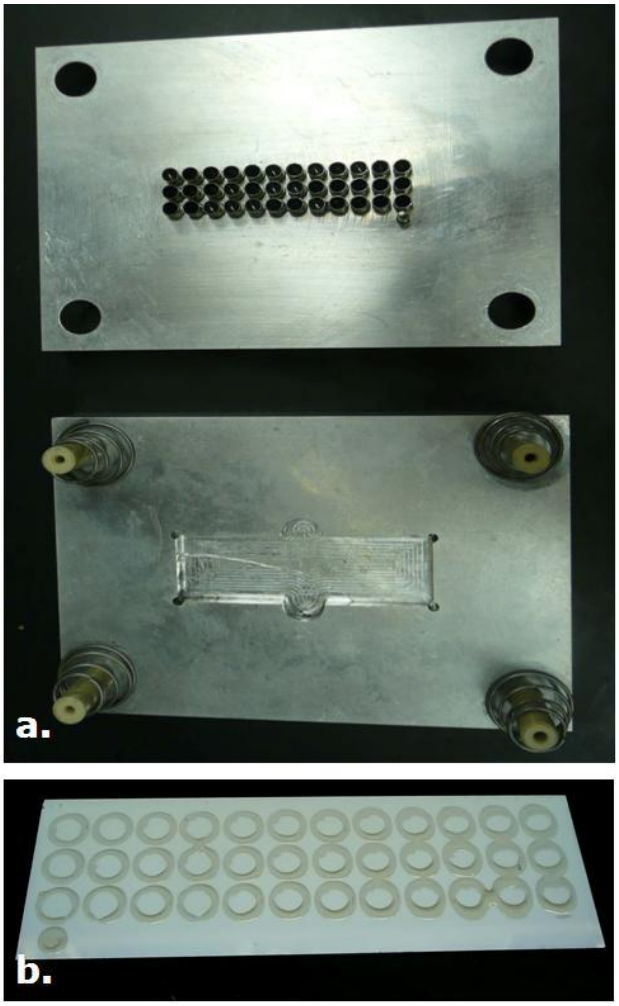

Figure 3.6. a) Photograph of the stamp assembly used for patterning nanorod substrates; Top portion represents the tubing that transfers polymer and the bottom portion hold the substrate during stamping. b) Photograph of a patterned Ag nanorod substrate containing 36 individual wells and a marker to denote nanorod growth.

corrected spectrum, demonstrating that no spectral information was lost during data processing. The spectrum contains all the spectral bands expected for this molecule. A surface enhancement factor[79] of 1 x 10^7 was computed for the 1360 cm^{-1} band relative to bulk analyte. This value falls within the range previously reported for SERS substrates produced by GLAD.[134]

Figures 3.7a and 3.8a present photographs of two adjacent wells from the same slide following evaporation of 50 picomoles of R6G dissolved in water and in 1X SSC buffer, respectively. In Figure 3.7a, the dotted line designates the area covered by analyte. In Figure 3.8a, the entire area of the well is covered by analyte suggesting that the presence of salt in the sample solution dramatically increases the wettability of the AgNR surface.

Spectra were acquired across each well in 25 μm steps, along the red dashed line in the photographs in the figures. The background corrected peak intensities obtained as a function of position are plotted in Figure 3.7b and 3.8b for the aqueous and buffered R6G solution, respectively. The span of the x-axis in both plots encompasses the diameter of each well. There is minimal variability in peak intensity of all four spectral bands across the well where analyte was deposited from water solution (Figure 3.7b). This data suggests that there is uniformity in both analyte concentration and SERS enhancement within the array.[126] In contrast, spectra acquired across the well containing buffered R6G displays peaks of lower intensity and greater variability (Figure 3.8b). The reduced intensity is presumably due to the increased spatial distribution of analyte across the well resulting in a decrease in number of analyte molecules within the laser spot. The

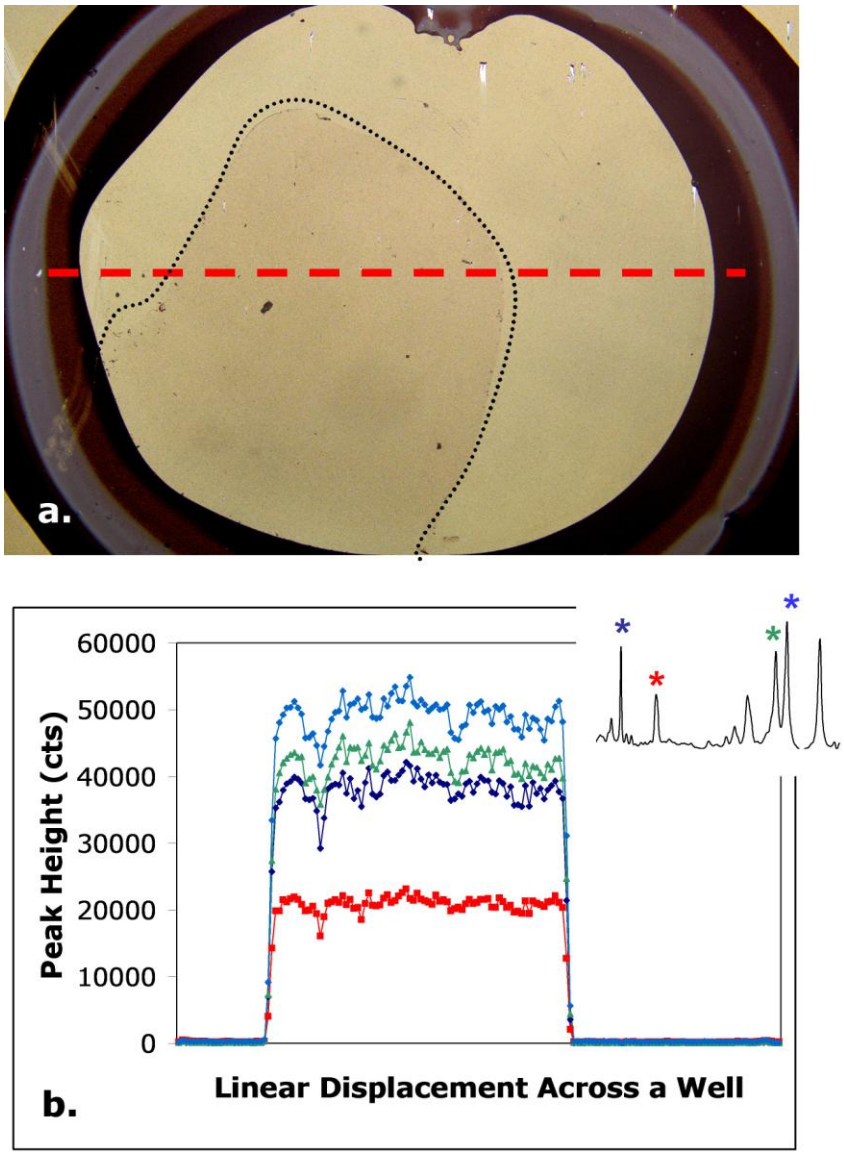

Figure 3.7. a.) Optical image of a well on the patterned SERS substrate following evaporation of 5.0 μL aliquots of R6G in nanopure water. b.) SERS spectra were acquired in 25 μm step increments along the red dashed line. SERS peak intensities for the spectral lines of R6G designated in the inset are plotted as a function of position across the well after background correction. Thin dashed line represents the evaporation spot for R6G. Note that the substrate used for this data had nanorods that were 900 ± 25 nm in length.

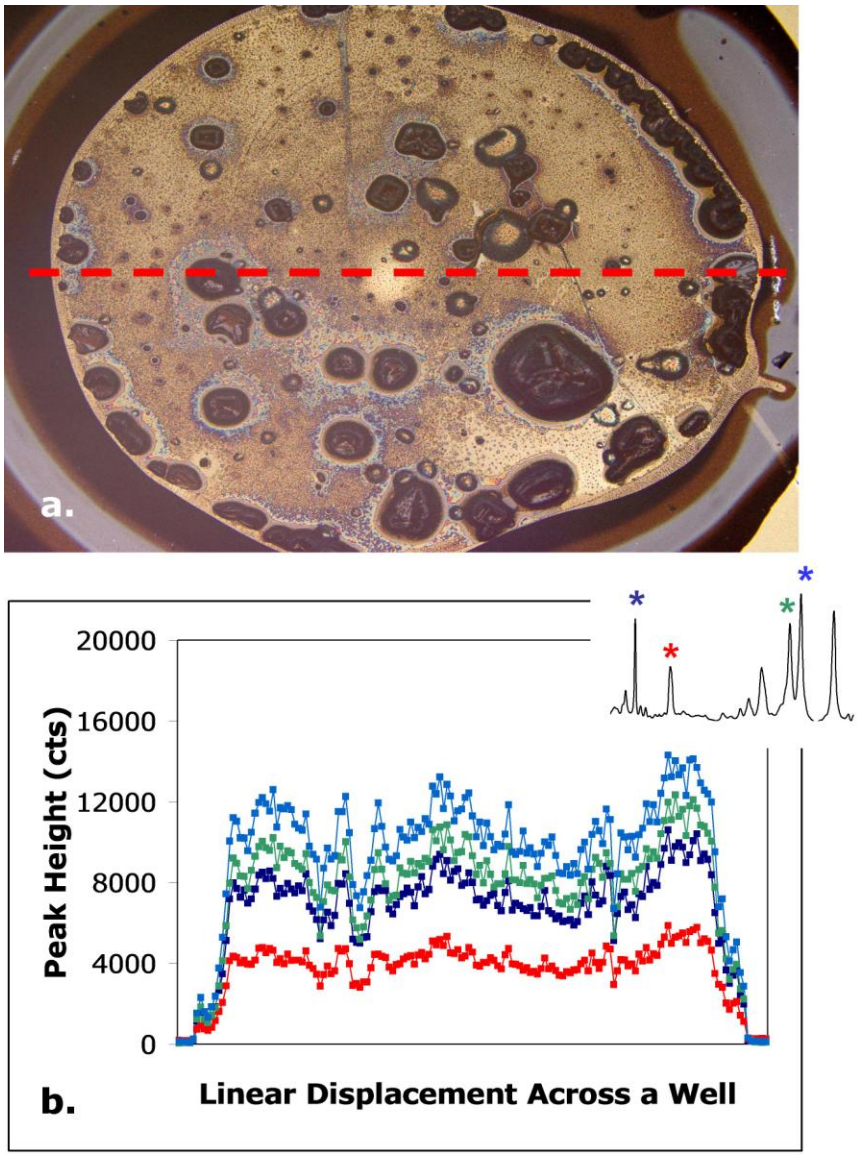

Figure 3.8. a.) Optical image of a well on the patterned SERS substrate following evaporation of 5.0 μL aliquots of R6G in 1X SSC buffer. b.) SERS spectra were acquired in 25 μm step increments along the red dashed line. SERS Peak intensities for the spectral lines of R6G designated in the inset are plotted as a function of position across the well after background correction. Note that the substrate used for this data had nanorods that were 900 ± 25 nm in length.

increased variability in signal intensity as a function of position is most likely a result of spectral interference from salt crystal deposits on top of and within the Ag nanorod array (Figure 3.8a). Figure 3.9 presents a zoomed in image of the crystal deposits. Based on this finding, comparison of the SERS performance from well to well, substrate to substrate, and batch to batch was assessed using an unbuffered solution of R6G.

Figures 3.10 through 3.13 compare the peak intensities for R6G acquired as a function of well number, substrate number and batch number. Each data point is the average intensity of at least five spectra acquired at different locations with the well. The error bar denotes the standard deviation from the average value. It has been previously shown that the magnitude of SERS enhancement depends upon nanorod length.[134] The length of the nanorod depends upon the plume density and duration of metal deposition. As a result of the design characteristics of our substrate holder, the edges of each slide are located at distance of 0.17 cm farther from the source than the middle of the slide. Similarly, the top of each slide is located at a distance of 3.37 cm farther from the source than the bottom of the slide.

Figure 3.10 presents a plot of peak intensity as a function of well number across a row of wells on a single substrate. Minimal variation in SERS peak intensity is observed across the row, suggesting nominal changes in nanorod length, a fact supported by SEM characterization. Figure 3.11 presents a plot of peak intensity as a function of well number down a column of wells on the same substrate. The variance in SERS peak intensity is greater than across the well. The curvilinear trend suggests that SERS

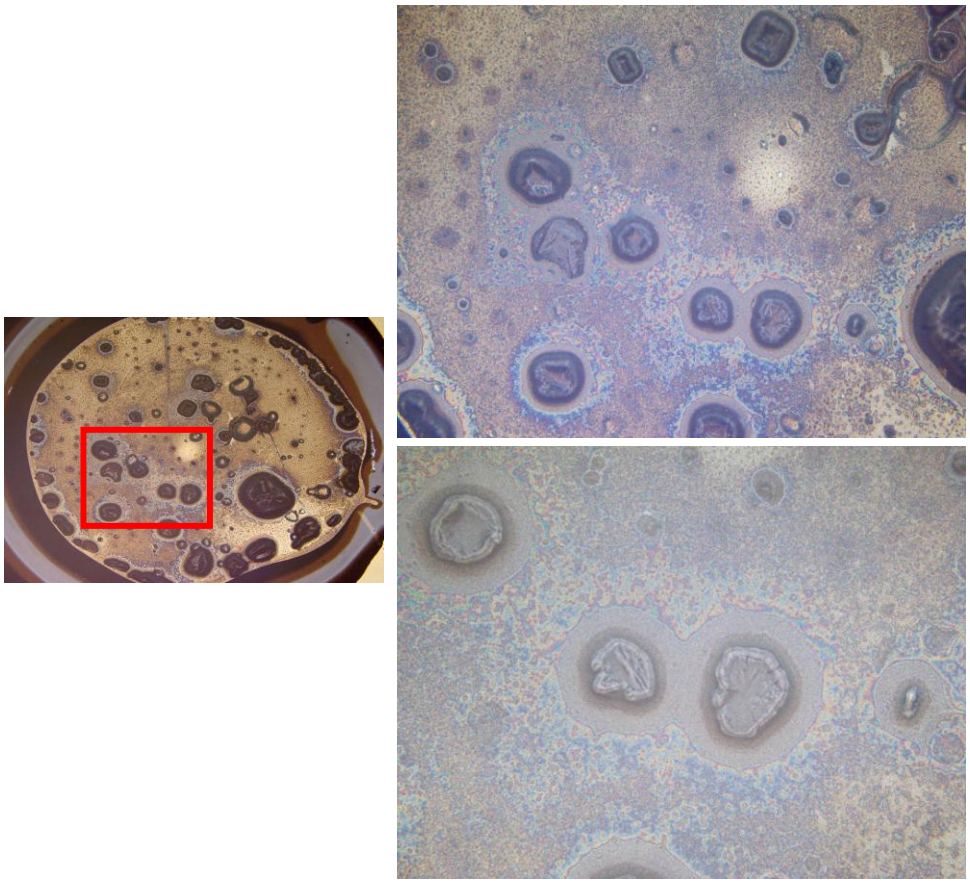

Figure 3.9. Optical micrographs of the same region within a well on a silver nanorod substrate at various magnifications. The red box in the image on the left designates the zoomed in region shown in a and b. The left image was acquired at 5x, a.) was acquired at 10 x and b.) was acquired at 20 x further demonstrating the effect the buffered environment has on the nanorod surface.

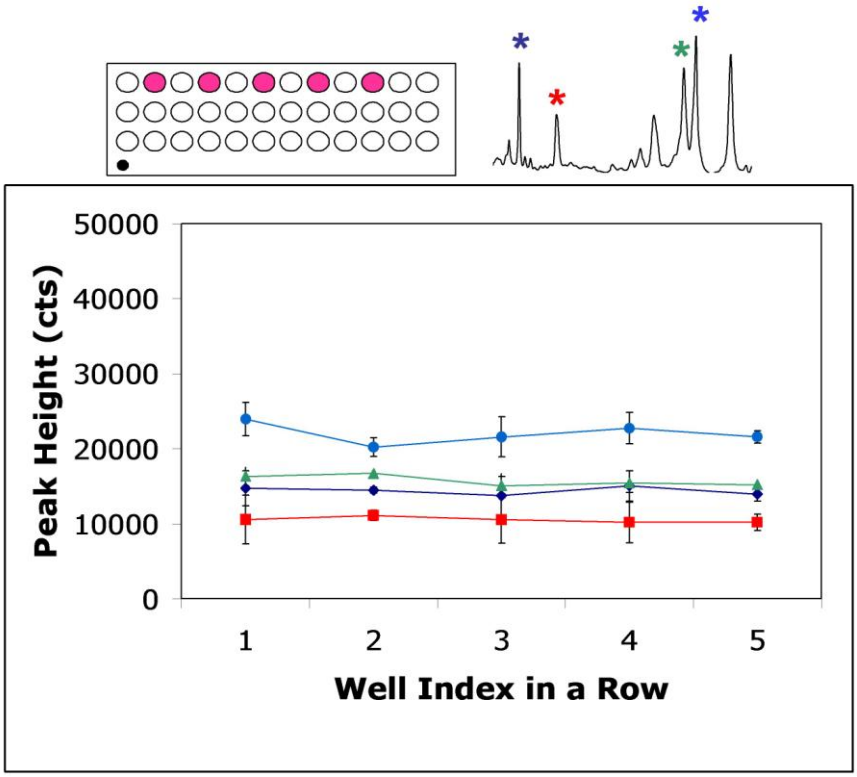

Figure 3.10. Plot of peak intensities for the bands identified in the small plot for R6G as a function of well number across a row on a single substrate made using the custom sample holder in Figure 3.3. The included substrate cartoon shows the wells corresponding to the data points.

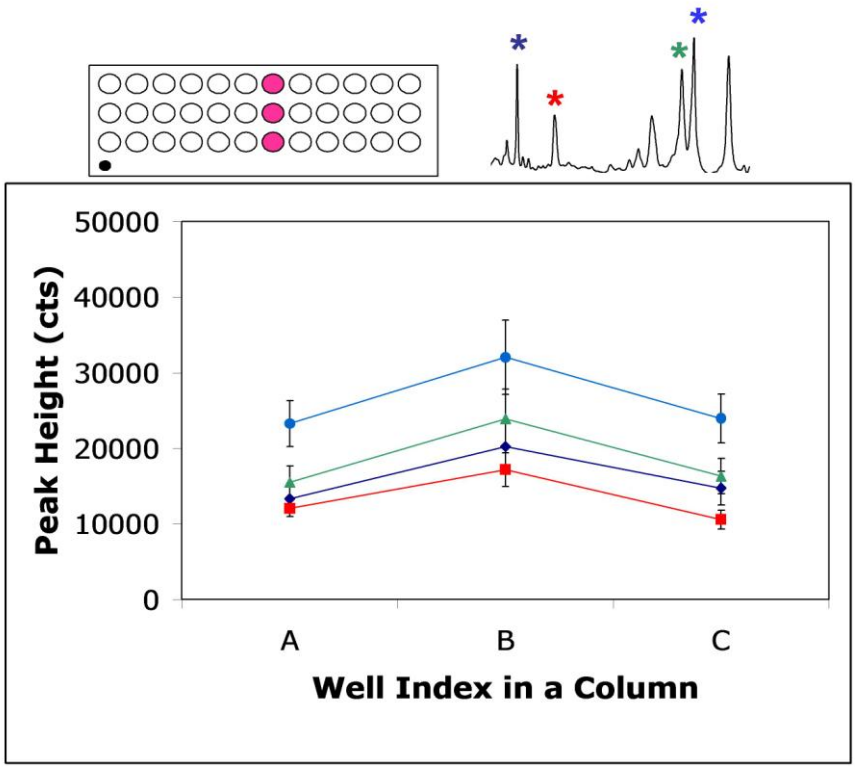

Figure 3.11. Plot of peak intensities for the bands identified in the small plot for R6G as a function of well number down a column on a single substrate made using the custom sample holder in Figure 3.3. The included substrate cartoon shows the wells corresponding to the data points.

enhancement is a function of both nanorod length and growth angle. The higher intensity of row B supports the optimization of the sample holder for the middle of the microscope slides.

Figure 3.12 presents a plot of peak intensity for the 771 cm^{-1} band acquired on specific wells across a row as a function of slide position within a given batch. A small amount of variability is observed from one substrate to another and reflects differences in the plume density from slide to slide. Because of our efforts to hold each slide at an exact distance from the source, we attribute this difference in plume density to the random and uncontrollable movement of the electrical arc on the ingot during deposition. This effect may be minimized by rotation of the platen during deposition, a feature outside the capability of our evaporator. Figure 3.13 presents a plot of peak intensity for the 771 cm^{-1} band acquired on specific wells across a row on slide #1 as a function of batch. The performance repeatability from batch to batch is a factor of two better than that previously reported.[134]

3.4. Conclusion

Multiple nanorod array substrates may be fabricated in a conventional electron beam evaporator by judicious placement of each substrate within the metal vapor plume. Careful control of evaporation parameters results in high uniformity of nanorod morphology and SERS performance characteristics from one batch to another. Patterning of the substrate following nanorod deposition increases the number of assays that can be performed from a single batch. Variability in SERS performance was 6% (relative

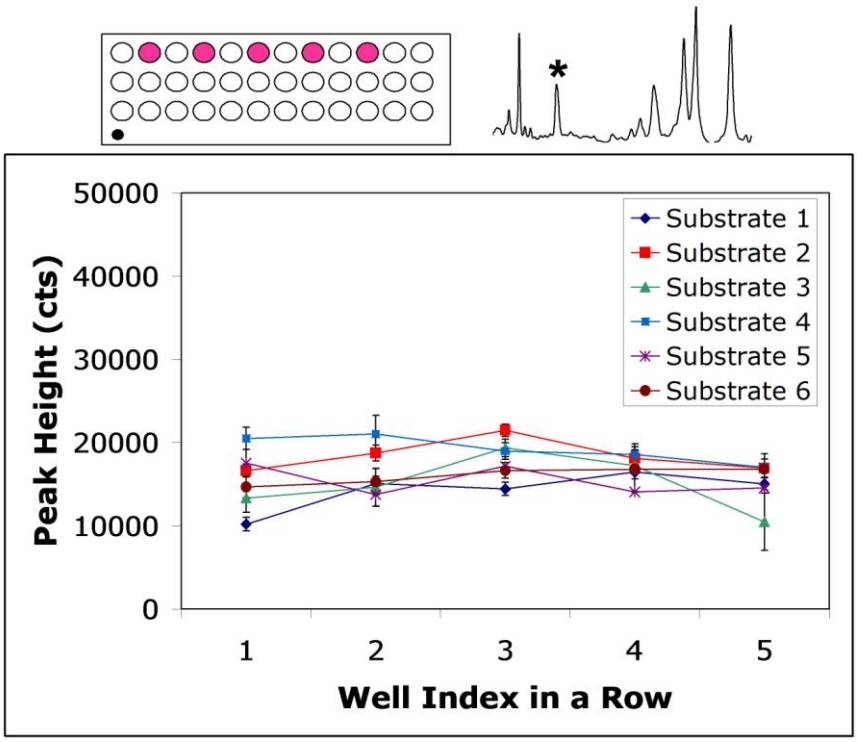

Figure 3.12. A plot of the peak intensity for the 771 cm^{-1} band as a function of well number across a row for all six substrates fabricated in the same batch made using the custom sample holder in Figure 3.3. The included substrate cartoon shows the wells corresponding to the data points.

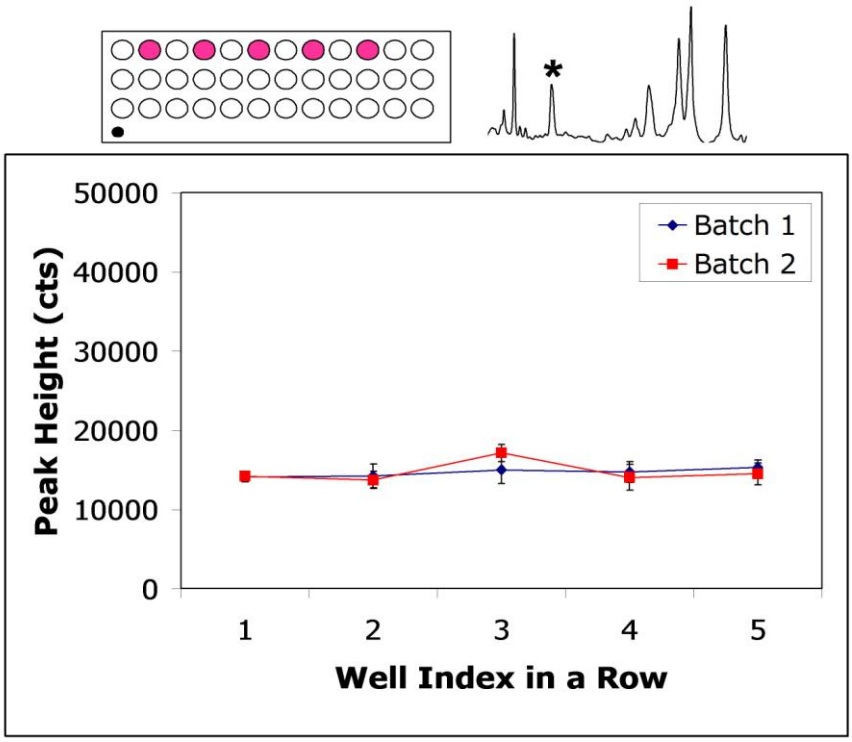

Figure 3.13. A plot of the peak intensity for the 771 cm^{-1} band as a function of well number across a row for all six substrates fabricated in the from two different batches made using the custom sample holder in Figure 3.3. The included substrate cartoon shows the wells corresponding to the data points.

standard deviation in intensity) across a substrate, 25% down a substrate, 15% from one substrate to another within a batch and only 8% from batch to batch. Note that these variations were determined from background corrected spectral intensities *without normalization*.

CHAPTER 4

THERMAL STABILITY OF SILVER NANOROD ARRAYS

4.1. Introduction

An issue in the continued development of silver nanorod (AgNR) array SERS substrates is their stability over time. One objective for these substrates was the development of a SERS-based nucleic acid hybridization assay using AgNR array substrates. A critical aspect of this application involves heating and cooling of nucleic acids on the array to promote formation of the hybrid and minimize mismatches.

A decrease in SERS performance upon thermal cycling was observed, prompting further investigation into the effect of temperature on AgNR structure. Thermally-induced changes in surface morphology were evaluated using SEM and x-ray diffraction (XRD) and correlated with changes in SERS enhancement. The findings presented in this chapter suggest that the shelf-life of AgNR arrays is limited by migration of silver on the surface. This rate of migration is enhanced by the presence of a surface layer of chemisorbed oxygen. Our analysis of the thermal stability of AgNR arrays is reported in this chapter. The application of AgNR arrays for DNA hybridization is presented in Chapter 7.

4.2 Methods and Materials

4.2.1. Substrate Fabrication

4.2.1.1. Method 1

See the method of fabrication described in detail in Chapter 3, section 3.2.1.

4.2.1.2. Method 2

The Ag nanorod substrates were fabricated using a custom-designed electron-beam/sputtering evaporation e-beam system. The apparatus used enabled the substrates to remain in vacuum for the entire fabrication process. The standard glass microscope slides were mounted on a sample holder and placed directly above the source. Thin films on the sample surface at normal incidence and then stepper motors rotated the substrates so that the flux angle was 86° from normal. AgNRs were deposited at a rate of 3 Å/sec, a base pressure of 1 x 10^{-6} Torr and grown to a final thickness of 900 nm in length.

Following deposition using either method, each AgNR substrate was cut into eight 12.5 mm x 18.75 mm chips. Chips were placed on a preheated hotplate, held at a fixed temperature for prescribed amounts of time, and then cooled under ambient conditions.

4.2.2. Substrate Characterization

Substrates were characterized by SEM and SERS as described in Chapter 3, section 3.2.3. For SERS measurements, solutions of 1x10^{-5} M R6G in nanopure water (18Ω) were prepared and 5 μL aliquots were applied to each chip following thermal treatment and allowed to evaporate. Chips were stored in slide holders and stored in a desiccator until

characterized. XRD was performed using a Panalytical X'Pert Pro Multi-Purpose Diffractometer (MPD) with an Anton Paar HTK1200 furnace. Samples were heated in air or under nitrogen, sampling XRD patterns every 5 min.

4.3 Results

Figure 4.1a presents an SEM micrograph typical of AgNR arrays prepared using Method One and stored under ambient conditions. Image analysis revealed a consistent growth angle of 57 ± 0.5° and nanorod lengths of 450 ± 15 nm across the middle of the slide. Figure 4.1b depicts the SERS spectrum obtained for R6G. This intensity equates to a SERS enhancement factor of ~10^7.[292] When a chip from the same substrate was held at 75 °C for just 5 min, both coarsening of the silver nanostructure (Figure 4.1c) and a ten-fold decrease in SERS enhancement were observed (Figure 4.1d). This decrease in enhancement with surface reorganization parallels the relationship previously observed between SERS intensity and AgNR length.[134] The substrate used in acquiring the data presented in Figure 4.1 was fabricated using Method One in which a break in vacuum and exposure to atmospheric oxygen occurred between deposition of the titanium and silver under layers and AgNRs.

Figure 4.2a shows an SEM micrograph typical of AgNR arrays prepared using Method Two and stored at room temperature (25 °C). With this method, both the under layers and the AgNR arrays are deposited without breaking vacuum. Image analysis revealed a consistent growth angle of 57 ± 0.5° and nanorod lengths of 870 ± 25 nm across the middle of the slide. A comparison of Figures 4.1a and 4.2a reveals that the Ag nanorods fabricated using Method Two have a higher aspect ratio than those fabricated using

Method One. Nanostructures fabricated with Method Two give SERS intensities for R6G of over 50,000 counts, as shown in Figure 4.2b. This equates to a SERS enhancement factor of 10^8.[134]

When a chip from this substrate was held at 75 °C for 30 min, no change in SERS signal intensities was found. Similarly, no change in SERS intensity was observed when a chip was held at 125 °C for 5 min. However, when this chip was held at 125 °C for 30 min, some coarsening of the surface was observed (Figure 4.2c). The resultant deformation of the nanostructure led to approximately a 30% decrease in overall SERS enhancement, as shown in Figure 4.2d. When a third chip from this substrate was held at 150 °C for 30 min, coarsening of the nanorod surface similar in extent to that shown in Figure 4.1d resulted (see Figure 4.2e). The original nanorod structures are no longer existent, having deformed into globular mounds. The corresponding SERS spectrum (Figure 4.2f) presents SERS enhancement so diminished that peak heights are approximately 90% smaller than those obtained from SERS spectra of the unheated AgNR array.

Figure 4.3 presents a comparison of SERS intensity as a function of temperature for substrates prepared by the aforementioned methods. Due to the variation in enhancement between the two, intensities were normalized to those observed for the 611 cm^{-1} band of R6G on chips held at ambient temperature. Substrates exposed to oxygen *prior* to nanorod fabrication undergo a sharp decrease in SERS enhancement when maintained at temperatures above 60 °C for only 5 min. In contrast, substrates exposed to oxygen *after*

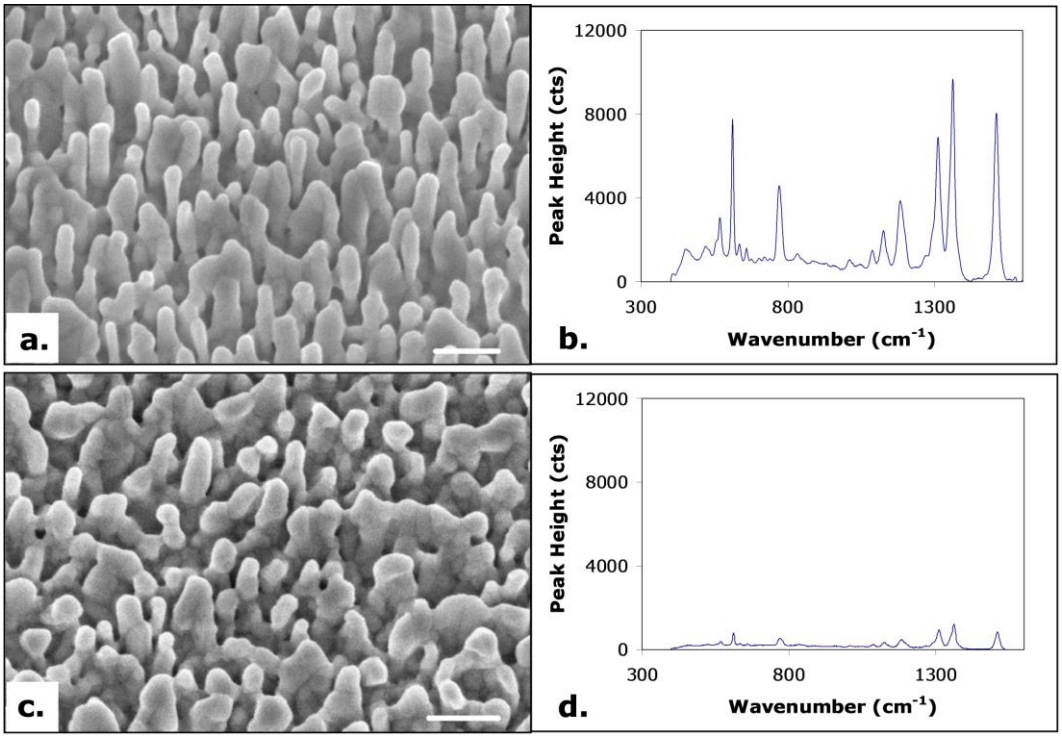

Figure 4.1. SEM micrographs of an AgNR array substrate acquired at an incident angle of 0° normal to the substrate surface. Substrates prepared using Method One before (a) and after (c) heating at 75 °C for 5 min in a conventional oven are provided. Scale bars in the images denote 1.0 μm. SERS spectra of 1.0 x 10^{-5} M R6G obtained on this substrate is shown before (b) and after (d) heating.

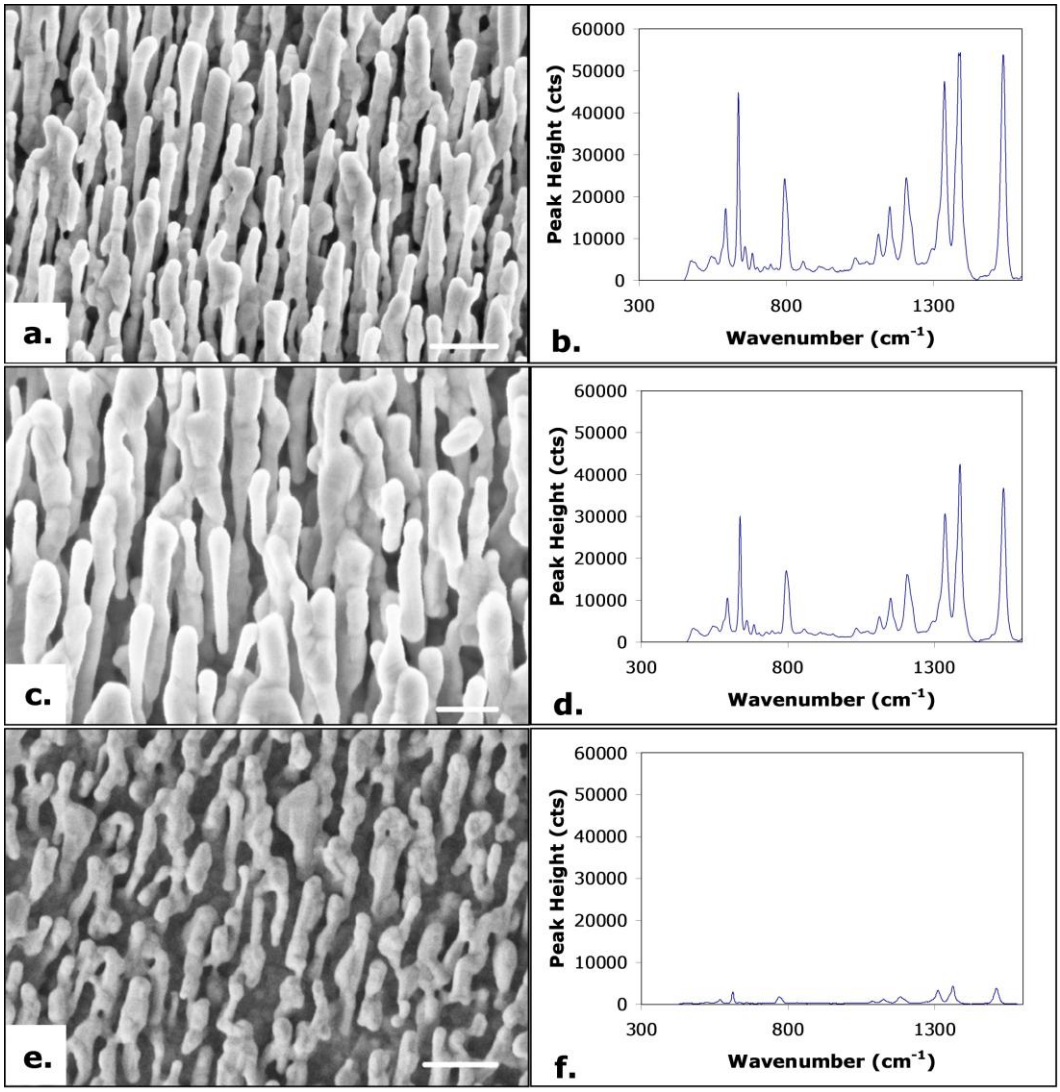

Figure 4.2. SEM micrographs of an AgNR array substrate prepared using Method Two (a) before, (c) after heating at 125 °C for 5 min, and (e) after heating at 150 °C for 5 min in a conventional oven. Images were acquired at an incident angle of 0° normal to the substrate surface. Scale bars in the images denote 1.0 μm. SERS spectra of 1.0 x 10^{-5} M R6G obtained on this substrate is shown before (b) and after (d & f) heating.

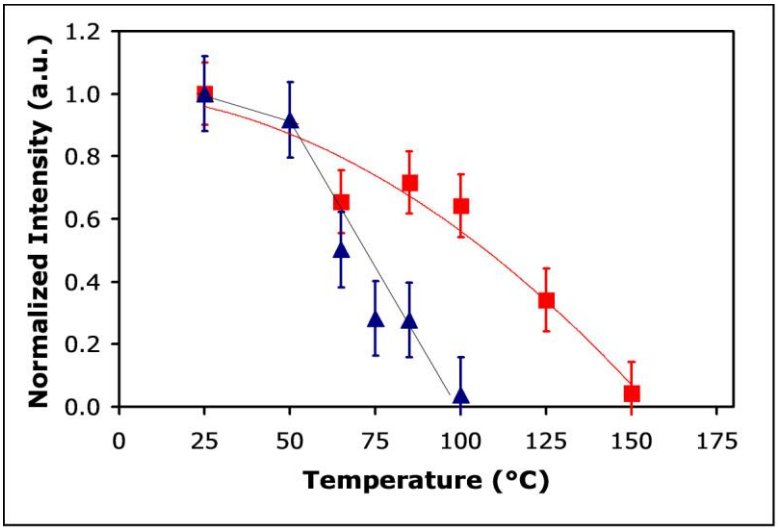

Figure 4.3. Plot of the normalized SERS intensity for the 611 cm^{-1} band versus temperature for the substrate prepared using Method One (triangle) and Method Two (square). The data points listed in this figure are the average intensities (with standard deviations indicated by the error bars) observed at five or more locations on the same chip. Trend lines have been added to aid in clarity.

nanorod fabrication exhibit a decrease in SERS intensity when maintained at temperatures above 100 °C for 30 min.

Silver surfaces are known to undergo rearrangement at temperatures well below their bulk melting point.[301-302] Degradation of SERS enhancements following thermal annealing of substrates has also been previously reported. Liu and coworkers have found a 20% decrease in SERS response when substrates prepared by electrochemical roughening were held at temperatures greater than 125 °C.[299, 303] Whitney *et al.* reported that shifts in the local surface plasmon resonance of silver nanoparticles were dependent upon annealing temperature.[120, 304] Previous studies of the thermal stability of structured silver surfaces were undertaken at higher temperatures. To our knowledge, this is the first report that the thermal stability of AgNR arrays depends upon the method of preparation.

Figure 4.4 presents the XRD data performed to determine crystal structure changes upon surface reorganization during heating. From the XRD spectrum only peaks for silver are seen with a strong (111) alignment in the initial spectrum prior to heating. As the temperature of the substrate was increased to 150 °C, the peak corresponding to (111) increased by 30% indicating an increasing number of silver crystallites with the (111) plane parallel to the sample surface. This correlates to a surface reorganization towards equilibrium. SEM taken of the substrate post XRD analysis and heating resembled the image presented in Figure 4.2e. No difference in the rate of change or appearance of the final XRD spectrum was observed when a control chip was heated under a nitrogen

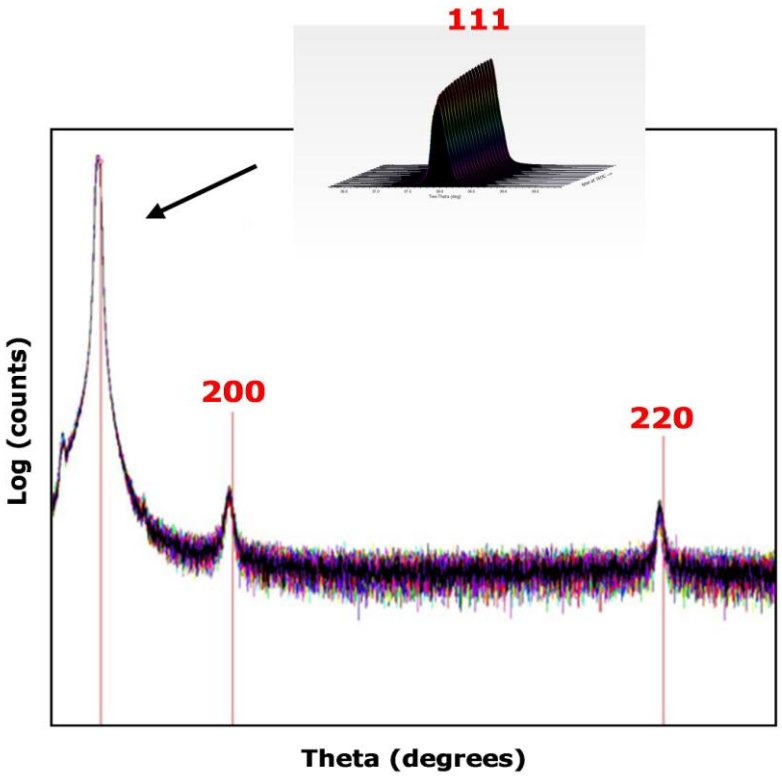

Figure 4.4. Plot of X-ray diffraction (XRD) data indicating the change in crystal structure upon surface reorganization as a result of heating. Peaks for the (111), (220), and (200) crystal directions were present in the initial spectrum taken before heating. Inset plot depicts the (111) peak growing by roughly 30% upon heating to 150 °C for a total of 90 minutes. Spectra were acquired every five minutes and overlaid to show the growth over time.

environment. These XRD results demonstrate the intrinsic instability of the nanorod structure and its tendency to reorganize into a more stable structure.[305]

4.4 Discussion

Our findings demonstrate that AgNR arrays are thermally unstable. Silver surface atoms are known to migrate at room temperature.[301, 305-324] This migration is rapid,[325] anisotropic,[326-328] and results from diffusion and coalescence of silver islands (i.e. Smoluchowski ripening) as well as diffusive mass transfer from smaller to larger islands (i.e. Oswald ripening) to minimize the free energy at step edges.[309, 322-323, 329] Heating increases the rate of nanostructure coarsening.[307, 320, 330-333] Several groups have studied the coarsening of silver using scanning tunneling microscopy.[320, 324] Semin *et al.*[320] found that the average silver island radii increased by approximately 35% when held at 42 °C for 4 hr. They showed that post-deposition coarsening is a thermally activated process with an activation energy of just 13 ± 2 kcal/mol. Our Ag nanorods increased in radius within minutes upon heating.

Upon exposure of silver to air, a layer of chemisorbed oxygen is formed.[309, 334-344] Layson *et al.* have shown that oxygen exposure activates low-temperature coarsening.[309-310] Molecular oxygen adsorbs preferentially at kink sites on the silver surface where the activation barrier to dissociation is lowered.[334, 339, 341, 344-347] Migration of silver atoms occurs upon dissociation of oxygen from the surface.[324-325, 334, 345] Thus, the greater the abundance of kink sites on the surface, the greater the extent of silver atom migration. As our XRD results have shown, nanorods are polycrystalline. In addition to the formation of silver-oxide, exposure to air can result in

adsorption of contaminants. Depending upon their chemical composition, contaminants can hasten the rate of migration[348] and/or provide spectral interference for SERS sensing applications.

Substrates exposed to atmospheric oxygen during fabrication (Method One) began surface restructuring at lower temperatures and shorter exposure times than those held in vacuum for the entire process (Method Two). One rationalization for this observed difference is that the oxygen underlayer impacts nucleation. Layson *et al.*[308] have demonstrated that when silver is deposited onto a layer of chemisorbed oxygen, silver atom mobility is increased resulting in the formation of larger islands with a concomitant decrease in island density. They propose several mechanisms that might account for this phenomenon. Fabrication of our AgNR arrays by either method begins with nucleation. In the GLAD process,[17] nanorods grow because the rate of silver deposition exceeds the rate of adatom migration, and because the nanorods are self-shadowing. If the silver islands formed during nucleation on the chemisorbed oxygen layer (during Method One) redistribute and coalesce on the surface by the mechanisms proposed by Layson and coworkers, the base of the nanorods would broaden, resulting in a more conical-shaped nanorod. In contrast, in the absence of an oxide underlayer, a more cylindrical-shaped nanorod is anticipated. Comparison of the shape of the nanorods formed by the two methods (see Figures 5.1a and 5.2a) is suggestive of oxygen-induced coarsening of the nucleates. The difference in nanorod shape may also be due to differences in substrate temperature during deposition.[274] It should be noted that neither evaporator is equipped with a substrate temperature monitor or means to control the substrate

temperature during deposition. Thus, the actual temperature during deposition is unknown. A higher deposition temperature is expected for substrates prepared by Method One since the platen that holds the substrates in the evaporator is closer to the silver source compared to the evaporator used for preparing substrates by Method Two.

In essence, Ag nanorods are kinetic, not thermodynamic products. Oswald and Smoluchowski ripening coarsens the surface and promotes the return of nanorods to their more thermodynamically stable form. Exposure to air hastens silver atom migration and surface contamination. Thus, while the shelf-life of the arrays can be improved by storing them at low temperature under vacuum or inert atmosphere, restructuring of the silver surface is unavoidable. The ultimate impact of this process is the concomitant decrease in surface enhancement when these arrays are used as SERS substrates in sensing applications.

CHAPTER 5

POLYSTYRENE BEADS AS PROBES OF THE SERS RESPONSE CHARACTERISTICS OF SILVER NANOROD ARRAYS

5.1. Introduction

Substrates comprised of silver nanorod (AgNR) arrays have been shown to be highly uniform in structure, easy to fabricate, and provide strong, highly reproducible, signal enhancements.[132, 134, 138-140, 162, 292] The high SERS signal enhancement seen with AgNRs may result from chemical and/or electromagnetic enhancement mechanisms.[58-59] Of particular interest is the electromagnetic enhancement resulting from the interaction of the incident light with the nanoscale roughness on the metal surface.[10-11, 59]

The electromagnetic field is theorized to be at a maximum for points with high curvature, ultimately resulting in greater SERS enhancement.[91] Evidence of this been reported by Murphy and co-workers on isolated silver and gold nanoparticles of various aspect ratios.[92] While it has been suggested that enhancement should be greatest between the nanorods in the array,[141] the 150 nm spacing between nanorods is too large for overlap in electromagnetic fields. The overlap of longitudinal and lateral electromagnetic waves along the nanorods may produce strong electromagnetic enhancement at the rod ends.[92]

To probe this possibility, polystyrene beads were chosen as Raman scatterers. By comparison of SERS signals from beads small enough to spread evenly throughout the

AgNRs with that from beads too large to fit within the AgNRs, the region of highest enhancement was investigated. SERS was used to monitor the enhancement as a function of bead position; SEM and fluorescence microscopy were used to probe the location of the beads within the array.

5.2. Methods and Materials

5.2.1. SERS Substrates

SERS substrates were fabricated and stamped as described in Chapter 3, section 3.2.1. and 3.2.2.

5.2.2. Analytes

Rhodamine-6G (R6G) was used as received (Tokyo Kasei Kogyo Co. Ltd., Toshima, Japan) and serially diluted to a concentration of 1×10^{-5} M in nanopure water. Poly (4-styrenesulfonic acid) solution was received from Sigma Aldrich (St. Louis, MO) and serially diluted in nanopure water. FluoSpheres® sulfate microspheres, 20 nm, yellow-green fluorescent (505/515) 2% solids and FluoSpheres® carboxylate-modified microspheres, 200 nm, orange fluorescent (540/560) 2% solids were obtained from Invitrogen Corporation (Carlsbad, CA). Serial dilutions of microsphere solutions were made in filtered nanopure water.

5.2.3. Substrate Characterization

Substrates were characterized by SEM and SERS as described in Chapter 3, section 3.2.3. The accelerating voltage was not adjusted for samples containing analyte. In some instances, spectra were acquired across a well at 25 μm intervals. Spectra were

background corrected to remove the characteristic fluorescence baseline. Spectra were processed as described in Chapter 3, section 3.2.3.

Fluorescence microscopy was performed after application and evaporation of FluoSphere® solutions using an Olympus 1 x 71 inverted microscope (Olympus Corporation, Tokyo, Japan), 20x objective, and acquisition times ranging from 2-10 msec depending upon the sample. Images were viewed and analyzed using ImageJ software provided by National Institutes of Health (Bethesda, MD).

5.3. Results and Discussion

In previous reports,[292, 349] R6G was used as a Raman probe to characterize the performance of AgNRs as SERS substrates. This probe possesses a favorable scattering cross section that gives rise to large SERS enhancements. However, this molecule is not adequate for identifying regions of highest enhancement due to its size and our inability to pinpoint its location within the AgNR array. Instead, polystyrene beads were chosen as Raman probes. SERS was used to monitor the enhancement as a function of bead position; SEM and fluorescence microscopy were used to probe the location of the beads within the array.

The AgNRs used in this study possessed the following average dimensions: 900 nm long, 100 nm in dia., and 150 nm spacing (as determined by SEM).[134] Since the flux angle was 86°during deposition, the growth angle of the array is 57° off the surface.[20] Figures 5.1 and 5.2 are a scaled drawing of a 1 μm^2 section of the array. Superimposed on the arrays are the two polystyrene bead probes (also drawn to scale) used in this study.

This schematic illustrates that the 20 nm dia. beads (Figure 5.1) are small enough to penetrate the nanorod array and deposit randomly over the surface whereas the 200 nm dia. beads (Figure 5.2) are too large to penetrate into the array. Thus, the smaller dia. beads interrogate enhancement over the entire surface of the AgNRs whereas the larger dia. beads serve as probes of enhancement over the tops and rounded ends of the AgNRs.

Figures 5.3 and 5.4 presents SERS spectra obtained on both polystyrene bead samples and R6G on AgNRs (Figure 5.3) and on a flat silver substrate (Figure 5.4). For each spectrum, 5 μL aliquots of test solutions were applied to the well and allowed to evaporate. The number density of FluoSphere® beads was 2×10^{10} beads per μL for the 20 nm dia. beads and 2×10^{7} beads per μL for the 200 nm dia. beads. The concentration of R6G was 10^{-5} M. Also included in this figure are spectra acquired on empty wells as a control.

As anticipated, the spectrum of R6G acquired on the AgNRs is very intense, more than an order of magnitude larger than that acquired for the polystyrene beads. The two microsphere solutions gave rise to peaks at 1000 cm^{-1} and 1030 cm^{-1} corresponding to well-characterized aromatic vibrations for polystyrene.[10] No bands characteristic of the fluorophores contained within the beads were found. If spectra bands for the fluorophore had been present, they would hve overpowered the polystyrene spectra as seen with R6G in Figure 5.3. The 20 nm dia. beads contained a green fluorophore whereas the 200 nm dia. beads contained a red fluorophore. The spectra acquired on flat silver (Figure 5.4)

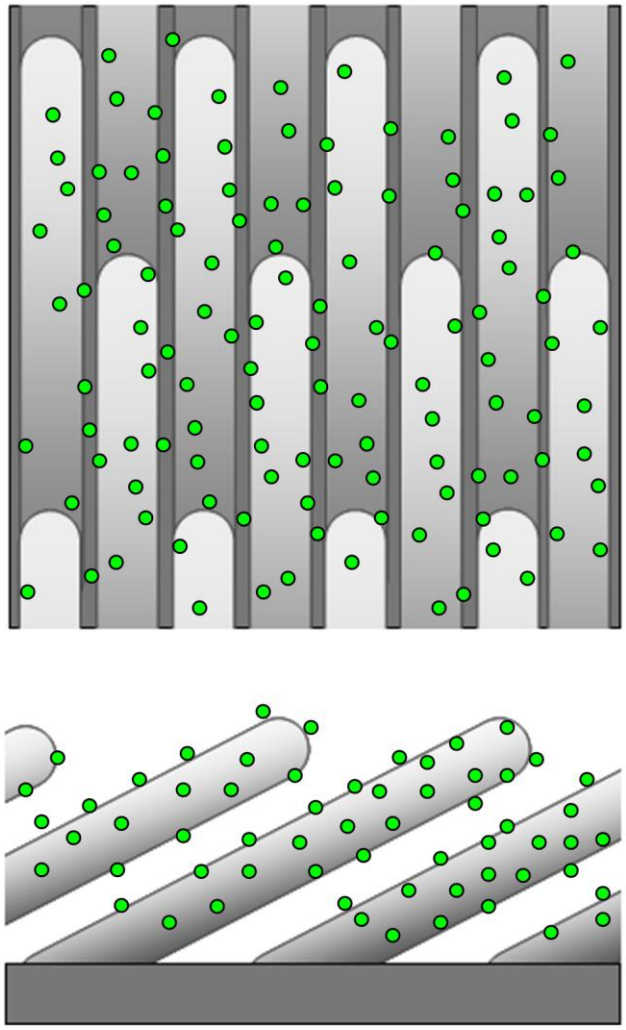

Figure 5.1. Schematic illustration of a 1 μm^2 section of the array drawn to scale. Superimposed on the array are 20 nm dia. polystyrene beads. This illustration treats the array as an idealized periodic structure.

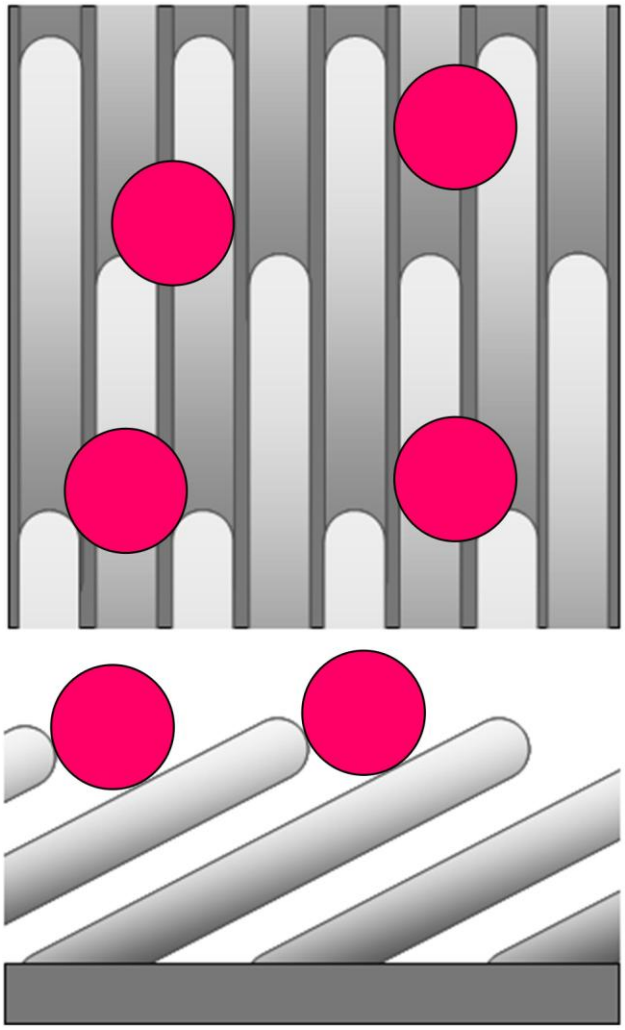

Figure 5.2. Schematic illustration of a 1 μm^2 section of the array drawn to scale. Superimposed on the array are 200 nm dia. polystyrene beads. This illustration treats the array as an idealized periodic structure.

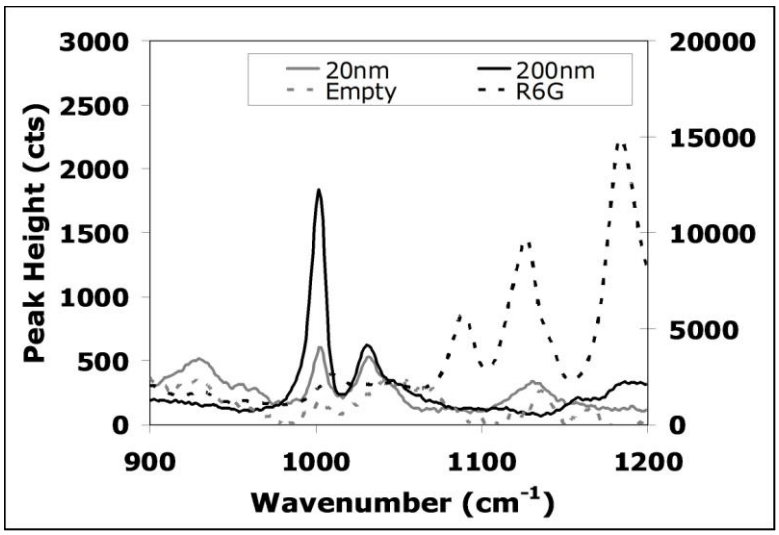

Figure 5.3. SERS spectra obtained on both polystyrene bead samples and R6G on a silver nanorod substrate. Only a portion of the spectra is displayed to spotlight the peaks of interest. R6G was plotted on the secondary y-axis.

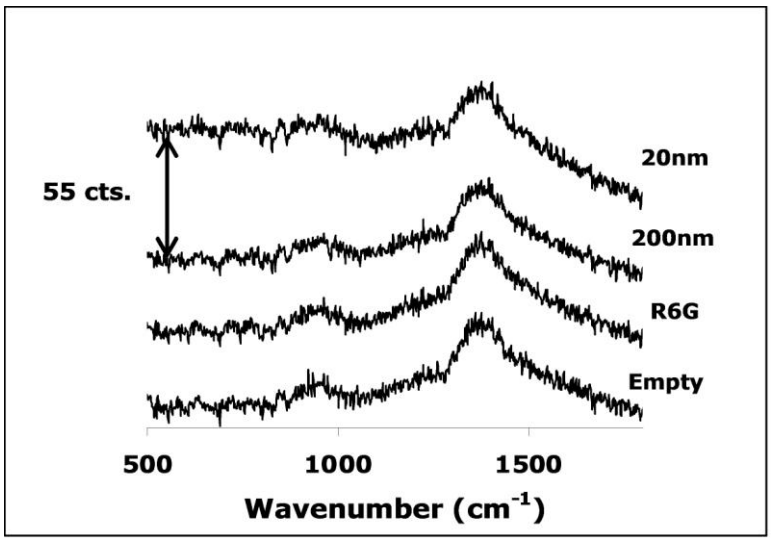

Figure 5.4. Normal Raman spectra obtained on both polystyrene bead samples and R6G on a flat silver substrate. The entire spectrum is displayed to show there were no peaks present in either spectrum.

are devoid of bands characteristic of the microspheres or R6G. This indicated that the spectrum acquired on AgNRs is a surface enhanced spectrum of the probe molecules.

Comparison of the SERS response between the two types of particles must take into account both the change in surface area available to each and their respective spatial distributions within the excitation laser spot. From the average nanorod dimensions and spacing, the surface area increase provided by the nanorod structure was computed to be 4.48. Thus, for a 3.0 mm dia. well, the AgNRs provide a surface area of 5.62 $x10^7$ μm^2 whereas flat silver provides a surface area of only 1.25 $x10^7$ μm^2. To completely cover the well with a monolayer of the smaller particles requires 1.4 x 10^{11} beads in comparison to the larger particles requiring only 3.1 x 10^8 beads. It should be noted that these values assume a complete, well-ordered monolayer structure of uniform particle dimension and devoid of evaporation-induced bead aggregation. Similarly, assuming that the R6G molecule lies flat on the silver nanorod surface, we computed that 5.73 x 10^{13} molecules are required to form a monolayer on the AgNRs surface. The spectrum presented in Figure 5.3 for R6G was acquired on what is estimated to be 0.5 monolayer coverage.

Figure 5.5a presents a scanning electron micrograph of the 20 nm dia. microspheres deposited on a well at monolayer coverage. This image was acquired near the center of the well. The location of beads on the nanorods has been identified by superimposing circles of appropriate diameter on top of the original image. Figure 5.6 presents the original SEM image without any altering. The microspheres show some degree of aggregation within the array and are non-uniformly distributed across the well. Images

acquired near the edges of the well show a much higher degree of aggregation. To further characterize the spatial distribution of beads across the well, SERS spectra were sequentially acquired as the excitation beam was rastered across this well in 25 μm steps. Figure 5.5b presents the background corrected intensity for the peak at 1000 cm^{-1}. The SERS signal variation across the well correlates with the number density observed in the SEM images as a function of location.

Figure 5.7a and 5.7b depict the corresponding results obtained following a ten-fold dilution of the 20 nm dia. microspheres (Figure 5.8 presents the original SEM image without any altering). The number density of beads near the center of the well (Figure 5.7a) is high enough that one would expect a SERS signal. The signal intensity distribution across the well (Figure 5.7b) shows that a measureable SERS response is seen only where evaporation-induced aggregation of the microspheres occurs (near the edge of the well).

Figure 5.9a presents a scanning electron micrograph of the larger dia. microspheres deposited on a well at monolayer coverage. Again, the location of beads on the nanorods has been identified by superimposing circles of appropriate diameter onto the image (Figure 5.10 presents the original SEM image without any altering). The larger dia. microspheres essentially cover the surface sitting atop the nanorod array and, in this particular image, appear uniformly distributed across the surface. Images acquired near the edges of the well show a multi-layered deposit. SERS spectra were acquired across the well in an identical fashion as described above.

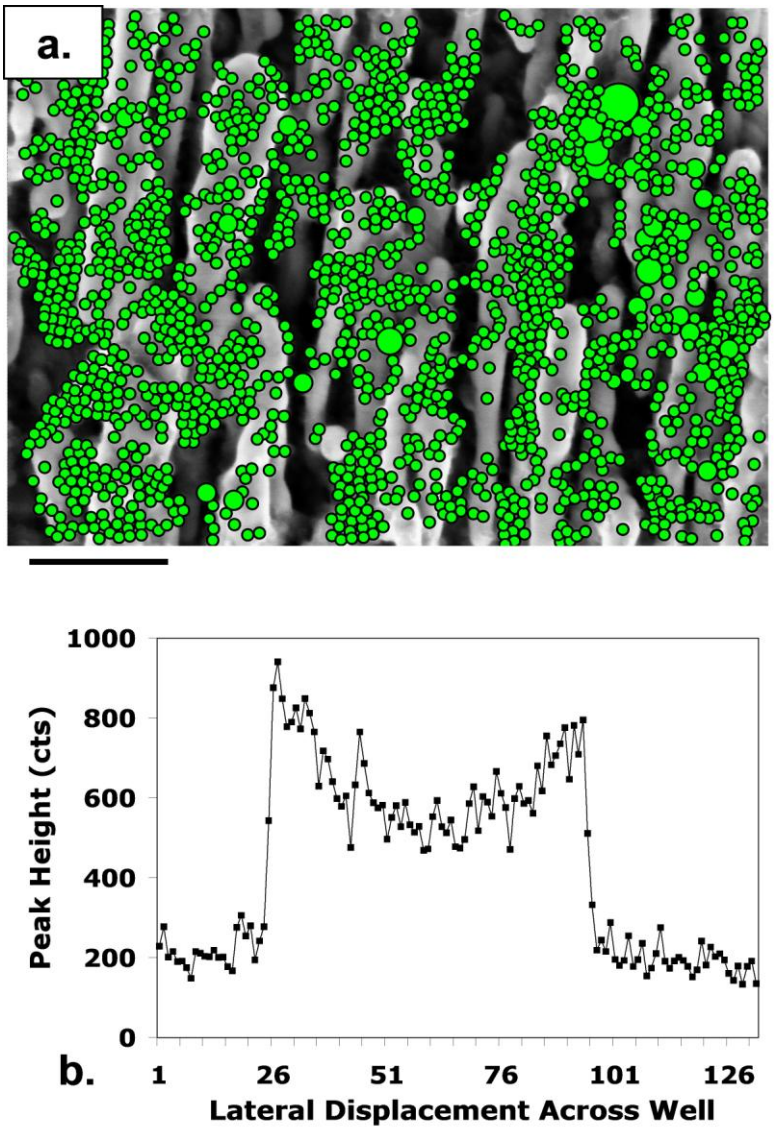

Figure 5.5. a.) Scanning electron micrographs obtained on the AgNRs after deposition of 20 nm dia. polystyrene microspheres by evaporation within a well at a concentration of 1 x 10^{11} beads per well. The scale bar represents 500 nm. b.) SERS spectra acquired in 25 μm step increments across the well. SERS peak intensities for the 1000 cm^{-1} spectral band for polystyrene (see Figure 6.3) are plotted as a function of position across the well at a number density 1 x 10^{11} beads per well.

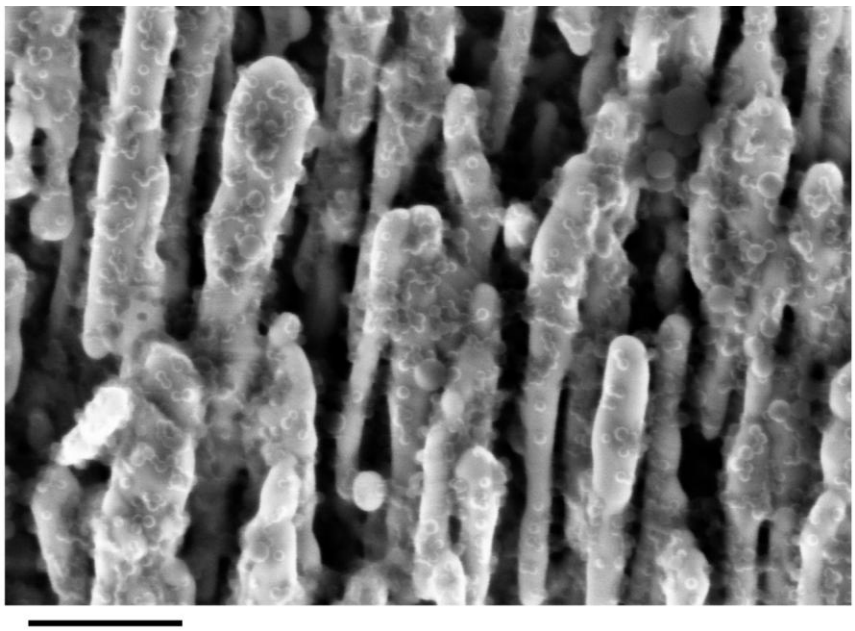

Figure 5.6. SEM obtained on AgNRs after deposition of 20 nm dia. polystyrene microspheres by evaporation of 1 x 10^{11} beads per well. The scale bar in the micrograph represents 500 nm. This figure is comparable to that of Figure 5.5a but does not contain the superimposed circles indicating the location of the beads within the AgNR.

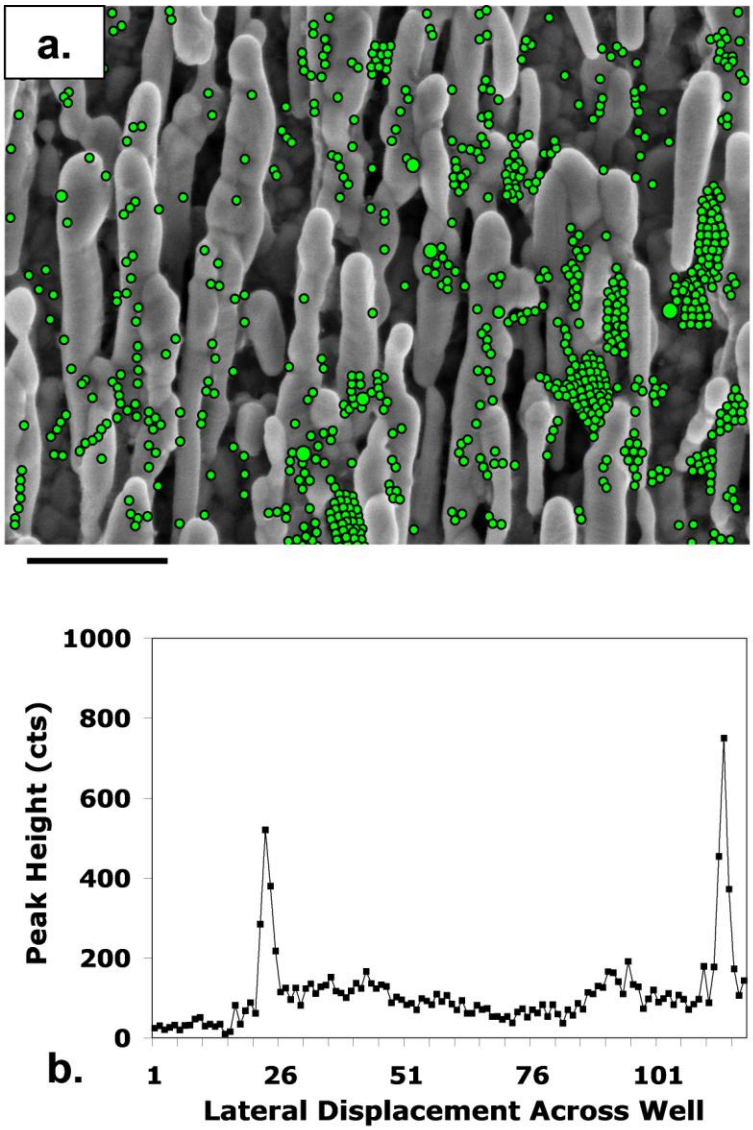

Figure 5.7. a.) SEM images obtained on the AgNRs after deposition of 20 nm dia. polystyrene microspheres by evaporation within a well at a concentration of 1 x 10^{10} beads per well. The scale bar represents 500 nm. b.) SERS spectra acquired in 25 μm step increments across the well. SERS peak intensities for the 1000 cm^{-1} spectral band for polystyrene (see Figure 5.3) are plotted as a function of position across the well at a number density 1 x 10^{10} beads per well.

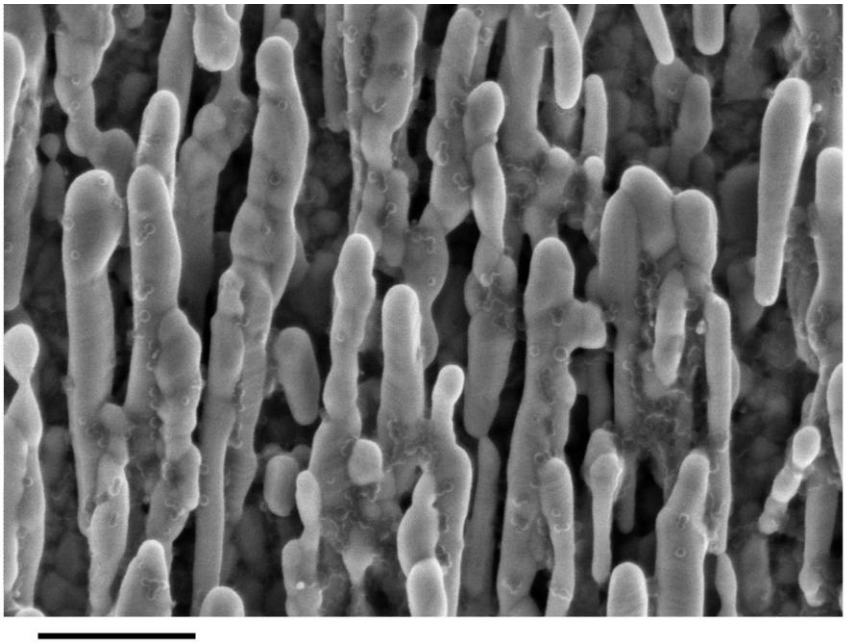

Figure 5.8. SEM obtained on the AgNRs after deposition of 20 nm dia. polystyrene microspheres by evaporation of 1 x 10^{10} beads per well. The scale bar in the micrograph represents 500 nm. This figure is comparable to that of Figure 5.7a but does not contain the superimposed circles indicating the location of the beads within the AgNR.

Figure 5.9b presents the background corrected intensity for the peak at 1000 cm^{-1} as a function of location. The SERS signal variation across the well correlates with the number density observed in the SEM images as a function of location. Figure 5.11a and 5.11b depict the corresponding results obtained following a ten-fold dilution of the 200 nm microspheres (Figure 5.12 presents the original SEM image without any altering). Non-uniform distribution of beads is also observed similarly to the smaller microspheres.

The electron micrographs reveal that the smaller beads are found both within and on top of the nanorod array, regardless of concentration, whereas the larger beads are found only on top of the array. Evaporation promotes aggregation of the smaller beads between the rods. It is interesting to note that the diameter of the laser spot is 20 μm. Thus, examination of the micrographs presented in Figures 5.5, 5.7, 5.9, and 5.11 reveals that, even at the lower concentrations, multiple beads are present within the laser spot. From this it is concluded that a SERS signal is obtained only when the coverage of beads approaches that of a monolayer.

The morphology of the AgNR array plays an important role in SERS signal intensity by impeding either delivery of the incident excitation beam to or collection of the scattered light from the microsphere. The SERS signal for small molecule scatterers distributed onto AgNR arrays is known to exhibit a strong dependence on the angle of the incident laser. Liu *et al.* found a five-fold enhancement at an incident angle of 45° (relative to the surface normal) with silver nanorods oriented with a tilt angle of 70° relative to the signal acquired at an incident angle of 0°.[141] With our current instrumentation, we can

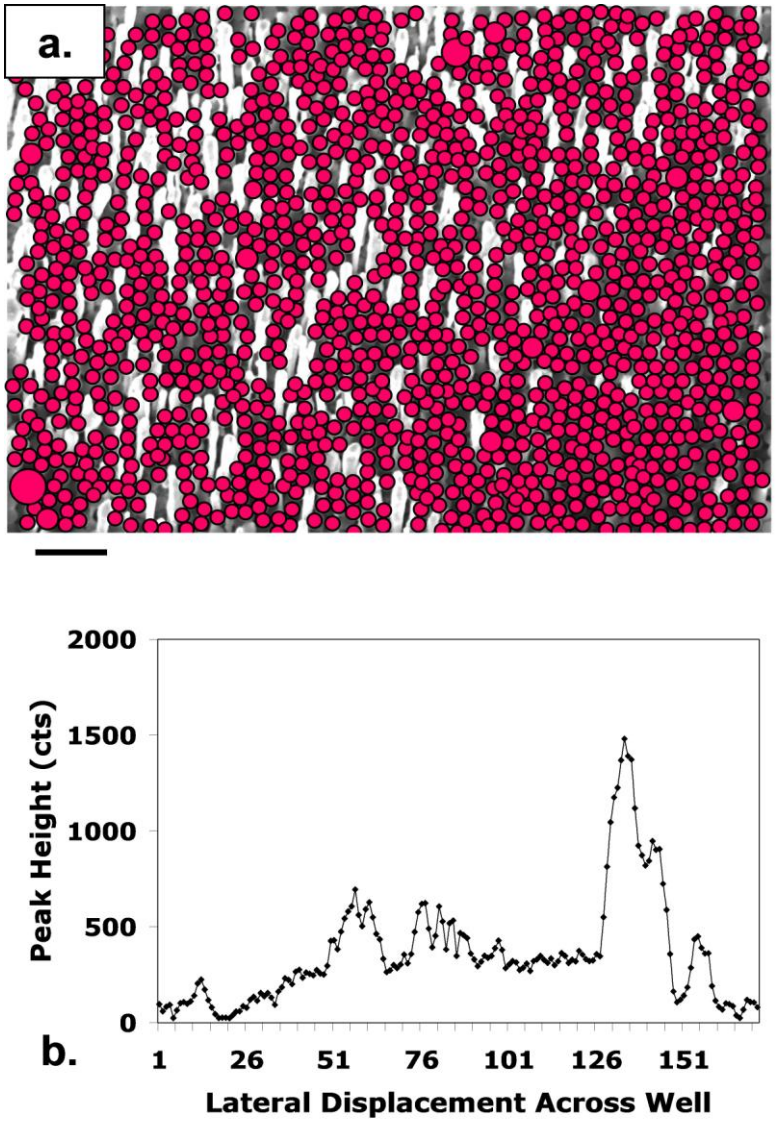

Figure 5.9. a.) SEM images obtained on the AgNRs after deposition of 200 nm dia. polystyrene microspheres by evaporation within a well at a concentration of 1 x 10^8 beads per well. b.) SERS spectra were acquired in 25 μm step increments across the well. The scale bar in the micrograph represents 1000 nm. SERS peak intensities for the 1000 cm^{-1} spectral band for polystyrene (see Figure 5.3) are plotted as a function of position across the well at a number density of 1 x 10^8 beads per well.

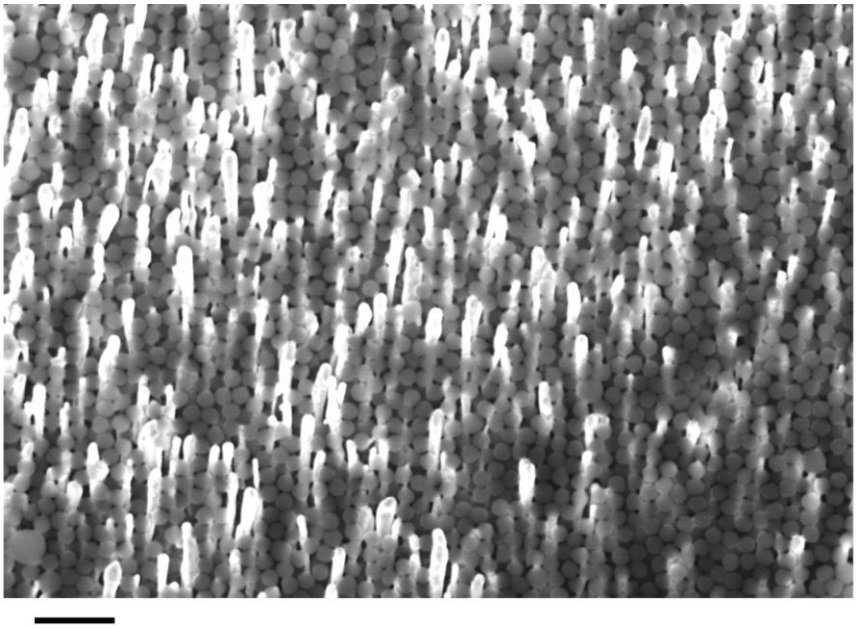

Figure 5.10. SEM obtained on the AgNRs after deposition of 200 nm dia. polystyrene microspheres by evaporation of 1 x 10^8 beads per well. The scale bar in the micrograph represents 1000 nm. This figure is comparable to that of Figure 5.9a but does not contain the superimposed circles indicating the location of the beads within the AgNR.

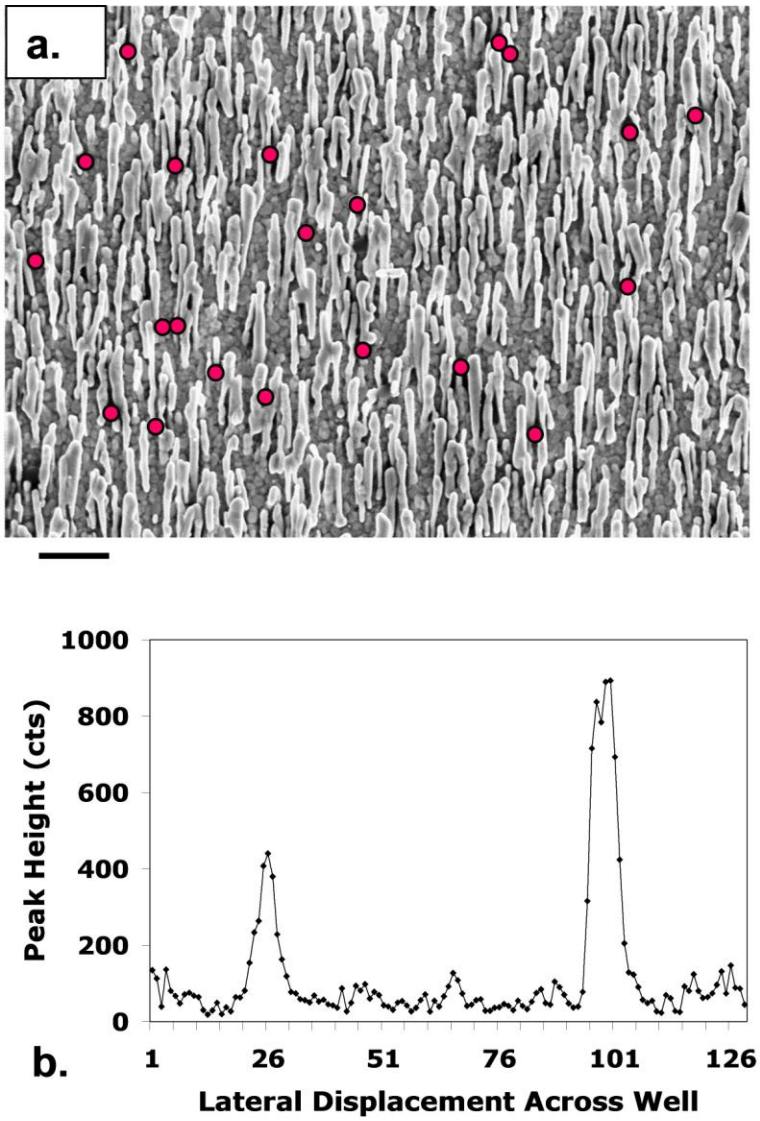

Figure 5.11. a.) SEM images obtained on the AgNRs after deposition of 200 nm dia. polystyrene microspheres by evaporation within a well at a concentration of 1 x 10^7 beads per well. b.) SERS spectra were acquired in 25 μm step increments across the well. The scale bar in the micrograph represents 1000 nm. SERS peak intensities for the 1000 cm^{-1} spectral band for polystyrene (see Figure 5.3) are plotted as a function of position across the well at a number density of 1 x 10^7 beads per well.

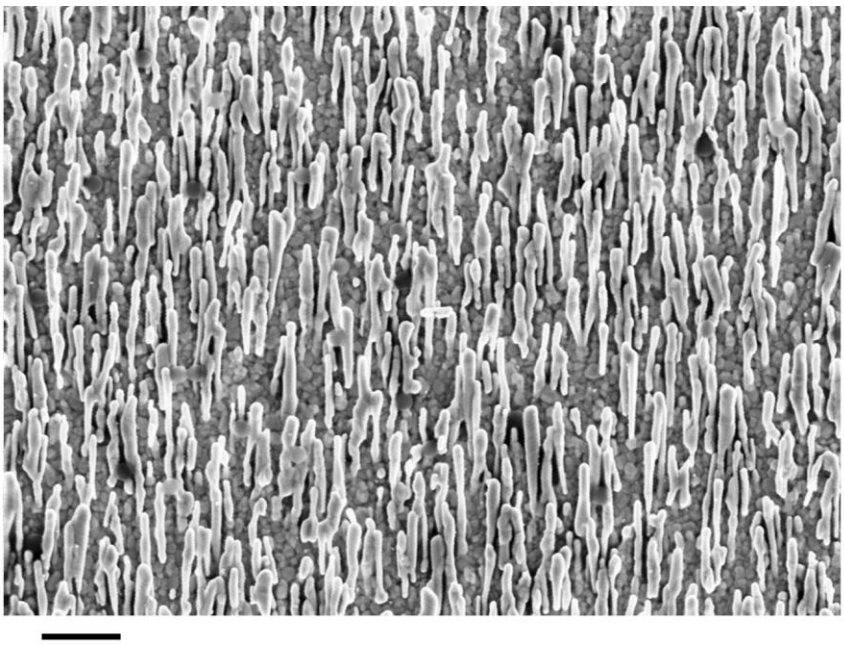

Figure 5.12. SEM obtained on the AgNRs after deposition of 200 nm dia. polystyrene microspheres by evaporation of 1 x 10^7 beads per well. The scale bar in the micrograph represents 1000 nm. This figure is comparable to that of Figure 5.11a but does not contain the superimposed circles indicating the location of the beads within the AgNR.

only deliver the incident beam and collect the back scattered light "normal" to the substrate surface. We suggest that given the pitch, angle, and density of our nanorods relative to the excitation wavelength, it is highly unlikely that we can detect light scattered by particles distributed within the nanorod array.

To illustrate the effect of AgNR morphology on the efficiency of collection of backscattered light, we acquired optical micrographs of our samples using fluorescence microscopy. Figures 5.13 and 5.14 presents fluorescence images acquired on microspheres deposited onto both AgNRs and flat silver surfaces. Figure 5.13a was obtained on a AgNR array following evaporation of a 5 μL aliquot of a 20 nm dia. bead solution containing 10^7 beads/mL. This image was acquired using 515 nm excitation and a 2 msec exposure. Bright spots in the image indicate the location of the beads on the array; the high contrast indicates that little or no fluorophore is leaching from the beads and adhering to the silver surface.

Figure 5.13b was obtained on a flat silver surface following evaporation of a 5 μL aliquot of a 20 nm dia. bead solution containing 10^4 beads/mL. This image was acquired using 515 nm excitation and a 5 msec exposure. The number density of bright spots in this image indicates a greater number of beads detected as compared to Figure 5.13a even though the concentration of beads was three orders of magnitude lower. It should be noted that images acquired on flat silver for the same particle density as that of Figure 5.13a saturated the detector and thus images could not be acquired. We conclude that

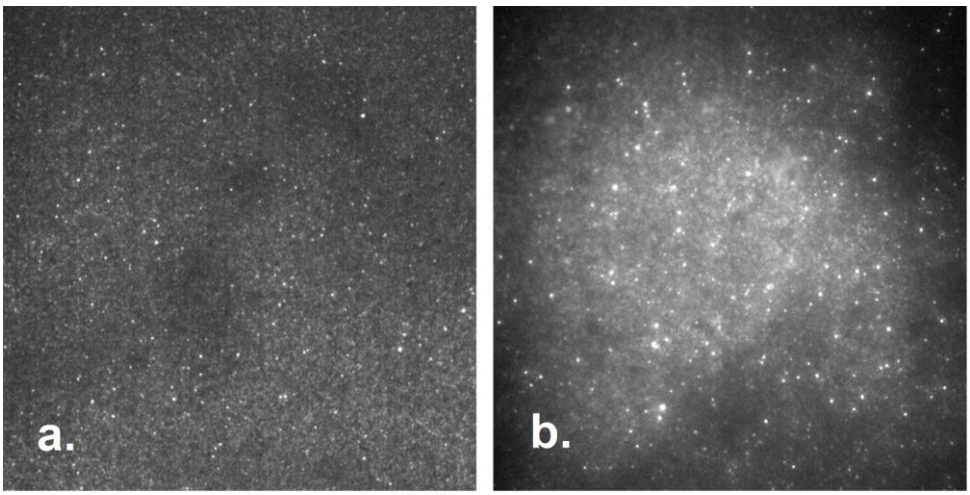

Figure 5.13. Fluorescence images acquired on 20 nm dia microspheres. a.) 10^7 beads/mL deposited onto AgNRs and b.) 10^4 beads/mL flat silver surfaces. Images were obtained following evaporation. The image represents a 400 μm^2 region within the well.

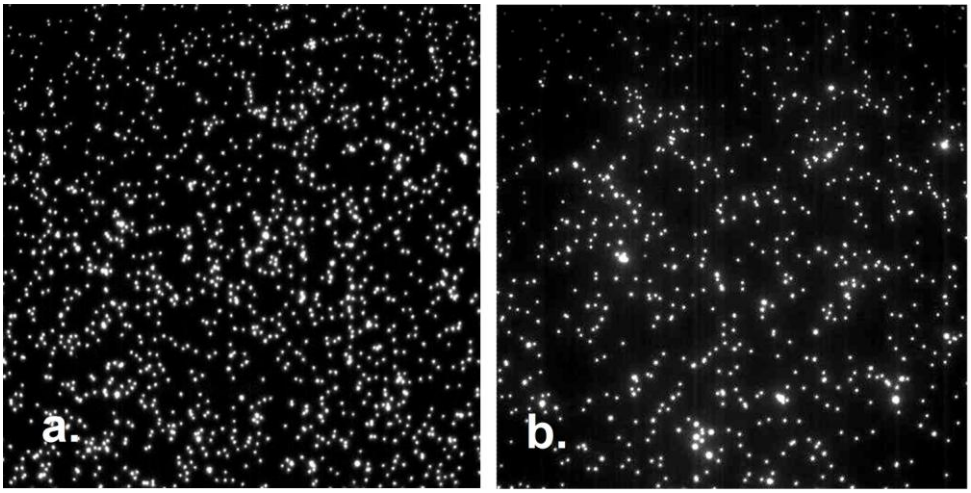

Figure 5.14. Fluorescence images acquired on 200 nm dia microspheres. a.) 10^4 beads/mL deposited onto AgNRs and b.) 10^4 beads/mL flat silver surfaces. Images were obtained following evaporation. The slight variation in number density is due to an uneven evaporation within the well. The image represents a 400 μm^2 region within the well.

this decrease in the number of beads detectable on the AgNRs is due to occlusion by the nanorods.

Similarly, fluorescence micrographs were obtained following evaporation of a 5 μL aliquot of a 200 nm dia. bead solutions containing 10^4 beads/mL onto AgNRs (Figure 5.14a) and flat silver (Figure 5.14b). These images were acquired using 540 nm excitation and a 5 msec exposure. Bright spots in the images indicate the location of the beads on the substrates. The number density of bright spots is comparable between these two images indicating that the particles reside on top of the AgNRs. No fluorescence was recorded from control experiments conducted on untreated flat silver and AgNR substrates.

Several aspects of this work are noteworthy. First, evaporation of the sample produces a non-uniform distribution of scatterers across the AgNR array. Evidence in support of this statement can be found in Figures 5.5, 5.7, 5.9, and 5.11 for polystyrene beads and in our previous reports for R6G.[292, 349] The degree of non-uniformity is due to solute concentration, affinity for the silver surface, and solvent volatility.

Second, single particle detection of latex beads was not possible with our instrument. In fact, SERS signals were only seen when the number of beads approached monolayer coverage. This observation reflects the low scattering efficiency of polystyrene, the spectral dispersion likely to result from the bead itself, occlusion of scattering from particles resident within the AgNRs, and limitations intrinsic to our collection optics.

Third, the enhancement found for beads located on top of the AgNRs was greater than that for beads located along the exposed surface of the AgNRs. Supporting evidence for this statement is provided in Figures 5.1, 5.2, 5.3 and 5.4. The intensity of the larger beads was approximately 3 times that of the small beads even though the number density of smaller beads exceeded that of the larger beads by 1000. Although the smaller beads were more abundant, their contribution to the overall SERS intensity is reduced because of their location within the array.

Liu and coworkers[141] have observed an eight-fold increase in SERS intensity for trans-1,2-bis-4-pyridylethene (BPE) as the angle of incident excitation and collection was optimized for the AgNR growth angle. Although we are unable to vary the angle of incidence or collection, it is unlikely that changing this angle will produce a signal increase sufficient to compensate for the difference in number density between the two sized beads. We suggest that the intensity of backscattered light comes predominately from scatterers located at the ends of the nanorods and the "top" surfaces.

Liu and coworkers have estimated that the SERS enhancement factor for BPE located on nanorod surfaces is about 50-200 times that for BPE located at the bottom of the AgNR array. [303] Their estimation was based on the assumption that BPE was uniformly distributed over the entire surface of the AgNR array. Given that we are able to pinpoint the location of the beads within the array, our findings suggest that the dependence of location on enhancement is significantly larger than their prediction. Taken collectively,

these findings suggest that the maximum enhancement will be found with closely-spaced ordered arrays of silver nanorods with an orientation nearly parallel to the incident excitation and collection beams.

CHAPTER 6

SURFACE ENHANCED RAMAN SCATTERING OF BACTERIAL GROWTH CULTURE MEDIA

6.1. Introduction

SERS is an emerging analytical tool for pathogen detection and identification.[9, 11, 55, 58, 350] Several recent publications have focused on determining the spectral bands characteristic of bacteria from different species and cell lines.[162-163, 165-166, 168-174, 177, 179-183, 204-205, 351-352] This research seeks to improve public health through the rapid identification of bacterial pathogens present in the environment, biological fluids, and in food products. A wide range of SERS substrates have been explored in classifying bacteria.

Silver nanorod (AgNR) array SERS substrates are suitable for detection of both viruses[132-133, 137-140, 147] and bacteria.[135, 162] Initially, we set out to explore the applicability of silver nanorod arrays as SERS substrates for distinguishing between bacterial types. Spectra were acquired on three different bacterial species, two Gram-positive (*Arthrobacter histidinolovorans* and *Bacillus cereus*) and one Gram-negative (*Escherichia coli*). Spectra for the latter two were comparable to those previously published for these bacteria. A remarkable similarity between the spectra for these bacterial species and that of the medium in which they were grown was observed. We began a systematic examination of commonly used bacterial growth culture media and compared the SERS spectral bands characteristic of the media with those previously

reported as characteristic of specific bacterial species. This chapter documents our findings.

6.2. Methods and Materials

6.2.1. Substrate Fabrication

SERS substrates were prepared using the method previously described in Chapter 3, sections 3.2.1 and 3.2.2.

6.2.2. Cell Culture Growth Media

The following cell culture media were obtained from BD Diagnostics (Franklin Lakes, NJ): Difco™ Nutrient Broth, Difco™ Meuller Hinton II Broth, Difco™ Luria Broth, BBL™ Selenite-F Broth, BBL™ GN (Gram Negative) Broth BBL™ Cooked Meat Medium, BBL™ Motility Test Medium, BBL™ Peptone Water, BBL™ Rapid Urea Broth, BBL™ Sabouraud Liquid Broth, Campylobacter Thioglycollate Medium, BBL™ LB Broth, BBL™ Standard Methods Agar. The following cell culture media were obtained from Athena Environmental Sciences, Inc. (Baltimore, MD): Turbo Broth™ and Superior Broth™. All stock cell culture solutions were prepared following the supplier's recipe. Cell culture media were serially diluted from "stock" solutions in nanopure water (18Ω).

6.2.3. Bacteria and Cell Culture Preparation

Bacterial samples *Arthrobacter histidinolovorans* (*A. histidinolovorans*), *Bacillus cereus* (*B. cereus*) and *Escherichia coli* (*E. coli*) were provided by Robert Martinez and Prof. Patricia Sobecky (formerly of the School of Biology, Georgia Institute of Technology, Atlanta GA). *A. histidinolovorans* and *E. coli* were grown at 30 °C to an optical density

(OD) of 0.2 and *B. cereus* was grown to 1.0 OD, all at 600 nm. Cell populations ~10^8 cfu mL^{-1} were achieved for all three bacterial strains. Bacteria samples were diluted serially in nanopure water (18Ω) or in the Nutrient Broth medium in which the cells were grown.

6.2.4. Substrate Characterization

Substrates were characterized by SEM and SERS before and after application of analyte samples as described in Chapter 3, section 3.2.3. SEM images were acquired on bacteria samples with a decreased accelerating voltage of 2 eV. In some instances, SERS spectra were acquired across the well at 25 μm intervals. In some instances, spectra were background corrected to remove the characteristic curvilinear baseline. Spectra were not rescaled or normalized unless otherwise noted.

6.3. Results

Nutrient broth is commonly used for culturing *E. coli* and *Staphylococcus aureus*. The upper portion of Figure 6.1 presents spectra obtained for Nutrient Broth. The spectrum for stock Nutrient broth (red trace) is featureless apart from the characteristic fluorescent background. The lack of spectral bands for stock medium agrees with previous SERS studies sensing bacterial samples.[162, 353] The lower portion of Figure 6.1 presents an SEM image acquired of the evaporated Nutrient Broth on the nanorod array substrate. The dried broth deposits within and on top of the nanorods.

Figure 6.1 also presents the SERS spectrum obtained on a sample of the broth diluted 1:100 (v/v) in nanopure water (blue trace) following background correction. This

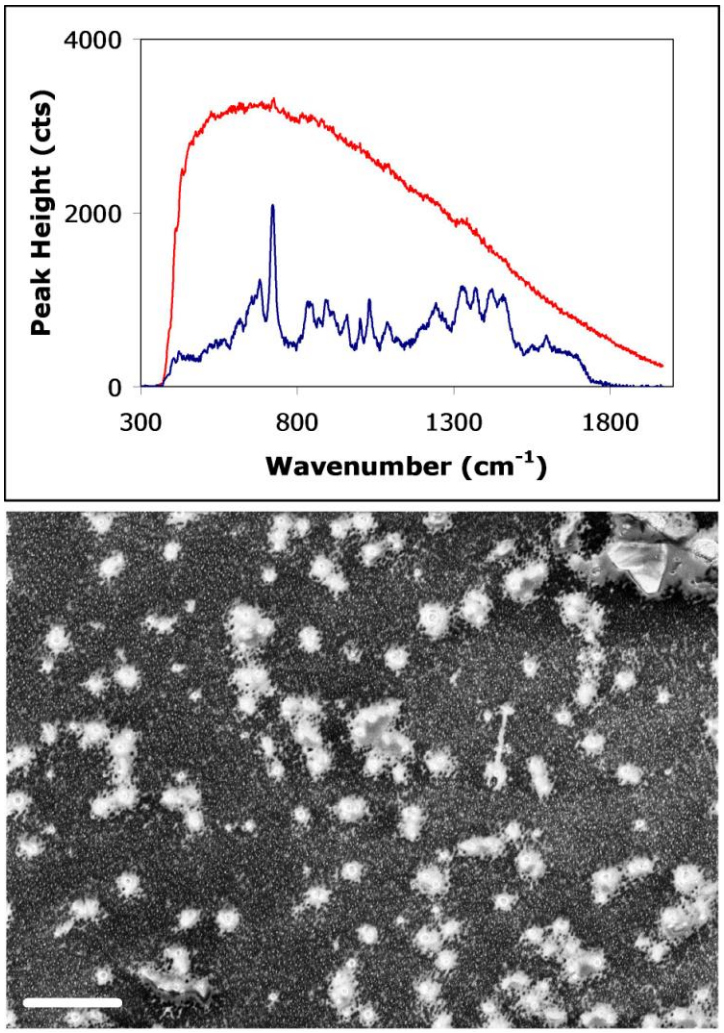

Figure 6.1. The SERS spectrum of Nutrient Broth stock (red trace), diluted 1:100 (v/v) (blue trace) is presented in the upper panel. The spectrum of the diluted sample was background corrected but not rescaled. The SEM image of stock Nutrient Broth on the AgNR array is presented in the lower panel. The scale bar represents 10 μm.

spectrum contains several well-defined bands that are characteristic of the components of this growth culture medium. Dilution reduces the amount of growth medium deposited onto the AgNRs by evaporation, improves the collection efficiency of the SERS signal, and decreases the fluorescent background.

Figure 6.2 presents three SERS spectra: one acquired on *B. cereus* at a concentration of 10^8 cfu mL^{-1} in Nutrient Broth (red trace), one acquired after 1:100 dilution of this solution in the growth medium (green trace), and one acquired after 1:100 dilution in water (blue trace). The red and green traces are identical to that obtained on undiluted Nutrient Broth; the red trace has been offset in intensity for clarity. The blue trace contains spectral features similar to those obtained by others for *B. cereus*.[177, 352, 354-355]

B. cereus is a Gram-positive bacterium. The spectral features are expected to be that representative of the peptidoglycan cell wall layer. While the structural components of the peptidoglycan layers are the same for both Gram-positive and Gram-negative bacteria, their structure and location in the cell wall differ. In Gram-negative bacteria, a direct crosslink exists through an amide bond; in Gram-positive bacteria, a pentaglycine bridge crosslinks the amino acids on adjacent chains. The peptidoglycan layer is the outermost layer of the cell wall for Gram-positive bacteria whereas it is an inner layer of the cell wall for Gram-negative bacteria.[356-358]

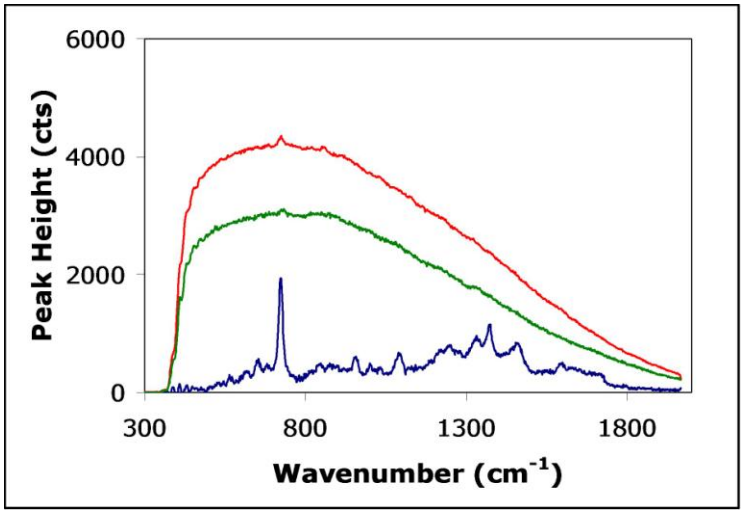

Figure 6.2. SERS spectrum of *B. cereus*: (red trace) 10^8 cfu mL^{-1} in stock Nutrient Broth; (green trace) 10^6 cfu mL^{-1} in stock Nutrient Broth; and (blue trace) 10^6 cfu mL^{-1} in diluted Nutrient Broth prepared by 1:100 (v/v) dilution in nanopure water. Spectra were offset along the intensity axis for clarity. Both the red and green spectra depict the raw, unprocessed counts whereas the blue spectrum was background corrected.

The outer wall structure of Gram-negative bacteria is comprised of lipopolysaccharides (LPS). The LPS layer is comprised of a base lipid embedded within the fatty acids of the outer membrane covalently linked to core oligosaccharides (e. g. heptose) and a polysaccharide chain referred to as the O-antigen. The O-antigen is the most variable portion of the LPS in relation to other gram negative bacteria. It is important to note that this LPS is only associated with Gram-negative bacteria.[356-358]

Thus, differences in spectral bands characteristic of the type of bacteria are expected. A schematic of the structural differences between Gram-positive and Gram-negative bacteria is depicted in Figure 6.3.

In some instances, a crystalline cell surface protein, referred to as the S-layer, binds to the outermost layer of both Gram-positive and Gram-negative bacteria. Eamples of bacteria with an S-layer include and are not limited to *B.cereus*,[359-361] *Bacillus sphaericus*,[362-363] *Mitsuokella multacida*,[364] *Lactobacillus kefir*,[365]and *Clostridium difficile*.[366] A few examples of bacteria lacking an S-layer include and are not limited to *Bacillus subtillus*, *Staphylococcus aureus* and mycobacteria.[367-369] Layer thickness ranges from 5-25 nm depending on the specific bacteria and length of culture.[360] In Gram-positive bacteria, the S-layer is bound to the peptidoglycan layer directly[370] or through covalent linkage to a pyruvylated carbohydrate associated with the peptidoglycan layer.[371-375] In Gram-negative bacteria, the S-layer is bound through interactions between the positive terminus of the layer and the liposaccharides located in the LPS on the outer cell membrane.[376-379] The composition is poorly

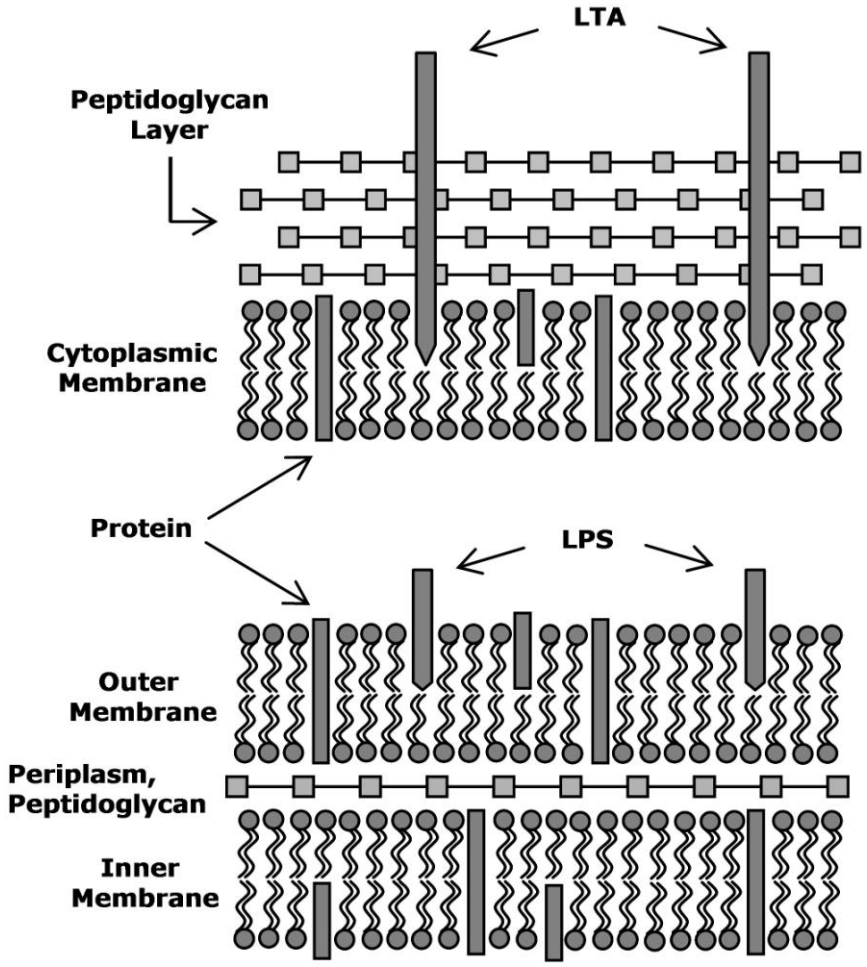

Figure 6.3. Schematic of both Gram-negative and Gram-positive bacteria cell wall components. Note the difference in cell wall structure that should be apparent in the respective SERS spectra.

conserved even between bacteria of related species. The layer also varies based on the incubation time of the bacteria. This has been shown specifically with *B. cereus.*[359]

Due to these structural differences, SERS should be able to distinguish between Gram-positive and Gram-negative bacteria with and without an S-layer. SERS spectra acquired on Gram-positive bacteria should contain bands representative of the peptidoglycan layer whereas spectra acquired on Gram-negative bacteria should contain bands representative of the LPS. For bacteria containing an S-layer, spectra should contain bands representative of the protein and glycoprotein subunits.

To test this hypothesis, SERS spectra were also acquired on another Gram-positive bacterium (*A. histidinolovorans*) as well as on a Gram-negative bacterium (*E. coli*). Cell colonies for both were grown in Nutrient Broth to a stock concentration of 10^8 cfu mL^{-1}. Figure 6.4 presents the SERS spectrum acquired on all three bacterial species following 1:100 (v/v) dilutions of their stock solutions in nanopure water. For comparison purposes, all spectra displayed in this figure were normalized to the peak of highest intensity and offset along the y-axis for clarity after background correction. The spectrum obtained for *E. coli* is in close agreement with that reported by others.[162-163, 172-173, 179, 183, 201, 352, 354-355] The spectrum of the diluted Nutrient Broth is also included in this figure. The four spectra are strikingly similar in appearance. The similarity in the spectra obtained on Gram-positive and Gram-negative bacterial cells is troubling.

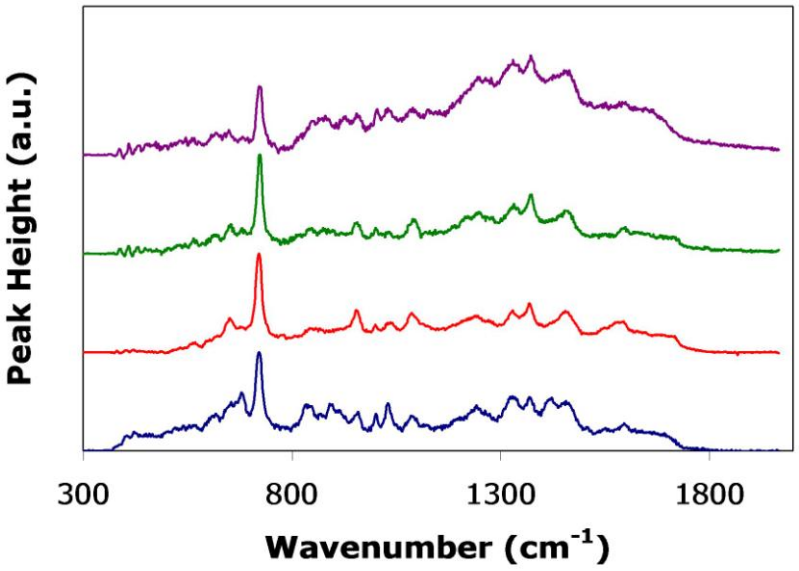

Figure 6.4. SERS spectra of *E. coli* (purple trace), *B. cereus* (green trace), and *A. histidinolovorans* (red trace) in Nutrient Broth diluted 1:100 (v/v) in nanopure water to a final concentration of 10^6 cfu mL^{-1}. The spectrum of diluted Nutrient Broth (blue trace) is also included for ease of comparison. All four spectra were normalized to the peak of highest intensity and offset along the intensity axis for clarity of presentation.

To verify that spectra presented in Figure 6.4 were indeed characteristic of the bacterium, two additional experiments were performed. First, SEM images were acquired on the nanorod arrays to verify that the bacterial cells were intact and spatially distributed throughout the well. The image obtained for *A. histidinolovorans* is presented in upper portion of Figure 6.5. This bacterium has a rod-like structure typically 1-2 μm in length. The inset presents an image whose features are consistent with this dimension. The SEM images show that the bacteria are not uniformly distributed across the well. Rather, they are clustered in random locations typically with 2-5 cells per cluster on top of the nanorod array.

Next, SERS spectra were acquired across the well in 25 μm steps; with a laser spot size of 20 μm in diameter depicted in Figure 6.5 as a circle. Comparison of spectra acquired across the well showed no significant changes in the Raman bands; the relative intensity of spectral bands was dependent upon location. The SERS intensity of the most intense peak in the spectrum (725 cm^{-1}) was plotted as a function of position across the well and is presented in the lower portion of Figure 6.5. Similar findings were obtained with *B. cereus* (Figure 6.6). This bacterium also has a rod-like structure with dimensions that are four to five times larger than that of *A. histidinolovorans*. The SEM images (upper portion of Figure 6.6) and SERS spectra acquired across the well (lower potion of Figure 6.6) are presented.

Since i) the Raman shifts are unchanged in spectra acquired across the well, ii) the bacteria are too large to fit between the nanorods in the array, and iii) the spatial

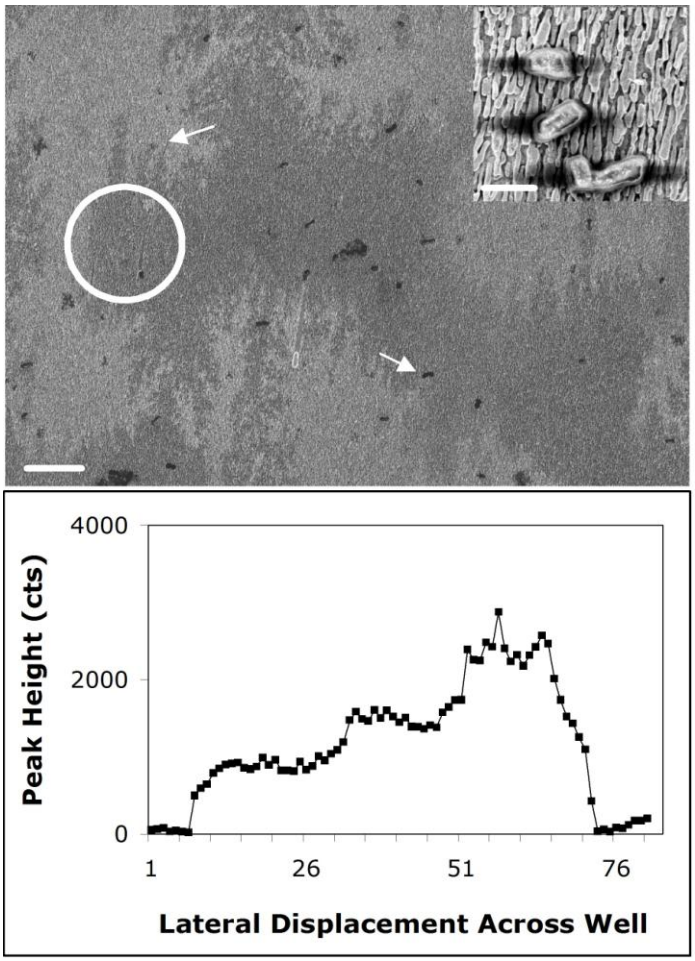

Figure 6.5. SEM image following evaporation of a 5 μL aliquot of *A. histidinolovorans* at 10^6 cfu mL^{-1} prepared by diluting the cells grown in stock Nutrient Broth by 1:100 (v/v) in nanopure water is presented in the upper panel (scale bar is 10 μm). The white circle denotes the laser spot. Arrows point out the location of two bacterial cell clusters. The inset depicts a SEM image at higher magnification (scale bar is 2 μm). The bottom panel presents SERS peak intensity for the 725 cm^{-1} band as a function of position following background correction. Spectra were acquired in 25 μm step increments across the well across prior to acquiring the SEM images shown in this figure.

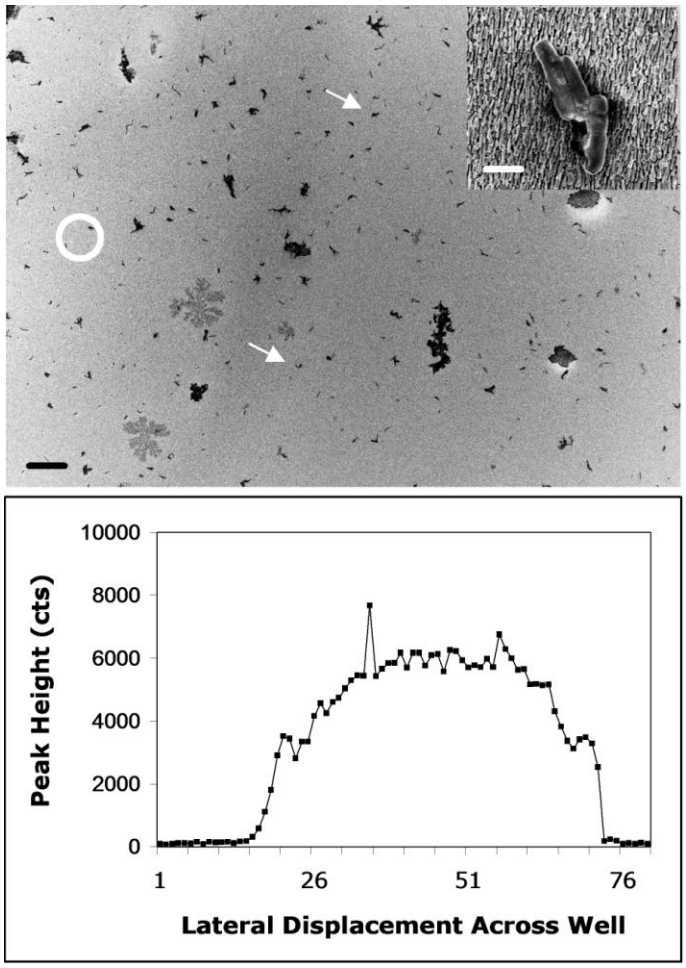

Figure 6.6. SEM image following evaporation of a 5 μL aliquot of *B.cereus* at 10^6 cfu mL^{-1} prepared by diluting the cells grown in stock Nutrient Broth by 1:100 (v/v) in nanopure water is presented in the upper pane (scale bar is 20 μm). The white circle denotes the size of the laser spot. Arrows denote the location of two bacterial cell clusters. The inset depicts a SEM image at higher magnification (scale shows 1 μm). The bottom panel presents SERS peak intensity for the 725 cm^{-1} band as a function of position following background correction. Spectra were acquired in 25 μm step increments across the well across prior to acquiring the SEM images shown in this figure.

distribution of bacteria across the well is non-uniform, we conclude that the Raman shifts observed are due to growth medium adsorbed onto the nanorod array. The troubling aspect of this conclusion is the similarity of our spectra to those previously published for the bacteria investigated herein.[162, 165-169, 172-174, 177, 179, 205, 352-355, 373]

This compelled us to investigate the spectral signatures of other bacterial growth culture mediums. Figure 6.7 presents the spectra acquired for 14 different media; all were diluted in nanopure water. Abbreviations and dilution factors were: Rapid Urea Broth (RU) diluted 1:100 (v/v); Selenite-F (SF) diluted 1:10,000; Campylobacter Thioglycollate Medium (CT) diluted 1:1,000; Turbo Broth (TB) diluted 1:1,000; Luria Broth (LB) diluted 1:10; Gram-negative Broth (GN) diluted 1:10,000; LB Broth (LBB) diluted 1:100; Peptone Water (PW) diluted 1:100; Motility Medium (MM) diluted 1:10; Nutrient Broth (NB) diluted 1:100; Cooked Meat Medium (CM) diluted 1:1,000; Sabouroud Liquid Broth Modified (SL) diluted 1:10; Meuller-Hinton II Broth (MH) diluted 1:100; Standard Methods Agar (SM) diluted 1:100. All spectra presented were normalized to the peak of highest intensity and offset along the y-axis for clarity after background correction. Many of the bands found in these spectra have been reported elsewhere as fingerprint bands for various bacteria. [162-163, 168-174, 177-178, 182, 204, 351, 353, 380-381]

6.4 Discussion

Bacterial cell growth media generally contain a source of amino acids, a carbon source (e.g. glucose or dextrose), water, and salts to promote bacterial growth. The amino acids are typically from protein hydrolysates, often referred to as peptones. Peptones are

classified by the source from which they are derived e.g. animal-free, meat, or casein and whey. Some growth media contain peptones from multiple sources.[382] For example, Nutrient Broth, the growth medium used to culture the three bacteria studied herein, contains 0.3% (w/v) beef extract and 0.5% (w/v) pancreatic digest of casein. Some media are optimal for culturing a specific bacterial cell line. For example, Mueller-Hinton II Broth is commonly used to culture *Staphylococcus aureus, Enterococcus faecalis,* and *Pseudomonas aeruginosa* whereas Standard Methods Agar is used in growing *Bacillus subtilus, Bacillus stereothermophilus,* and *Enterococcus hirae*. Some bacterial cell lines can be cultured in a variety of growth media. For example, *E. coli* can be grown in several of the media studied herein.[382]

The spectral bands we observed for diluted media are consistent with the components that comprise the medium. Many possessed spectral features that were similar to those of other media. For example, the spectra presented in Figure 6.7 for Nutrient Broth, Standard Methods Agar, Mueller-Hinton II Broth, Cooked Meat Medium, and Sabouroud Liquid Broth Modified all contained an intense Raman band between 725-730 cm^{-1} as well as a band between 1325-1330 cm^{-1} whose intensity varies among the five media. The 725-730 cm^{-1} band has been attributed in the literature to adenine from flavin,[182, 380] the rocking vibration of CH_2,[168] and C-O-O^- bend.[353] The 1325-1330 cm^{-1} has been attributed to a C-H deformation for guanine or protein[174, 178, 351, 380-381] and specifically the amino acid tyrosine.[168] Most of the spectra contained bands at 1000 and 1030 cm^{-1}, a region typically attributed to aromatic components such as

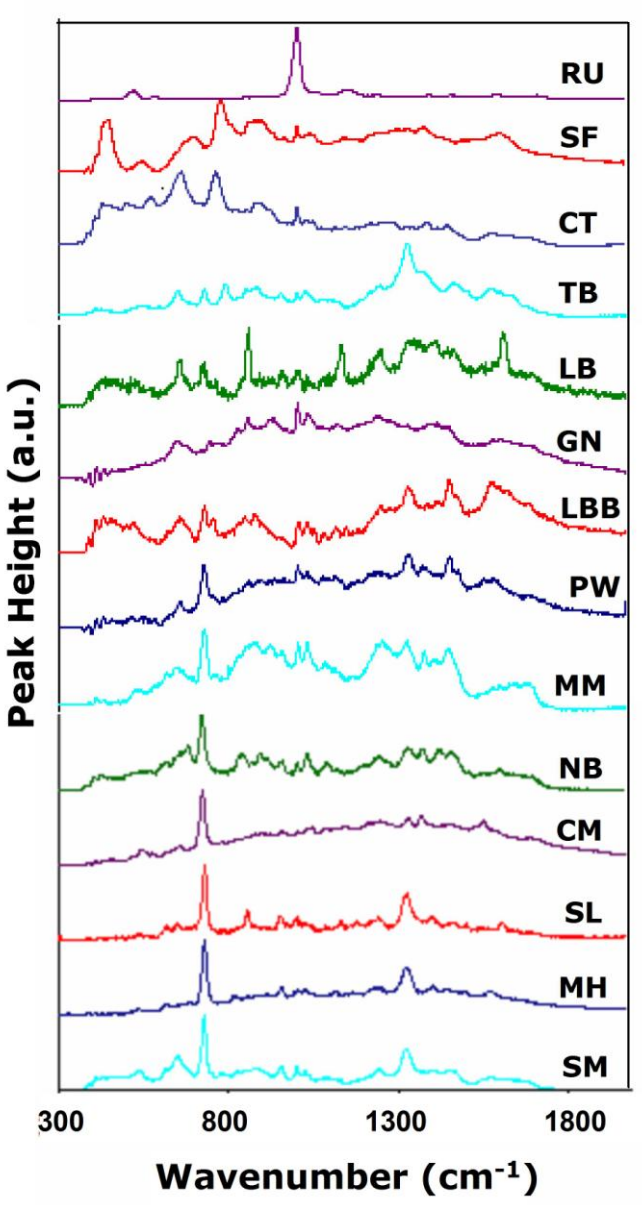

Figure 6.7. SERS spectra acquired on bacterial growth media. All stock media, prepared according to the manufacturer's recipe, gave spectra similar in structure to that presented in Figure 6.1 (red trace). Each medium was diluted in nanopure in varying ratios. The spectra presented in the figure were normalized to the peak of highest intensity and offset along the intensity axis for clarity of presentation.

phenylalanine[168, 178, 204, 380] and between 960-965 cm^{-1}, a band often attributed to the C-N stretch. All of these bands are expected for protein hydrolysates.

Interestingly, these bands have also been assigned as signatures of specific bacteria (e.g. *B. cereus*,[177, 352, 355, 380, 383] *Bacillus lichenformis*,[163] *Bacillus megaterium*[163, 172] *Bacillus subtilus*[168] and *E. coil*.[163, 167, 172, 174, 179, 297, 383-384] Spectral characteristics present in Raman and SERS spectra have been assigned to components of the protein coat and cell wall for various bacteria. Some of the designated peaks for bacterial identification parallel peaks observed in diluted media spectra presented in this work. Table 6.1 provides a more detailed listing of peaks observed in various growth media. Also included in this table is a comparison of these spectral bands to those reported for both *E. coli* and *B.cereus*.

Efrima and Zeiri[166] have previously commented on the fact that published SERS spectra on the same bacterium varies widely from group to group while the normal Raman spectra are quite similar. Differences in SERS spectra have been attributed to variations in sample and substrate preparation, excitation wavelength, the type and shape of the SERS substrate (e.g. nanoparticles, nanorods), as well as the laser spot location and diameter relative to the bacteria. In this context, we have compiled the spectra previously published for *E. coli* (Figure 6.8) and *B. cereus* (Figure 6.9) and compared them with our spectra. The spectrum we report for *E. coli*, located at the top of Figure 6.8, has features that are common to all other published spectra for this bacterium.

Table 6.1. This table presents the spectral band assignments found in literature for *E. coli* and *B. cereus* with those found for the bacterial growth media presented in **Figure 6.7.**

Bands	Medium	Bacteria
~450	Selenite-F	
~525	Standard Methods Agar, Rapid Urea Broth	*E. coli* [163, 172]
~540	Sabouroud Liquid Broth Modified, Gram Negative Broth, Meuller-Hinton II Broth	*E. coli* [353, 384]
~560	Cooked Meat Medium, Selenite-F, Turbo Broth	
~575	Nutrient Broth	*E. coli* [174, 179]
~585	Campylobacter Thioglycollate Medium, Cooked Meat Medium, Rapid Urea Broth	*E. coli* [163]
~630	Meuller-Hinton II Broth, Nutrient Broth	*E. coli* [172, 174, 179]
~660	Peptone Water, Gram Negative Broth, Luria Broth, Nutrient Broth, Sabouroud Liquid Broth Modified, Standard Methods Agar, Turbo Broth, LB Broth, Cooked Meat Medium, Campylobacter Thioglycollate Medium	*E. coli* [163, 172, 353, 383, 385] *B. cereus* [383]
~700	Meuller-Hinton II Broth, Selenite-F	*E. coli* [174]
~730	Cooked Meat Medium, Nutrient Broth, Sabouroud Liquid Broth Modified, Superior Broth, Peptone Water, LB Broth, Luria Broth, Meuller-Hinton II Broth, Motility Test Medium, Standard Methods Agar, Turbo Broth	*E. coli* [163, 172, 384-385] *B. cereus* [383]
~750	Gram Negative Broth	*E. coli* [174, 179, 384]
~780	Campylobacter Thioglycollate Medium, Selenite-F, Turbo Broth	*E. coli* [384]
~800		*E. coli* [163, 353]
~810		*E. coli* [174, 179, 384]
~830	Turbo Broth	
~860	Gram Negative Broth, Luria Broth, Rapid Urea Broth, Sabouroud Liquid Broth Modified, Turbo Broth Selenite-F	*E. coli* [174, 179, 384]
~870		*E. coli* [353, 385]
~890	Campylobacter Thioglycollate Medium, Selenite-F, Turbo Broth	
~930	Gram Negative Broth	*E. coli* [163] *B. cereus* [383]
~960	Cooked Meat Medium, LB Broth, Nutrient Broth, Sabouroud Liquid Broth Modified, Standard Methods Agar, Turbo Broth, Meuller-Hinton II Broth	*E. coli* [163, 172, 174, 179, 353, 385]

Table 6.1. Continued

~1000	Campylobacter Thioglycollate Medium, Cooked Meat Medium, Gram Negative Broth, LB Broth, Meuller-Hinton II Broth, Motility Test Medium, Nutrient Broth, Peptone Water, Selenite-F, Standard Methods Agar, Turbo Broth	*E. coli* [384]
~1030	Cooked Meat Medium, Gram Negative Broth, LB Broth, Meuller-Hinton II Broth, Motility Test Medium, Nutrient Broth, Peptone Water, Standard Methods Agar, Turbo Broth	*B. cereus* [383]
~1060	Turbo Broth	*E. coli* [163, 172, 174, 179]
~1070		*E. coli* [353]
~1090	Nutrient Broth	*E. coli* [174]
~1100	Nutrient Broth, Turbo Broth	*B. cereus* [383] *E. coli* [163, 172]
~1130	Meuller-Hinton II Broth, Sabouroud Liquid Broth Modified	*E. coli* [385]
~1150		*E. coli* [172]
~1160	Rapid Urea Broth	*E. coli* [174, 179]
~1220	Turbo Broth	*E. coli* [163, 384]
~1230	Motility Test Medium, Sabouroud Liquid Broth Modified, Rapid Urea Broth	*E. coli* [172] *B. cereus* [383]
~1240		*E. coli* [174, 179, 383]
~1250	LB Broth, Luria Broth, Meuller-Hinton II Broth, Nutrient Broth	
~1270		*E. coli* [353]
~1280	Campylobacter Thioglycollate Medium	*E. coli* [174, 179]
~1290		*E. coli* [384]
~1320	Nutrient Broth	
~1330	Standard Methods Agar, Meuller-Hinton II Broth, Motility Test Medium, Nutrient Broth Peptone Water, Selenite-F, Turbo Broth	*B. cereus* [383] *E. coli [163, 383-384]*
~1340	LB Broth, Cooked Meat Medium	*E. coli* [353]
~1350	Sabouroud Liquid Broth Modified	*E. coli* [174, 179]
~1370	Nutrient Broth	*E. coli* [383]
~1380	Campylobacter Thioglycollate Medium, Cooked Meat Medium, Motility Test Medium, Nutrient Broth	*E. coli* [172]
~1390	Rapid Urea Broth	
~1410	Meuller-Hinton II Broth	*E. coli* [174, 179, 353]

Table 6.1. Continued

~1420		*E. coli* [385]
~1450	Motility Test Medium, Peptone Water, Turbo Broth	*E. coli* [163, 383]
~1460	LB Broth, Nutrient Broth, Rapid Urea Broth, Sabouroud Liquid Broth Modified, Turbo Broth	*E. coli* [172, 174, 179]
~1470		*B. cereus* [383]
~1540	Nutrient Broth	*E. coli* [172, 174, 179]
~1560	Cooked Meat Medium	*B. cereus* [383]
~1570		*E. coli* [384]
~1580	Meuller-Hinton II Broth, Motility Test Medium, Turbo Broth	*E. coli* [174, 179, 353]
~1600	Cooked Meat Medium, Luria Broth, Nutrient Broth, Nutrient Broth, Rapid Urea Broth, Sabouroud Liquid Broth Modified, Selenite-F	*E. coli* [383] *B. cereus* [383]
~1630		*E. coli* [174, 179]
~1650		*B. cereus*[383] *E. coli*[384]
~1710	Rapid Urea Broth	*E. coli*[383]

Similarly, the spectrum we report for *B. cereus*, located at the top of Figure 6.9, also has features that are common to three of the four published spectra for this bacterium.

Careful examination of the spectra presented in these two figures reveals spectral features that are consistent throughout the set. For example, the band at 725 cm^{-1} is present in every spectrum in the figure. Its relative intensity is, in most instances, the strongest in the spectrum. Other spectral features are inconsistent from spectrum to spectrum. For example, the 930-1130 cm^{-1} band, previously assigned to membrane phospholipids,[386] is expected in the spectrum of Gram-positive bacteria. However, it is observed in spectra of both *E. coli* and *B. cereus* with varying intensities. Relative intensities in SERS are known to vary with incident beam wavelength, substrate composition and structure as well as orientation of the scattering moiety on the substrate and its position within the plasmon field.[24, 76, 92, 122, 125-126, 130, 153, 207, 209]

Principle component analysis has been used to assess spectral differences between different bacterial types, species, and strains.[162, 168, 177, 387-390] Often, classifications were based on subtle differences in spectra. Heretofore, it has been widely assumed that washing of the bacterial sample with water effectively removes the growth medium and that the spectrum obtained on the sample is that of the cell wall. It should be noted that published spectra of the media is featureless. The results presented in Figures 6.1 and 6.2 show that the spectra of diluted media are far from featureless. Thus, by washing bacterial cell samples, previous workers may have been inadvertently diluting the medium. This holds for both nutrient broths and nutrient agars. We suspect that the

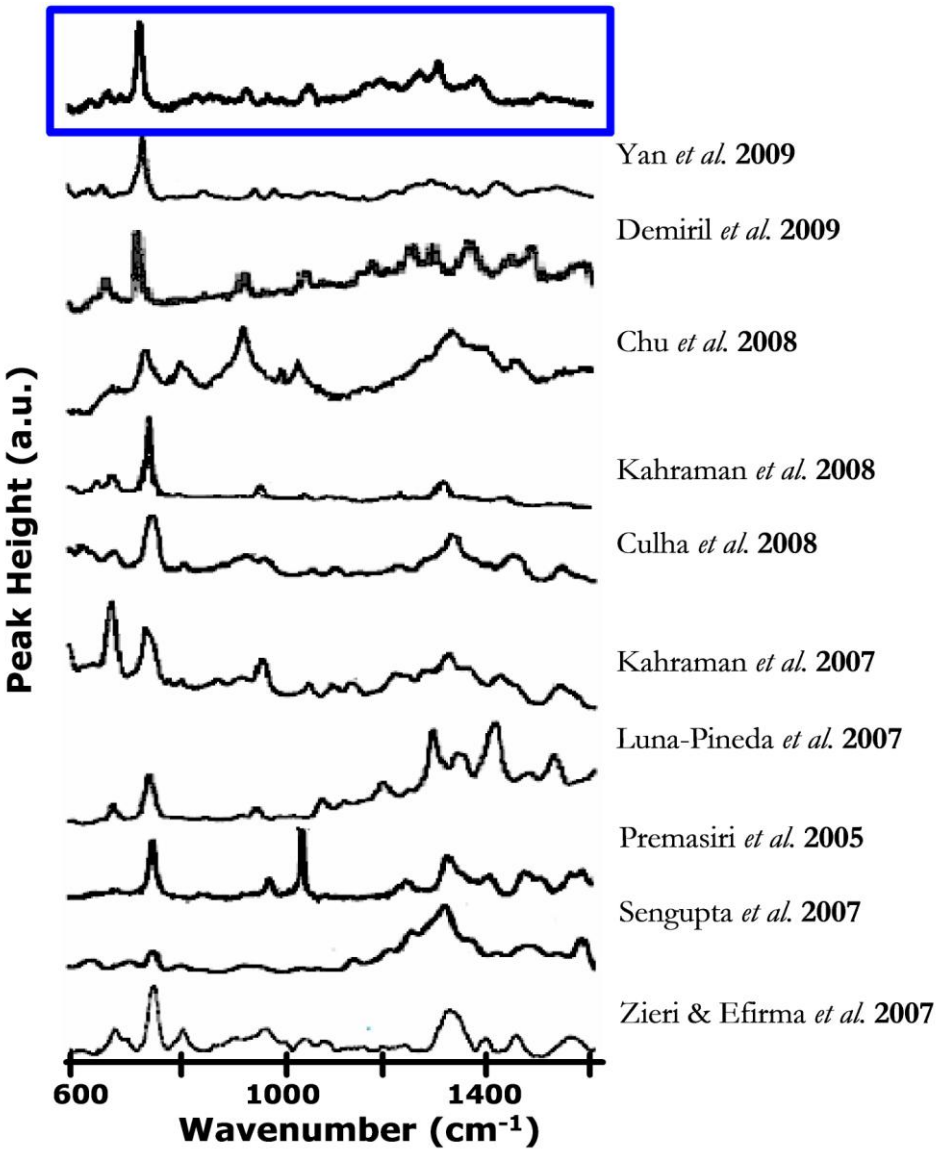

Figure 6.8. Published SERS spectra acquired on *E. coli*. The spectra presented in the figure were taken from the papers designated by the reference. Spectra were offset along the intensity axis for ease of comparison. The box outlines the spectrum acquired for my sample of *E. coli*.

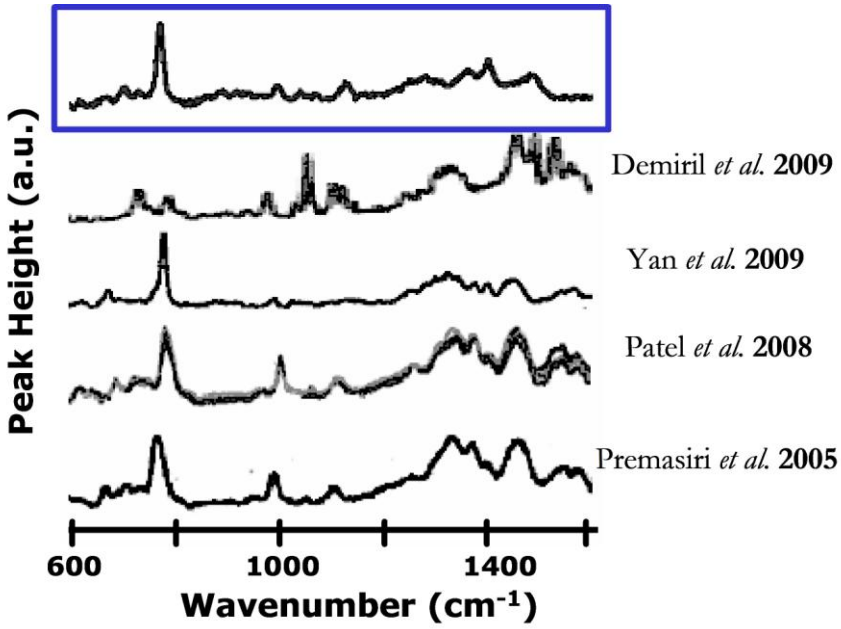

Figure 6.9. Published SERS spectra acquired on *B. cereus*. The spectra presented in the figure were taken from the papers designated by the reference. Spectra were offset along the intensity axis for ease of comparison. The box outlines the spectrum acquired for my sample of *B. cereus.*

resultant hierarchical clustering may have been influenced more by residual growth medium in the sample rather than by differences in the components of the bacterial cell wall. We invite experts in multivariate analysis of SERS spectra to test this suspicion by challenging the spectra of diluted growth media against the existing hierarchical clusters for bacteria.

Regardless of whether the above hypothesis is disproven, our findings provide strong impetus for a re-investigation of protocols commonly used in discriminating between bacterial cell type, species, and strain by SERS. Given i) the structural and compositional similarities in the bacterial cell wall structure, ii) the lack of consensus on the spectral attributes of a specific bacterial species, iii) the similarity in spectral features between the medium and the bacterium, and iv) the variability in sample and substrate preparation methods, there exists a clear need for acquisition of SERS spectra on bacterial samples *devoid* of growth medium.

We have definitively demonstrated that small quantities of medium present in the sample give rise to a strong SERS response. This response reflects the affinity of medium components for the substrate surface and their favorable mass transport characteristics, relative to that of the intact bacterial cell. Should the preparation of a medium-free, intact and viable bacterial sample prove elusive, then spectra characteristic of a given bacterial type, species and strain will be obtainable using either confocal Raman[158, 167, 178, 204-205, 384] or optical tweezer[161, 204] based Raman techniques.

CHAPTER 7

LIMITATIONS OF A SERS-BASED ASSAY OF DNA HYBRIDIZATION

7.1. Introduction

Silver nanorod (AgNR) arrays fabricated by glancing angle deposition (GLAD) have found application as substrates for surface enhanced Raman scattering (SERS).[134-140, 145, 147-148, 198, 292, 303, 391] Recently, there have been several reports for the use of SERS for biomolecular detection. Of particular interest has been the detection of whole cell bacteria,[177, 179, 181] whole virus particles,[132, 139] viral biomarkers,[197] biofilms[203] and viral genomic material such as DNA.[1, 6, 115, 207] Currently, diagnostic methods for viruses are based on polymerase chain reaction (PCR), enzyme-linked immunosorbent assay (ELISA) and cell cultures.[392-394] Both PCR and ELISA are time consuming, expensive and require skilled technicians with little to no virus recovery after testing. Although cell cultures allow for viral recovery, samples require a few days to culture as well as a skilled technician to carry out the testing.[394] Thus, a rapid, reliable, and sensitive means of viral detection is still needed.

A possible means for accomplishing this is a DNA or RNA hybridization assay to detect a specific strain of a virus. An attractive virus to use for these initial studies is respiratory syncytial virus (RSV) as it is a fairly simple virus with only two known strains. RSV is a negative sense RNA virus from the *Paramyxoviridae* family[12] mainly affecting small children and the elderly during a yearly 4-6 month outbreak period.[395] It is the leading

cause for hospitalization for children under the age of one with more than 120,000 admissions each year.[396-397] RSV is highly contagious and causes a considerable portion of lower respiratory tract infection in young children, the elderly and the immune compromised.[398] A rapid, reliable, and sensitive method of detection would be beneficial to aid in diagnosing, treating and preventing infection.

In this chapter, the use of AgNR substrates for assaying nucleic acid hybridization is critically evaluated. Oligonucleotide (oligo) pairs specifically designed to detect RSV in nasal fluids were prepared and evaluated (see Table 7.1). SERS spectra acquired on oligos, alone or in combination, contain the known spectral signatures of the nucleotides that comprise the oligo. Spectra acquired on an oligo with a 5'- or 3'-thiol were distinctly different from that acquired on the identical oligo without a thiol pendant group suggesting some control over the orientation of the oligo on the nanorod surface. The signal enhancement in SERS depends markedly upon the location of the probe relative to the substrate surface.[9, 23, 82-83] By systematic placement of nucleotide markers along the oligo chain, we have identified the point at which the nucleotide disappears from the spectrum. Additional studies were performed using silver nanoparticle (AgNP) substrates using dynamic light scattering (DLS), scanning electron microscopy (SEM), and tunneling electron microscopy (TEM) to provide further support that thiolated DNA was standing up off the surface. Additionally, atomic force microscopy (AFM) studies were performed on an atomically flat silver surface. The findings presented in this chapter suggest that the applicability of SERS for detecting nucleic acid hybridization is limited.

7.2. Materials

Rhodamine-6G (R6G) was used to test SERS activity of the AgNR array substrate (see Chapter 3 for a more detailed description of SERS activity using R6G as a Raman active probe analyte). A 1X solution of saline-sodium citrate (SSC) buffer was prepared using 150 mM sodium chloride and 15 mM trisodium citrate in nanopure water (Ω) and adjusted to a pH of 7 using hydrochloric acid. Ammonium acetate (AmAc) was used to prepare a 50 mM buffer solution (all purchased from Fischer Scientific, Pittsburgh PA).

DNA sequences Poly-A, Poly-C, Poly-T, Poly-G, RSV-1 thiol, RSV-2, RSV-3 thiol, RSV-4, RSV-5 thiol, RSV-6, RSV-7 thiol, RSV-8, RSV-9 thiol, and RSV-10 were purchased from Integrated DNA Technologies Inc. (Coralville, IA) and RSV-2 thiol, RSV-4 thiol, RSV-6 thiol, RSV-8 thiol, RSV-10 thiol, 1AC, 1AC-2, 2AC, 3AC, 4AC, 5AC, 6AC, 7AC, 8AC, 9AC, 10AC, A3C12, C3A3C9, C5A3C7, C7A3C5, A5C10, C5A5C5, C10A5, and A10C5 were purchased from Midland Certified Regent Company, Inc. (Midland, TX). All sequences are listed in Tables 7.1 and 7.2. DNA was used as received without further purification and stock solutions were prepared in nanopure water. Further dilutions were made using nanopure water, 1X SSC, and 50 mM AmAc buffer.

7.3. Methods

7.3.1. SERS Substrates

AgNR SERS substrates were fabricated and stamped as described previously in Chapter 3, section 3.2.1. Silver nanoparticles (AgNP) were synthesized using citrate reduction[399] by Steven Hayden in Professor Mostafa El-Sayed's research lab at the

Georgia Institute of Technology. Briefly, a 1 mM silver nitrate solution was prepared and brought to a rolling boil followed by addition of a 10 mg/mL solution of trisodium citrate. The reaction mixture was held at a constant temperature and boiled until the solution turned yellow-grey in color. The absorbance spectrum of stock nanoparticles was obtained using a Shimadzu UV -1601 UV-visible spectrophotometer (Columbia, MD). A single peak centered at ~430 nm was observed over the spectral range from 200 to 900 nm.

Particles were functionalized with both ssDNA and dsDNA. DNA was added in a threefold excess to ensure complete functionalization of the surface and incubated for at least 8 hours prior to analysis. A control solution was prepared where nanopure water was added in place of DNA to keep the particle densities consistent between all samples. Samples were washed by centrifugation for three minutes at 14,000 rpm followed by re-suspension in nanopure water to remove any residual DNA.

7.3.2. SERS Characterization

SERS measurements were carried out as described in Chapter 3, section 3.2.3. Spectra were not normalized or rescaled unless otherwise noted. For AgNP substrates, a 5 µL aliquot of functionalized nanoparticles were deposited and allowed to evaporate on a silver coated 1" x 3" glass microscope slide. The same experimental parameters were used for both AgNRs and AgNPs substrates.

7.3.3. Scanning Electron Microscopy (SEM) Characterization

SEM micrographs were acquired as described in Chapter 3, section 3.2.3 for AgNR arrays. The same used for SERS analysis were also imaged using the SEM. Images were

Table 7.1. Sequences designed to unique portions of the RSV genome. Odd numbered and thiolated sequences correspond to the probe capture oligo and the even numbered nonthiolated sequences correspond to the compliment. Custom designed oligos correspond to RSV in general as well as the two strains, A and B. Each sequence was synthesized with and without a pendent thiol group. For 5' thiol groups a C_6 linker was used and for 3' thiol groups a C_3 linker was used.

Oligo Name	Sequence (ssDNA)	Additional Information
RSV-1	5'-GCATTCATAAACAATCCTGCA-3’	RSV
RSV-1-SH	5'-SH-GCATTCATAAACAATCCTGCA-3’	RSV
RSV-2	5’-TGCAGGATTGTTTATGAATGC-3’	RSV
RSV-2-SH	5’-TGCAGGATTGTTTATGAATGC-SH-3’	RSV
RSV-3	5'-CTTCATTGTTATCAAATGTTTC-3’	RSV
RSV-3-SH	5'-SH-CTTCATTGTTATCAAATGTTTC-3’	RSV
RSV-4	5’-GAAACATTTGATAACAATGAAG-3’	RSV
RSV-4-SH	5’-GAAACATTTGATAACAATGAAG-SH-3’	RSV
RSV-5	5’-TGCAGTATCATCTGTCTC-3’	RSV, Strain A
RSV-5-SH	5’-SH-TGCAGTATCATCTGTCTC-3’	RSV, Strain A
RSV-6	5’-GAGACAGATGATACTGCA-3’	RSV, Strain A
RSV-6-SH	5’-GAGACAGATGATACTGCA-SH-3’	RSV, Strain A
RSV-7	5’-TGGGGTACTGTCGGCTTC-3’	RSV, Strain B
RSV-7-SH	5’-SH-TGGGGTACTGTCGGCTTC-3’	RSV, Strain B
RSV-8	5’-GAAGCCGACAGTACCCCA-3’	RSV, Strain B
RSV-8-SH	5’-GAAGCCGACAGTACCCCA-SH-3’	RSV, Strain B
RSV-9	5’-AGCTCATCTTAAAGC-3’	RSV
RSV-9-SH	5’-SH-AGCTCATCTTAAAGC-3’	RSV
RSV-10	5’-GCTTTAAGATGAGCT-3’	RSV
RSV-10-SH	5’-GCTTTAAGATGAGCT-SH-3’	RSV

acquired using the same settings and protocols described for AgNR arrays in Chapter 3, section 3.2.3.

7.3.4. Transmission Electron Microscopy (TEM) Characterization

TEM micrographs were acquired by Adam Poncheri in Professor Mostafa El-Sayed's research lab at the Georgia Institute of Technology. A JEOL JEM 100CX II electron microscope (JEOL Ltd., Tokyo 196-8558, Japan) was used to acquire images with an accelerating voltage of 100 kV. Images were taken at 40K and 100K time magnification for AgNPs functionalized with thiolated and nonthiolated DNA.

7.3.5. Dynamic Light Scattering (DLS) Measurements

DLS measurements were taken by Nicholas Haase in Professor Nils Kroger's research lab at the Georgia Institute of Technology using a Zetasizer Nano Series Nano-ZS (Malvern Instruments, Ltd., Worcestershire, United Kingdom). The material parameter was set to silver with a refractive index of 0.56 and the absorbance at 633 nm was 0.00. Measurements parameters were as follows: measurement beam was set to 633 nm, collection was at 173° backscatter and a total of 10 runs at 10 sec/run were averaged together to give the diameter for silver nanoparticle solutions. Measurements were acquired for AgNPs functionalized with thiolated and nonthiolated DNA.

7.3.6. DNA Melting Curves

Melting curves were performed by Ragan Buckley in Professor Nicholas Hud's research lab at the Georgia Institute of Technology. An Agilent 8453 UV-Vis diode array spectrophotometer with an Agilent 8909A Peltier temperature control device was used to take measurements. Specifically, two heating (5 – 95 °C) and two cooling (95 – 5 °C)

cycles were carried out at 1 °C increments. The cuvette path length was 1 cm. Melt curves were obtained by plotting absorbance at 260 nm versus temperature and taking the 1st derivative. The sample size was 625 µL at a concentration of 60 µM. Melts were carried out in 1X SSC, 50 mM AmAc and nanopure water.

7.3.7. AFM Imaging

AFM imaging was performed by Kelsey Beavers in the Bottomley research lab. Substrates were prepared using a custom made polydimethylsiloxane (PDMS) stamp created from a Sylgard 184 Silicone Elastomer Kit (Dow Corning, Midland, MI). PDMS was allowed to set for 24 hours at room temperature. A 1.0 mm diameter circle was cut into the PDMS to allow for a void in transferred material at the surface. For height comparison studies, a 1.0 mM solution of 1-dodecanethiol (Sigma-Aldrich®, St. Louis, MO) in ethanol was applied to the stamp and transferred to a freshly cleaved template-stripped silver surface. Excess ethanol was allowed to evaporate prior to backfilling the circular void with 1 µL of 0.1 mM thiolated or nonthiolated DNA. Samples were allowed to evaporate and stored in a desiccator until imaging. All images were acquired using a Nanoscope IIIa (Veeco, Santa Barbra, CA) scanning probe microscope operating in tapping mode under a nitrogen atmosphere using NSC35/AlBS cantilevers (Mikromasch, San Jose, CA). Scan domains were varied from 1-4 µm, while scan rates ranged from 1-2 Hz. Force curves and cantilever resonance data were acquired under atmospheres of N_2 and air using an MLCT-AUHW cantilever (Veeco, Santa Barbra, CA) with a spring constant of 0.067 N/m, and a deflection sensitivity of 54 nm/V.

7.4. Results and Discussion

Oligomers were designed to analyze the sensitivity of the AgNR SERS substrates for DNA detection. Initially, spectra were acquired on oligos consisting of a single base, namely Poly-A, Poly-C, Poly-T and Poly-G. Due to stability issues, Poly-G was alternating GGGA segments. Because of this, adenine peaks were expected in the spectrum. The resulting spectra for all poly DNA is presented in Figure 7.1. The spectral bands in the individual spectra for each base correspond to results reported previously in literature regarding SERS of single DNA bases.[6, 8] It is clear from these spectra as well as previous literature[1-8] that the relative intensities of several peaks changes with sequence. These are: 680, 730, 790, 1300, 1320, and 1360 cm^{-1} as they are the sharpest and most sensitive to any variation in DNA sequence. Figure 7.2 presents a spectrum for a DNA oligo containing all four nucleotides. The major spectral bands are labeled to designate the major spectral features associated with each nucleotide. Table 7.2 provides these assignments compiled from literature for each peak in the spectrum.

Oligos with sequences specific to unique portions of RSV genome were designed and synthesized. Table 7.1 presents the single stranded DNA (ssDNA) sequences used in these studies relating to regions of the RSV genome. Odd numbered sequences correspond to the oligo used as the probe molecule, and the even numbered sequences correspond to the strand complementary to the probe. Oligos were designed to target strain A (RSV-5 and RSV-6) and strain B (RSV-7 and RSV-8) separately as well as RSV in general (RSV-1, RSV-2, RSV-3, RSV-4, RSV-9 and RSV-10).[391] Spectra were

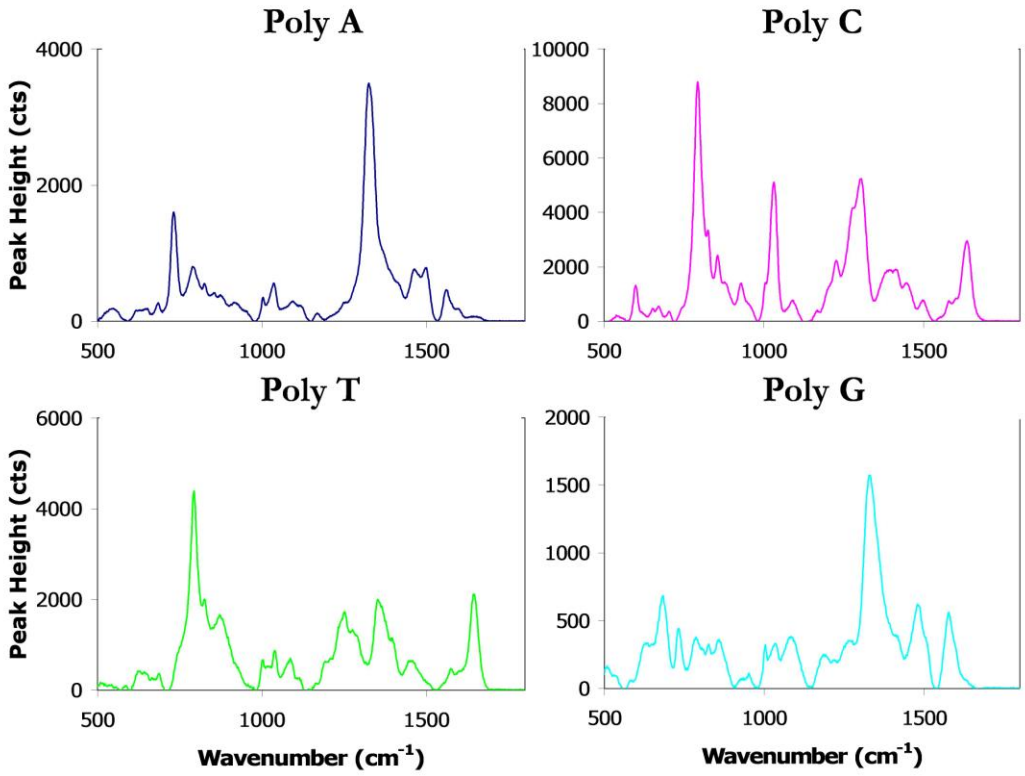

Figure 7.1. SERS spectra acquired for Poly-DNA oligos. All oligos were diluted in nanopure water. For analysis, 5 µL aliquots of a 1 x 10^{-5} M solution were applied to the AgNR substrate and allowed to evaporate.

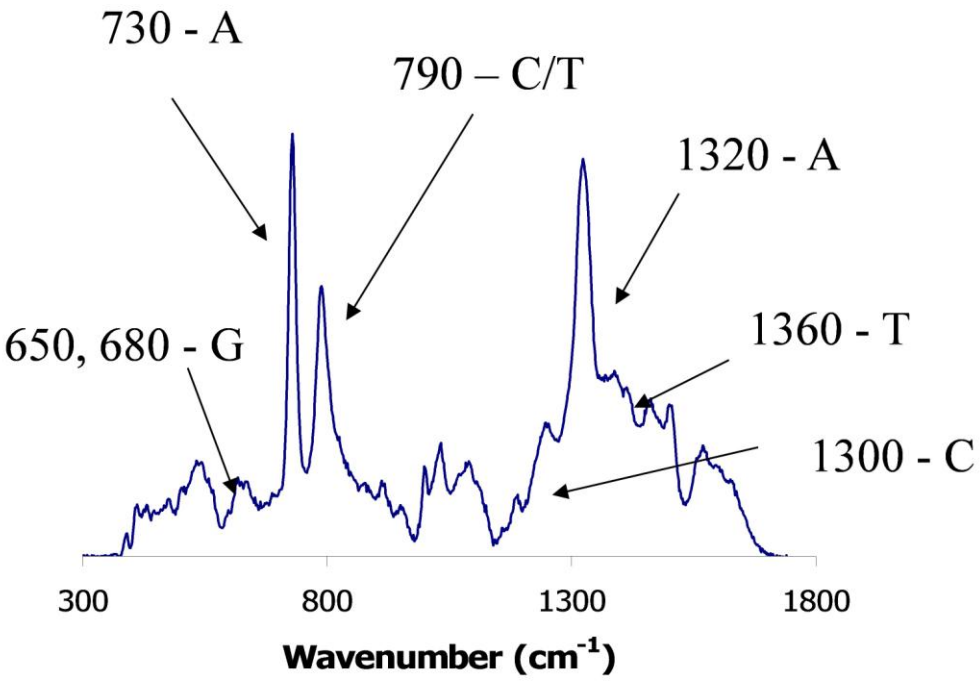

Figure 7.2. Generic SERS spectrum for a DNA oligo. The peaks of interest are indicated with an arrow and are labeled with the corresponding base. Specific bands of interest are 730 cm^{-1} and 790 cm^{-1} corresponding to the ring breathing and stretching modes for adenine and cytosine/thymine, respectively.

Table 7.2. Complied list of spectral band assignments specific to each DNA nucleotide from literature.[1-8]

Cytosine	**Spectral Band (cm^{-1})**
Ring Breathing	796
Amino Group (NH_2)	1020, 1212
C=C Stretching	1640
Thymine	
Ring Stretch and CH Bending	1275
C=O Stretching	1652
C=C Stretching	1562, 1584
Sym. Ring Stretching	776
C-CH_3	992, 1372
Adenine	
Ring Stretching	732
External Amino	960, 1028,1122
Single Bond Stretching	1334
Guanine	
Symmetric Ring Stretching	656
Single Bond Stretching	1384, 1458, 1514,1582
C=O	1680

acquired on all ten oligos in nanopure water to investigate spectral variations correlating to changes in the sequence. Figure 7.3 presents the resulting spectra. The spectra have been background corrected, normalized to the peak of highest intensity and offset for clarity. The spectral bands that appear in the spectra match those previously reported in literature for DNA bases.[1-2, 6-8, 109, 184, 400]

Specific bands of interest are the intense and sharp peaks at 730 cm^{-1} and 790 cm^{-1} corresponding to the ring breathing and stretching modes for adenine and cytosine/thymine, respectively. The strong peak at 1030 cm^{-1} was not used in analysis because the overall intensity is influenced by shoulders off the main peak corresponding to thymine and cytosine ring stretching. The ratio of the 730 cm^{-1} and 790 cm^{-1} peak intensities were compared for all spectra acquired on single stranded RSV oligos and compared to one another. Figure 7.4 presents the plot of intensities for the 730 cm^{-1} and 790 cm^{-1} bands versus sequence composition, designated as ΣA's/(ΣC's + ΣT's). The resulting linear relationship validates the use of the intensity ratio for tracking the sensitivity of the SERS spectrum to a variation in sequence composition. Additionally, this ratio can be utilized to correct for day to day variability in peak intensities.

Experiments were carried out on both complementary and noncomplementary pairs of DNA to distinguish between non-specific binding and hybridization. Experimental conditions were systematically adjusted to enable and inhibit DNA hybridization. The adjustments included changing buffer type and concentration, orientation of the probe strand, and an annealing/cooling cycle, essential for hybridization to take place. Spectra

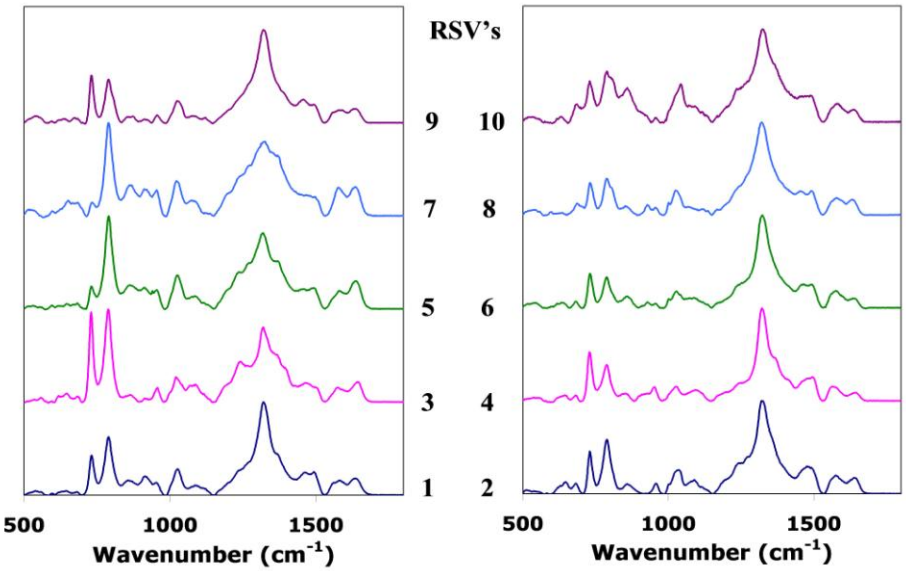

Figure 7.3. SERS spectra for the RSV oligos listed in Table 7.1. All oligos are nonthiolated and diluted in nanopure water.

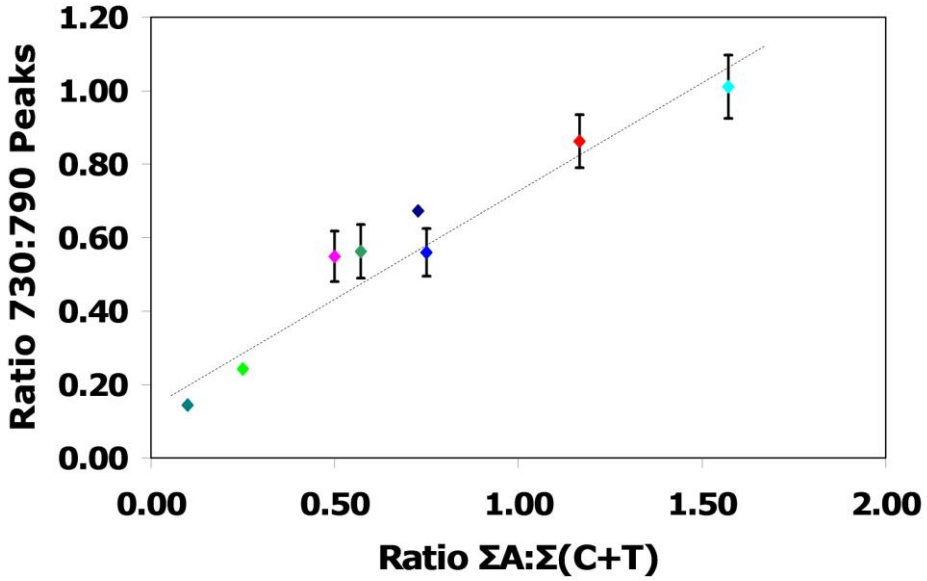

Figure 7.4. Plot of intensities for the 730 cm^{-1} and 790 cm^{-1} bands versus sequence composition, designated as ΣA's/(ΣC's + ΣT's) for the nonthiolated single stranded RSV oligos presented in Table 7.1. The linear trace supports the use of the use of the intensity ratio for tracking the sensitivity of the SERS spectrum to a variation in sequence composition.

were acquired on each pair of oligos alone and in combination, for both complementary and noncomplementary pairs. Noncomplementary pairs were analyzed in water rather than 1X SSC buffer to ensure that incomplete or partial hybridization did not occur.

Figure 7.5 presents the background corrected SERS spectra acquired for one set of complementary oligos, RSV-7 (blue trace) and RSV-8 (pink trace). The plot depicts the oligos alone and in combination (green trace) in a 1X SSC buffered solution. The hybrid was pre-formed in a centrifuge tube prior to application to the well and hybridization was verified through a DNA melting curve of the sample (see Figure 7.6). The relative peak intensities varied for the ssDNA versus hybridized dsDNA indicating that differences in the DNA sequences were detected at the AgNR surface. However, no new or unique peaks to be associated with the hybridization event were observed. The results presented for RSV-7 and RSV-8 were typical of all pairs of complementary RSV oligos listed in Table 7.1.

Spectra acquired in SSC buffer solution possessed much lower peak intensities relative to spectrum acquired in the absence of buffer. This is due to crystal deposits within the nanorod array (See Chapter 3, Figures 3.7 and 3.8 for a direct comparison of water and 1X SSC solutions of R6G). Since cations are required for formation and stabilization of dsDNA, alternative buffers were investigated. All nonvolatile buffers gave similar results. Spectra acquired on ssDNA and dsDNA prepared in 50 mM AmAc buffer (Figure 7.7) gave modest improvement. Since AmAc is a volatile buffer, crystalline deposits within the nanorods should be eliminated if sufficient time is allowed for the

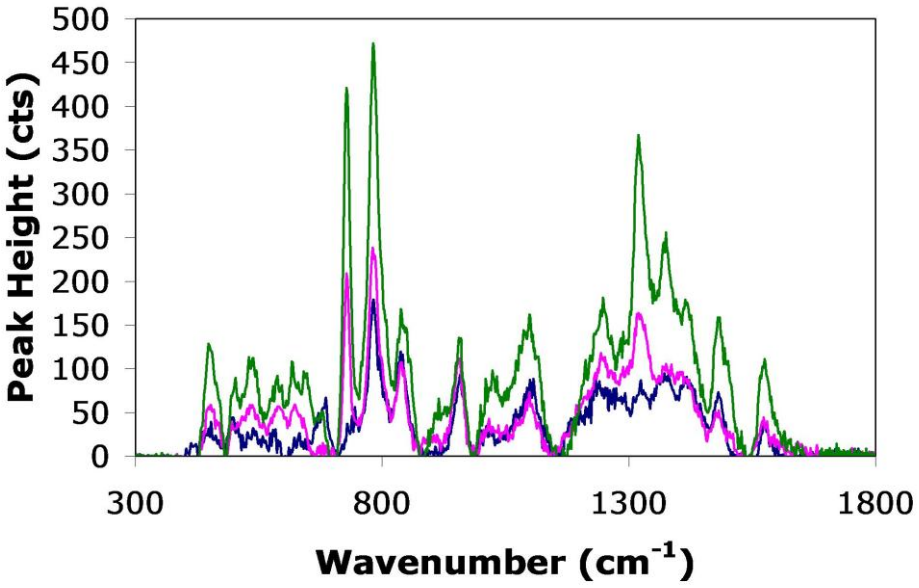

Figure 7.5. Plot of the SERS spectra acquired for a set of complementary oligos. RSV-7 (blue trace) and RSV-8 (pink trace) are presented alone and in combination (green trace) in a 1X SSC buffer solution. The green trace is representative of the hybridized form, as verified through a DNA melting curve of the sample (Figure 7.5).

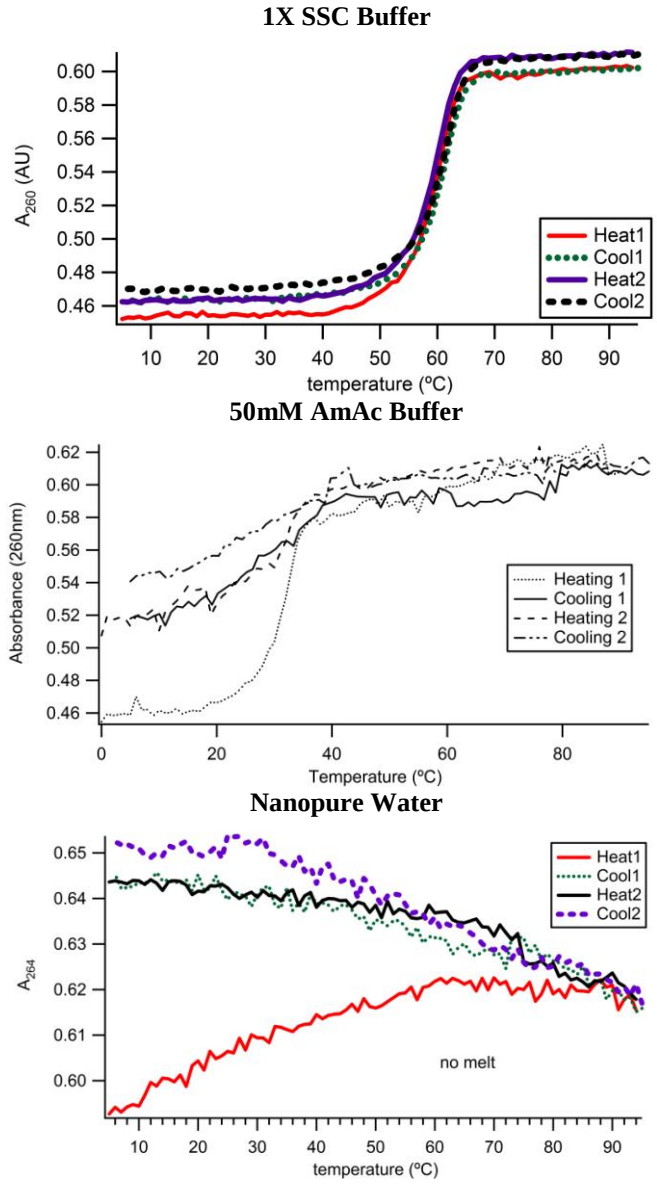

Figure 7.6. Plot of the DNA melting curves obtained for a set of complementary oligos. A total of two heating and two cooling steps were employed for all curves. The three plots were acquired on DNA in different solutions; 1X SSC, 50 mM AmAc, and nanopure water. It is clear that 1X SSC and AmAc provides and environment conducive for hybridization and water does not.

buffer to sublime off the surface. The relative intensities for the single stranded and double stranded oligos acquired from AmAc buffered samples change in a similar fashion to those obtained from 1X SSC buffer samples. This provides further support that the spectra track changes in DNA sequence when the oligos lie on the AgNR surface.

Studies were also conducted on noncomplementary oligos with thiol termini. Figure 7.8 presents the background corrected SERS spectra for thiolated RSV-7 and RSV-10 oligos alone (pink and blue traces) and in combination (green trace). The results obtained for this set of oligos was consistent with the results obtained on other combinations. Examination of the three spectra shows that a change in relative peak intensities is still observed, however one cannot determine that this change is due to a hybrid or non-specific binding at the AgNR surface. This discovery is troublesome in regards to developing a hybridization assay for viral diagnosis.

It is interesting to note that the peaks corresponding to adenine acquired on thiolated RSV-7 was barely distinguishable from the background. Since RSV-7 contains a single adenine located seven nucleotides from the pendent thiol linker, the low intensity of the 730 cm^{-1} band may indicate poor sensitivity of the assay or that the adenine is too far from AgNR surface to be detected. Many studies have shown that detection of a single base mismatch is possible with SERS.[1-2, 6, 400] The latter explanation is plausible if and only if the ssDNA oligo is "standing up" off the surface. To test this hypothesis, all RSV oligos were synthesized with and without a pendent thiol group. Spectra were

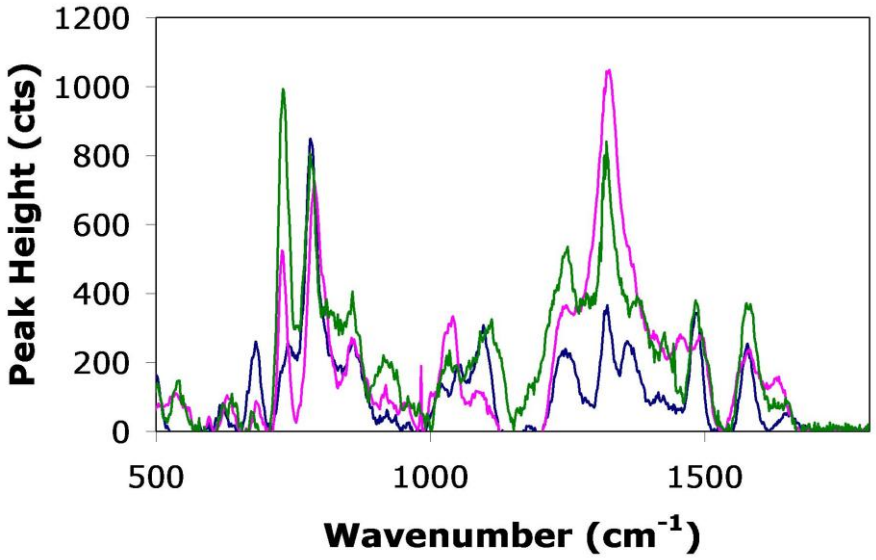

Figure 7.7. Plot of the SERS spectra acquired for one set of complementary oligos. RSV-7 (blue trace) and RSV-8 (pink trace) are presented alone and in combination (green trace) in a 50 mM AmAc buffer solution. The green trace is representative of the hybridized form, as verified using a DNA melting curve (Figure 7.6).

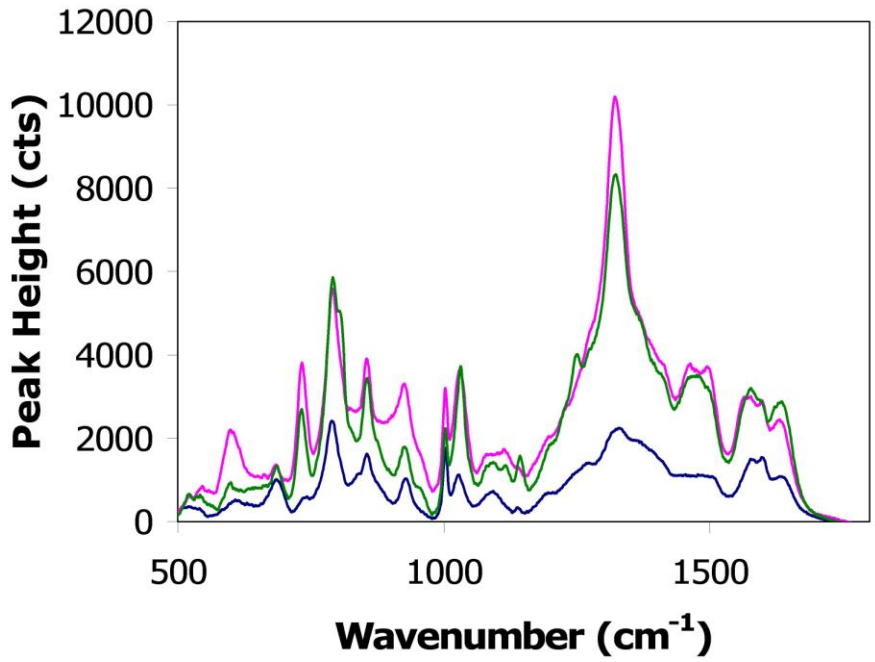

Figure 7.8. Plot of noncomplementary ssDNA; RSV-7 (blue trace) and RSV-10 (pink trace) are presented alone and in combination (green trace). The two strands are not complementary to one another and will not produce a double stranded hybrid. From the plot it is clear that a change in relative peak intensities is still seen, and one cannot discriminate non-specific binding at the AgNR surface.

acquired for all single stranded RSV oligos with and without a pendent thiol linker in nanopure water (see Table 7.1 for listing of sequences).

Figure 7.9 presents SERS spectra acquired on two of the ten RSV oligos, RSV-3 and RSV-9. Data was background corrected and the plots were truncated to focus on a portion of the entire SERS spectra. Both the thiolated (blue trace) and nonthiolated (pink trace) forms of the DNA oligo are presented. The variation in the relative intensities of the 730 cm^{-1} and 790 cm^{-1} peaks are evident. For RSV-3, the ratio of 730 to 790 cm^{-1} is 0.96 for the non-thiol and 0.38 for the oligo with a pendent thiol linker. For RSV-9, the ratio of 730 to 790 cm^{-1} is 1.08 for the nonthiolated form and 0.52 for the thiolated oligo. These results suggest that there is a definite difference in orientation between the thiolated and nonthiolated forms of ssDNA oligo on the silver surface

To test this hypothesis, oligos comprised of only adenine and cytosine were designed. The rationale behind using only A and C is: 1) the response from these two bases is the strongest; thus there should be a higher degree of sensitivity to change in relative position of A (see Figure 7.1)[6, 8], 2) any change in the 730 to 790 cm^{-1} ratio is a function of the nucleotide concentration and distance from the surface since the 730 cm^{-1} peak is unique to adenine and the 790 cm^{-1} peak is unique to cytosine. The sequences used for these "Moving A" studies are presented in Table 7.3.

Spectra were acquired on DNA probes where a set number of adenine was at the beginning of the oligo and closest to the AgNR surface in the same manner as described

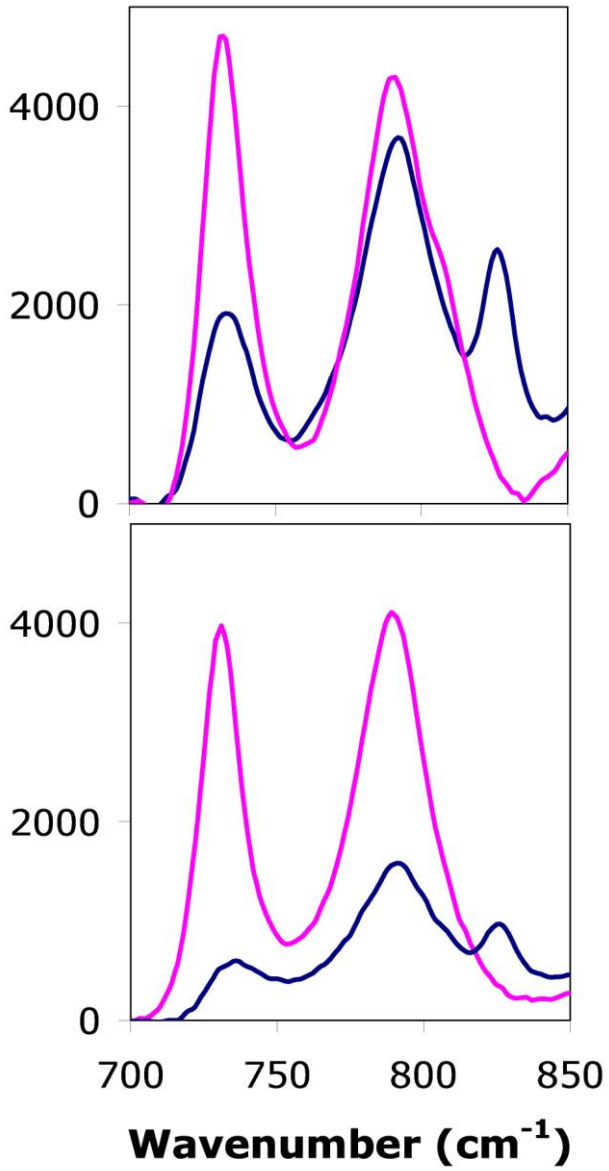

Figure 7.9. Plot of the SERS spectra acquired for two oligos with (blue trace) and without (pink trace) a pendent thiol group. The top plot provided the truncated spectra acquired for RSV-9 and the bottom spectra presents the spectra for RSV-3.

Table 7.3. Sequences designed to probe the dependence of the position and number of adenines on SERS intensity.

Oligo Name	Sequence (ssDNA)
1AC	5'-CCCCCCCCCCCCCC**A**-SH-3'
1AC-2	5'-CCCCCCCCCCCCCC**A**-3'
2AC	5'-CCCCCCCCCCCCC**A**C-SH-3’
3AC	5'-CCCCCCCCCCCC**A**CC-SH-3’
4AC	5'-CCCCCCCCCCC**A**CCC-SH-3’
5AC	5'-CCCCCCCCCC**A**CCCC-SH-3’
6AC	5'-CCCCCCCCC**A**CCCCC-SH-3’
7AC	5'-CCCCCCCC**A**CCCCCSH--3’
8AC	5'-CCCCCCC**A**CCCCCC-SH-3’
9AC	5'-CCCCCC**A**CCCCCCC-SH-3’
10AC	5'-CCCCC**A**CCCCCCCCSH--3’
A3C12	5'-CCCCCCCCCCCC**AAA**-SH-3'
C3A3C9	5'-CCCCCCCCC**AAA**CC-SH-3'
C5A3C7	5'-CCCCCCC**AAA**CCCC-SH-3'
C7A3C5	5'-CCCCC**AAA**CCCCCC-SH-3'
A5C10	5'-CCCCCCCCCC**AAAAA**-SH-3'
C5A5C5	5'-CCCCC**AAAAA**CCCC-SH-3'
C10A5	5'-**AAAAA**CCCCCCCCC-SH-3'

for the RSV oligos. Figure 7.10 presents the plot of the ratio of peak intensities versus number of As proximal to the silver surface. If the strand lies on the surface, all nucleotides should be sensed as seen in Figure 7.3. If the strand is standing up off the surface, then the known distance dependence of the SERS signal should result in a decrease in sensitivity as the given nucleotide moves further away. The relationship for this subset of Moving A oligos is not linear; the ratio of intensities plateaus after only 5 nucleotides from the surface. This suggests an orientation difference between thiolated and nonthiolated ssDNA oligos. This result is consistent with the established distance dependence for the electromagnetic enhancement mechanism.[82, 86]

Additional 15mers were designed moving single or multiple adenine bases systematically from the AgNR surface. These sequences are also provided in Table 7.3. Oligos were designed in three different sets where a single adenine (1A), three adenines (3A), or five adenines (5A) were moved further from the surface. In addition to these three sets, an oligo was designed without a pendent thiol. This data point was used to establish a distance of zero from the AgNR surface. The results from SERS spectra acquired on these subsets of DNA oligos is presented in Figure 7.11. For all three sets, 1A, 3A, or 5A, a clear fall-off of intensity occurs when the adenine are moved further from the surface. The trend of the intensity fall-off mimics that presented in previous reports.[82, 86] These results also confirm and support the strong distance dependence of the SERS electromagnetic enhancement mechanism. The dramatic decrease in sensitivity with distance from the surface is problematic for development of a hybridization assay since almost all probe molecules will be longer than 5 or 6 bases.

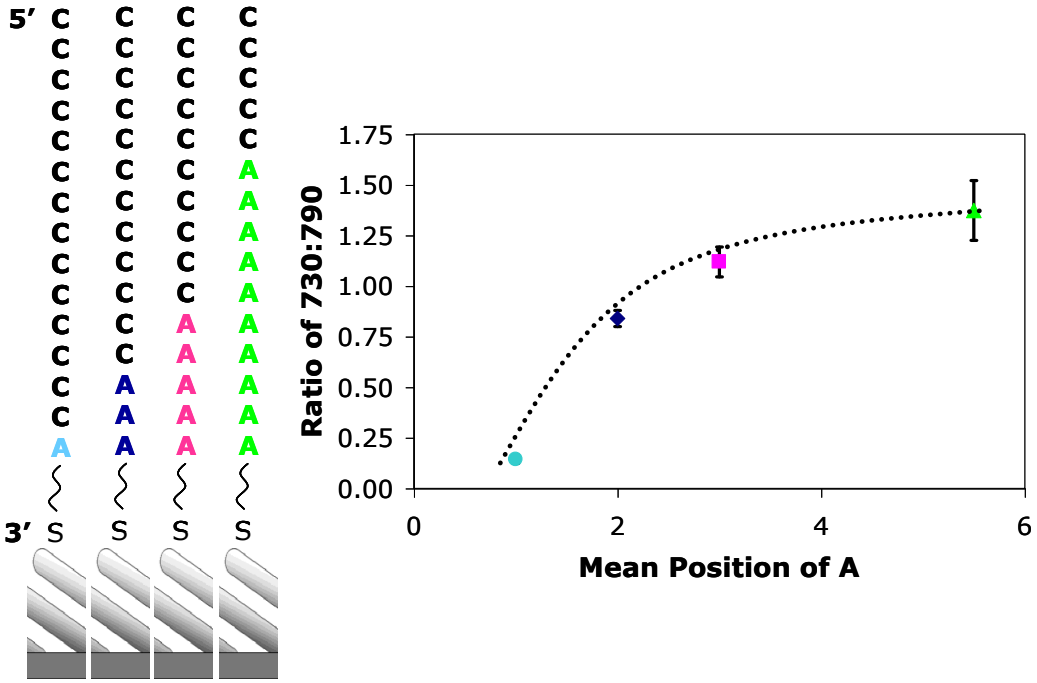

Figure 7.10. Schematic representation of the DNA oligos used to investigate the distance dependence of SERS at the AgNR surface. Also presented is a plot of the ratio of peak intensities for 730 to 790 cm^{-1} peaks as a function of adenine concentration. The curvi-linear relationship provides additional support that thiolated DNA stands up off the surface.

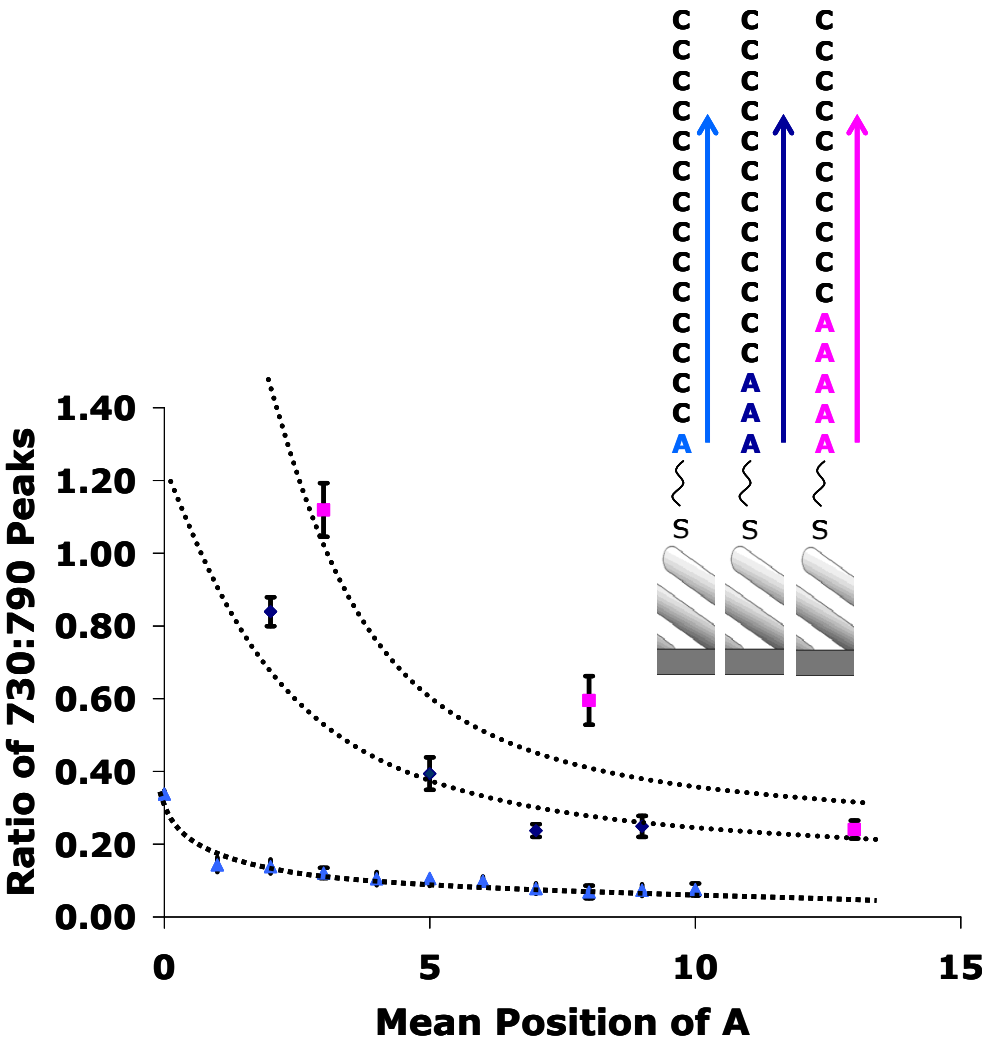

Figure 7.11. Plot of the ratio of intensities for the 730 to 790 cm^{-1} peaks as a function of the mean position of adenines. The inset is a schematic representation of oligo sequences designed to probe the distance dependence at the AgNR surface. Also presented is the ratio of. The curved shape of the lines clearly depicts the distance dependence as the adenine base is moved further from the surface.

Differences in the SERS spectra of thiolated and nonthiolated DNA clearly indicate that the thiolated DNA is "standing up" off the surface. To determine the distance and angle that the ssDNA oligos extend from the surface additional studies were carried out. Silver nanoparticles (AgNPs) were employed as a base substrate instead of AgNRs to enable examination of the adlayer by dynamic light scattering (DLS), SEM and transmission electron microscopy (TEM). Flat silver surfaces were examined using cyclic voltammetry (CV) and atomic force microscopy (AFM) to probe binding of DNA through the thiol terminus and examine the packing density and surface coverage.

SEM micrographs were obtained for AgNPs with and without DNA functionalization. Figure 7.12 presents the images for (a.) untreated, (b.) thiolated and (c.) nonthiolated RSV-5 AgNP solutions. Images were acquired on the evaporation ring to determine the shape and size distribution of the AgNP samples.

DLS was used to investigate determine whether a change in the hydrodynamic radius of the AgNPs occurred when they were functionalized with thiolated vs. nonthiolated DNA solutions. AgNPs were treated with thiolated and nonthiolated RSV-5 and RSV-6 (see Table 7.1 for the sequences). Both ssDNA and dsDNA were analyzed in comparison to naked AgNPs used as a control. The dsDNA was hybridized prior to incubation with the AgNPs.

Figure 7.13 presents the DLS results for single stranded thiolated RSV-5, single stranded nonthiolated RSV-5, and untreated AgNPs (as a control). A dashed blue line has been

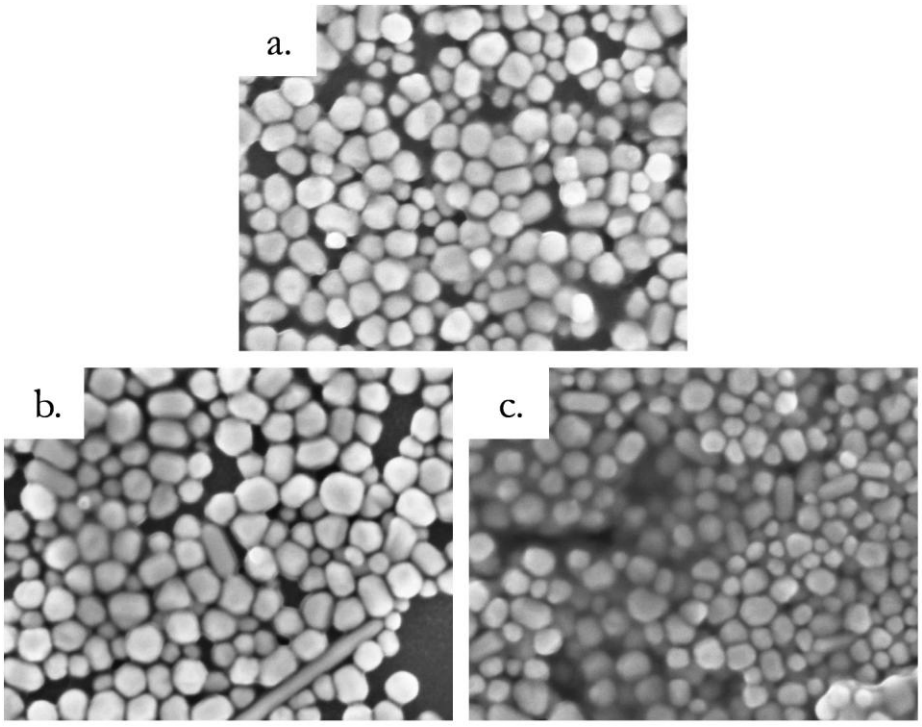

Figure 7.12. SEM micrographs depicting control AgNPs (a.) and RSV-5 both thiolated (b.) and nonthiolated (c.) for comparison. Because of the evaporation effects upon drying of the solution, the particles were all aggregated in an ring on the flat silver substrate.

superimposed on the plots to aid in peak comparison and is centered on the control AgNPs peak. The average diameter for the RSV-5 thiol solution (Figure 7.13a.) was centered at 80.84 nm whereas the non-thiol solution (Figure 7.13b.) was centered at 95.21 nm suggesting a difference in the hydrodynamic radius. Comparison of the control (Figure 7.13c.), where the radius is 96.08 nm, with the nonthiolated DNA indicates that their hydrodynamic radii are very similar. Prior to acquiring DLS measurements, the particles were washed to remove excess and unbound DNA. The sensitivity of the values for the nonthiolated DNA sample and the control suggest that washing the particles essentially removed the DNA. The trend observed with RSV-5 was similar to RSV-6; thiolated RSV-6 had a radius centered at 83.45 nm and nonthiolated RSV-6 has a radius centered at 99.71 nm. Again, the nonthiol is very close to the control AgNPs radius. Upon DNA binding, the radius should have increased, but instead the radius decreased. A possible explanation for the trends observed is that a decrease in the degree of aggregation occurred upon DNA functionalization of the AgNPs.

The dsDNA was analyzed in the same manner as the ssDNA samples. Figure 7.14 presents the DLS plots for single stranded RSV-5, double stranded thiolated RSV-5/6 hybrid, and the control AgNPs. The dotted blue line has been included in a similar fashion to Figure 7.13, and centered on the control peak. For the hybrid, the radius is centered around 89.93 nm. It is clear in the figure that both thiolated RSV-5 and thiolated RSV-5/6 hybrid peaks fall to the right of the control peak suggesting that both forms of the thiolated DNA are bound and standing up off AgNP surface, as dsDNA has been shown to be a rigid structure that stands off a surface.[401-405]

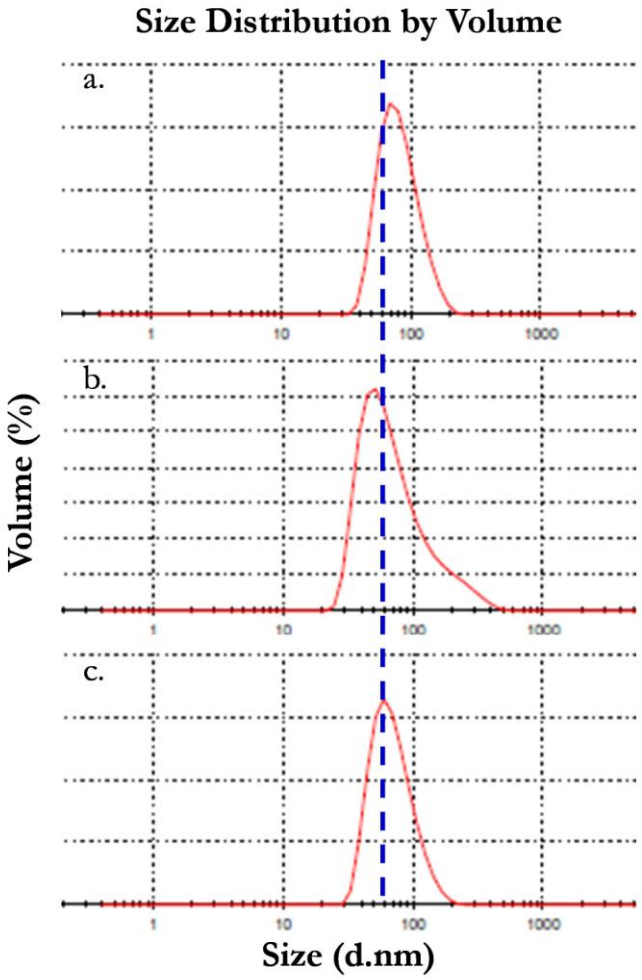

Figure 7.13. Plots of the DLS measurements obtained on AgNP solutions containing single stranded thiolated RSV-5 (a.), single stranded nonthiolated RSV-5 (b.), and the control (c.). The dashed blue line has been superimposed on the plots to aid the reader in peak comparison. The line is centered on the peak for the control AgNP solution.

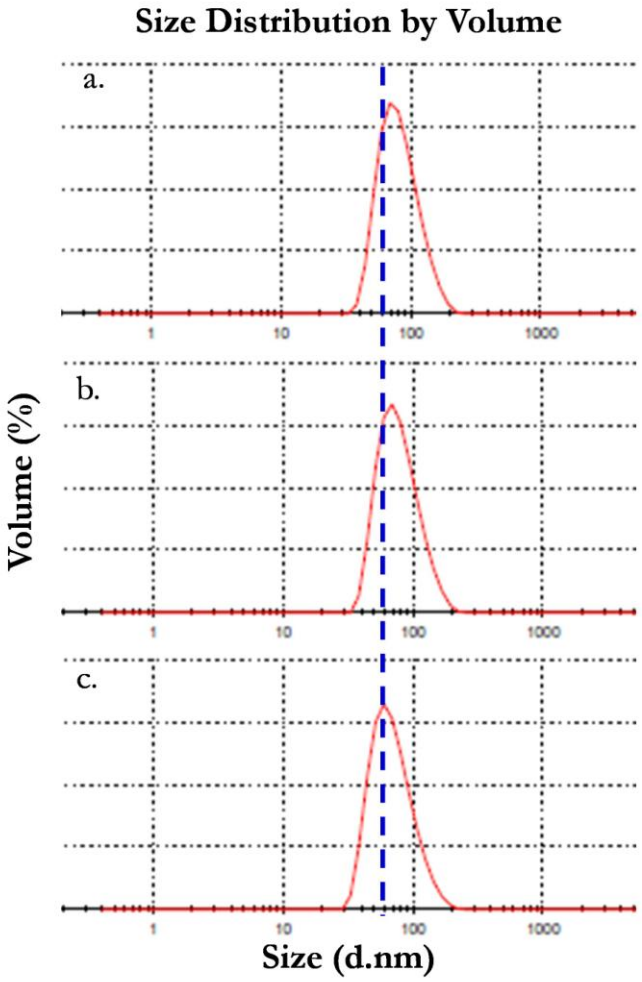

Figure 7.14. Plots of the DLS measurements obtained on AgNP solutions containing single stranded RSV-5 thiol (a.), double stranded RSV-5/6 hybrid (b.), and the control (c.). The dashed blue line has been superimposed on the plots to aid the reader in peak comparison. The line is centered on the peak for the control AgNP solution.

SERS measurements were acquired on each AgNP solution to determine if the DNA was indeed bound to the nanoparticle surface. Prior to SERS analysis, each nanoparticle solution was washed to remove any excess analyte not bound to the AgNP surface. Because of this, SERS spectra would result only if the probe molecule was bound to the surface. In addition to RSV-5 and RSV-6, AgNPs were functionalized with R6G to compare the intensities of the nanoparticles with that of the AgNR arrays. Specifically, 5 μL aliquots of each AgNP solution was allowed to evaporate onto a flat silver base substrate. Because of the evaporation effects, spectra were obtained on the evaporation ring (see the SEM image in Figure 7.12).[406] Figure 7.15 depicts the spectrum obtained for R6G on both AgNRs (blue trace) and AgNPs (red trace). The intensity is much lower for the AgNPs than AgNRs under the same experimental conditions. It is conjectured that the decrease in sensitivity is due to the incident beam being non-resonant with the AgNPs, significantly diminishing enhancement at 785 nm excitation.

Spectra acquired for single stranded thiolated and nonthiolated RSV-5 functionalized nanoparticles (blue and green trace, respectively) are presented in Figure 7.16. Also includes is the spectrum for the untreated nanoparticles (red trace). When compared to the spectrum obtained for thiolated RSV-5 on AgNRs (see Figure 7.17) the locations and relative intensities of the peaks are comparable suggesting that thiolated DNA binds to the surface of AgNPs in a similar fashion as AgNR arrays. The characteristic DNA peaks were absent from the spectra acquired on the control particles as well as on AgNPs functionalized with nonthiolated RSV-5 (see Figure 7.16). This finding suggests that

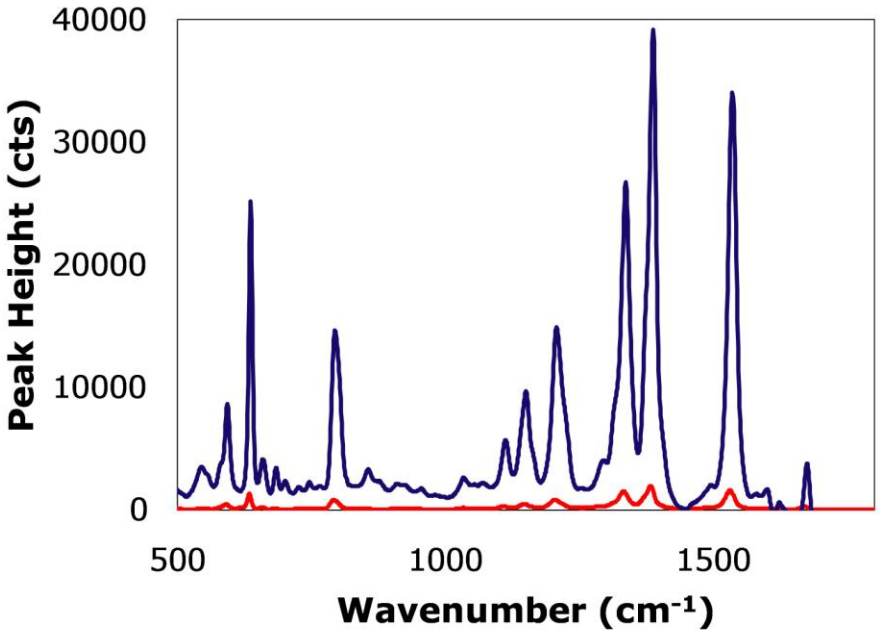

Figure 7.15. SERS spectra acquired on AgNRs (blue trace) and AgNPs (red trace) for comparison using R6G as the probe analyte. It is clear that the enhancement provided by the nanorod array is far superior to that of the nanoparticles.

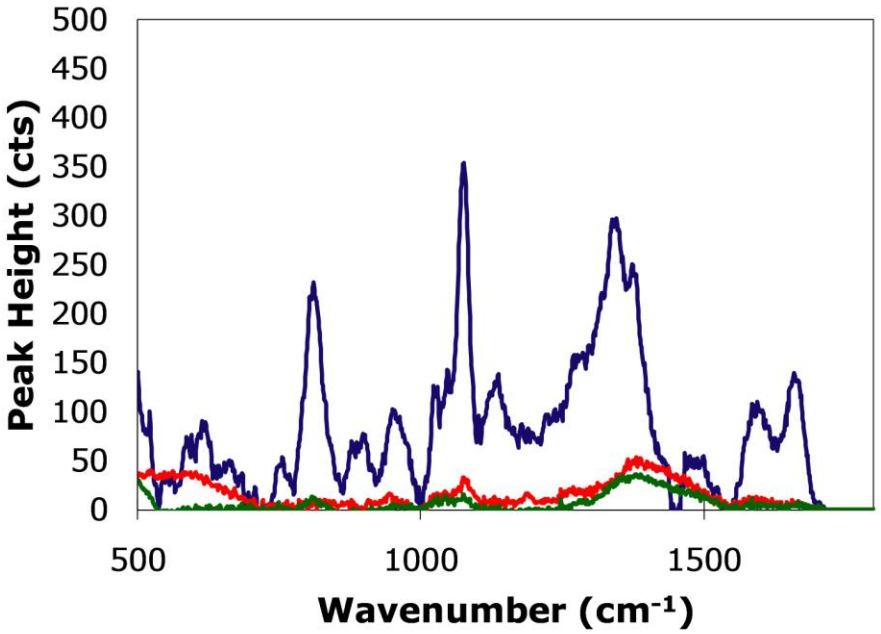

Figure 7.16. SERS spectra acquired on both thiolated (blue trace) and nonthiolated (green trace) RSV-5. Included for comparison is the spectrum acquired on the control AgNPs (red trace). It is clear that the thiolated DNA is binding to the nanoparticles and the nonthiolated is being removed with the washing step.

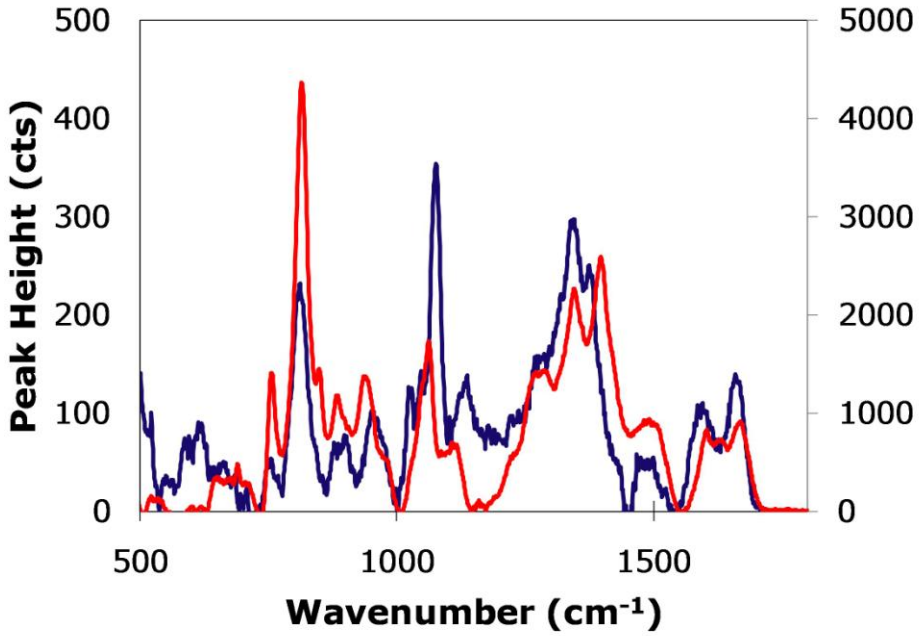

Figure 7.17. SERS spectra acquired on thiolated RSV-5 for both AgNPs (red trace) and AgNRs (blue trace). The experimental parameters were the same for both SERS substrates. The spectrum obtained on the AgNRs is presented on the secondary axis because of the large difference in intensity.

thiolated DNA is bound to the particles and nanorod array surface via the thiol terminus. Similar results were obtained for single stranded RSV-6 on both base substrates.

To verify reactivity of the thiol with the silver surface, CV was performed by Megan Damm of the Bottomley research group. Cyclic voltammetry measurements were made by the potentiostat mode of the WaveNano, manufactured by Pine Instruments (Raleigh, NC). Two experiments were performed. The first examined the stripping of a well characterized alkanethiol from the surface of gold and silver. For this experiment a 5.0 mM solution of 6-mercapto-1-hexanol was made in 0.1 M KNO_3. The solution was purged with Ar for five minutes to displace dissolved oxygen from solution. The counter electrode was a platinum wire, and the reference electrode was an Ag/AgCl wire 2 mm in diameter. Figure 7.18 (blue trace) depicts the CV obtained at a gold disc working electrode approximately 5 mm in diameter. The potential sweep began at -0.3 V, rose to 0.25 V, fell to -1.0 V, and returned to -0.3 V at a scan rate of 100 mV/s , completed for a total of two scans. The reduction peak of the thiol occurred at -0.790 V with an I_p of -98.6 µA on the first scan, and on the second scan, the peak appeared at -0.800 V with an I_p of -93.2 µA. The oxidative peak appeared on both scans as well, the first scan peak appeared at -0.580 V with a peak height of 3.23 µA whereas the second scan peak occurred at -0.584 V with a peak height of 2.75 µA. Figure 7.18 (red trace) depicts the CV obtained on a silver disc working electrode of approximately 2mm in diameter. The potential region of interest and the scan rate were the same as the previous experiment. The traces of both scans overlapped and redox peaks were hard to determine against capacitive current. After this, the reaction cell and electrodes were again rinsed, and the

Ag electrode was allowed to soak in the 5.0 mM thiol solution for 30 minutes. The experiment was repeated with the thiol-coated Ag electrode. Thiol reduction peaks appeared on the first and second scans at -0.685 V, -2.20 μA and -0.680 V, -1.59 μA, respectively, and an oxidation peak occurred at -0.340 V and 0.356 μA. The peak observed at -0.790 V corresponds to the well-characterized reductive desorption of alkanethiol from the Au surface.[407-408] The similarity in the location and shape of the peak observed at -0.685 V for the silver electrode suggests that thiols desorb from the silver surface in a similar fashion.

For the second experiment, working electrodes were coated with thin films of both thiolated and nonthiolated DNA. Monolayer films were prepared by pipetting precise volumes of known concentration onto the working electrode surface and allowed to evaporate for 30 minutes. This procedure was performed instead of the one described in the first experiment due to the volume of the electrochemical cell and the limited amount of DNA available. The working electrode was immersed in solution and the scan was initiated as described above. The nonthiolated DNA showed a peak at -0.510 V with a peak height of -1.16 μA while the thiolated DNA displayed peaks at -0.810 V, -1.94 μA on the first scan and -0.830 V, -0.841 μA on the second scan. This is shown in Figure 7.19. The similarity in the shape and position of the peak for desorption of C6 thiol and thiolated DNA on the silver surface is further evidence that thiolated DNA binds to the silver surface through a Ag-S bond. Further electrochemical studies are underway to test this conclusion.

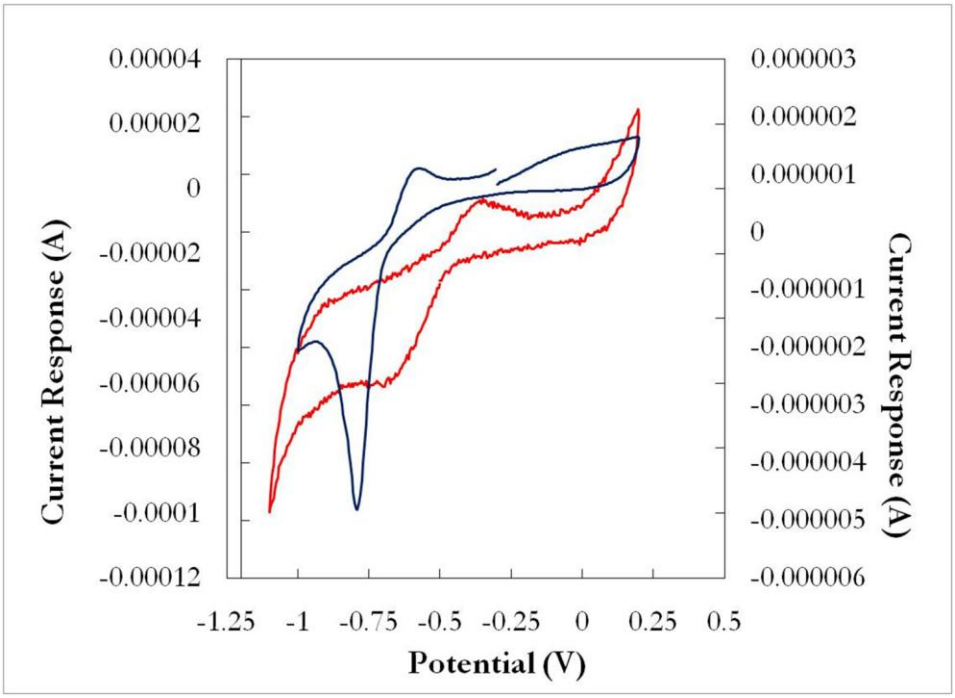

Figure 7.18. Cyclic voltammograms of 5 mM thiol solutions using gold (blue trace) and silver (red trace) working electrodes. The silver electrode is plotted on the secondary axis for ease of comparison between the two.

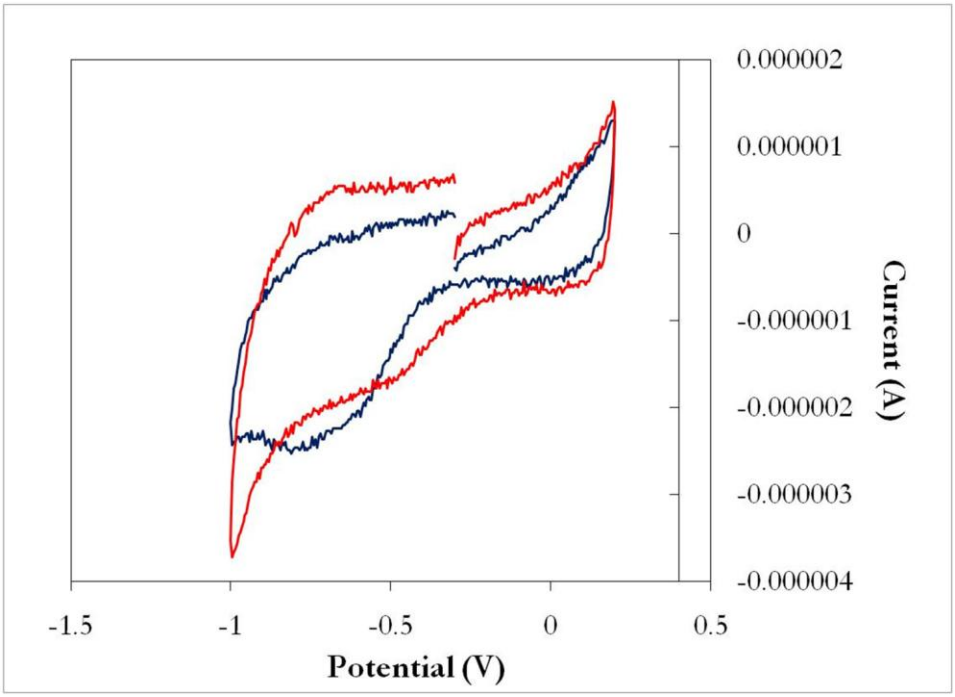

Figure 7.19. Cyclic voltammograms of thiolated (blue trace) and nonthiolated (red trace) RSV-6 DNA adsorbed to silver working electrodes.

TEM images were acquired to investigate the length of DNA standing up off the AgNP surface. Figure 7.20 presents TEM images of untreated (control) AgNPs. These images were acquired following evaporation of the same solutions of AgNPs used for DLS, SERS, and SEM. Apparent in these images are the differing shapes and sizes of particles that comprise this sample. Figure 7.21 presents TEM images of nonthiolated RSV-5 functionalized AgNPs. The particle shapes and sizes are comparable to those of the naked AgNPs. Figure 7.22 presents TEM images of thiolated RSV-5 functionalized AgNPs. These samples contained an added feature, or "halo," surrounding the particles. This feature was not confined to aggregate assemblies, but was found on isolated particles coated with thiolated DNA as well. Figure 7.23 shows a comparison of isolated nanoparticles for control, nonthiolated, and thiolated DNA. It is clear from the TEM image of the AgNP functionalized with thiolated RSV-5 that a halo exists around the outside of the particle. The thiolated RSV-5 sample appears to have more spacing between the particles, however it is difficult to determine if the halo observed for the single AgNP exists for all the particles in the aggregate (see Figure 7.22).

Since dsDNA is a rigid structure and has been shown to "stand-up,"[401-405] TEM images were also acquired on AgNPs treated with thiolated dsDNA. The micrographs are presented in Figure 7.24, with the control and thiolated single stranded DNA for direct comparison. Similar to the single stranded thiolated RSV-5 thiol sample, dsDNA particles appear to have a halo as well.

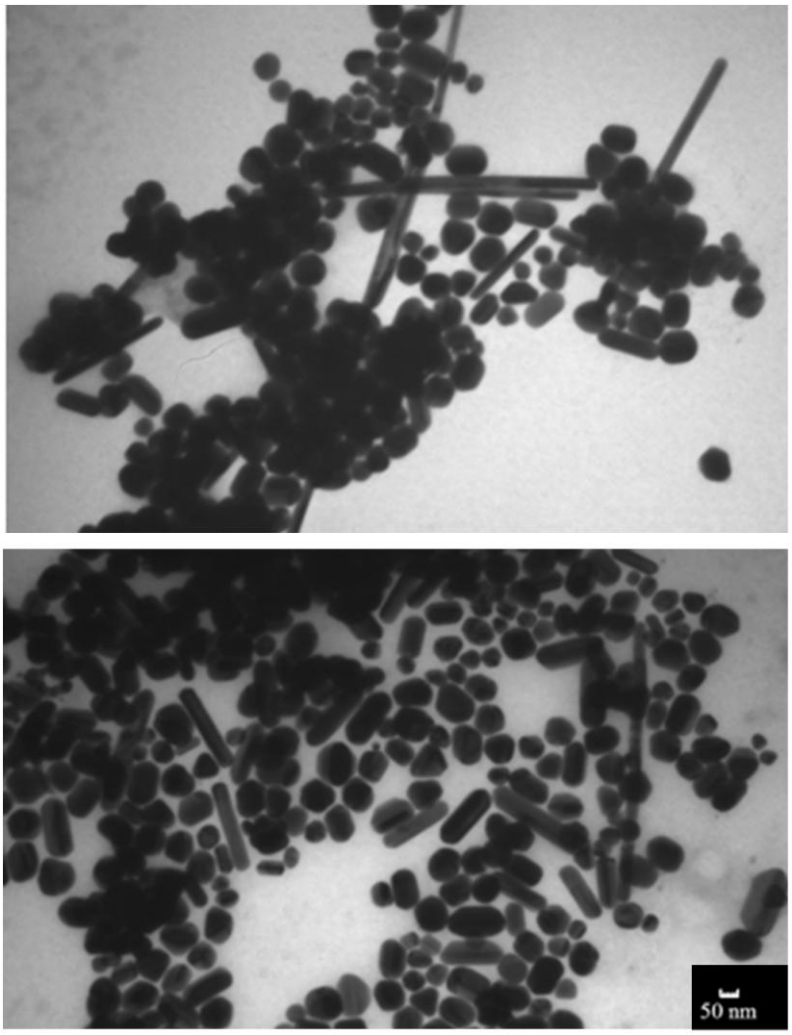

Figure 7.20. TEM micrographs depicting untreated (control) AgNPs. Images were acquired on separate samples.

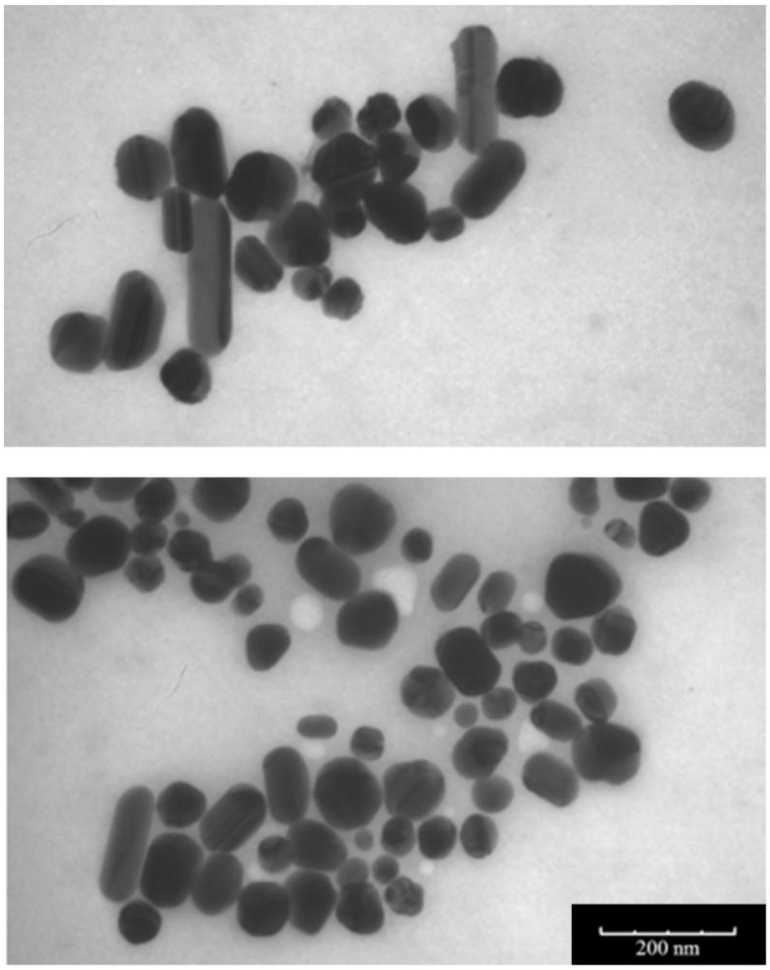

Figure 7.21. TEM micrographs depicting nonthiolated AgNPs. Images were acquired on separate samples.

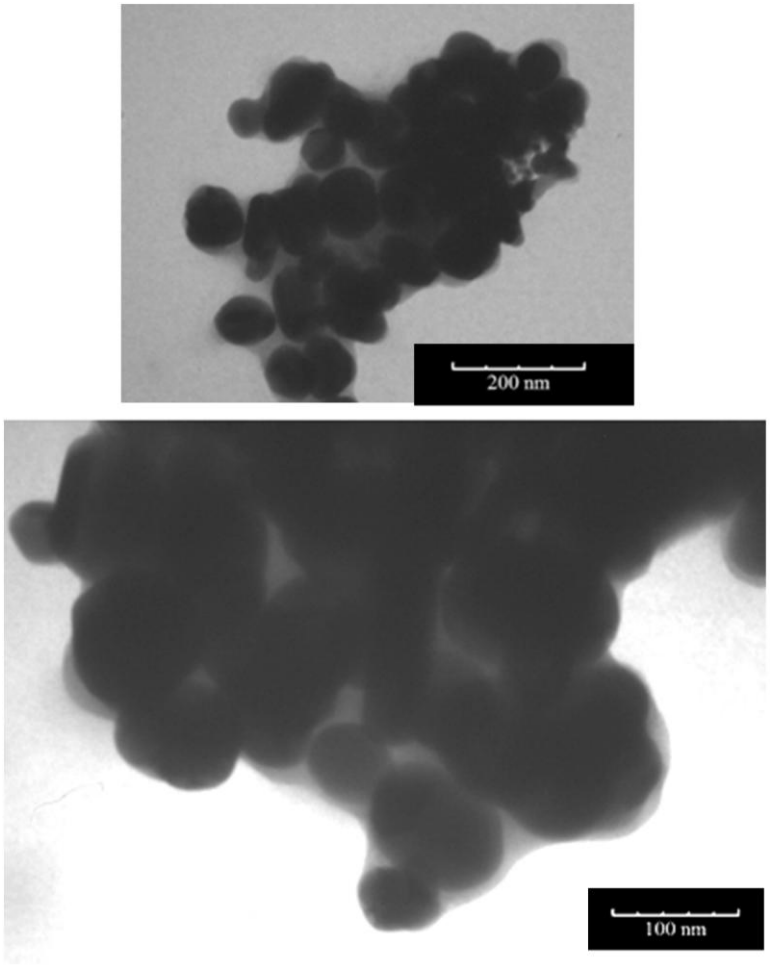

Figure 7.22. TEM micrographs depicting thiolated AgNPs. Images were acquired on separate samples.

A few possibilities could be responsible for this halo effect. If one particle was in front of another on the TEM grid, an outer ring may appear around the smaller center nanoparticle. The halo effect is not observed in control samples. Another possibility is that a contaminant is present in solution from the DNA that is coating the nanoparticle surface. However, since the halo is only present on nanoparticles functionalized with thiolated DNA, and not all DNA treated samples. This explanation is unlikely. Additionally, since all DNA oligos were acquired from the same supplier and treated in a similar fashion, the chances of a contaminant intrinsic to the thiolated DNA is very low. Lastly, and most probably, the halo could be due to DNA physically bound and standing up off the AgNP surface.

Both SERS and electrochemistry studies indicated that thiolated DNA binds to the silver surface through the pendent thiol. The shadows in TEM images support this as well. Due to the close packed nature of the DNA adlayer at the surface, a halo appears. By measuring the dimensions of this halo, the average height and perhaps the angle of DNA standing off the surface may be determined.

Analysis of TEM images acquired on thiolated samples, both ssDNA and dsDNA, is presented in Table 7.3. Various AgNPs from multiple samples where individual particles and aggregates of particles were analyzed. Thicknesses were measured by hand using the scale bar provided by the imaging software, so a degree of error is expected in the measurements however the trend is still clear. The halo around the AgNPs for ssDNA is approximately twice as long as the AgNPs functionalized with dsDNA.

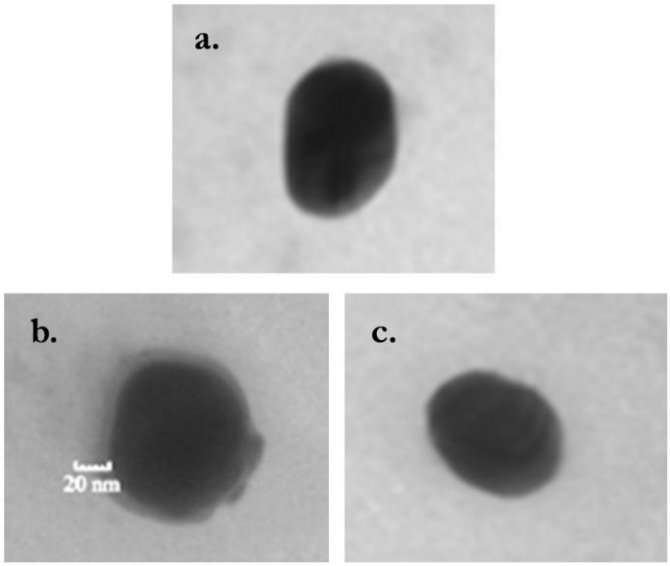

Figure 7.23. TEM micrographs depicting single AgNPs. Control AgNPs (a.), thiolated (b.) and nonthiolated (c.) RSV-5 are presented for comparison. Again, only the thiolated RSV-5 sample has the halo throughout the aggregate similar to the one observed for a single AgNP.

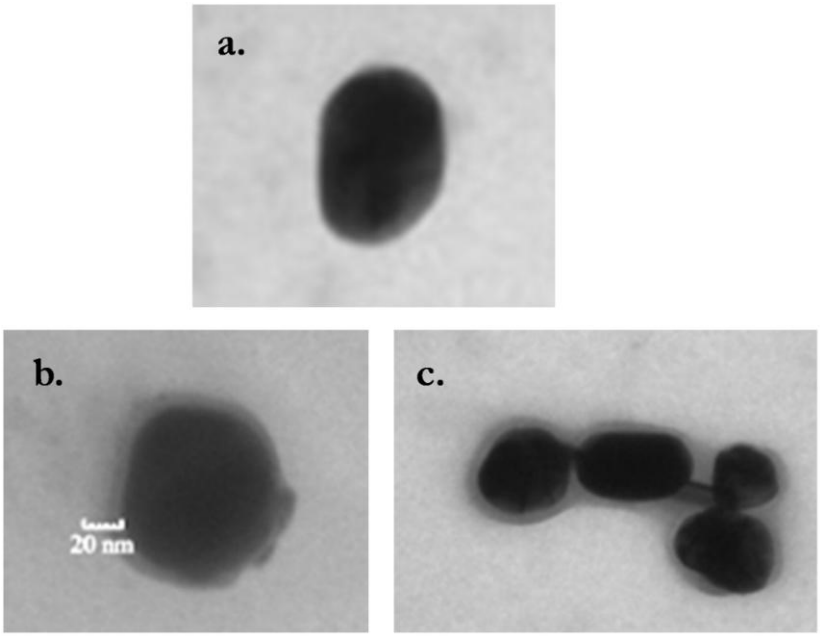

Figure 7.24. TEM micrographs of AgNPs functionalized with and without DNA. a.) presents an image acquired on control AgNPs where no DNA was introduced into the solution, b.) presents the image acquired for AgNPs functionalized with single stranded RSV-5 thiol, and c.) presents the image acquired for AgNPs functionalized with double stranded RSV-5/6. The scale bar of 20 nm in image b is applicable to all three images**.**

Table 7.3. Sample details and the average thickness of the halo present on AgNPs functionalized with thiolated DNA.

	ssDNA	**dsDNA**
# of Samples Imaged	3	2
# of Particles Measured	10	8
Average Thickness (nm)	26.3 ± 9.0	13.8 ± 3.4

Since RSV-5/6 is 18 nucleotides long, the distance the DNA bases are contributing is a little over 6 nm, with 0.34 nm per base pair. The 6 carbon chain thiol linker bound to the silver surface contributes approximately 1.0 nm, combining to a total of ~7.0 nm off the surface if there was no stacking angle. Studies carried out on alkane-thiols have shown that there is a stacking angle of 30 - 60° for the monolayers.[409] Taking this into consideration, and using an angle of 45°, the expected thickness of the DNA layer is 4.9 nm. Using a ratio of the calculated to measured thicknesses in the TEM images, the ssDNA stands approximately 9.34 nm off the surface. To further interrogate this distance, as well as the orientation of thiolated and nonthiolated DNA at the silver surface, AFM studies were carried out.

Figure 7.25 presents an AFM image of a freshly cleaved template-stripped Ag surface. Analysis of this image reveals that apart from two particles of debris, the silver surface is flat. When 1-dodecanethiol is stamped onto the surface, the alkanethiol chains form a densely-packed self assembled monolayer (SAM), as shown in Figure 7.26. In contrast, Figure 7.27 depicts an AFM image of template-stripped silver coated with nonthiolated

RSV-4. A cross-section of this image indicates that the average height of the layers formed atop the silver is 0.81 ± 0.21 nm. This observed height is consistent with ssDNA lying on its side, as the height should be approximately half of the diameter of double-stranded DNA (~2nm). The region of the image highlighted in red indicates the scan domain of the previous image, suggesting that as the cantilever tip rasters across the surface, it is able to push aside molecules of the nonthiolated DNA. This phenomenon is not seen when imaging thiolated RSV-4 (Figure 7.28), evidencing that the nonthiolated oligos are not bound as tightly to the surface as the oligos containing the thiol pendant group. Furthermore, a cross-sectional analysis of the micrograph in Figure 7.28 indicates that the monolayer of thiolated RSV-4 has an average height of 4.69 ± 1.17 nm. Since RSV-4 is 22 nucleotides long, the length of the duplex DNA equates to 7.48 nm. The three carbon chain thiol linker contributes approximately 0.5 nm, combining to a total length of 7.98 nm. Using the same angle approximation as previously described with TEM results, the layer of dsDNA off the surface is expected to be closer to 5.64 nm. The observed height of the thiolated ssDNA is therefore within the range of heights expected for thiolated duplex DNA containing the equivalent number of base-pairs. Single-stranded DNA should, however, be longer than dsDNA. It is therefore likely that the vertical load placed on the monolayer while imaging compressed the olgios and decreased their observed heights. A series of force curves were taken both to investigate this possibility, and to further interrogate the orientation of the thiolated DNA on the Ag surface.

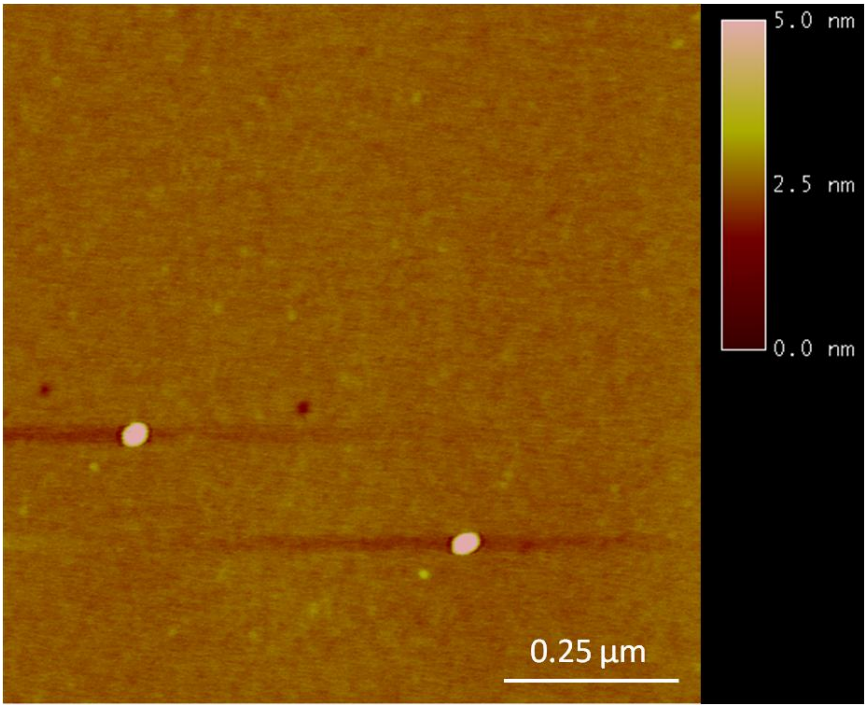

Figure 7.25. AFM micrograph of template-stripped Ag. Color scale bar indicates the height of surface features.

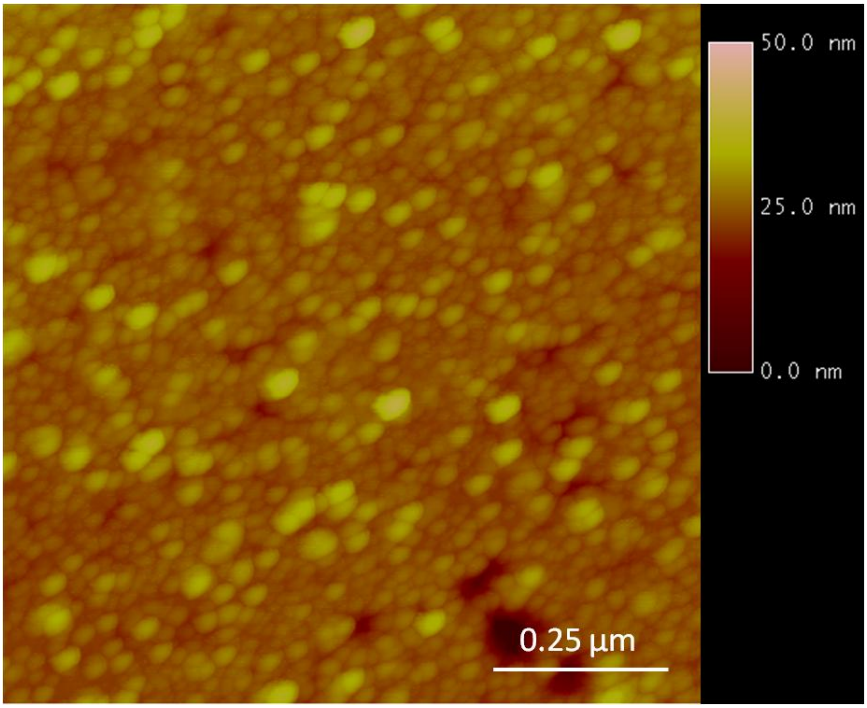

Figure 7.26. AFM micrograph of a self-assembled monolayer of 1-dodecanethiol on template-stripped silver. Color scale bar indicates the height of surface features.

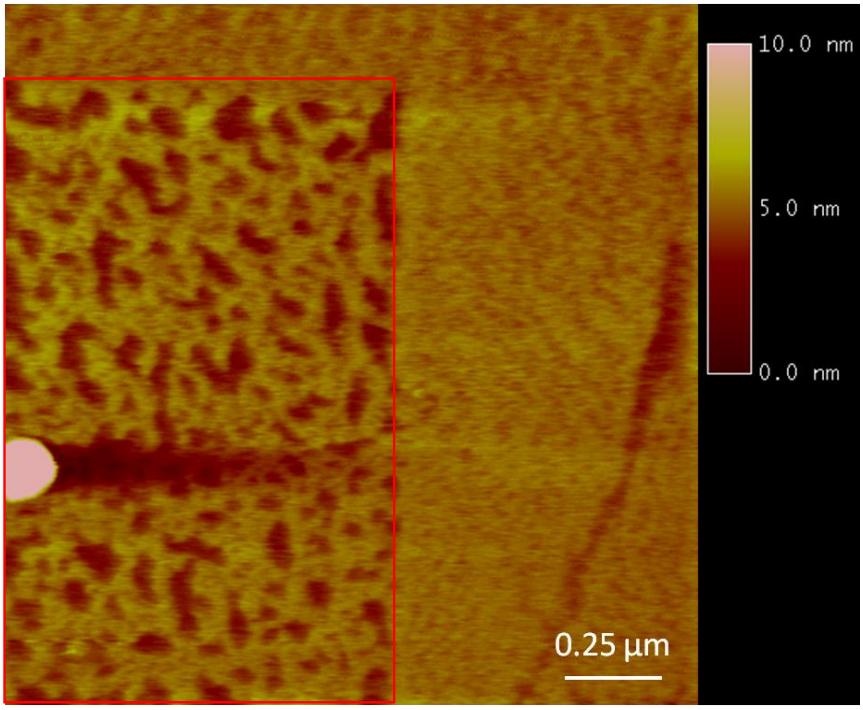

Figure 7.27. AFM micrograph of nonthiolated RSV-4 on template-stripped silver. Color scale bar indicates the height of surface features. The region highlighted in red indicates where the cantilever tip was rastered across the surface prior to acquiring this image.

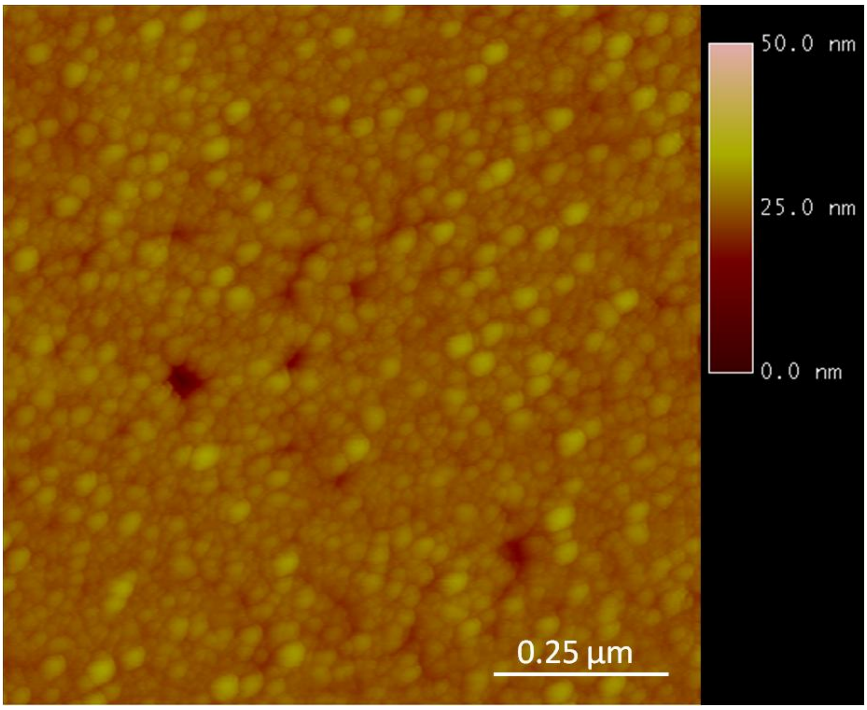

Figure 7.28. AFM micrograph of thiolated RSV-4 on template-stripped silver. Color scale bar indicates the height of surface features.

Force curves were acquired on each of the modified surfaces. The blue and red traces indicate changes in the force exerted on the cantilever as the surface extends towards and retracts away from the tip. At the beginning of each cycle, the cantilever tip is not in contact with the surface. As the surface is extended towards the tip, weak attractive forces between the tip and surface cause a small decrease in the sensed force to a negative value. This event is known as the "jump-to-contact." As the tip is compressed into contact with the surface, there is a corresponding linear increase in force, followed by a linear decrease in force as the surface retracts. As the scanner pulls away from the tip, adhesive forces maintain contact between the tip and surface, bending the cantilever downwards. When the restoring force of the cantilever overcomes the adhesive force, the cantilever snaps back to its original position in free space. The strength of the adhesion is represented as the maximum negative force exerted on the cantilever before it releases the surface. When the force curves are acquired in air rather than under N_2, the retracting curve often exhibits a larger amount of adhesion due to the strong capillary forces that exist as a result of the water layer on the surface.

A minimum of ten force curves were acquired on each surface to obtain average values of adhesive force. Example force curves are provided in Figures 7.29 - 7.32. Figure 7.29 contains a set of force curves for experiments on template-stripped silver done under N_2 (7.29a) and in air (7.29b). The average adhesive force for template-stripped silver under N_2 is 0.84 ± 0.02 nN. Because of capillary forces from layers of water on the surface, this adhesion force increases to 1.06 ± 0 .004 nN for experiments performed in air. When the surface is stamped with 1-dodecanethiol, the average adhesion under N_2 decreases by

almost 50% to 0.42 ± 0.09 nN (Figure 7.30a). This decrease in adhesion most likely reflects a decrease in amount of water on the substrate surface modified with a hydrophobic monolayer (dodecanethiol) compared to the clean template-stripped silver surface. When the sample is exposed to atmosphere, the adhesion increases dramatically to 1.10 ± 0.04 nN (Figure 7.30b). Nonthiolated RSV-4 is more hydrophillic than either clean Ag or 1-dodecanethiol and is very loosely bound to the silver surface. As a result, when the template-stripped silver surface is backfilled with nonthiolated RSV-4, the average adhesion force increases to 3.50 ± 0.11 nN under N_2, and 4.03 ± 0.52 nN in air (Figure 7.31). In contrast, when the same oligo is terminated with a 3' thiol pendant group, the average adhesion value decreases to 0.12 ± 0.03 nN under N_2 and 0.17 ± 0.02 nN in air (Figure 7.32). While it is intuitive that a closely-packed monolayer of ssDNA would be less adhesive than loosely-bound ssDNA lying on its side, it seems unusual that the adhesive force would be approximately 3.5 times smaller than that of a SAM of 1-dodecanethiol because of the hydrophillicity of the phosphate groups in the backbone of the oligo. The vertical load applied to the monolayer during experiments on 1-dodecanthiol was greater than that applied to the monolayer of thiolated RSV4 because the tip was compressed 10 nm further into the alkanethiol surface than the thiolated RSV-4 surface. Because of this, the contact area between the tip and surface was smaller for experiments on the thiolated oligo, resulting in a decrease in observed adhesion.

Multidimmensional Force Spectroscopy, or MDFS, was used to further characterize differences in the thin films of thiolated and nonthiolated DNA. MDFS involves the simultaneous monitoring of cantilever deflection and thermally-driven resonance during

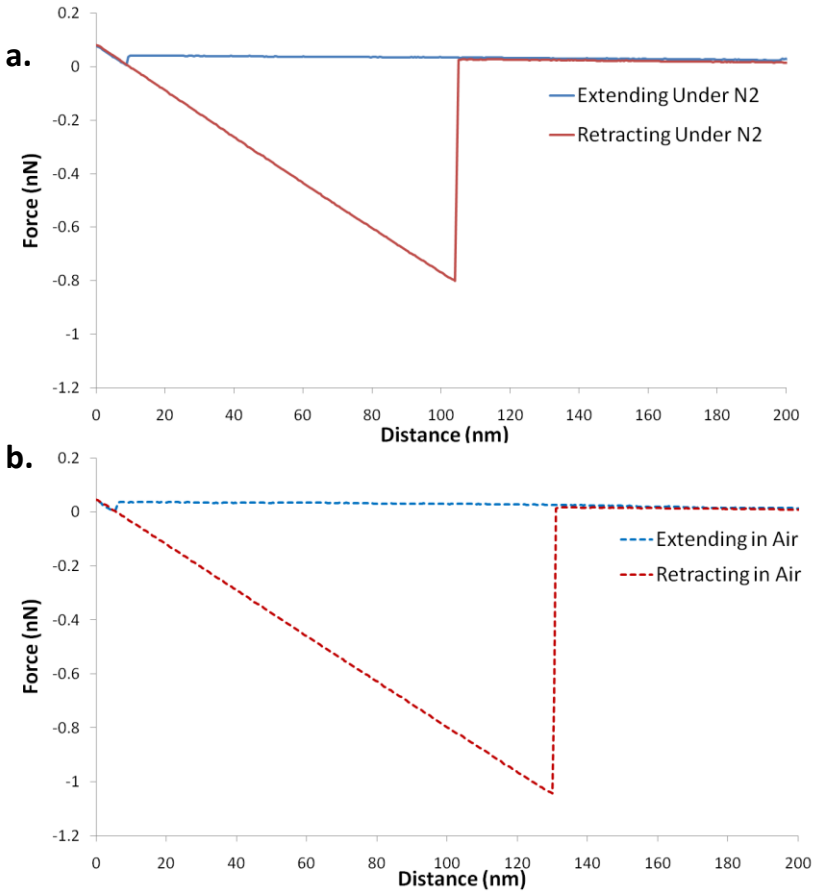

Figure 7.29. Force curves acquired on a freshly cleaved, template-stripped silver surface under N_2 atmosphere (a.) and in air (b.).

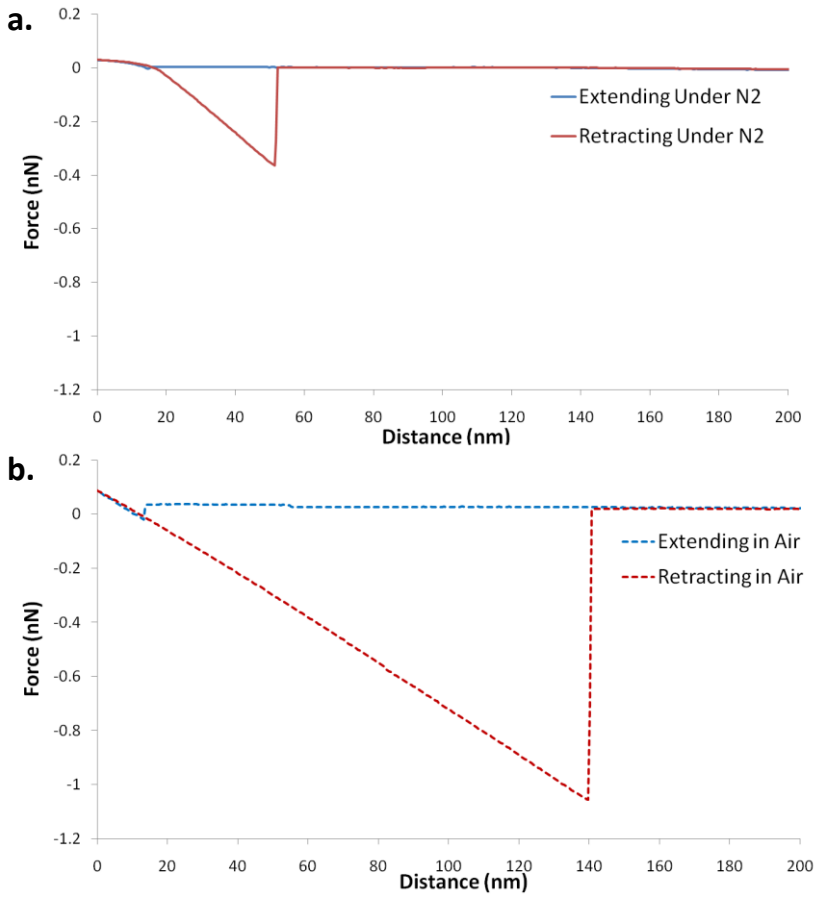

Figure 7.30. Force curves acquired on a template-stripped silver surface stamped with 1-dodecanethiol under N_2 atmosphere (a.) and in air (b.).

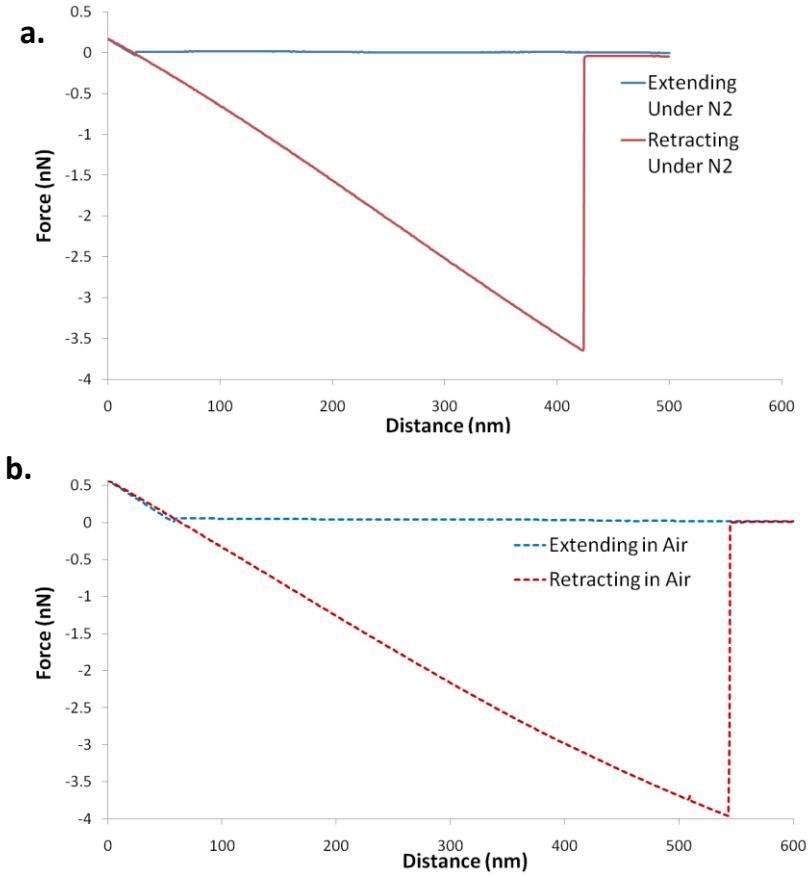

Figure 7.31. Force curves acquired on a template-stripped silver surface backfilled with nonthiolated RSV-4 under N_2 atmosphere (a.) and in air (b.).

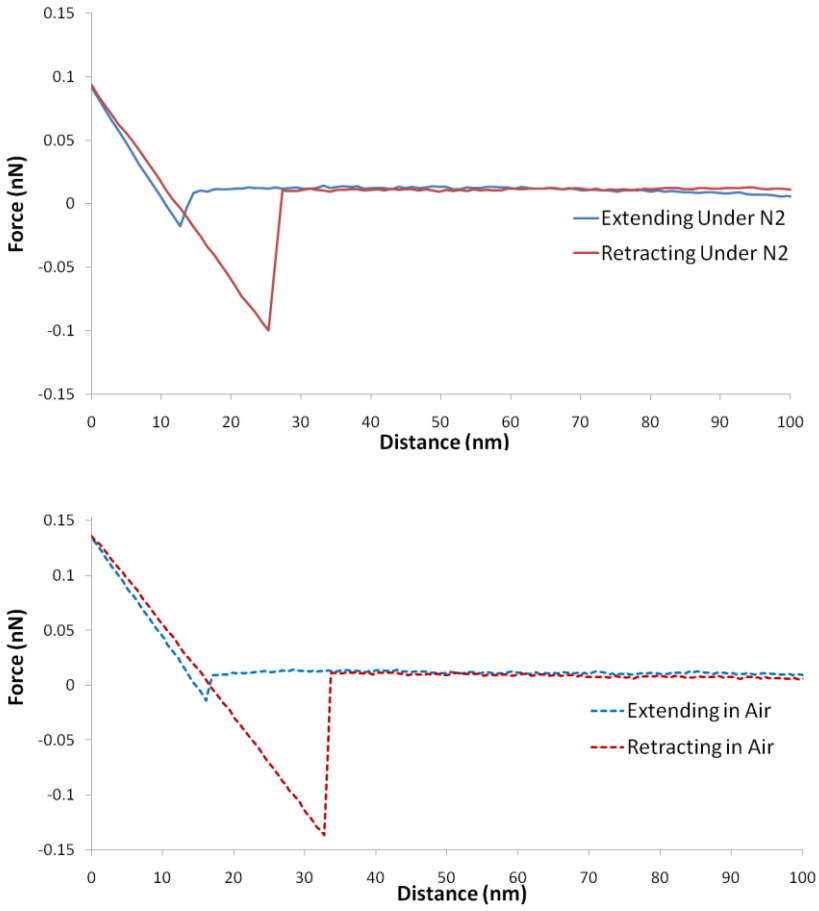

Figure 7.32. Force curves acquired on a template-stripped Ag backfilled with thiolated RSV-4 under N_2 atmosphere (a.) and in air (b.).

cycled movement of the atomic force microscope (AFM) scanner. As the cantilever tip interacts with the surface, it undergoes a shift in thermal resonance frequency. These frequencies, coupled with knowledge of scanner movement and cantilever deflection provide excellent means of describing sample-tip interactions, ultimately enabling a more accurate description of the mechanical properties of the surface.

To access the raw cantilever deflection signals required for MDFS, the base of the Nanoscope III AFM was modified as shown Figure 7.33. The instrument was warmed up for 1 hr to allow the scanner to reach thermal equilibrium, after which time the microscope was falsely engaged with the surface. In force mode, the tip was brought into contact with the surface by monitoring cantilever deflection and amplitude. A stepper motor controlled the amount of compressive force applied to the surface. Cantilever resonance data was obtained at a scan rate of 12 nm/s, z-range of 500 nm, and 1024 samples/line.

The frequency of the primary mode of cantilever resonance in free space is 33.6 kHz. When the cantilever tip contacts the surface it undergoes a change from a clamped-free to a clamped-pinned system, which in turn causes a shift in the frequency of the primary mode of resonance. This shift during contact is dependent on the mechanical properties of the surface. When the tip is brought into contact with a clean template-stripped silver surface (see Figure 7.34), the surface is noncompliant and therefore the frequency shifts from 33.6 kHz to ~ 140 kHz, where it remains fairly constant while in contact until the tip snaps free from the surface and returns to its free space value. When a layer of

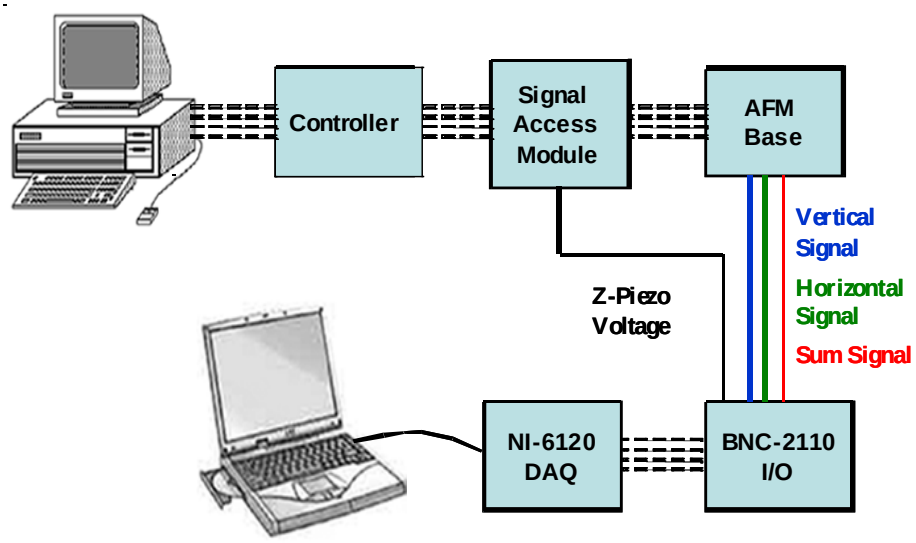

Figure 7.33. Schematic of the MDFS experimental setup. The commercial components of the setup include the AFM base, the signal access module, the controller, and a computer. The commercially provided software is used to control and acquire conventional force spectroscopic data. The additional components, the I/O interface, the data acquisition card (DAQ), and a computer with custom software are used to acquire the extra parameters that define MDFS.

compliant material is added into the system, it acts like a dashpot and causes the frequency in contact to shift to a lower value than is the case with a non-compliant surface.

Figures 7.35 and 7.36 demonstrate this effect on a SAM of 1-docanethiol and thiolated RSV-4, where the frequencies of the primary mode of resonance shift to 130 kHz and 125 kHz respectively. Furthermore, as the layer beneath the cantilever becomes more compliant, the cantilever resonance frequency in contact with the surface shifts from lower frequencies to higher frequencies during compression, and then back to lower frequencies as the scanner reverses directions and adhesive interaction cause the tip to deflect downwards. This phenomenon can be seen for thin films of both 1-dodecanethiol and thiolated RSV-4 (see Figures 7.35 and 7.36). As was seen previously in the force curve analysis of nonthiolated RSV-4, the nonthiolated oligos are sticky and cause a significant downward deflection of the cantilever beam before it is able to overcome the adhesive interactions and snap away from the surface. This manifests itself during MDFS experiments as the large decrease in cantilever deflection voltage overloading the instrument and introducing a large amount of noise in the thermal spectrum. The result is a severely low signal-to-noise ratio and an inability to track the primary mode of resonance in the last stages of contact (Figure 7.37). Further MDFS analysis is currently ongoing (Beavers, Ferri, and Bottomley, *manuscript in preparation*).

These preliminary results from cantilever resonance, coupled with force curve and atomic force image analysis suggest that nonthiolated DNA lies down and has very little

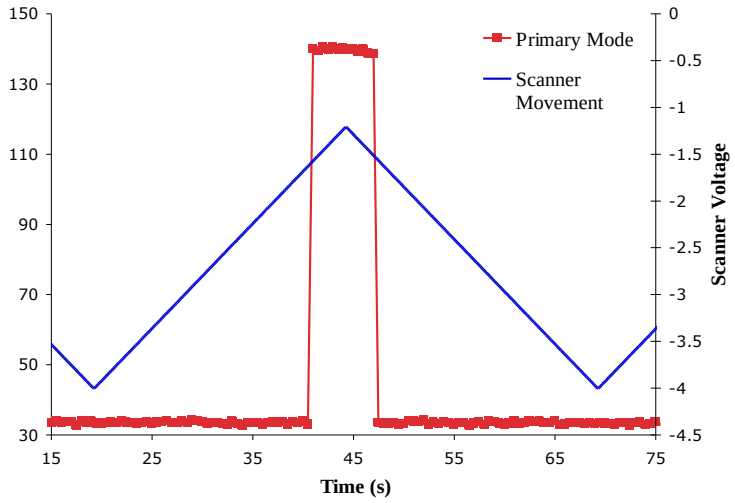

Figure 7.34. Change in cantilever resonance frequency on a template-stripped silver surface during cycled movement of the scanner in air.

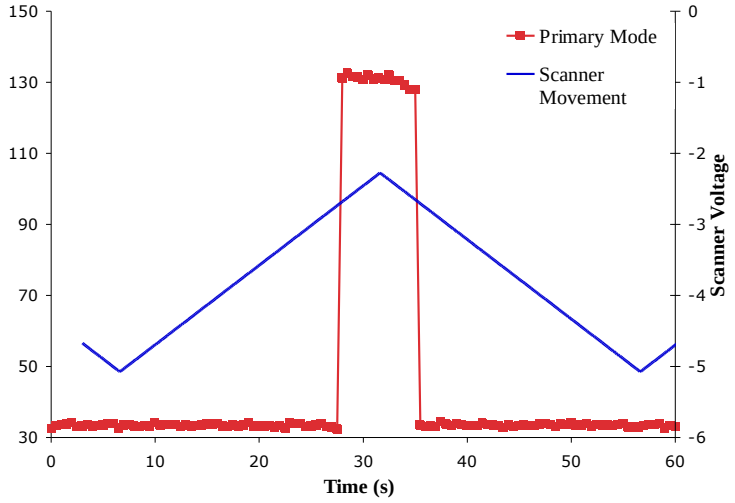

Figure 7.35. Change in cantilever resonance frequency on a SAM of 1-dodecanethiol during cycled movement of the scanner in air.

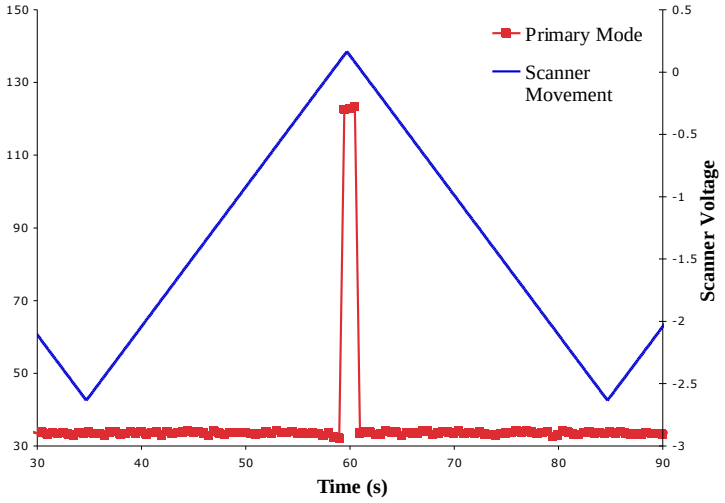

Figure 7.36. Change in cantilever resonance frequency on a thin film of thiolated RSV4 during cycled movement of the scanner in air.

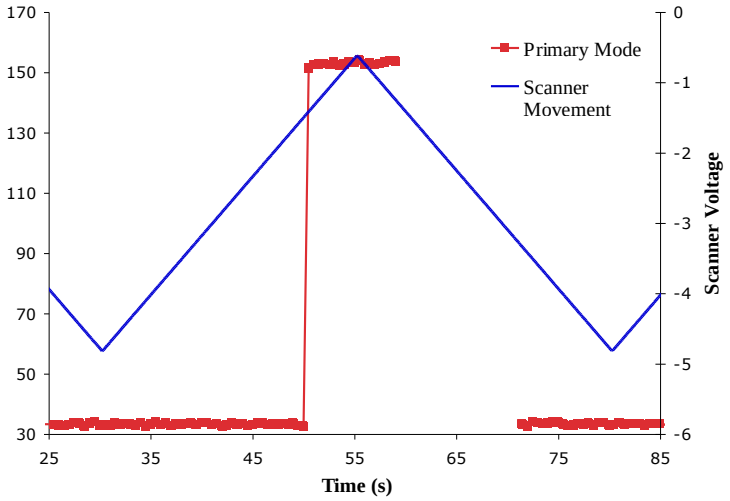

Figure 7.37. Change in cantilever resonance frequency on a thin film of nonthiolated RSV4 during cycled movement of the scanner in air.

interaction with the surface. As a result, it can be easily displaced by the tip of the cantilever, whereas the thiolated DNA is not displaceable. Although the resolution of the AFM images presented cannot provide conclusive evidence of stacking direction, cross-sectional analysis allows one to see that the height of the monolayer formed by the thiolated DNA is comparable with that of dsDNA oriented upright and at an angle off the surface. Similarly, the height of the layers of nonthiolated DNA on the surface is consistent with DNA lying on its side. These findings are in turn supported by the degree of compliance illustrated by the force curve and cantilever resonance data of both 1-dodecanethiol and thiolated RSV-4 as compared with template-stripped silver and nonthiolated RSV-4.

7.5. Conclusion

SERS spectra acquired on oligos chemisorbed onto AgNR arrays possess the signature peaks associated with the corresponding DNA bases. However, SERS using AgNR arrays does not appear to be a viable method for assaying DNA hybridization. While, spectra acquired on samples comprised of complementary and noncomplementary oligo pairs possessed bands characteristic of the nucleotides present on the nanorod surface, there are no new spectral bands representative of a hybridization event. Additionally, one cannot distinguish between hybridization and non-specific binding at the nanorod surface. Another issue lies in the buffer conditions required for hybridization. Upon evaporation of the solution, salt crystals deposit within the nanorod array increasing variability and decreasing sensitivity. The distance dependence poses a large problem as well. When probe oligos are oriented in a way that promotes capture of the target strand via hybridization, the SERS intensity to a specific nucleotide falls off dramatically with

distance from the substrate surface. Because of this, the resultant hybridization assay is sensitive to only the first few nucleotides that define the probe sequence.

CHAPTER 8

CONLCUSIONS AND FUTURE WORK

Goals of this research project involved the fabrication of multiple SERS substrates for use in pathogen detection. Batch fabrication of silver nanorod (AgNR) array SERS substrates was accomplished using a conventional electron beam evaporator and a custom built substrate holder. Careful placement of multiple base substrates within the metal vapor plume combined with careful control of the evaporation parameters resulted in substrates with nominal variability in nanorod morphology and SERS performance from substrate to substrate and batch to batch. Post fabrication patterning of substrates allowed for an increase in the number of assays performed from a single batch of substrates. Using this method, the variability in SERS response was reduced to 6% across a single substrate, 25% down a substrate, 15% from substrate to substrate and 8% from batch to batch.

Continued characterization of these substrates was carried out prior to developing SERS-based bioassays. Fabrication methods were compared to establish the conditions that provided the most stable AgNR substrates. It was found that substrates exposed to oxygen during the fabrication process were less stable than those fabricated without oxygen exposure and provided a much lower SERS response. Stability, and ultimately the SERS response, may be improved by storing the substrates in a controlled environment. In addition to comparing fabrication methods, the region of the AgNR array producing the highest enhancement was investigated using different sized fluorescent microspheres. It was found single particles were not detected, even though

multiple beads were located within the laser spot and SERS signals were only seen when the number of beads approached monolayer coverage. Additionally, the enhancement found for beads located on top of the AgNRs was greater than that for beads located within the array.

Results indicating the tops of the nanorods produced the greatest SERS enhancements were promising for bacterial studies where intact cells would rest atop the array. Three bacterial cells lines were compared and spectra features matched those presented in recent literature. Unfortunately, the spectral bands also matched those present in the spectra acquired on both the medium in which the cells were grown as well as many other popular bacteria growth medium. Looking at the components that make up growth media and the structures on the cell wall of bacteria cells, there is a strong similarity. Because of this, SERS spectra must be acquired on bacterial samples devoid of growth medium, to establish the response from different bacterial species.

Continued work concerning pathogen detection was carried out using SERS active AgNR arrays DNA hybridization assays. Spectra were acquired on samples comprised of complementary and noncomplementary oligo pairs and resulting spectra possessed bands characteristic of the nucleotides present on the nanorod surface. However, no new spectral bands representative of a hybridization event occurred, complicating spectra analysis. Successful hybridization versus non-specific binding at the nanorod surface cannot be distinguished from on another. Additionally, buffer conditions required for hybridization provided salt crystal deposits within the nanorod array upon evaporation

increasing variability and decreasing sensitivity. The largest impedance of the assay proved to be the distance dependence related to the surface enhancement. When probe oligos were oriented in such a way that capture of the target strand via hybridization was promoted, the SERS intensity for specific nucleotides falls dramatically with distance from the substrate surface. The resultant assay is sensitive to only the first few nucleotides of probe sequence, hindering the use of AgNR array SERS substrates for hybridization assays.

Further studies related to this work include a more detailed look at the distance from the surface the assay is sensitive. SERS, electrochemistry, and AFM results confirmed that thiolated DNA stands up off the surface. The length and angle of the thiolated DNA is still unknown. TEM results confirmed that ssDNA is longer than dsDNA but because of the limitations involved with making the distance measurements, and exact value was not determined. Due to this, it is suggested that varying lengths of DNA be investigated further using both TEM and AFM. In varying both the length of the thiol linkers and the number of nucleotides systematically, the angle and length of specific DNA strands may be extrapolated.

Additionally, SERS studies suggested that after five nucleotides, a change in sequence was no longer detected. One apparent solution to the distance dependence would be to use of a hairpin or aptamer probe molecule with a Raman reporter moiety incorporated into its structure. By doing so, one would be taking advantage of the distance

dependence by monitoring the disappearance of spectral bands associated with the reporter molecule upon hybridization.

APPENDIX A

SYNTHESIS OF UNIQUE DNA STRUCTURES FOR AFM PULLING STUDIES

A.1 Introduction

The conformation of an adsorbed polymer, or molecule, on a surface directly impacts the interfacial properties of this surface. Polymers adsorb by two mechanisms: chemisorption and physisorption.[410-412] Chemisorption includes mechanisms such as covalent bonding, while physisorption refers to mechanisms such as electrostatic interaction and van der Waal's forces.[413-417] Once adsorbed, a polymer's conformation can be described by three different regions: loops, trains, and tails.[418] Several techniques have been used to characterize polymer adsorption; the majority of these provide information about the average film thickness, density, and/or polymer film thickness.

Recently, our research group and others have used dynamic force spectroscopy (DFS) to examine the conformation of individual polymer molecules at the air-substrate and liquid-substrate interface.[419-427] This technique uses an atomic force microscope (AFM) to bring two surfaces into and out of contact. The principal measurement in dynamic force spectroscopy is the acquisition of a force curve. A typical force curve is shown in the upper portion of Figure A.1. When a polymer is attached to both the probe and the surface, it undergoes elongation as the gap between the probe and the surface

increases. This elongation increases tension on the molecule which induces a downward deflection of the cantilever. When a segment of the polymer chain is pulled off the surface, the tension is momentarily released and a sudden decrease of cantilever deflection is observed (see lower portion of Figure B.1). This sequence of polymer stretching and release continues until either the polymer is pulled from the surface or from the probe. A distinguishing feature of our preliminary work is that a single polymer molecule was stretched using a specially prepared AFM probe and a mica surface.[419-420]

Relating features in the force curve to polymer surface conformation requires some knowledge about the points of contact to the polymer and a precise estimate of the number of molecules undergoing elongation. Interpretation of force curve[428] data obtained during the elongation and detachment of macromolecules from surfaces as well as the molecular structure that gives rise to the observed phenomenon is often based on a set of assumptions.[424, 426, 429-442] The primary objective of this chapter is to carry out the synthesis of molecules to test these assumptions. Included in these molecules is a loop structure made from double stranded DNA (see Figure A.2) as well as a block-copolymer consisting of repeating DNA and polyethyleneglycol (PEG) units of a fixed length (see Figure A.3 and A.4).

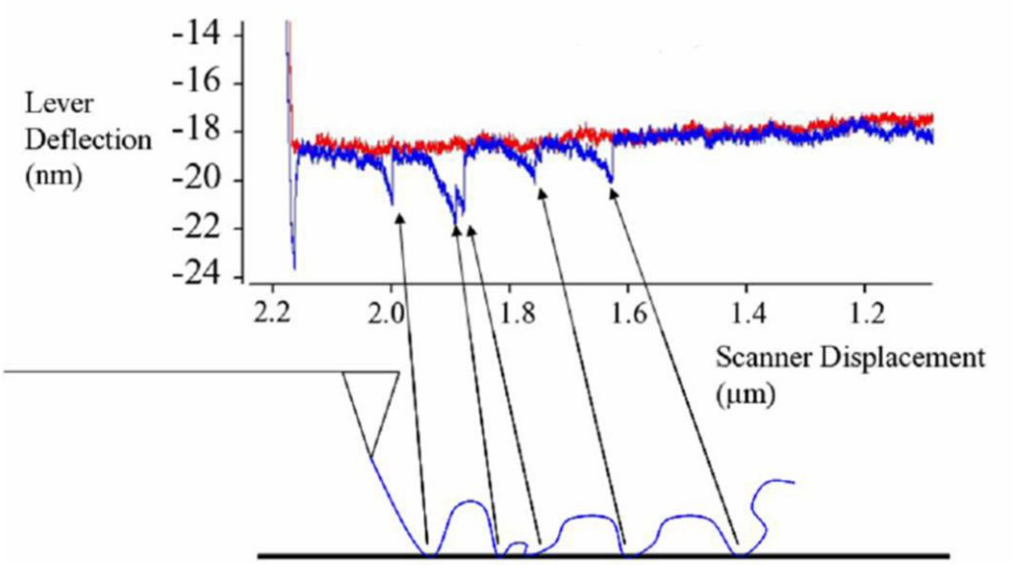

Figure A.1. In the upper portion, a force curve is presented relating cantilever deflection as a function of scanner displacement as the surface is brought towards (red) and away (blue) from the probe tip. The lower portion is a schematic illustration of how this force curve provides information about the conformation of the polymer on the surface.

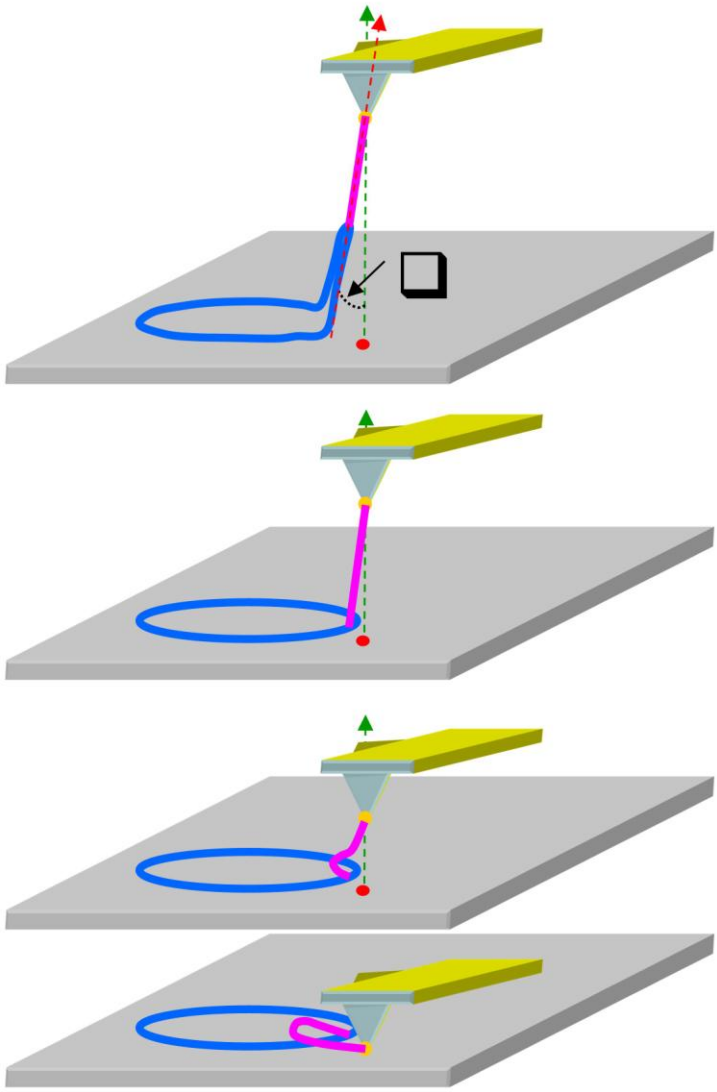

Figure A.2. Schematic illustration of the expected results from pulling on an loop structured molecule.

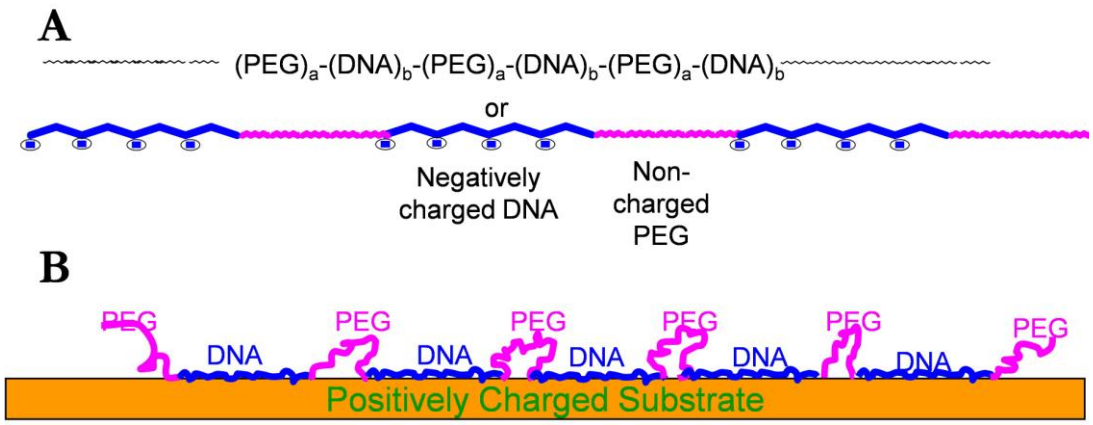

Figure A.3. Structure of novel alternating block copolymer comprised of PEG and DNA and its expected interaction with a positively charged substrate. A depicts the components of the polymer and B presents how the polymer will react with a positively charger surface. See Figure A.4 for a schematic of pulling this molecule off of the surface.

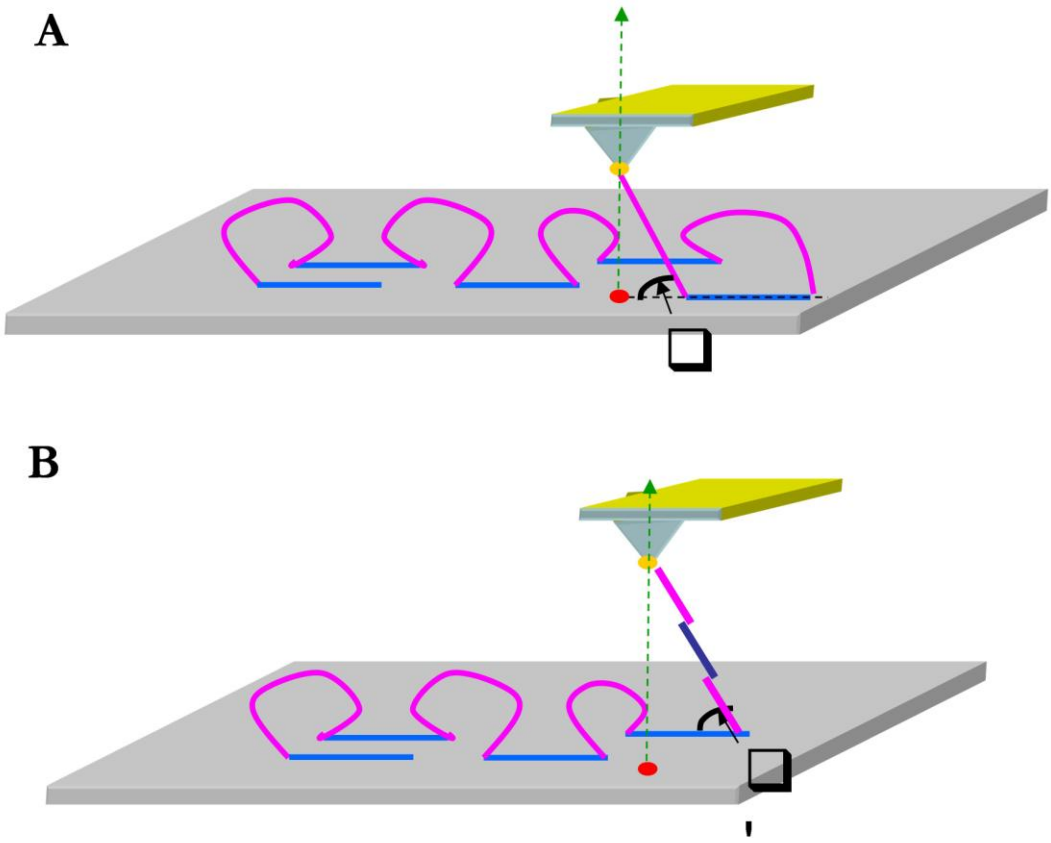

Figure A.4. Schematic illustration of the expected results from pulling on an alternating multiblock copolymer molecule. A) initial loading; B) after complete detachment of the first surface-active segment

A.2. DNA Loop Structure

A.2.1. Materials

10X stock tris acetate EDTA (TAE) buffer was prepared using 48.4 g tris base (JT Baker Reagent Chemicals, Phillipsburg, NJ), 2.92 g boric acid (VWR, Westchester, PA) and 10.9 g glacial acetic acid (EMD Chemicals, Gibbstown NJ) and brought to a pH of 8.3 using sodium hydroxide (Fischer Scientific, Pittsburgh, PA). For atomic force microscopy (AFM) imaging experiments, a 10X buffer of 200 mM ammonium acetate and 5 mM $MgCl_2$ (AmAc) buffer was prepared and adjusted to a pH of 7.

A.2.2. Methods

A.2.2.1. Digestion of Plasmids

pBR322, pUC19, and pTWIN1 vectors were purchased from New England Biolabs (Ipswich, MA) and used without further purification. A double digest was carried out using EcoRI and BamHI on all three plasmids to create two linear segments, as only a single cut site for both EcoRI and BamHI exits for all three plasmids. Single digests were carried out for each enzyme for comparison purposes. Figure A.6 depicts the sequence at which these restriction enzymes cut and the resulting sticky ends. To ensure successful digestion and subsequent ligation, calf intestinal phosphatase (CIP) was used. Bovine serum albumin (BSA) was used with digestions with BamHI. Initially buffer and DNA were mixed, followed by CIP, BSA, EcoRI and BamHI enzymes. Prior to enzyme addition, the mixture was gently vortexed to ensure a homogenous solution of DNA within the buffer. Digestions were incubated at 37 °C for 1 hour and the reaction mixture was immediately separated on an agarose gel to prevent over digestion. Bands were cut

from the gel and purified using Promega's Wizard® SV gel and PCR clean up system (Promega Corporation, Madison, WI). For all digestions, a reaction volume of 50 μL was used. The concentration of plasmid and units of enzyme were used accordingly. All digest products were stored a -20 °C freezer.

A.2.2.2. Ligation of Plasmid Fragments and Inserts

Ligations were carried out using a plasmid to insert DNA ratio of 1:3. DNA for the insert was purchased from Integrated DNA Technologies, Inc (Coralville, IA) and used without further purification. The sequences are provided in Table A.1 and were designed to compliment the sticky ends depicted in Figure A.5. New England Biolabs quick ligation kit was used for all ligation reactions. Initially buffer, plasmid DNA and insert DNA were mixed, followed by addition of the T4 DNA Ligase. Prior to enzyme addition, the mixture was gently vortexed to ensure a homogenous solution of DNA within the buffer. Although the ligation kit designates a 5 minute reaction time, to ensure full ligation, reactions were incubated at 16 °C overnight in varying reaction volumes, dependent upon the plasmid fragment being ligated. Ligations were confirmed using agarose gels. Once confirmed, the entire reaction volume was separated to remove the ligated product and the bands were cut from the gel and purified using the same protocol mentioned above. Ligation products were stored at -20 °C.

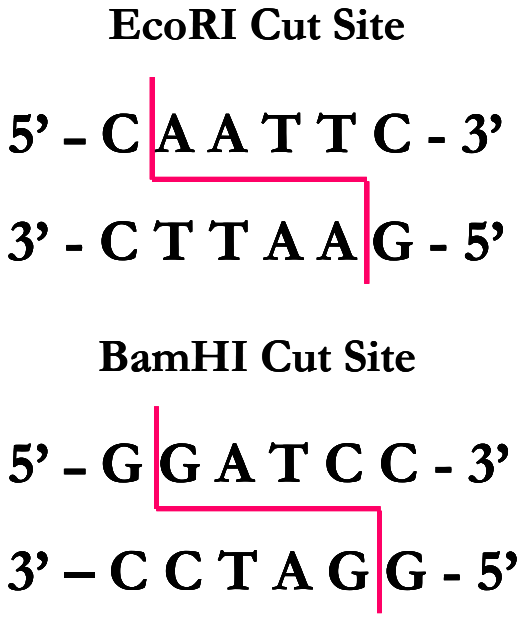

Figure A.5. Cut sites for EcoRI and BamHI restriction enzymes. These two enzymes were used to cut the three plasmids used in this study in a double digest reaction.[12]

Table A.1. Tether DNA Sequences used to form the insert for the cute DNA plasmids, pBR322, pUC19, or pTWIN1. The /iUniAmM/ is an internal amino used to attach a thiol linker for AFM tip attachment

Oligo Name	Sequence (ssDNA)
Tether-1	5' - GAT CAA ACA ACC AAG ACG AAG AAC CGG AAG ACC - 3'
Tether-2	5' - AAT TGG TCT TCC GGT TCT /iUniAmM/TCG TCT TGG TTG TTT - 3'

A.2.2.3. DNA Gel Electrophoresis

All separations were carried out using 1.0-1.2 % agarose gels in 1X TAE Buffer at 100V. 0.5 μg/mL ethidium bromide (EtBr) was added to the gel for staining purposes. EtBr was removed from the running buffer prior to disposal. Both 100 bp and 1 kb DNA ladders were used to verify strand lengths post digestion and ligation reaction. 6X Blue Orange loading dye (Promega Corporation, Madison, WI) was used to monitor the progress of the products through the gel. Gels were viewed using an UltraLum Model EA40 UV Transilluminator (Claremont, CA) and images were acquired using an Alpha Innotech Imager 2000 (Cell Biosciences, Santa Clara, CA). Both digestion and ligation products were cut from the gel with a razor blade and purified using Promega's Wizard® SV gel and PCR clean up system (Promega Corporation, Madison, WI). All were stored at -20 °C.

A.2.2.4. Preparation of AFM Cantilevers

Cantilevers purchased from Mikromasch (San Jose, CA) with rectangular and triangular levers were used for the pulling and peeling experiments. Tips were prepared by coating layers of metal onto the tips and then preferentially milling a hole in the outermost later. Metal was deposited using a CVC-SC5000 electron beam evaporator (Consolidated

Vacuum Corp., Rochester, NY) at a base pressure of 1 x 10^6 Torr. Initially, a 20 nm chrome adhesion layer was deposited at a deposition rate of 1 Å/sec followed by 150 nm of gold and 250 nm of chrome, both deposited at a rate of 3 Å/sec. During deposition, the cantilevers were rotated at approximately 1 Hz to ensure even coating of the entire tip. Deposition thicknesses were monitored using a quartz crystal microbalance (QCM) located inside the evaporator and placed normal to the vapor flux. Post metallization, cantilevers were stored in a desicator until milling.

A hole was milled through the outer chrome layer to expose a small region of the underlying gold. In doing so, the number of molecules attached to the AFM tip may be controlled. Additionally, by knowing the area of the milled region, the total number of molecules able to bind may be determined. This is advantageous when performing the pulling and peeling experiments. Milling was carried out on a FEI Nova NanoLab 200 dual ion/electron beam microscope (FEI Corp., Hillsboro, OR). The ion beam used is a Ga ion source. To prevent beam induced damage of the surface, the ion beam was not used to image the surface. Scanning electron micrographs were obtained before and after milling using a Zeiss SEM Ultra60 scanning electron microscope (Carl Zeiss SMT Inc., Peabody, MA). Images were acquired with an accelerating voltage of 5 eV with the cantilever tip oriented parallel to normal. To minimize charging artifacts during imaging, cantilevers were attached to the holders using double-sided carbon tape. Post milling and imaging, cantilevers were stored in a desicator until use.

A.3.3. Results

A.3.3.1. Plasmid pBR322 Digestion

Figure A.6 presents the enzyme map for pBR322 as provided by New England Biolabs. The plasmid is a total of 4361 base pairs with a variety of restriction enzyme cut sites. Boxes have been superimposed to point out the individual cut sites for EcoRI and BamHI restriction enzymes, the two enzymes used in these studies. Based on these cut sites, after a double digest DNA fragments of 377 and 3984 base pairs will result. The two fragments were separated from one another on 1.2 % agarose gel using both 100 bp and 1 kb ladders. Figure A.7 presents a photograph of a gel resulting from the double digest of pBR322. Superimposed on the image are rectangles and labels to indicate both band locations and assignments. The smaller 377 bp fragment was saved, however was too small to be of interest for future AFM pulling studies. Because of this, ligations were only carried out on the larger 3984 bp fragment.

A.3.3.2. Plasmid pBR322 Ligation

A ligation was carried out with the larger fragment, 3984 bp, and the insert DNA piece at a 1:3 ratio. The insert piece was hybridized prior to carrying out the ligation. Figure A.8 presents an image of the gel used to confirm that the ligation was successful. Also included on the gel is the pBR322 plasmid without any modifications, a single digestion with EcoRI producing a single linear fragment of DNA, the 3984 bp double digest fragment purified from a gel, as well as the 1 kb ladder for comparison between the bands. Results from the gel indicate that the unmodified plasmid has two bands as opposed to one. This is most likely due to a complete closed plasmid (lower band) as well as a nicked open circle (upper band) as no further purifications were performed on

the plasmids. Also observed on the gel is the fact that the EcoRI digest product is further up the gel in comparison to the 3984 bp double digest product, confirming successful enzyme cutting and different sized fragments. Lastly, it is evident that the ligated product is at a different spot than the unmodified plasmid, the 3984 bp product, and the EcoRI digest product. Based on these results, it was determined that a successful ligation was carried out. A total of four ligations were completed and the products were stored separately until the insert was functionalized with the pendant thiol group.

A.3.3.3. Plasmid pUC19 Digestion

Figure A.9 presents the enzyme map for pUC19 as provided by New England Biolabs. The plasmid is a total of 2665 base pairs with a variety of restriction enzyme cut sites. Boxes have been superimposed to point out the individual cut sites for EcoRI and BamHI restriction enzymes, the two enzymes used in these studies. Based on these cut sites, DNA fragments of 2644 and 21 base pairs will result after the double digest. The two fragments were separated from one another on a 1.0 % agarose gel using both 100 bp and 1 kb ladders. Figure A.10 presents a photograph of a gel resulting from the double digest of pUC19. Superimposed on the image are rectangles and labels to indicate both band location and assignment. The smaller digested piece was too small to remain on the gel so ligations were only carried out with the 2644 bp fragment.

A.3.3.4. Plasmid pUC19 Ligation

Similar to pBR322, a ligation was carried out with the larger 2644 bp fragment and the insert DNA piece. The insert piece was hybridized prior to carrying out the ligation. Figure A.11 presents an image of the gel used to confirm that the ligation was successful. In a similar fashion to the gel run for pBR322, pUC19 plasmid without any

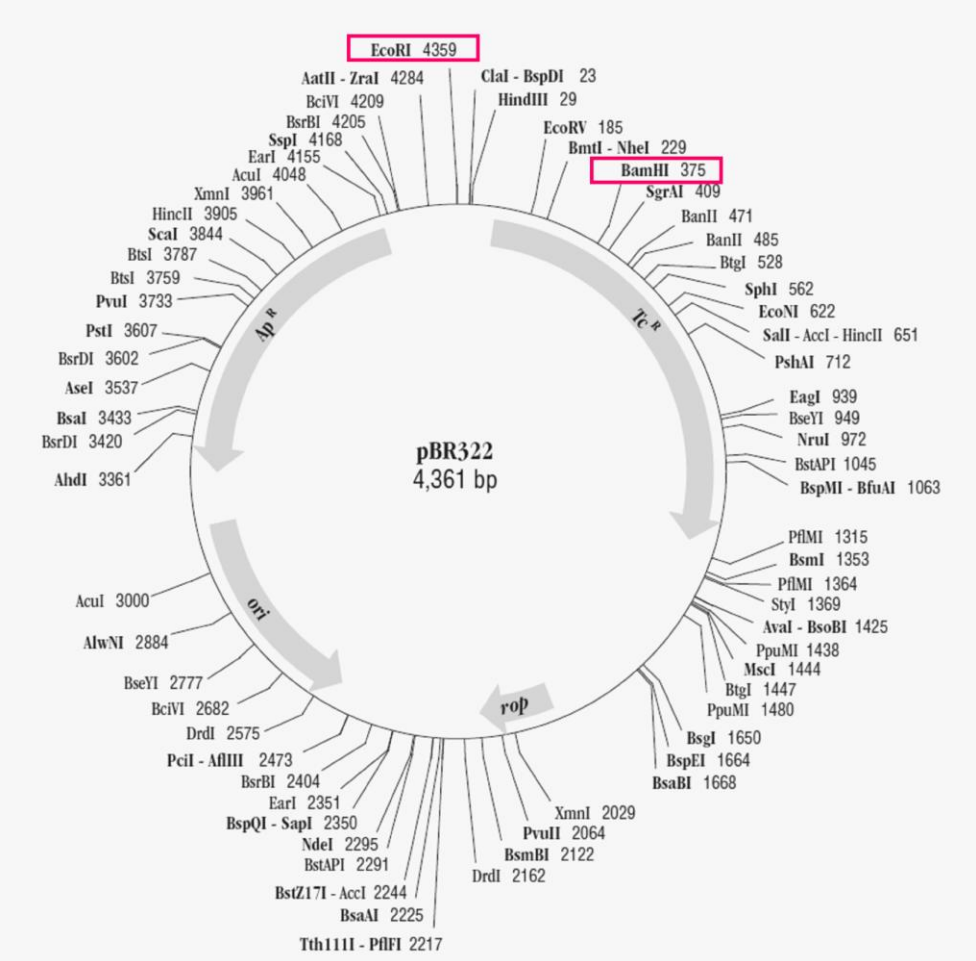

Figure A.6. Sequence map for the pBR322 vector. The enzyme cut sites for EcoRI and BamHI are highlighted.

Figure A.7. Digestion of pBR322 with EcoRI and BamHI to yield fragments of 3984 and 377 base pairs. Both 100 bp and 1 kb ladders were used for ease of comparison between bands. EtBr was used to stain the gel and visualize the location of the bands within the gel.

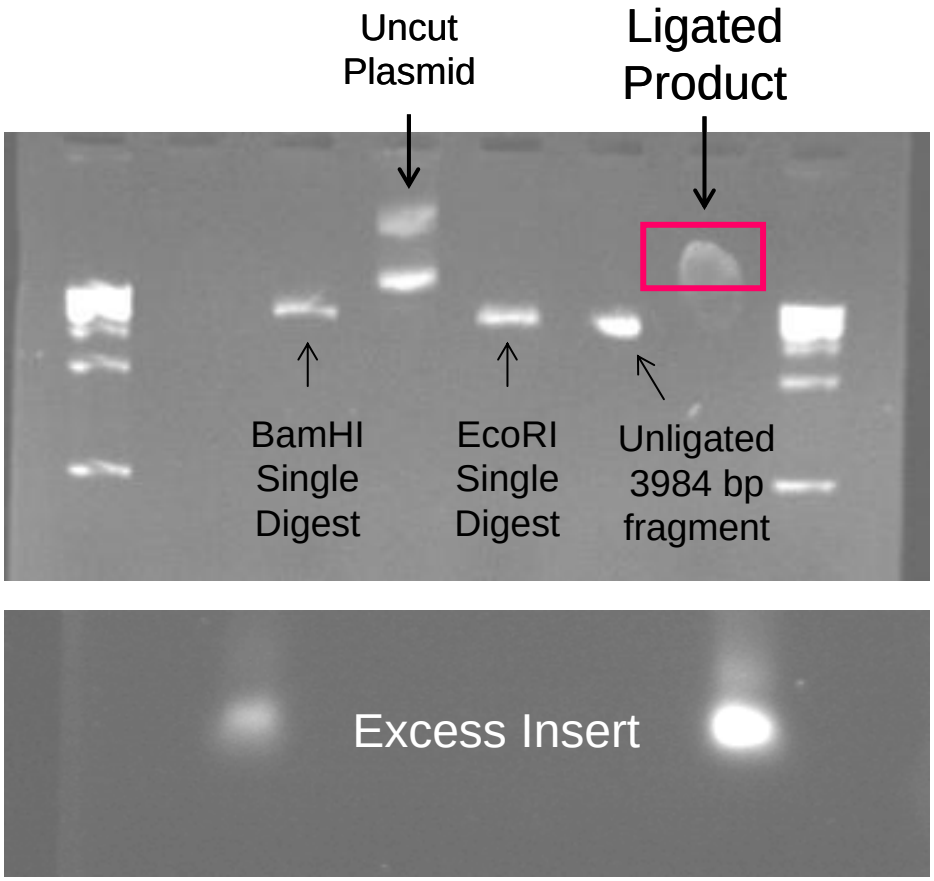

Figure A.8. Ligation of pBR322 3984 bp fragment and the specially designed insert. Only the 1 kb ladder was utilized for ease of comparison between bands due to the size of the fragments. EtBr was used to stain the gel and visualize the location of the bands within the gel.

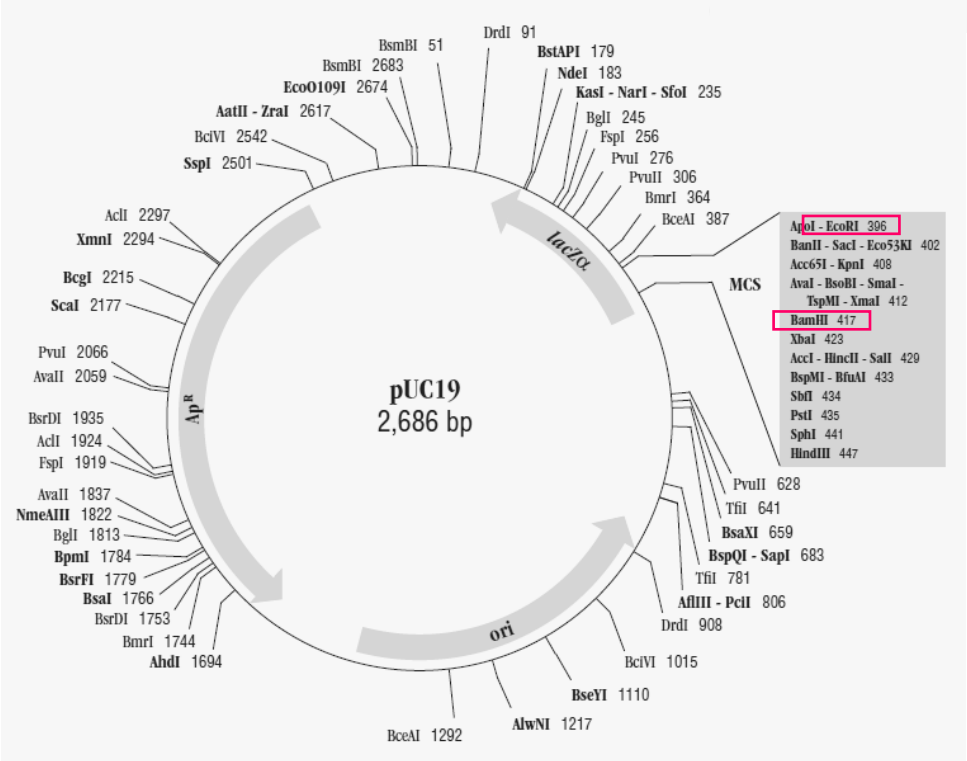

Figure A.9. Sequence map for the pUC19 vector. The enzyme cut sites for EcoRI and BamHI are highlighted.

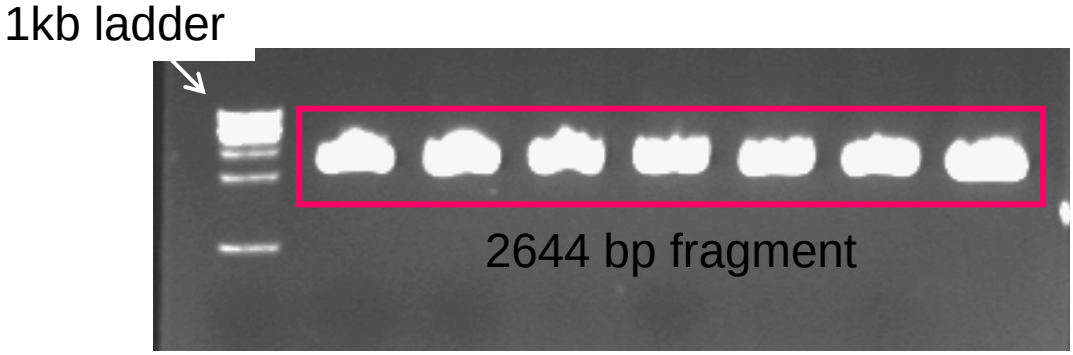

Figure A.10. Digestion of pUC19 with EcoRI and BamHI to yield fragment 2644 and 21 (not shown on gel) base pairs. Only the 1 kb ladder was utilized for ease of comparison between bands due to the size of the fragments. EtBr was used to stain the gel and visualize the location of the bands within the gel.

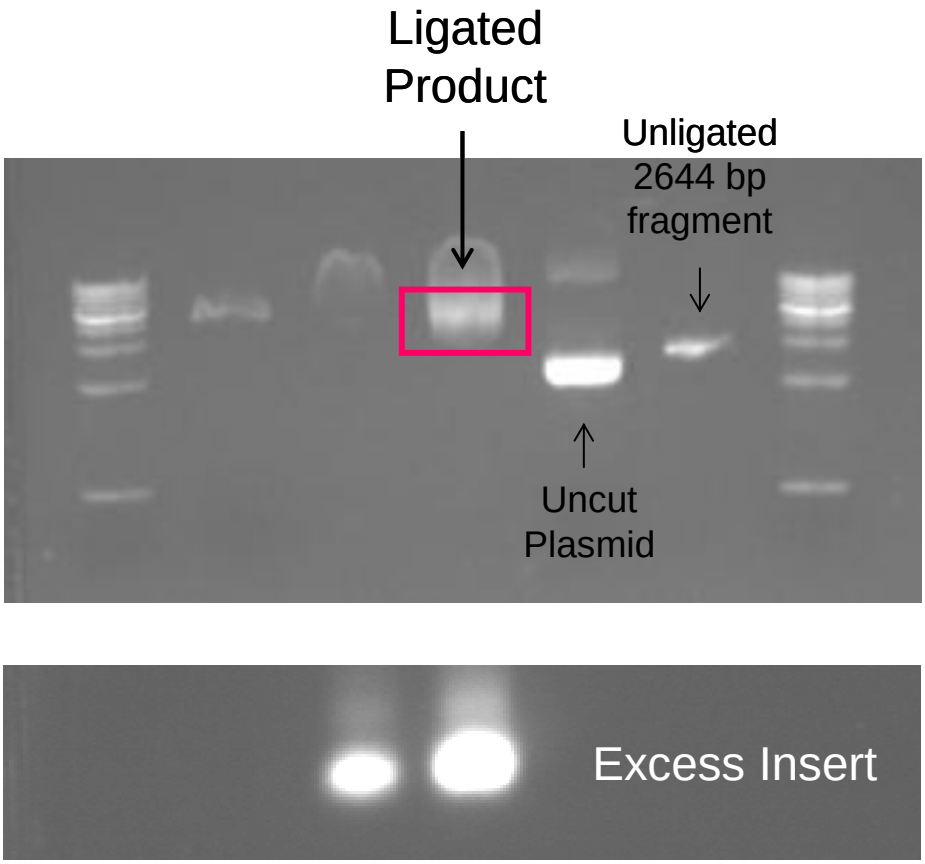

Figure A.11. Ligation of pUC19 2644 bp fragment and the specially designed insert. Only the 1 kb ladder was utilized for ease of comparison between bands due to the size of the fragments. EtBr was used to stain the gel and visualize the location of the bands within the gel.

modifications, a single digestion with EcoRI, the 2644 bp double digest fragment and the 1 kb ladder were included for comparison. Results from the gel indicate that this unmodified plasmid also has two bands. Again, this is most likely due to a completely closed plasmid and a nicked open circle. Also observed was that the EcoRI digest fragment was further up the gel similar to with pBR322. Finally, it is also evident that the ligated product is at a different location confirming a successful ligation. A total of three ligations were completed and the products were stored separately until the insert was functionalized with the pendant thiol group.

A.3.3.5. Plasmid pTWIN1 Digestion

Figure A.12 presents the enzyme map for pTWIN1 as provided by New England Biolabs. The plasmid is a total of 7375 base pairs with a variety of restriction enzyme cut sites. Boxes have been superimposed to point out the individual cut sites for EcoRI and BamHI restriction enzymes, the two enzymes used in these studies. Based on these cut sites, after a double digest DNA fragments of 6385 and 990 base pairs will result. Figure A.13 presents a photograph of a gel resulting from the double digest of pTWIN1. Superimposed on the image are rectangles and labels to indicate both band locations and assignments. Although both fragments were recovered from the gel, the larger piece would create a loop with dimensions non-ideal for AFM pulling and peeling studies. Because of this, ligations were only carried out on the 990 bp fragment.

A.3.3.6. Plasmid pTWIN1 Ligation

Unlike both pBR322 and pUC19, a ligation was carried out with the smaller 990 bp fragment and the insert DNA piece for pTWIN1. Figure A.14 presents an image of the ligation products in an agarose gel. In a similar manner to the other two plasmids,

pTWIN1 plasmid without any modifications, a single digestion with EcoRI, the 990 bp double digest fragment and the 1 kb ladder were included on the for comparison purposes. Again, the unmodified plasmid has two bands corresponding to a closed plasmid and a nicked open circle. Additionally, the EcoRI digest fragment was further up the gel similar to previous results with the other two plasmids. Finally, it is also clear that the ligated product is at a different location than other DNA molecules confirming a successful ligation. A total of two ligations were completed and the products were stored separately until the insert was functionalized with the pendant thiol group.

A.3.4. Work Left to Be Done

Before loop pulling experiments may be carried out, the conformation of the loops on the gold surface must be analyzed. Using AFM imaging techniques, the degree of super coiling of the plasmid structure may be determined, although little to no supercoiling was indicated by electrophoresis. If supercoiling is found, it can be removed using topoisomerase to relax the plasmid. Once the structures are verified, they may be attached to the FIBed AFM tip. Prior to attachment, the plasmids must go through an additional reaction to attach the thiol linker to the molecule. Since the insert DNA contains an amino terminated tether, a carbon chain with both an NHS and thiol group may be reacted to produce the appropriate thiol connector to bind the exposed gold region of the AFM tip. Upon successful linking of the DNA loop to the AFM tip, pulling experiments may be carried as described in the introduction of this appendix. These studies will be conducted in the near future by Kelsey Beavers and Linda Van Rosmalen of the Bottomley research group.

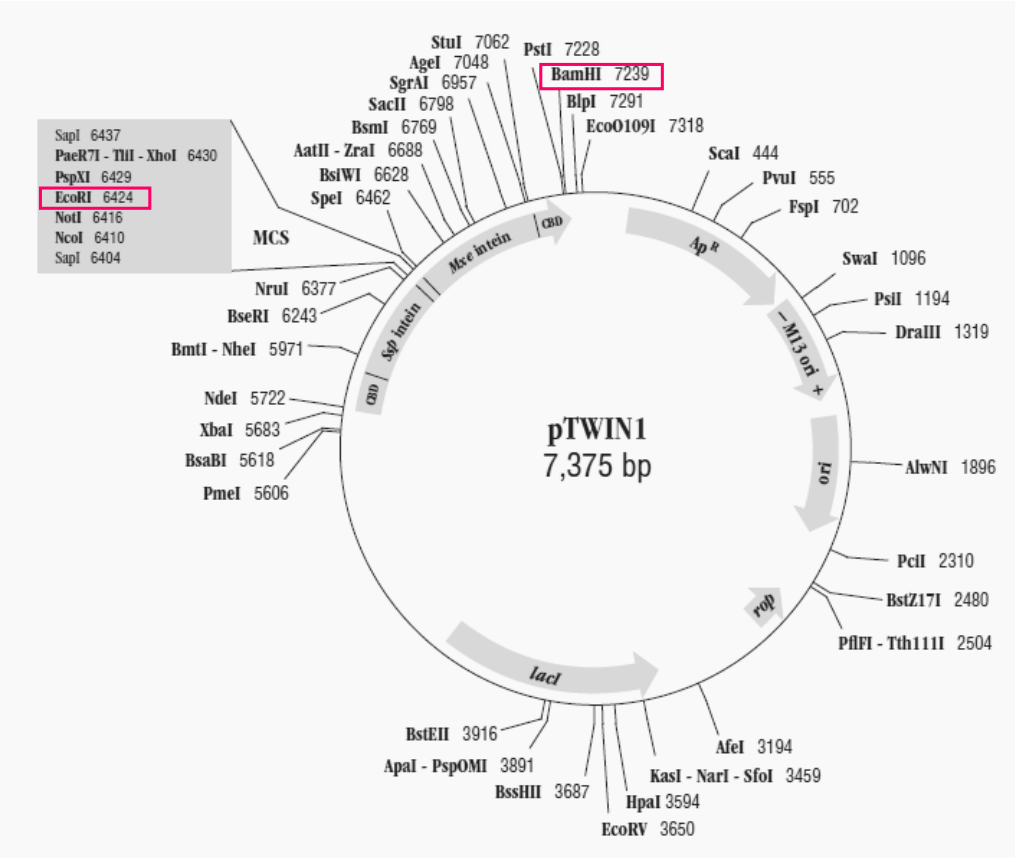

Figure A.12. Sequence map for the pTWIN1 vector. The enzyme cut sites for EcoRI and BamHI are highlighted.

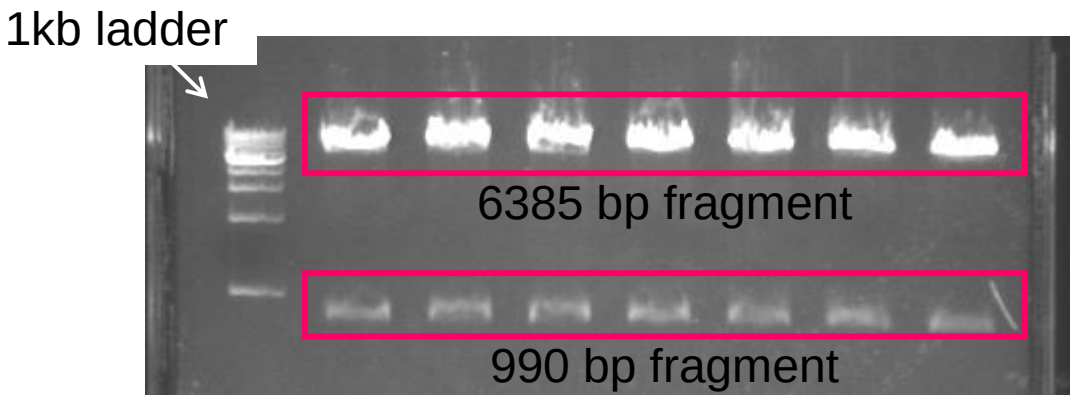

Figure A.13. Digestion of pTWIN1 with EcoRI and BamHI to yield fragment 6385 and 990 base pairs. Only the 1 kb ladder was utilized for ease of comparison between bands due to the size of the fragments. EtBr was used to stain the gel and visualize the location of the bands within the gel.

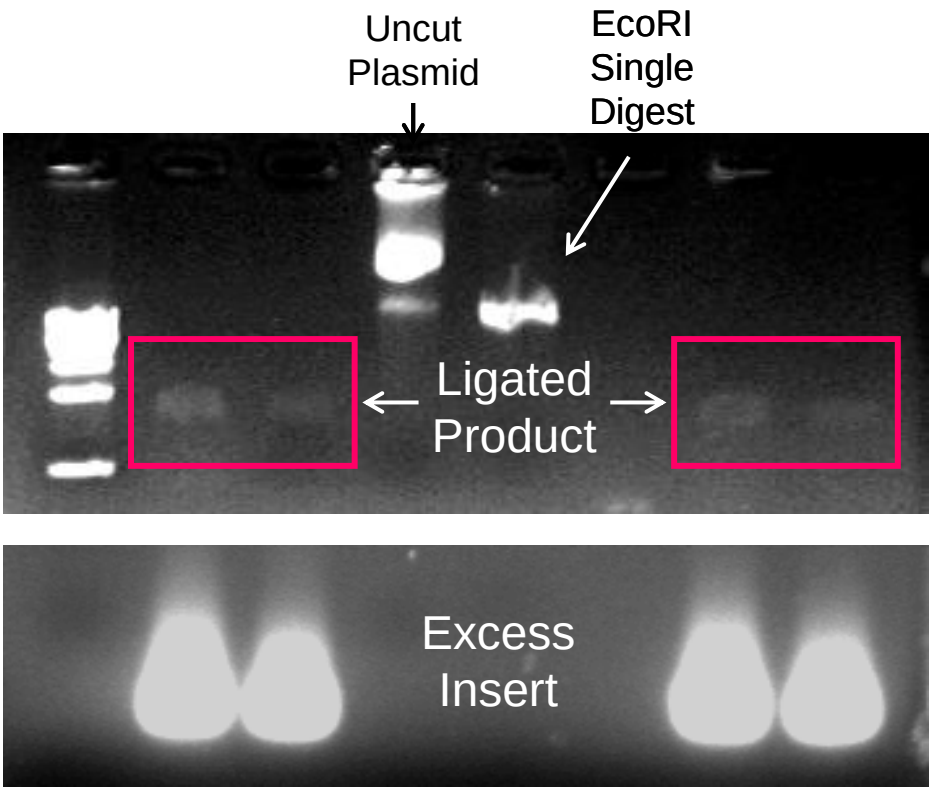

Figure A.14. Ligation of pTWIN1 990bp fragment and the specially designed insert. Only the 1kb ladder was utilized for ease of comparison between bands due to the size of the fragments. EtBr was used to stain the gel and visualize the location of the bands within the gel.

A.3. DNA Block Co-polymer Structure

A.3.1. Materials

A bis-succinimide ester-activated PEG compounds, $BS(PEG)_9$, was purchased from Thermo Scientific (Rockford, IL) and used without further purification. Stock solutions were prepared in anhydrous dimethylsulfoxide (DMSO) at a concentration of 250 mM, per the instructions from Pierce Protein Research Products.[443] Two DNA molecules were purchased from The Midland Certified Reagent Company, Inc. (Midland, TX) and used without any further purification. Oligonucleotides consist of either a single run of 10 thymine bases (or two runs separated by a dithiol linker) with both 3' and 5' ends functionalized with an amine. Stock solutions for both DNA molecules were mane in nanopure water (18Ω). The structures for all three molecules are presented in Figure A.1.

A.3.2. Methods

A.3.2.1. Synthesis Reaction

The starting materials presented in Figure A.15 were mixed in varying ratios to produce polymers of multiple lengths. A total of three reaction ratios were carried out, listed in Table A.2. The purpose of the $T_{10}SST_{10}$ starting material was to create essentially a cutting point in the synthesized polymer. Tris((2-carboxyethyl)phosphine) (TCEP·HCl) was purchased from Pierce Biotechnology, Inc. (Rockland, IL) to reduce the disulfide bonds within the block-copolymer, resulting in smaller segments with a pendent thiol group. To create polymers of varying lengths, the $T_{10}SST_{10}$ was held constant for all three reactions. With an increased amount of T_{10} and PEG, the polymers would be

longer. The pendent thiol was used to attach the molecules to the AFM tip for pulling and peeling experiments.

Table A.2. Ratios used during the synthesis of the PEG-DNA block co-polymer. $T_{10}SST_{10}$ was held constant for all reactions.

Component	Ratio: Rxn 1	Ratio: Rxn 2	Ratio: Rxn 3
$T_{10}SST_{10}$	1	1	1
T10	5	10	20
PEG	6	11	21

A.3.2.2. HPLC Separation

High performance liquid chromatography (HPLC) was performed using an Agilent 1100 series (Santa Clara, CA) with a Torrey Pines Scientific Echo Therm Model C030 HPLC column chiller/heater (San Marcos, CA). A reverse phase Phenomenex Luna C-18 column (Torrence, CA) and a Dionex DNA-Pac PA100 (Sunnyvale,CA) ion exchange column were used for separation of the cut segments of the synthesized polymer. For the reverse phase column, the gradient used was 30 mM ammonium acetate (NH_4OAc) and acetonitrile while the ion exchange column used 2 M NH_4OAc and distilled water. Starting materials as well as reaction products were run and compared.

A.3.3. Results

HPLC Separations were carried out on starting materials and reaction products to determine peaks associated with each compound. The chromatograms of the starting materials is presented in Figure A.16 for both a C18 reverse phase and ion exchange

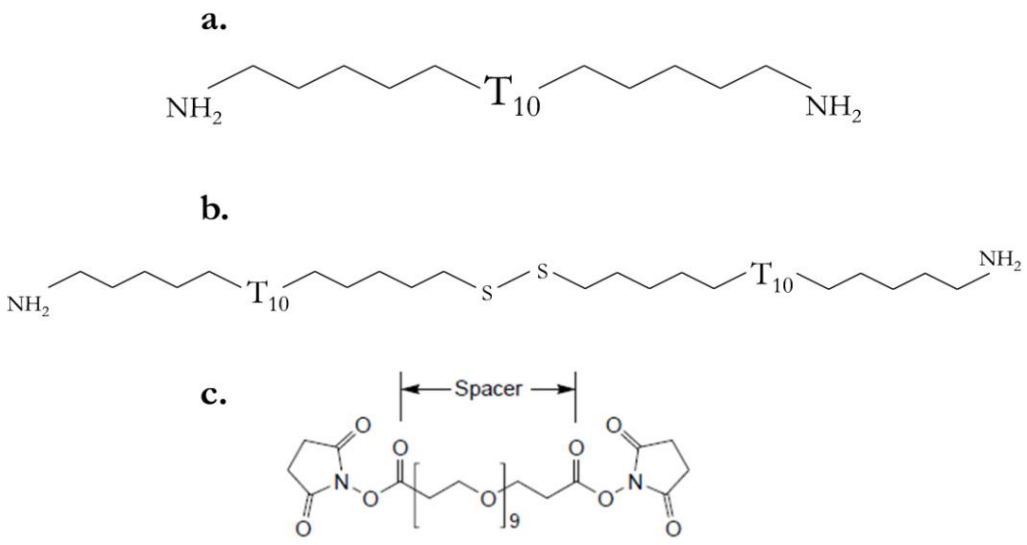

Figure A.15. Molecules used for DNA block-copolymer synthesis. a.) referred to as T_{10}DNA, b.) referred to as $T_{10}SST_{10}$DNA, and c.) referred to as PEG.

column. The chromatogram of T_{10} DNA is the red trace, $T_{10}SST_{10}$ is the blue trace and PEG is the green trace for both columns. It is clear that the ion exchange column provided better separation and was the column chosen to separate the reaction products. The three reactions described in Table A. 2 were run on the same ion exchange column as the starting materials. The results are presented in Figure A.17. Reaction run is presented as the blue trace, reaction two as the red trance, and reaction three as the green trace. It is clear that the starting materials are still in solution, especially for T_{10} DNA and PEG as they were in excess for all three reactions. It is not clear, however, if there are definitive product peaks. A possible explanation for the lack of product peaks was that the TCEP used to reduce the disulfide bond had become ineffective over time or that the amounts used during the reaction were not sufficient. To test this possibility, $T_{10}SST_{10}$ was treated in the same fashion and run on the ion exchange column. The results are presented in Figure A.18. Both T_{10}, $T_{10}SST_{10}$ and $T_{10}SST_{10}$ treated with TCEP are included for comparison. Based on these results, TCEP was not responsible for the lack of product peaks. An additional explanation may be that the concentration of each polymer length was not high enough to provide a distinct peak in the HPLC trace.

A.3.4. Work Left to Be Done

Successful separation of the polymer products must be carried out prior to continued analysis. Preliminary HPLC results suggested that the technique may not be sensitive enough to the low quantities of product in the reaction. Other techniques that may be employed are gel electrophoresis separation followed by mass spectrometry to verify the composition of the polymer. Additionally, a size exclusion column may be used in an attempt to separate the polymer lengths. Once the polymers are separated, they may be

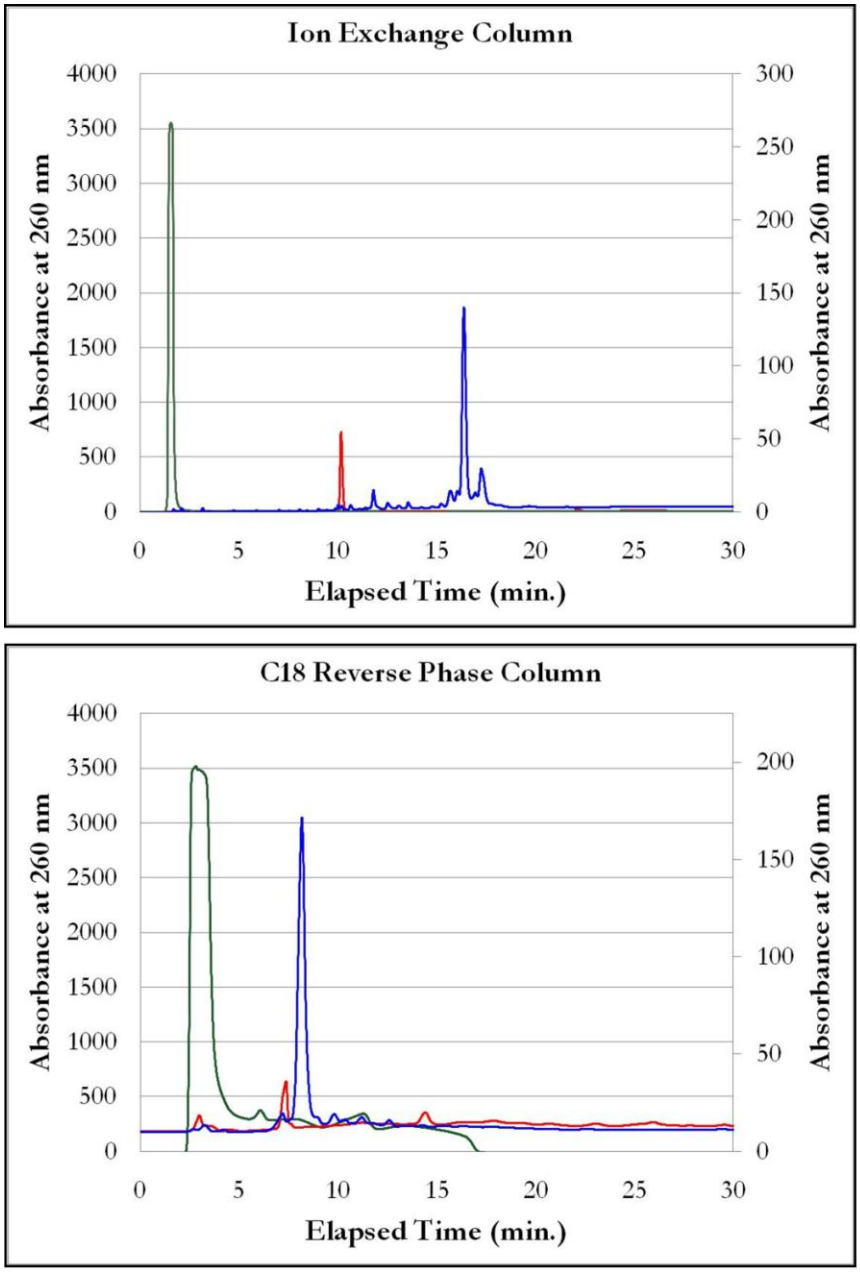

Figure A.16. HPLC chromatograms for starting materials run on both an ion exchange and C18 reverse phase column. Chromatogram of the T_{10} DNA is the red trace, $T_{10}SST_{10}$ is the blue trace and PEG is the green trace. Both columns separated the three materials successfully, however the ion exchange column provided better separation.

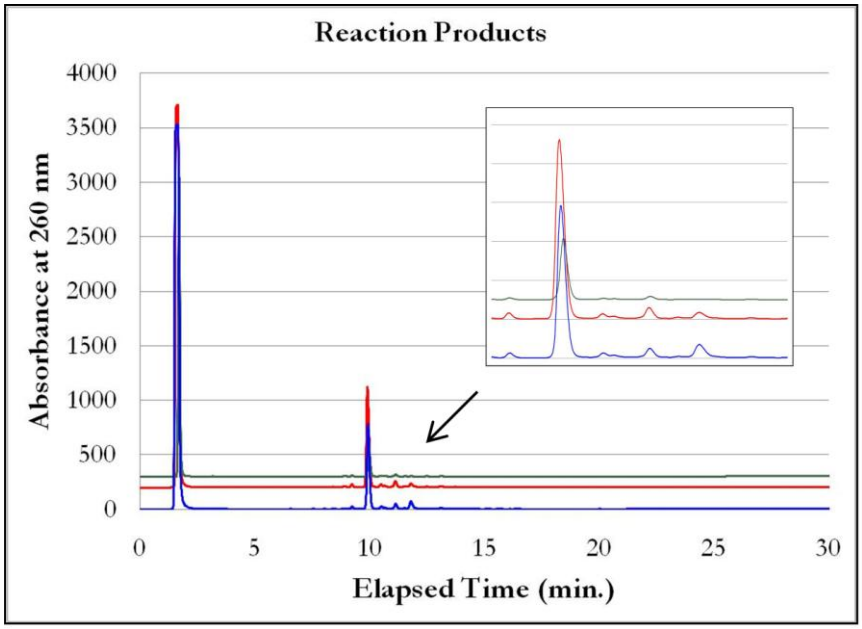

Figure A.17. HPLC traces for reactions 1 (blue trace), 2 (red trace), and 3 (green trace) presented in Table A.2. The inset is a zoomed in region of the plot surrounding the peak corresponding to $T_{10}SST_{10}$ starting material. The products were run on the same ion exchange column as the starting materials presented in Figure A.16.

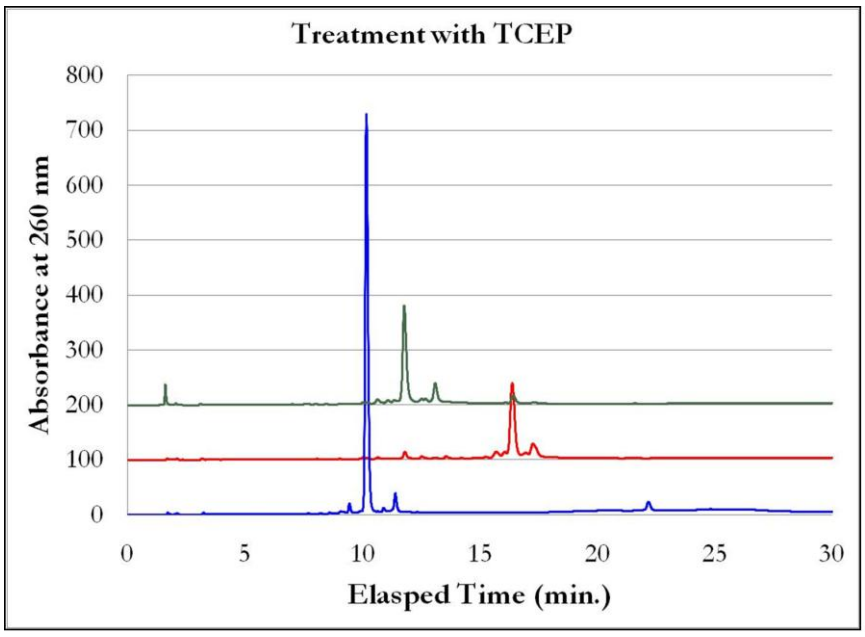

Figure A.18. HPLC traces of T_{10} (blue trace), $T_{10}SST_{10}$ (red trace) starting materials and $T_{10}SST_{10}$ treated with TCEP (green trace). The materials were run on the same ion exchange column as all other materials. The traces have been offset for clarity and ease of comparison between the three. The shift in the peak when $T_{10}SST_{10}$ was treated with TCEP verifies that successful reduction of the disulfide bond is occurring.

attached to the FIBed AFM tip. The pendent thiol group with attach the copolymer to the exposed gold region of the AFM tip for pulling experiments described in the introduction of this appendix.

APPENDIX B

FABRICATION OF A MICRO-DSC HEATER DEVICE

B.1. Introduction

This appendix describes research focused on the design, fabrication and testing of a microelectronic differential scanning calorimetry (μDSC) device designed for sensing airborne analytes. Specifically, the fabrication of pairs of sensors comprised of a metal oxide film electrically isolated from a heater on a suspended platform comprised of alumina. The heater required low power and was capable of maintaining the temperature of the metal oxide layer at 600 ºF for extended periods of time. Four electrical connections were made to the serpentine heater intended for a four point probe measurement. Additionally, each sensor possessed a resistive thermal device (RTD) integrated sensing element.

B.1.1. Thermal Modeling

Thermal modeling was done by Jabulani Barber of our research lab to identify the best materials to use in fabricating the first prototype microDSC device. The optimum component match and dimensionality was sought after to provide rapid and uniform heating of the metal oxide catalyst to the desired temperature. Simulations were conducted using the engineering software package Comsol Multiphysics 3.4 (Burlington, MA) to model the thermal conduction of the device. Component pairs that enabled rapid and uniform heating with low power requirements and minimized thermally-induced

stresses were focused on. The results of this modeling study were used in selecting the material combinations and subcomponent dimensions. For thermal isolation of the hotplates within the device from one another, a cantilever-based design was employed. Modeling revealed that complete thermal isolation of devices from each other would be achieved; the sapphire base substrate could be thinned beneath the serpentine heating element to reduce the thermal capacitance of the device. The serpentine heating element was positioned further from the top edge of the cantilever to decrease the heat loss to the sapphire substrate and the surrounding gas stream flowing over the cantilever. From modeling studies, the serpentine heater required 50 μm line widths and 10 μm spacing to reduce its resistance in response to the large voltage required to achieve the desired temperature.

B.1.2. Process and Mask Design

The process flow was designed around the base substrate made of sapphire. A serpentine platinum RTD was incorporated above each heater region. The metal oxide catalyst was designed to have an area identical to that of the RTD sensor, ensuring high uniformity in temperature across the catalyst surface. Mask sets were designed by Kane Barker of the Bottomley research group using AutoCad (Autodesk, Inc., San Rafeal, CA) based on the results obtained from the thermal modeling and the process design. Mast alignment markings and device identifiers were integrated into the mask designs to facilitate identification of chip sets after wafer dicing. Mask sets were fabricated by Photo Sciences, Inc. (Torrance, CA). The following section describes in detail the photolithography processing steps designed to fabricate the first and second μDSC prototype devices.

B.2. Prototype #1 Initial Process Flow

The process design for prototype #1 was built around commercially available sapphire wafers. Ten 2" diameter sapphire wafers (300 μm thick) were purchased to serve as substrates. The following subsections lay out the steps involved in bringing a single wafer to completion. The process flow is in bulleted form to emphasize the detailed steps involved in the fabrication of the μDSC device.

B.2.1. Deposition of Silicon Nitride Mesas for micro-Heater (Figure B.1)

Step 1. Plasma-enhanced chemical vapor deposition (PECVD) was employed to deposit a 1 μm layer of silicon nitride (Si_xN_y) over the entire sapphire wafer. PECVD was chosen because it provides a means for depositing a low stress film of desired thickness which is critical to reduce accumulated stresses as the number of layers on the sapphire wafer increases. Uniformity in this layer is critical for isolation of the nickel serpentine heater.

Step 2. Photolithography patterning is the standard tool for producing patterns on a wafer. The intended resist was AZ4260 along with the appropriate dark-field mask #1, and developer AZ400K.

Step 3. An RIE process was used to etch the Si_xN_y over other options because it is capable of producing straight and vertical walls. This etching step resulted in the formation of the Si_xN_y mesas which were used to define the dimensions of the serpentine heater.

Step 4. Post etching, the photoresist was removed using the appropriate solvent.

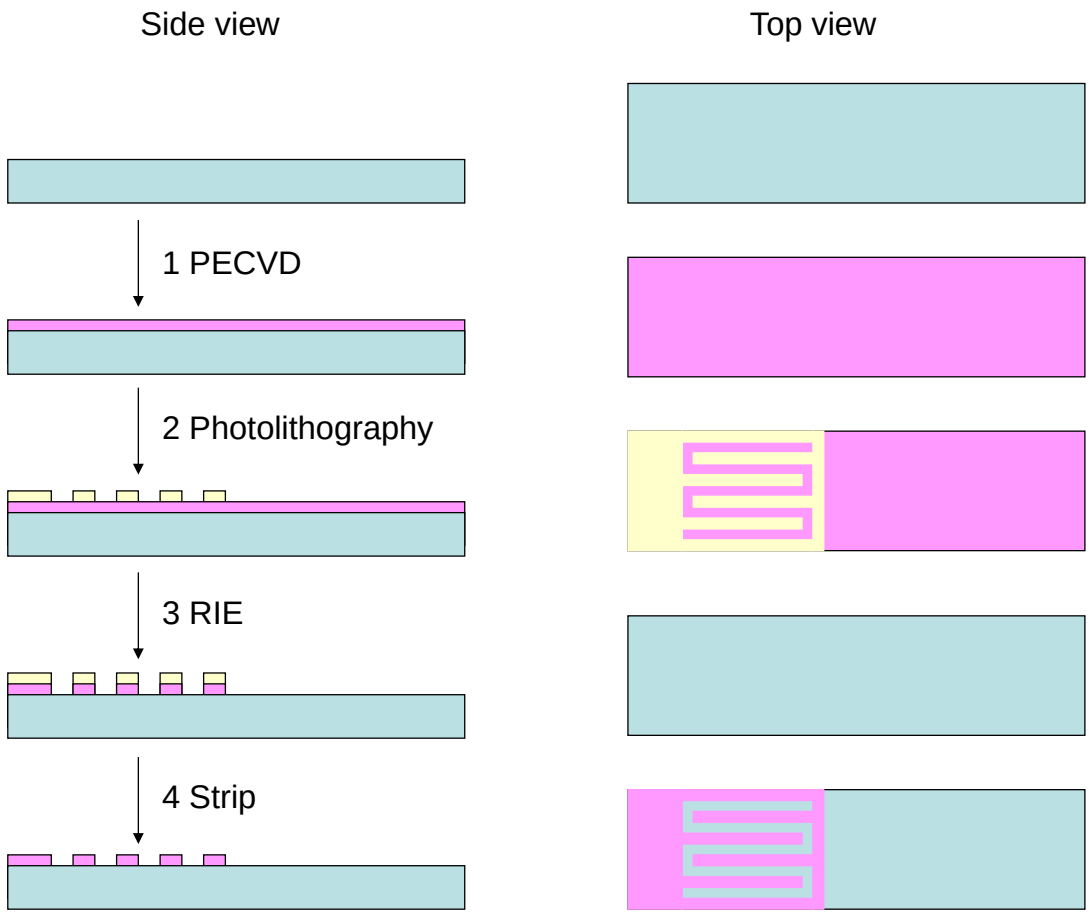

Figure B.1. Schematic of the proposed process flow for deposition of silicon nitride mesas onto a clean sapphire wafer substrate. Both side and top views are provided.

B.2.2. Creation of Wiring for micro-Heater (Figure B.2)

Step 5. The pattern for the lead wires was created by openings in the photoresist. The intended resist was SC1827 along with light-field mask #2 and developer Microposit 351.

Step 6. PVD was carried out using an e-beam metallization tool to produce a smooth thin film of titanium to serve as an adhesion layer for the subsequent deposition of gold. The gold leads serve as the connections to the serpentine heater.

Step 7. Excess metal deposited by the PVD process was removed from the wafer surface, leaving behind the metal in the desired location.

B.2.3. Deposition of Nickel Serpentine for micro-Heater (Figure B.3)

Step 8. The pattern for the serpentine heater was created by the openings in the newly deposited photoresist corresponding to the mesas created in the initial Si_xN_y layer. Photolithographic patterning step #3 was performed using SC1827 resist and clear-field mask #3.

Step 9. PVD was carried out using an e-beam metallization tool to produce a smooth surface of gold. Nickel was an ideal heating element because of its intrinsic resistivity. The thickness of the nickel deposition was adjusted based on the thickness of the Si_xN_y mesas.

Step 10. Excess metal was removed from the surface, leaving nickel in the desired location.

Step 11. Thermal annealing was required to fill gaps or discontinuities that were created during metal deposition. In doing so, electrical contact between the previously deposited gold leads and the nickel heater were made.

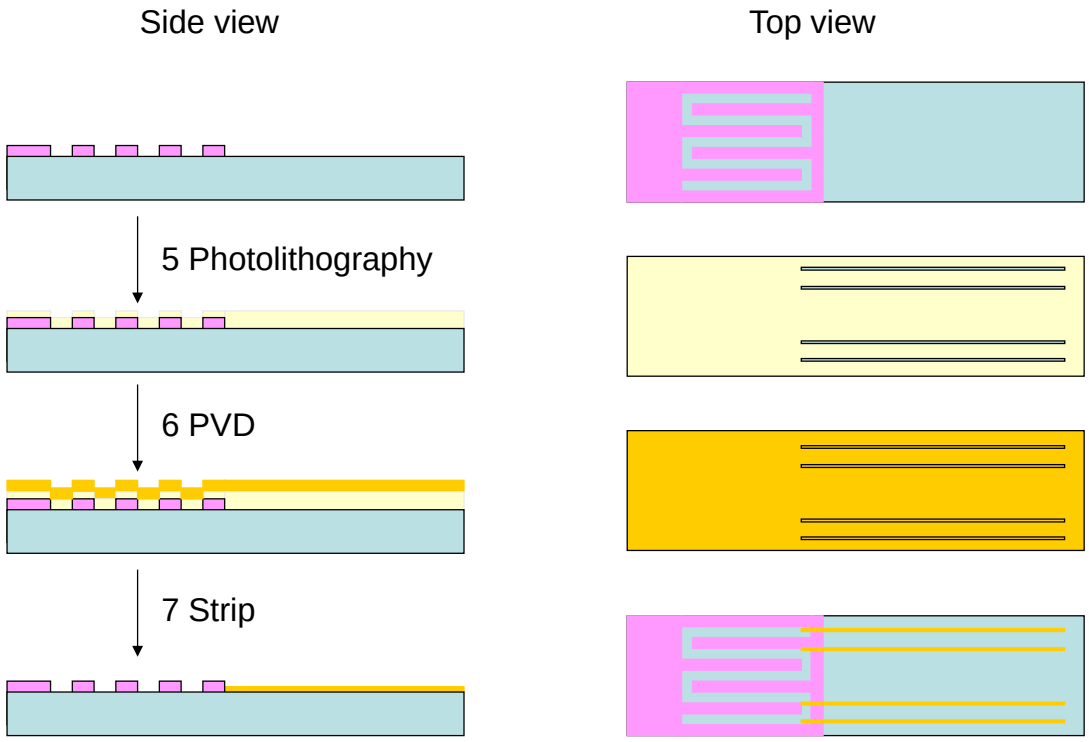

Figure B.2. Schematic of the proposed process flow for creation of lead wires for serpentine heater. Both side and top views are provided.

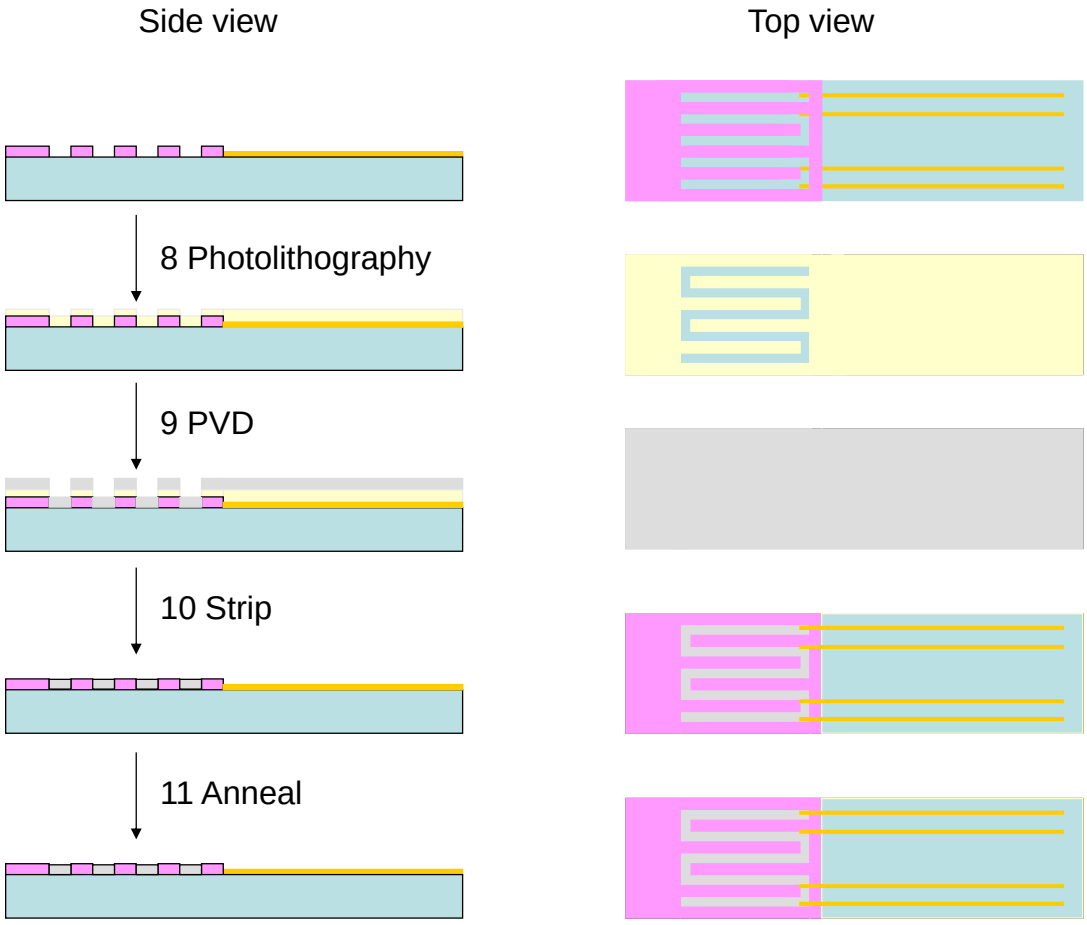

Figure B.3. Schematic of the proposed process flow for deposition of serpentine nickel heater. Both side and top views are provided.

B.2.4 Deposition of Silicon Nitride Barrier Layer (Figure B.4)

Step 12. Si_xN_y was deposited using PECVD to produce an isolating layer, both electrically and chemically, between the nickel heater and gold leads and future layers. Again, a low stress deposition method was employed to minimize surface stress.

Step 13. Photolithographic patterning step #4 was performed using SC1827 resist and clear-field mask #4.

Step 14. A wet chemical etch of the Si_xN_y was carried out to remove excess Si_xN_y, decreasing the possibility of thermal loss during testing. A wet chemical etch was required as Georgia Tech Cleanroom policy excludes metals from the RIE tools previously used to etch Si_xN_y.

B.2.5. Creation of Wiring for RTD (Figure B.5)

Step 15. The pattern for the wiring for the RTD was created by the openings in photoresist SC1827 and the appropriate clear-field mask #5.

Step 16. PVD was carried out using an e-beam metallization tool to produce a smooth thin film of titanium. Titanium served as an adhesion promoting layer for the subsequent deposition of gold onto the Si_xN_y layer.

Step 17. Excess metal deposited by the PVD process was removed, leaving metal in the desired location.

B.2.6. Deposition of Platinum RTD (Figure B.6)

Step 18. The pattern for the RTD was created by the openings in photoresist SC1827 and the appropriate clear-field mask #6.

Step 19. PVD was carried out using an e-beam metallization tool to produce a smooth thin film of platinum, completing the RTD. No adhesion layer was required because

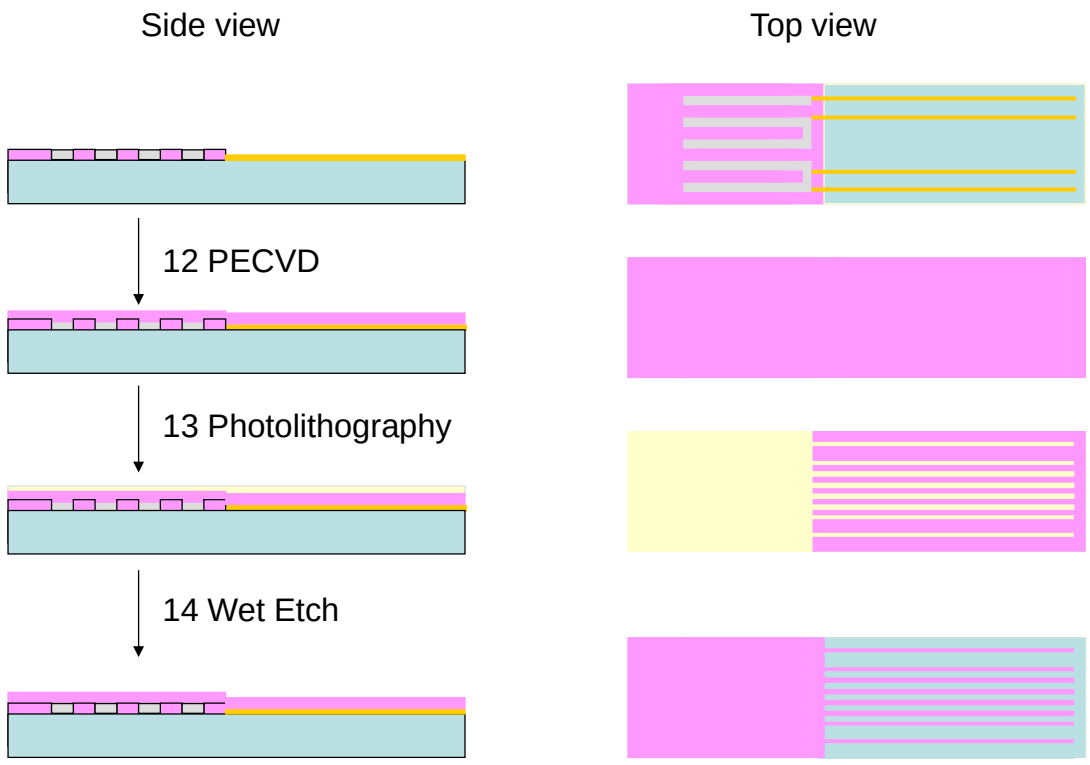

Figure B.4. Schematic of the proposed process flow for deposition of the first silicon nitride barrier layer. Both side and top views are provided.

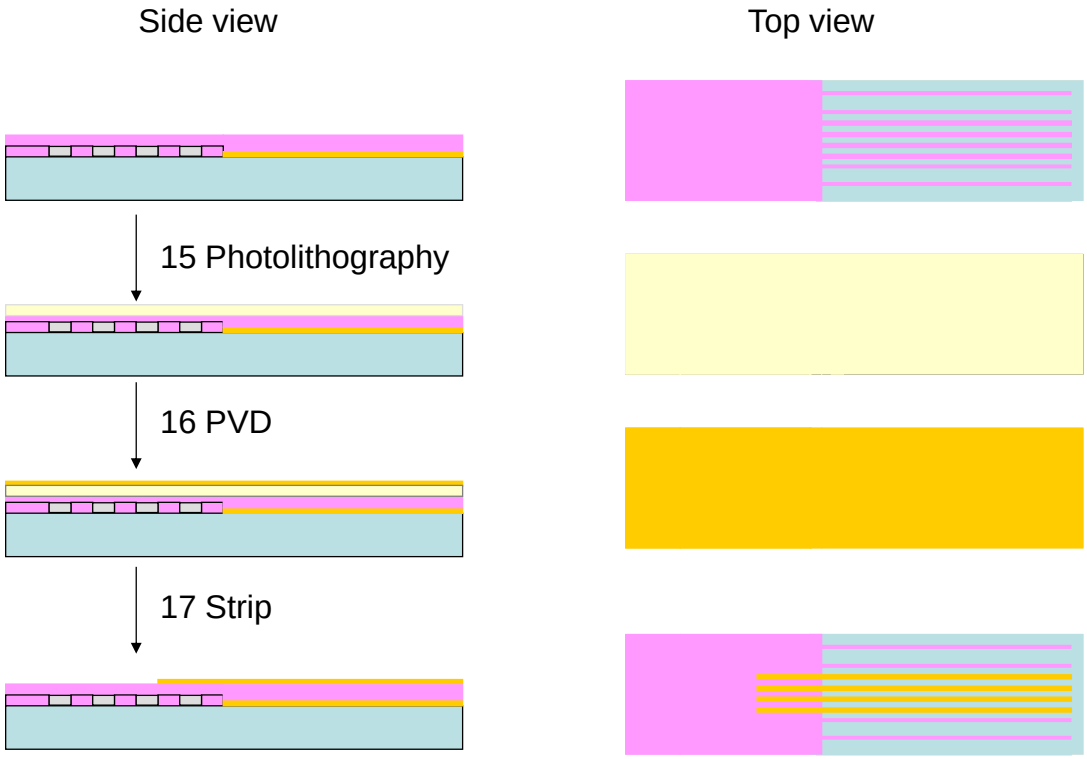

Figure B.5. Schematic of the process flow for deposition of RTD connection wires. Both side and top views are provided.

platinum is adherent to Si_xN_y. The dimensions of the serpentine RTD were determined from the thermal modeling studies described previously in this Appendix, section A.1.1.

Step 20. Lift off of the resist removed the excess metal deposited by the PVD process, leaving metal in the desired location.

Step 21. A sintering/anneal step was critical to allow the metals to fill gaps or discontinuities created during PVD of metal layers.

B.2.7. Deposition of Silicon Nitride Barrier Layer (Figure B.7)

Step 22. Si_xN_y was deposited using PECVD to produce an isolating layer, both electrically and chemically, between the nickel heater and gold leads and future layers. Again, a low stress deposition method was employed to minimize surface stress.

Step 23. Photolithographic patterning step #7 was performed using SC1827 resist and clear-field mask #7.

Step 24. A wet chemical etch was used to remove excess Si_xN_y. Similar to the first Si_xN_y barrier layer, any excess Si_xN_y functions as a pathway for thermal loss.

B.2.8. Deposition of Gold Bonding Pads (Figure B.8)

Step 25. The pattern for the gold bonding pads was created by the openings in photoresist SC1827 and the appropriate clear-field mask #8 onto the Si_xN_y barrier layer.

Step 26. A wet chemical etch was performed to remove Si_xN_y covering the gold bonding pads. The gold deposited in steps photolithography steps #6 and #16 served as the etch stop.

Step 27. Upon etch completion, PVD was carried out using an e-beam metallization tool to produce a smooth film of gold, completing the bonding pads. Gold was the preferred choice for bonding pads because it is easily bonded to other metals and wires.

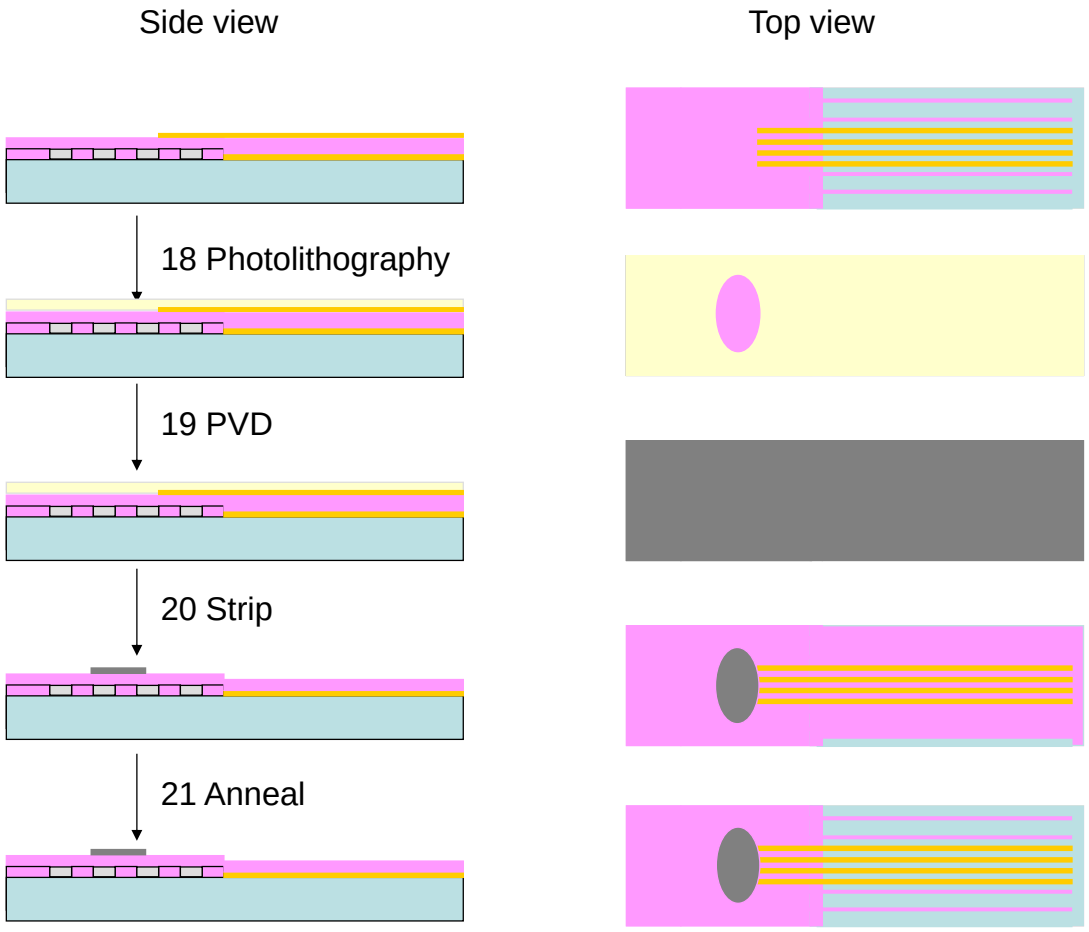

Figure B.6. Schematic of the process flow for creation of the temperature sensing element. Both side and top views are provided.

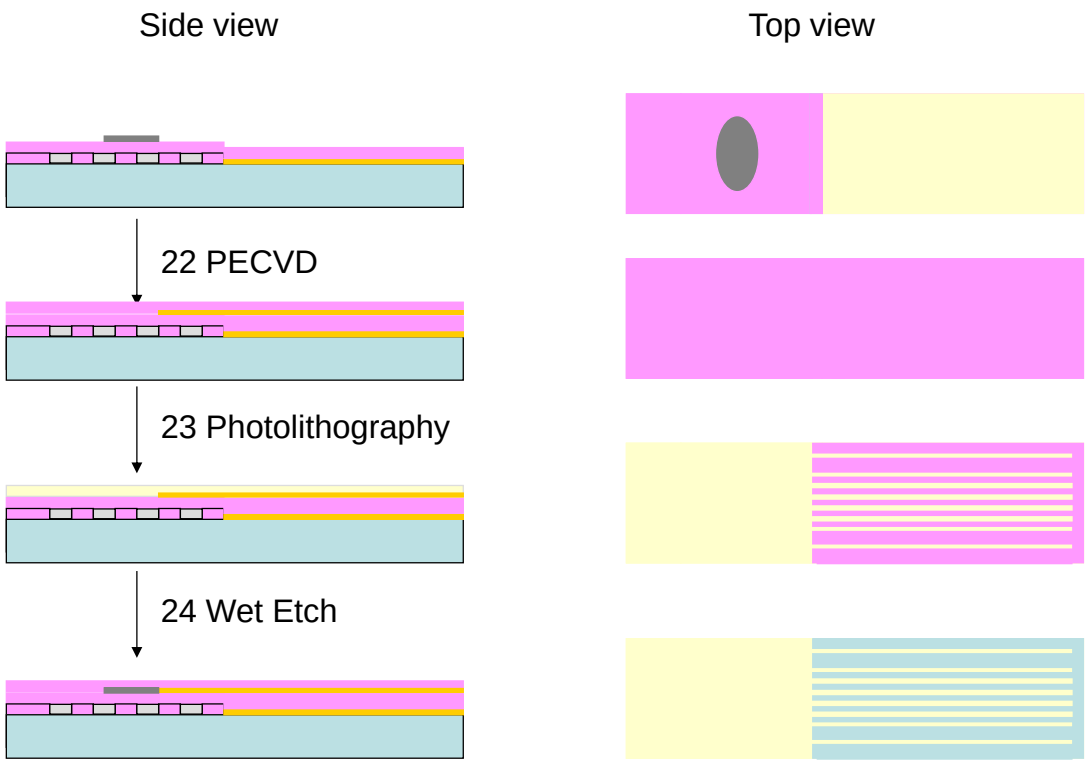

Figure B.7. Schematic of the process flow for the deposition of the second silicon nitride barrier layer. Both side and top views are provided.

Step 28. Lift off of the resist removed the excess metal deposited by the PVD process, leaving metal in the desired location.

B.2.9. Deposition of Metal Oxide Catalyst Layer (Figure B.9)

Step 29. The pattern for the metal oxide catalyst was created by the openings in photoresist SC1827 and the appropriate clear-field mask #9.

Step 30. For deposition of the metal oxide catalyst layer an RF sputtering method will be employed as opposed to PVD. The area of the metal oxide is identical to the area of the platinum RTD.

Step 31. Lift off of the resist removed the excess metal deposited by the PVD process, leaving metal in the desired location.

Step 32. After deposition of the catalyst layer, a thick layer of photoresist was applied to the topside of the wafer to preserve the devices during shipping, milling, and dicing. The resist layer was easily removed once the diced chips were returned.

B.2.10. Shipping, Dicing, and Wire-bonding (Figure B.10)

Step 33. The wafer(s) were shipped to Cidra Technologies, LLC for milling & dicing.

Step 34. Milling was done to thin the device from the end of the serpentine heater out to the end of the cantilever. Thinning results in a significant improvement in device temporal response to analyte gas stream composition.

Step 35. Wire bonding will be done in-house onto a specially designed package.

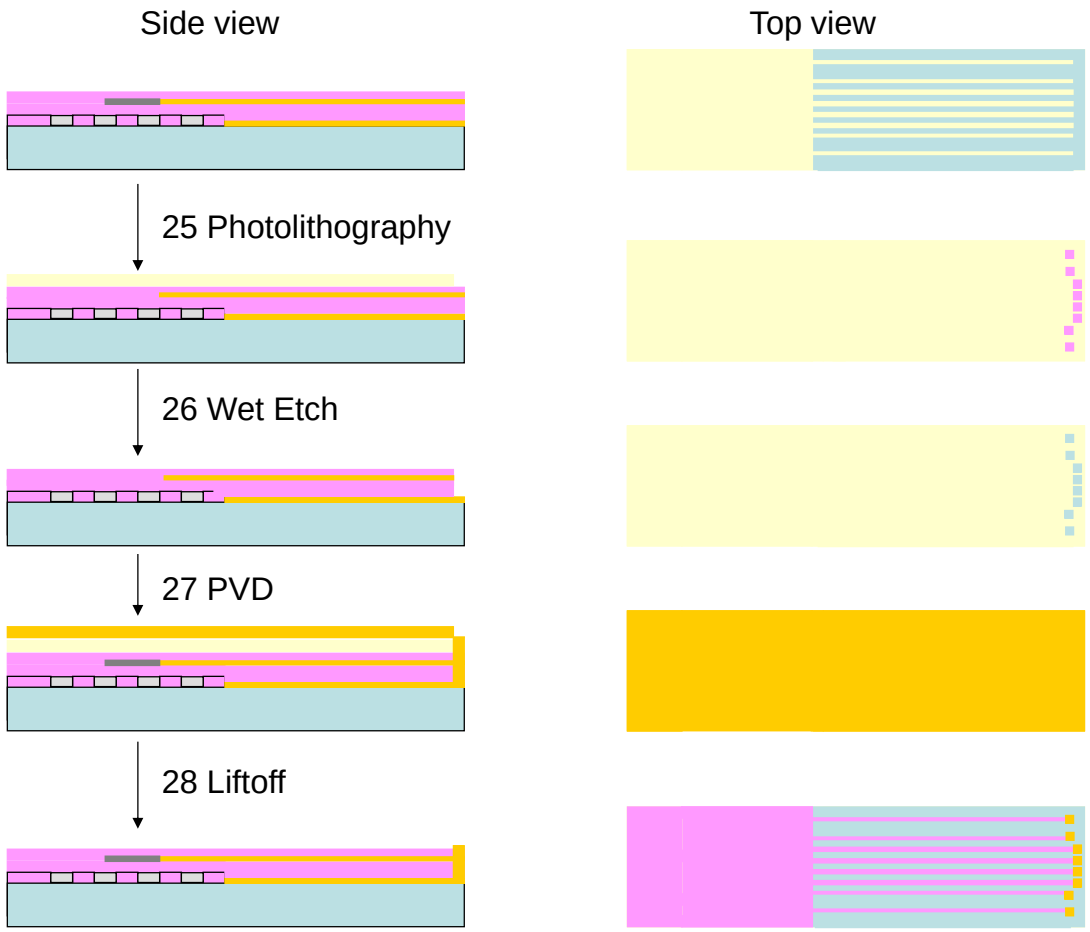

Figure B.8. Schematic of the process flow for the deposition of the gold wire bonding pads. Both side and top views are provided.

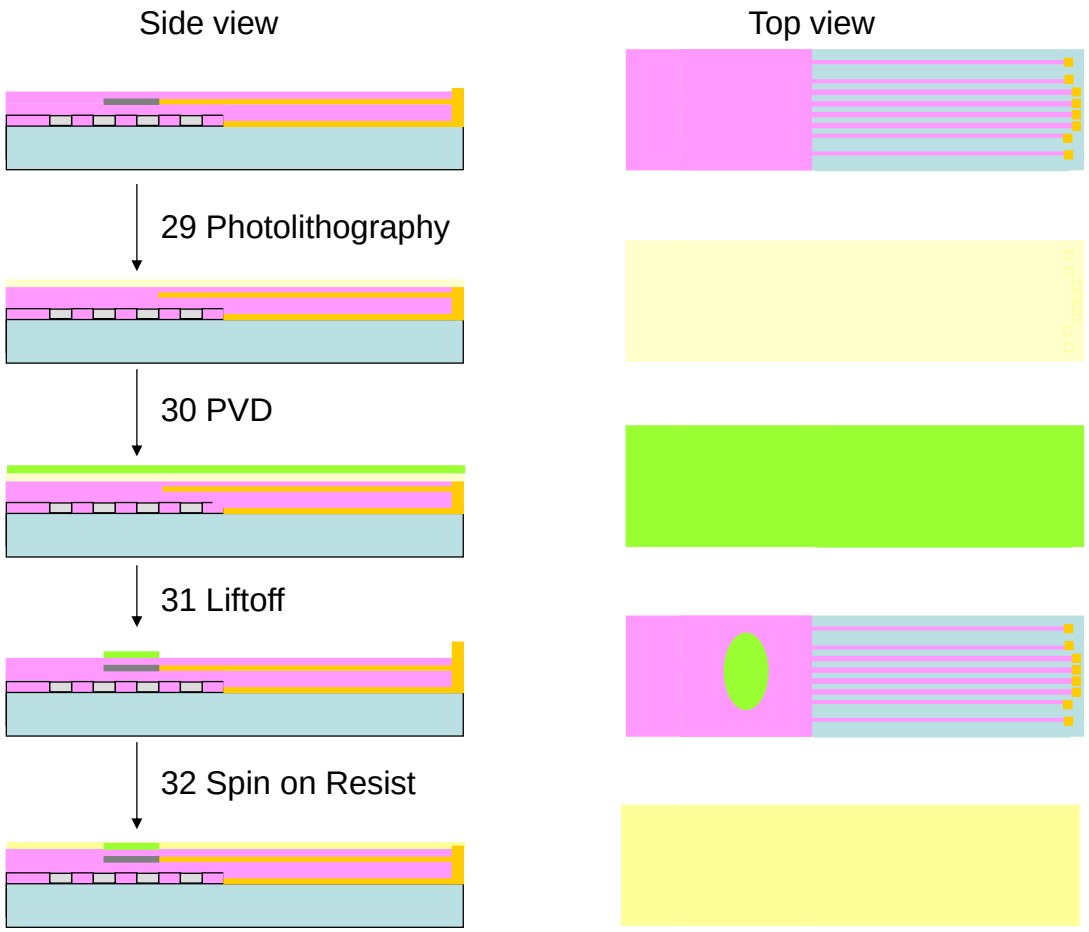

Figure B.9. Schematic of the process flow for deposition of the metal oxide catalyst layer by sputtering. Both side and top views are provided.

Figure B.10. Schematic of process flow for deposition of photoresist protective layer for shipping and dicing. Both a side and top view is provided.

B.3. Necessary Modifications to the Initial Process Flow for Prototype #1

B.3.1. Photolithography Processing

Initially photoresist AZ4260 was chosen for the initial Si_xN_y layer patterning. Based on the feature sizes for the Si_xN_y mesas, this resist is not optimal. Instead, photoresist SC1827 was used. This resist was used for all processing steps, including the protective layer prior to shipment after the wafers were completed. In addition to a change in resist, both the developer and stripper were changed accordingly. For the developer, MF-319 and MF-341 were compared and MF-319 was deemed optimal. For the stripper, sonication in acetone proved to be sufficient for removal of excess resist.

Extreme difficulty was encountered during processing for the first metallization step. Multiple steps were taken in an attempt to pinpoint the issue in the process. To verify that there was complete development of the resist, profilometry was employed. An additional process step was added and performed in the RIE. The "Descum" process step aids in the removal of residual resist after developing as well as any other contaminants that may be preventing metal for adhering to the wafer surface. Additionally, a new titanium target was melted to be sure that contamination in the ingot was not responsible for the lack of adhesion. Successful deposition and lift-off was acheived only when pretreatment of the wafer with hexamethylsilazane (HMDS) was intentionally omitted. HMDS is a commonly used covalent linker for photoresist on silicon and gallium arsenide wafers. Based on this discovery, HMDS was not used for any of the metallization process steps.

B.3.2. Nickel Serpentine Heater Deposition

Upon deposition of nickel using the electron beam evaporator, the wafer was heated to high and the resist baked onto the surface. Excessive cleaning in acetone and numerous Descum runs in the RIE did not remove the residual resist. Because of this, a custom made cooling plate was implemented in order to keep the surface of the wafer cool. Upon deposition of the nickel serpentine using the cooling plate, resist was successfully removed with acetone alone. For all depositions of a high melting temperature metal, the cooling plate was employed to ensure that resist could be removed fully from the surface.

B.3.3. Etching of the Silicon Nitride Barrier Layers

Originally, the Georgia Tech Cleanroom staff limited the use of the RIE based on metals exposed on the wafer. Potential sputtering of the metal within the chamber would contaminate the tool for the next user. Upon looking into the gases used for the Si_xN_y etch; sputtering of the metals on the surface would not occur. Specifically, fluorine gas is used in the recipe and it will not sputter gold. Therefore, a dry etch could be employed as opposed to the BOE wet etch.

B.3.4. RTD Deposition

Originally, platinum was to be deposited for the RTD sensing unit based on the thermal properties. The boiling point of platinum is 3825 °C; much higher than the nickel (2732 °C) which previously presented a problem with excessive heating of the wafer. The cooling plate designed for nickel deposition was used to test platinum deposition, but the degree of cooling was not enough to prevent photoresist from baking onto the surface. In

addition to the photoresist, platinum was baked onto the wafer. Based on these results, nickel was chosen for the RTD sensing unit instead.

B.3.5. Annealing

The original protocol called for an annealing step after deposition of wiring to be sure that electrical contacts were made and there weren't any disconnects in the metal layers Annealing was performed in a rapid thermal processor (RTP) which is the tool typically used to heat silicon wafers to a high temperature. Upon performing RTP under a nitrogen environment for 2 minutes at 700 °C (included a ramp up period from 0 °C). Inspection of the wafer post annealing revealed that the Si_xN_y layers were cracked and the surface of the metals appears to have roughened. Figure B.11 depicts optical images of the features on the wafer surface. It is clear that an annealing step is not plausible based on the effect the high amount of heat has on the materials on the wafer surface. The purpose of for annealing the materials was to ensure electrical contacts, however resistance measurements obtained without annealing the layers provided good results so this step was removed from the process all together. The substrate heating during the nickel deposition most likely acted as an annealing step and reduced the disconnects within the metal layers.

B.3.6. Gold Bonding Pads

Wet chemical etching of the Si_xN_y to release the underlying gold for stress relief and to provide regions for the bonding pads was problematic. The etch rate for BOE through Si_xN_y can be as slow as 50 Å/min so the wafer was submerged in the solution and checked periodically to determine if the etch was completed. The BOE would not have affected the underlying gold if the wafer was left in the etchant for too long. Figure B.12

shows a wafer following BOE etching for 30 minutes. It is clear in the optical images that the resist partially delaminated during the process exposing regions of the pattern to etchant (see red arrows superimposed on the images). The underlying Ni heater is no longer isolated from the RTD. The fact that the delamination is limited to regions adjacent to patterns suggests that loss of adhesion of the resist is localized and not a result of thermally-induced stress that accompanies the BOE process. If thermal stress or pinhole defects in the resist were the cause of failure during the etch process, we would anticipate more widespread damage. The Georgia Tech Cleanroom staff were consulted on the issue, and permission was granted to perform the etch in the RIE, as the gold would not sputter in the fluorine gas environment.

In addition to a revised etch process for the gold bonding pads, and additional alignment was implemented to be sure gold was deposited precisely in the correct region. Once the Si_xN_y etch was completed, the resist was removed and the wafer was realigned with the same mask. During the etch process, the developed features may have altered slightly in shape and size resulting in gold deposition in unwanted areas. The additional alignment avoids this issue.

B.3.7. Protective Resist Coating

Originally SU-8 was chosen as the protective coating during shipment and dicing. However, this resist is difficult to remove from a surface without harming the features underneath. Additionally, the resist may put stress on the wafer and possibly cause it to bend. For these reasons, SC1827 was chosen instead. At a thickness of 2.5 μm, it should provide the necessary protection for shipment and dicing.

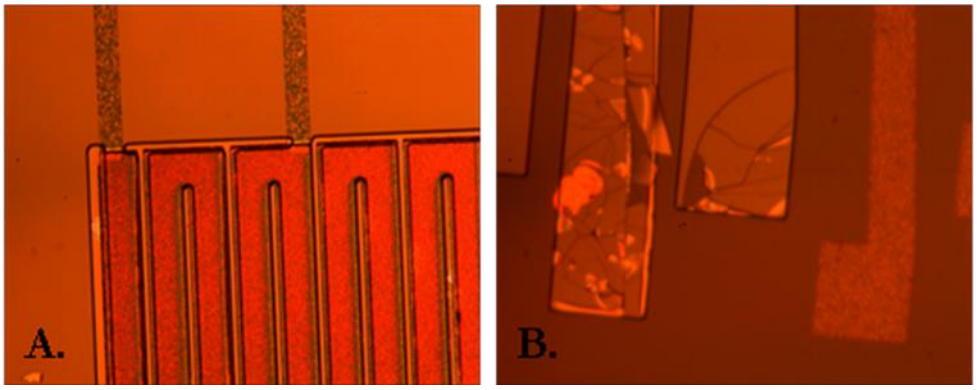

Figure B.11. Optical micrographs following RTP annealing. A depicts the heater region where both the gold leads and the nickel serpentine heater.. B presents the Si_xN_y mesas following the anneal step. It is clear that all the materials on the wafer surface appear to have been negatively affected by the anneal.

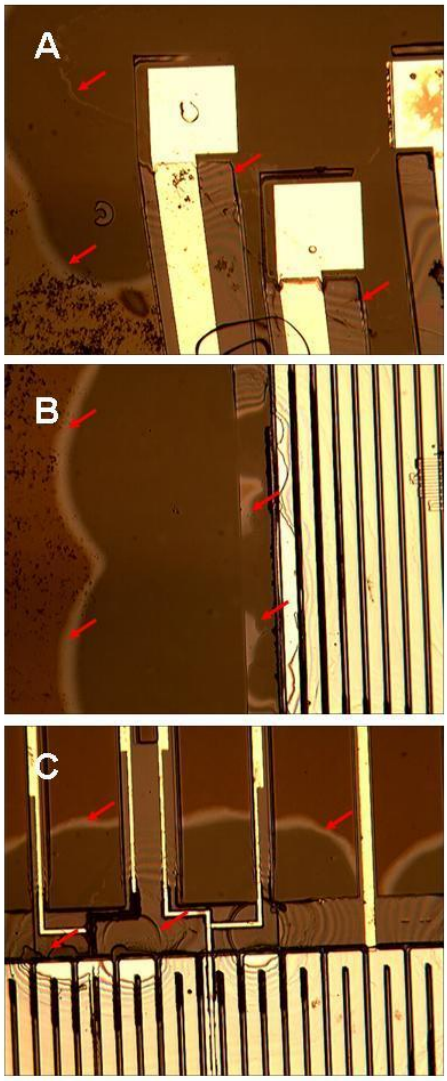

Figure B.12. Optical micrographs following BOE. A depicts the area encompassing the wire bonding pads; B depicts area adjacent to Au interconnects; C depicts area adjacent to serpentine heater. Red arrows have been added to emphasize regions where the BOE created defects.

A.4. Revised Prototype #1 Initial Process Flow

The substrates used were C-axis, 50.8 mm diameter and 300-350 μm thick sapphire wafers purchased from Wafer World, Inc. (West Palm Beach, FL). Wafers were RCA cleaned to remove residual organic and inorganic contaminants from the surface prior to any processing.

For brevity, "photolithography patterning" includes the following process steps: spin-coat photoresist; soft-bake; mask alignment; exposure; hard bake; and develop resist. Photolithography patterning was carried out using a Karl Suss MA-6 Mask Aligner (Suss Microtec, Waterbury Center VT) for all steps. Patterning was completed using Microposit SC 1827 positive resist and Microposit MF®-319 developer (Shipley Company Inc., Marlborough MA). The resist was spun to a thickness of 2.5 μm, followed by a 5 minute soft bake in a 150 °C oven, exposed using a 405 nm UV lamp source on the aligner, developed and hard baked for 10 minutes in 150 °C oven prior to the next step**.**

B.4.1. Deposition of Silicon Nitride Mesas for micro-Heater

Initially, 1.05 μm of Si_xN_y was deposited using a Unaxis PECVD (OC Oerlikon Corporation, Pfaffikon, Switzerland). A low-stress recipe was created using the set points and parameters displayed in Table B.1. Both helium and nitrogen gases were used to control the level of stress on the sapphire wafer. Since the deposition rate of Si_xN_y in this tool is ~100 nm/min, the deposition was run for 105 minutes to ensure adequate deposition of material (Note: This recipe was used for all Si_xN_y depositions). The thickness and uniformity was verified using a Nanospec 3000 refractometer

Table B.1. Process parameters used for silicon nitride deposition in the UNAXIS PECVD, silicon nitride etching and O_2 plasma cleaning in the Vision RIE.

Silicon Nitride Deposition	
Settings	
Heat Exchange	60 °C
Wat Low	250 W
Pressure	1100 Torr
RF Power	60 W
Reflectance	0
DC Bias	7
SiH_4 gas	200 sccm
NH_3 gas	8 sccm
He gas	560 sccm
N_2 gas	150 sccm

Silicon Nitride Etch	
Settings	
RF Power	350 W
Ar gas	20 sccm
O_2 gas	6 sccm
CHF_3 gas	40 sccm

O2 plasma cleaning	
Settings	
RF Power	350 W
O_2 gas	50 sccm

(Nanometrics, Inc., Milpitas CA)**.** A total of 5 measurements were taken for each wafer to evaluate deposit uniformity across the wafer. A plot of the average thicknesses as well as the standard deviation is provided in Figure B.13 for a batch of 8 wafers. Patterning step #1 was completed using the mask pattern presented in Figure B.14. Upon completion of patterning, Si_xN_y was dry etched in a Vision 320 reactive ion etch (RIE) plasma system (Advanced Vacuum AB, Lomma Sweden) using the parameters presented in Table B.1. Since the etch rate in this tool for Si_xN_y is 500 Å/min, a 15 minute etch was required to pattern the SixNy.. This was the tool and recipe used for all Si_xN_y etching. Remaining resist was removed through sonication in acetone for 15 minutes followed by O_2 plasma cleaning in the Vision RIE using the parameters displayed in Table B.1. Sonication in acetone followed by O_2 plasma cleaning was used to lift-off remaining resist for all patterning steps unless otherwise noted. The step height of the Si_xN_y was measured using a P15 OF profilometer (KLA Tencor, Milpitas CA) to be 1.05 μm. This profilometer was used to measure all step heights for both deposited and etched layers throughout the process flow. Figure B.15 presents optical micrographs of the initial Si_xN_y mesa on the sapphire wafer surface. Images presented include the barriers for the serpentine heater (photolithography step #2), the region for RTD/gold lead connections (photolithography steps #5 and #6), as well as the region where the gold bonding pads will be deposited (photolithography step #7).

B.4.2. Creation of Wiring for micro-Heater

Photolithography patterning step #2 was completed using the process parameters described previously (see Figure B.16 for the mask pattern used). After successful patterning, a titanium adhesion layer was deposited at 1 Å/sec (recipe deposition

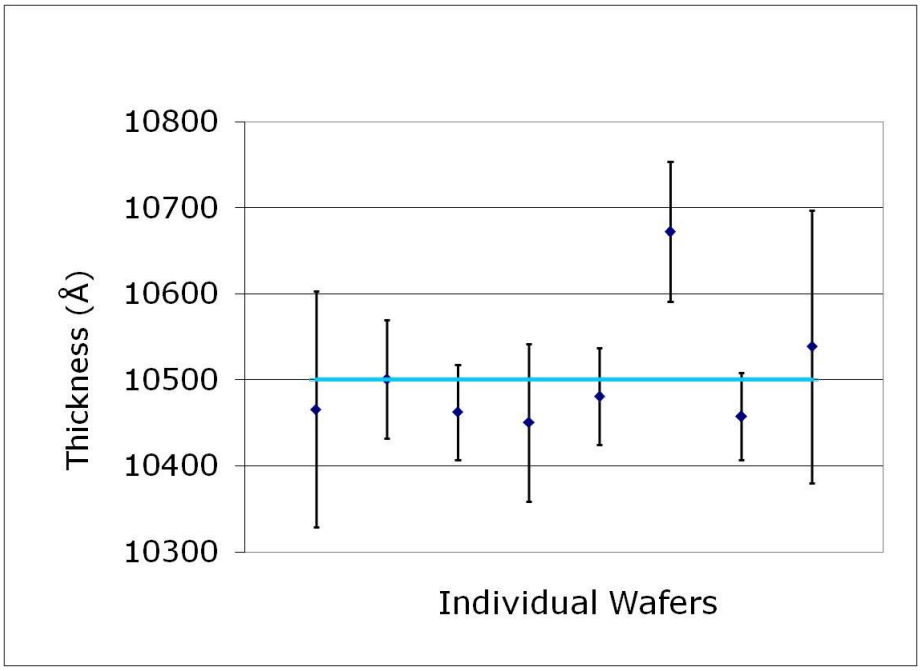

Figure B.13. Plot of the average thicknesses after PECVD deposition of silicon nitride using the recipe presented in Table B.1. Error bars are included to depict the deviation from the average for a total of 5 measurements. The line represents the thickness expected from the length of deposition.

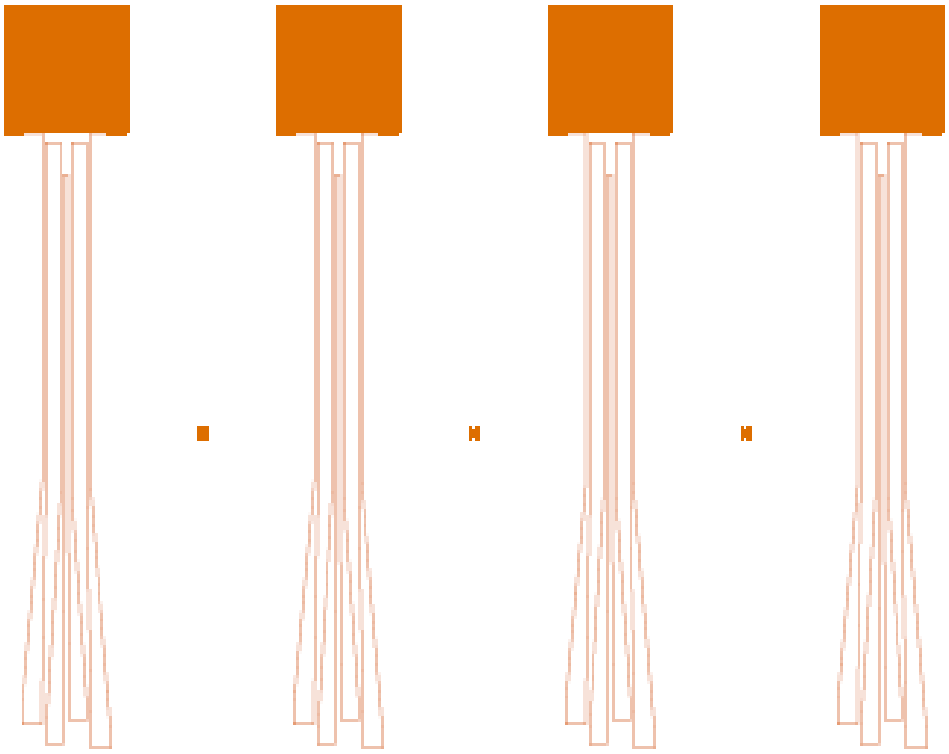

Figure B.14. Feature details for a single chip, representative of the mask used during photolithography pattering step #1, deposition of the Si_xN_y mesas.

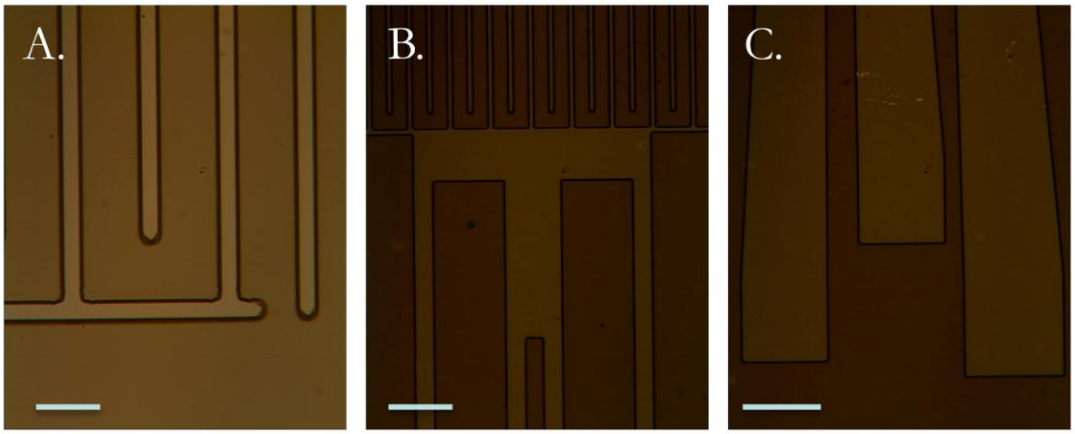

Figure B.15. Optical micrographs of the sensor following etching of the silicon nitride to create the heater pattern. A depicts is the heater region barriers, B presnets the region where the RTD connects will be deposited in phtolithography step #5, and C depicts where the gold bonding pads will be located. The scale bar denotes 50 µm in A and B and 250 µm in C.

thickness 500 Å) followed by successive deposition of gold at 3 Å/sec (recipe deposition thickness 4000 Å) in a CVC-SC5000 electron beam evaporator (Condensed Vacuum Corp., Rochester NY) at a base deposition pressure of 1 x 10^{7} Torr (Note: Unless otherwise noted, all metallization steps were carried out in this tool). Excess metal was stripped from the surface using the method previously described. The step heights of each layer were measured to be ~3800 Å. Figure B.17 presents optical micrographs of the gold leads following deposition and lift-off. Both the point of contact with the serpentine heater (photolithography step #3) and the bonding pad regions are included.

A.4.3. Deposition of Nickel micro-Heater

Photolithography patterning step #3 was completed using the process parameters described previously (see Figure B.18 for the mask pattern used). After successful patterning, nickel was deposited at 2 Å/sec (recipe deposition thickness 1.1 μm) using a custom fit cooling plate at a base pressure of 1 x 10^{-7} Torr. Excess metal and resist was removed from the surface using the method described previously with an additional 10 minutes of sonication in acetone and additional 15 minutes of O_2 plasma cleaning. The step height of the nickel serpentine was measured to be 0.928 μm. Resistivity measurements were obtained inside the cleanroon, to verify electrical contact was made between the gold and nickel serpentine. Values ranging from 150 to 200 Ω were measured for both inner and outer gold leads, respectively. Figure B.19 presents optical micrographs showing the serpentine heater after deposition of the nickel.

B.3.4. Deposition of Silicon Nitride Barrier Layer #1

Using the low stress recipe previously described, 1.05 μm layer of Si_xN_y was deposited over the entire wafer. Photolithography patterning step #4 was completed using the

Figure B.16. Feature details for a single chip, representative of the mask used during photolithography pattering step #2, deposition of the serpentine heater gold leads.

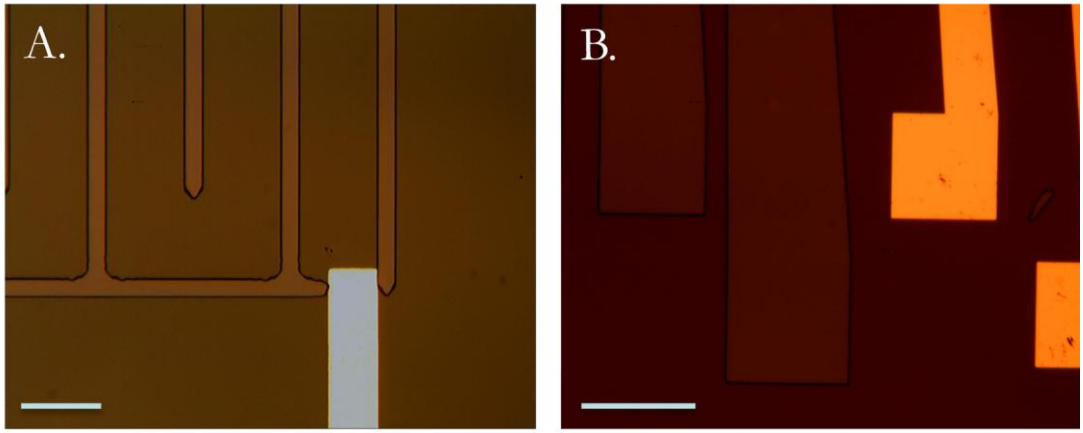

Figure B.17. Optical micrographs of the gold serpentine heater leads. A depicts the contact area of one of the leads (white) for the serpentine heater to be deposited between the Si_xN_y (orange). The scale bar depicts 50 µm. B depicts the wire bonding pads at the bottom of the device (orange) as well as the Si_xN_y mesa (brown). The scale bar depicts 250 µm. In both images the dark brown in the base sapphire substrate.

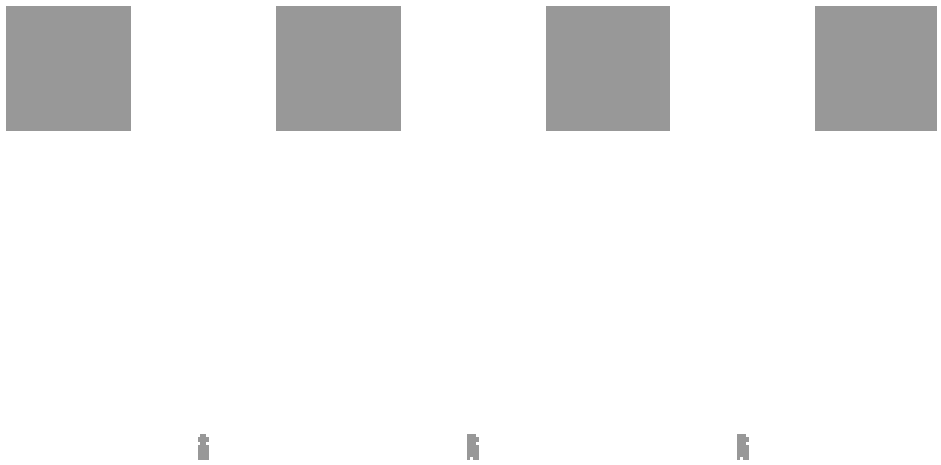

Figure B.18. Feature details for a single chip, representative of the mask used during photolithography pattering step #3, deposition of the nickel serpentine heater.

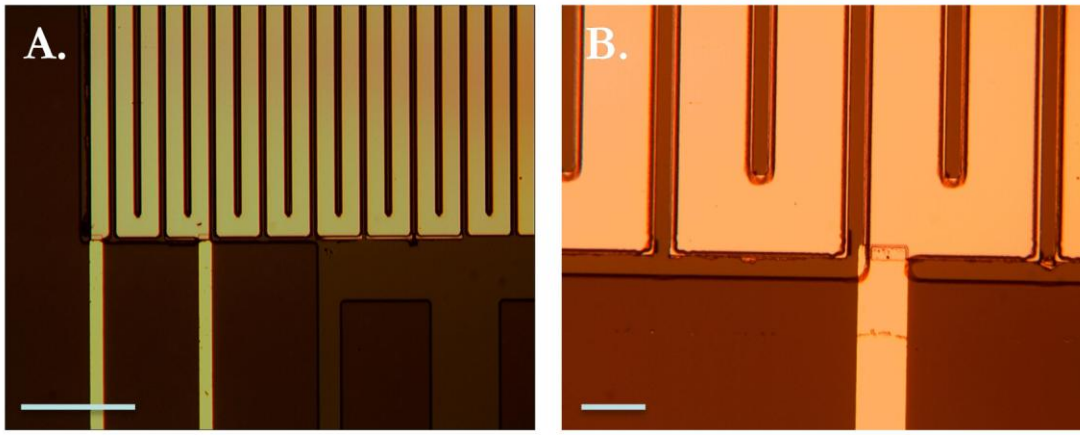

Figure B.19. Image A is an optical micrograph depicting a portion of the Ni serpentine heater pattern. Image B is a higher magnification image of the Au/Ni contact made between a gold lead and the serpentine heater. The scale bar in A denotes 250 μm and in B denotes 50 μm.

process parameters described previously using the mask pattern presented in Figure B.20. Following patterning, Si_xN_y was etched in the same fashion as the mesas using the Vision RIE. Excess photoresist was stripped from the wafer and the step height was measured to be 1.04 μm. Figure B.21 presents optical micrographs of the first Si_xN_y barrier layer. Both the serpentine heater and bonding pad regions are presented.

B.3.5. Creation of Wiring for RTD

Photolithography patterning step #5 was carried out using the resist and developer previously described (see Figure B.22 for the mask pattern used). Post patterning, a titanium adhesion layer was deposited at 1 Å/sec (recipe deposition thickness 500 Å) followed by successive deposition of gold at 3 Å/sec (recipe deposition thickness 3800 Å) at a base pressure of 1 x 10^6 Torr to create the gold leads required for wiring to the RTD. The excess metal and photoresist were removed from the surface and the step height was measured to be ~3500 Å. Figure B.23 presents optical micrographs following deposition of the gold lead connections for the RTD circuit. Both the region where connections with the RTD are to be made and the bonding pads are presented.

B.4.6. Deposition of Nickel RTD

Photolithography patterning step #6 was carried out using the resist and developer described in previous steps. See Figure B.24 for the mask pattern used. After successful patterning, titanium was deposited at 1 Å/sec (recipe deposition thickness 300 Å) followed by successive deposition of nickel at 2 Å/sec (recipe deposition thickness 4000 Å) using a custom made cooling plate at a base pressure of 1 x 10^7 Torr to fabricate the RTD. Excess metal was removed from the surface using the method previously described, with an additional 10 minutes of sonication in acetone. Profilometry results

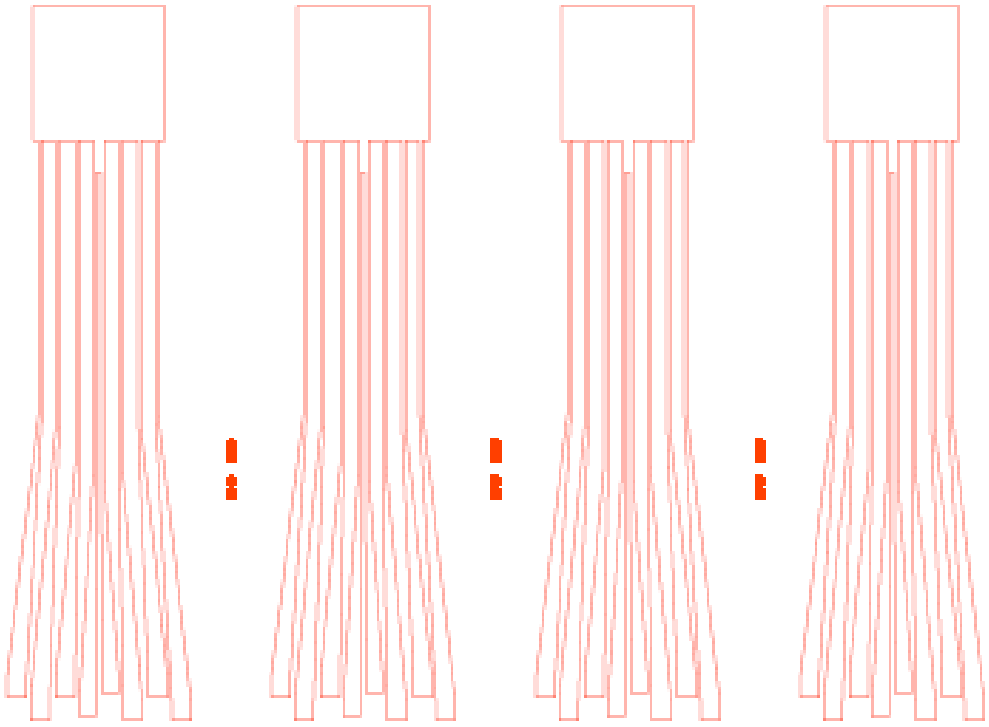

Figure B.20. Feature details for a single chip, representative of the mask used during photolithography pattering step #4, deposition of the Si_xN_y barrier layer.

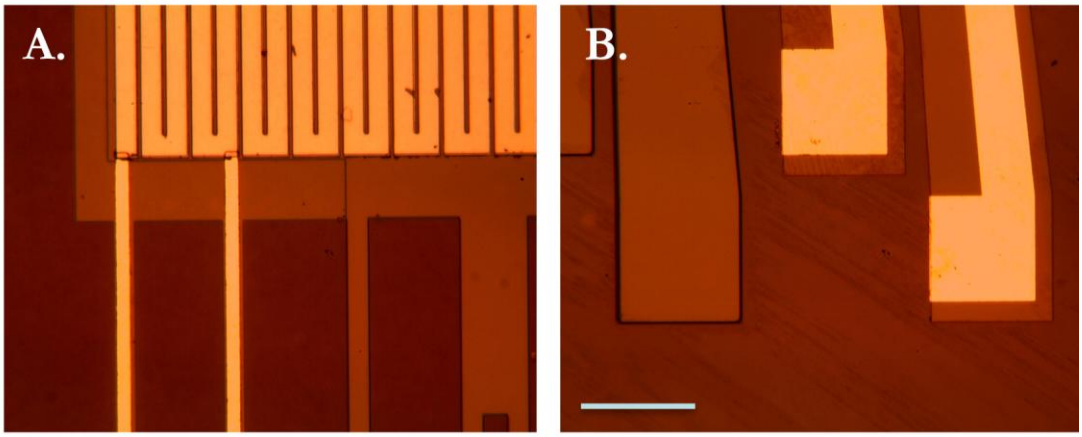

Figure B.21. Optical micrographs obtained following deposition of the first silicon nitride barrier layer over the serpentine heater (A) and gold leads (B). In the images, the yellow represents the deposited metals, the orange is the Si_xN_y, and the brown is the sapphire base substrate. The scale bar denotes 250 μm for both images.

Figure B.22. Feature details for a single chip, representative of the mask used during photolithography pattering step #5, deposition of the wiring for the RTD.

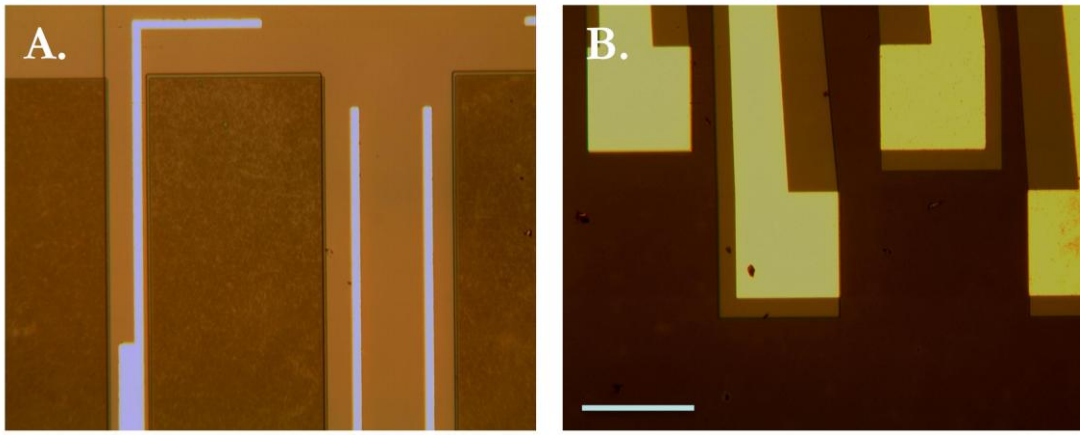

Figure B.23. Optical micrograph of the gold leads (A) interconnecting the thermal sensor to the gold bonding pads (B). The scale bar denotes 250 μm for both images.

indicated the RTD thickness was 2500 Å. Figure B.25 presents optical micrographs following deposition if the nickel RTD. Two images were overlaid to allow for a high resolution photo of a larger region. Both the RTD as well as the nickel/gold lead connections are presented.

B.4.7. Deposition of Silicon Nitride Barrier Layer #2

A 1.0 μm thick layer of Si_xN_y was deposited using the same low stress recipe used previously. Upon completion of the deposition, photolithography patterning step #7 was completed (see Figure B.20 for the mask pattern used). The Si_xN_y layer was etched in the Vision RIE using the recipe previously described to create the second Si_xN_y barrier layer. Excess photoresist was removed and the step height of this layer was measured to be 1.08 μm. Figure B.26 presents optical micrographs of both the serpentine heater and bonding pad regions after deposition of the second Si_xN_y barrier layer.

B.4.8. Deposition of Gold bonding Pads

Photolithography patterning step #8 was completed using the resist and developer previously described (see Figure B.27 for the mask pattern used). Post patterning, Si_xN_y was etched in the Vision RIE. The run was carried out at 15 minute intervals followed by profilometry to monitor the progress of the etch towards the gold leads, for a total of 60 minutes. Upon etch completion the resist was removed using sonication in acetone followed by a 15 minute O_2 plasma clean. The wafer was then re-aligned and patterned for the gold deposition. Gold was deposited at 3 Å/sec (recipe total deposition thickness of 8000 Å) at a base pressure of 1×10^{-6} Torr. The excess metal and photoresist were removed from the surface and the thickness of the deposited gold was measured to be 3500 Å, resulting in a total gold bonding pad thickness of 7500 Å for the outer four leads

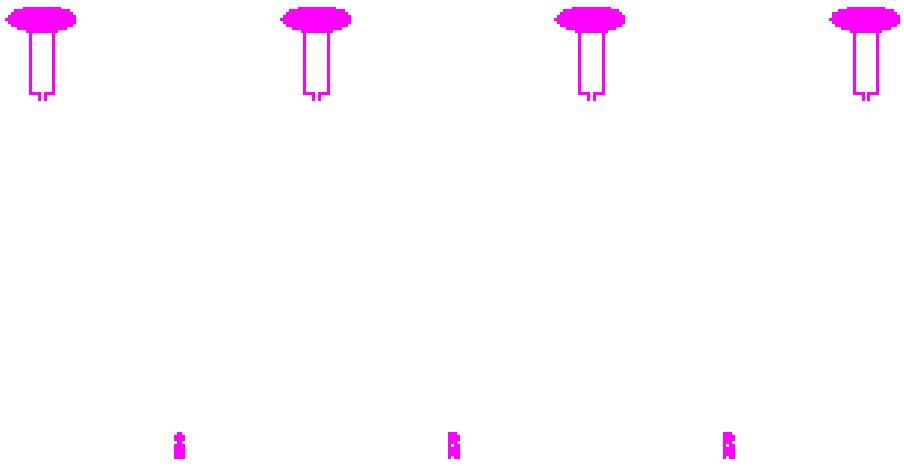

Figure B.24. Feature details for a single chip, representative of the mask used during photolithography pattering step #6, deposition of the nickel RTD

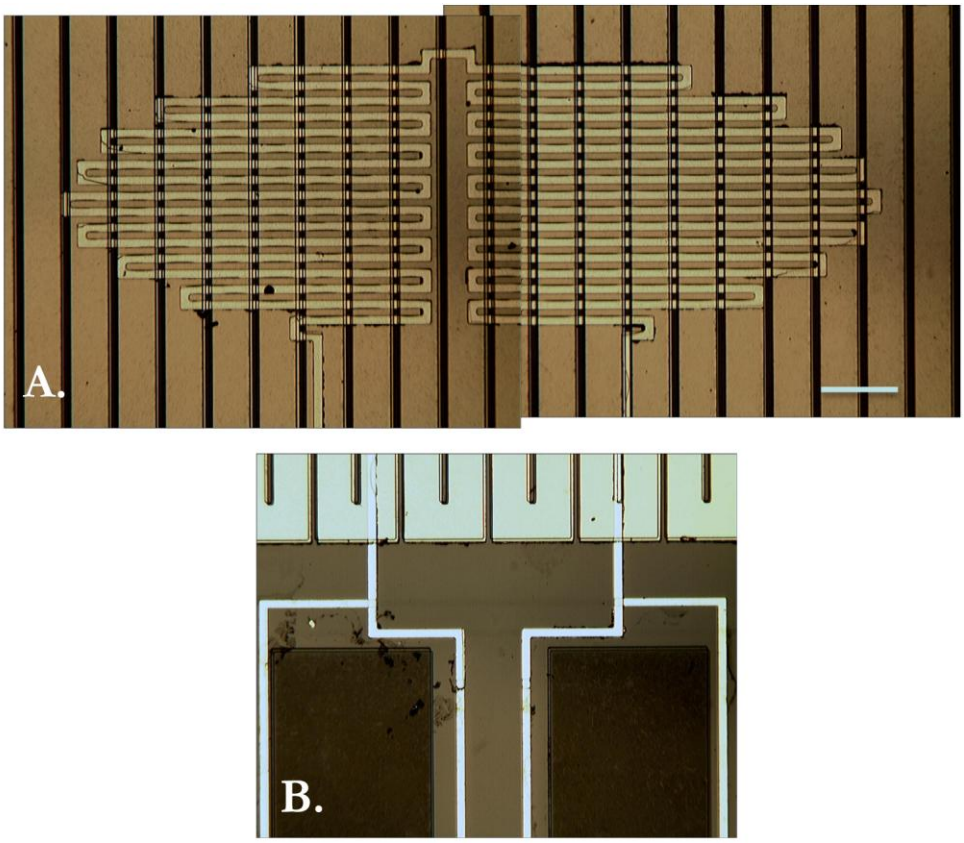

Figure B.25. Optical micrograph following deposition of Ni RTD (A). Note that two images are overlaid to provide an image of a wider area of the device. Optical micrograph of the gold and nickel connections for the RTD circuit (B). The scale bare denotes 100 μm for both images.

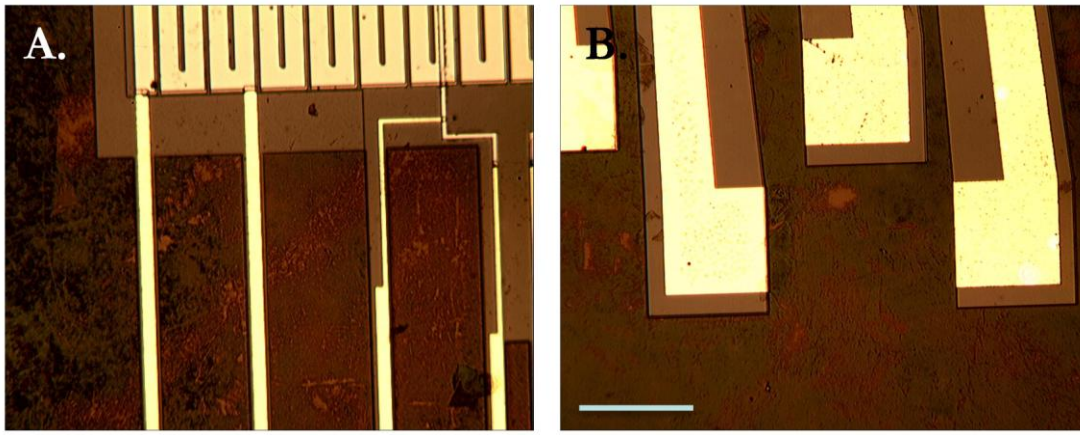

Figure B.26. Optical micrograph following deposition of the second silicon nitride barrier layer. A depicts the base of the heater region showing the gold connections leading to the bonding pads shown in B. The scale bare denotes 250 μm for both images.

(heater connections) and 7000 Å for the inner four leads (RTD sensor connections). Figure B.28 presents optical micrographs of the gold bonding pads after etching away Si_xN_y and depositing gold.

B.4.9. Deposition of Metal Oxide Active Catalyst - Copper

Photolithography patterning step #9 was completed using the appropriate photoresist and developer previously described (see Figure B.29 for the mask pattern used). For the first prototype, a metal oxide catalyst of copper was chosen. Once patterned, the copper catalyst was deposited at 3 Å/sec (final recipe deposition thickness of 4000 Å) at a base deposition pressure of $1x10^{-6}$ Torr. Excess metal and photoresist was stripped from the surface using and the step height of the catalyst was measured to be 3000 Å. Figure B.30 presents an optical micrograph of the copper catalyst post deposition on one of the sensors. Two images were overlaid to allow for a high resolution photo of a larger area.

B.4.11. Preparation for Shipment

To protect the wafer during shipment and the dicing process, Shipley SC1827 photoresist was spun onto the wafer to a final thickness of ~2.5 μm and hard baked for 20 minutes. A photograph of an entire wafer is presented in Figure B.31 prior to shipping the wafer off for dicing. Dicing was carried out to create chips with a single reference sensor and three active catalyst sensors per chip. In addition to cutting the chip out of the wafer, the fingers were thinned.

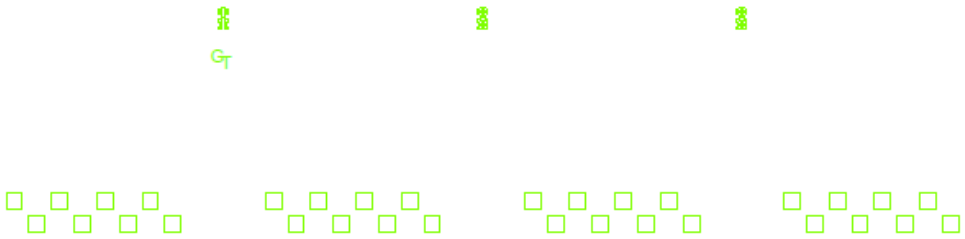

Figure B.27. Feature details for a single chip, representative of the mask used during photolithography pattering step #8.

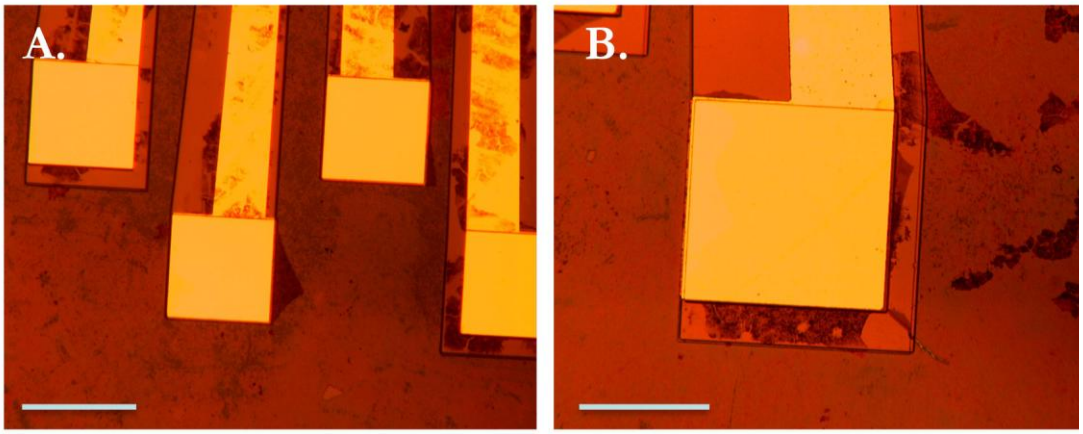

Figure B.28. Optical micrographs of the gold bonding pads following dry etch and gold deposition. A depicts the 4 inner pads and B depicts a zoomed in image up of a single bonding pad. The scale bars denote 250 µm in A and 125 µm in B.

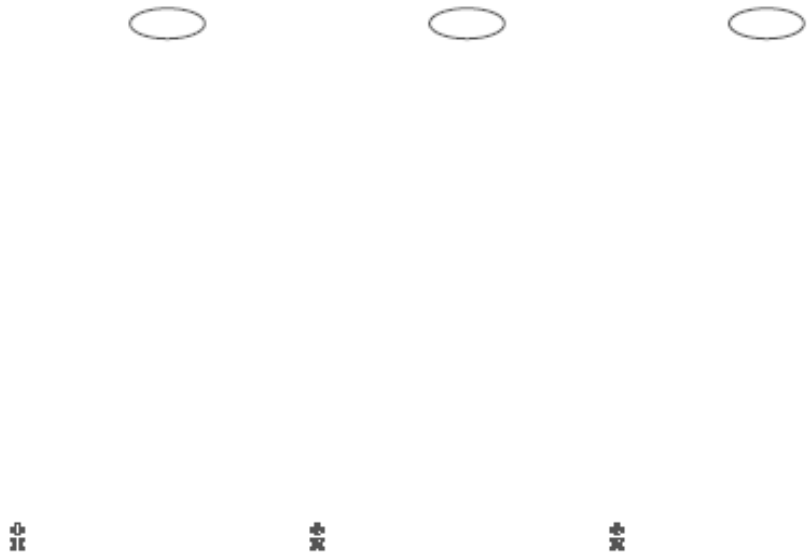

Figure B.29. Feature details for a single chip, representative of the mask used during photolithography pattering step #9, deposition of the active metal oxide catalyst (copper).

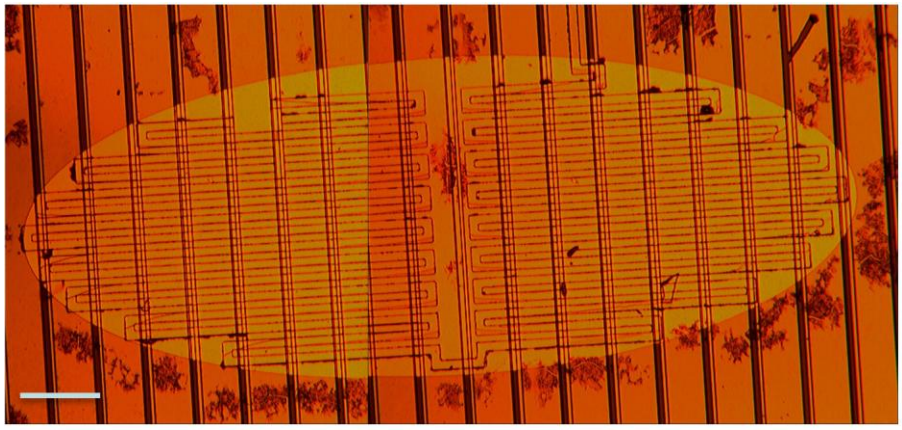

Figure B.30. Optical micrograph of the heater RTD following deposition of the metal catalyst. Note that two images are overlaid to provide a photo of a larger region of the device. The copper is the yellow circle and the nickel serpentine RTD can be seen underneath. The scale bar denotes 100 μm.

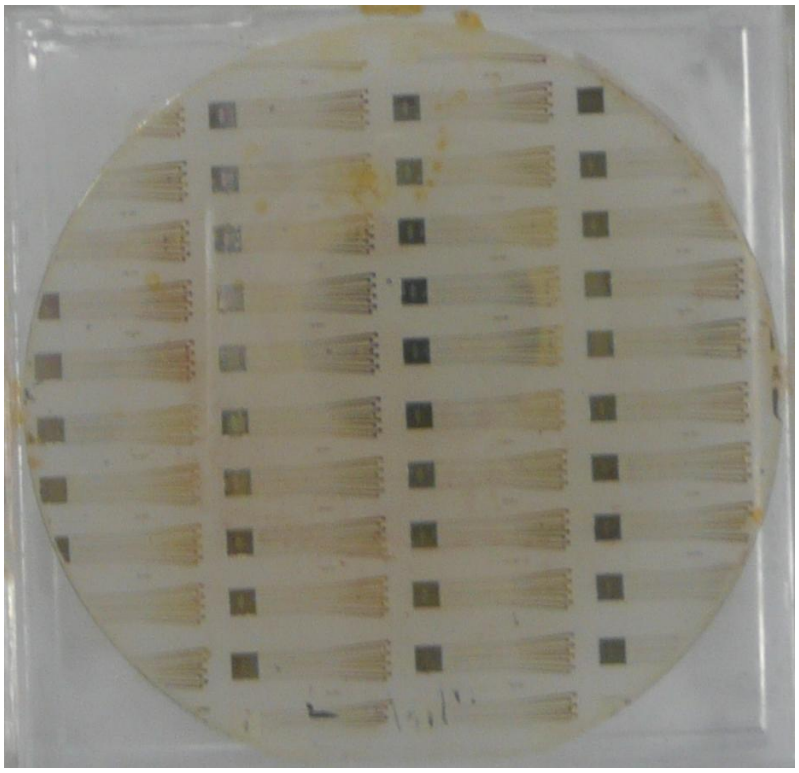

Figure B.31. Photograph of a completed wafer. The devices are clearly visible. Since the photograph was taken prior to shipment for dicing, the yellowish color is due to the protective photoresist layer.

B.5. Prototype #1 Device Testing

Upon examination of the heater units post dicing, the catalyst appears to have been removed during the dicing process. Figure B.32 presents optical micrographs of all four heaters on a single chip. Note that the catalyst no longer appears to be present (see Figure B.28 for a zoomed in image after successful deposition of the catalyst). The reference heater (a.) unit looks identical to the other 3 sensors (b. - d.) where catalyst should have been present. Because of this, devices could not be tested for the intended use as a gas sensor. However, to verify that the process provided functional chips in all other aspects, the electrical contacts were examined. Since the lack of catalyst occurred post dicing, part of the dicing process must have removed the catalyst from the surface. Because of this, dicing will not be used for future prototypes.

B.5.1. Resistance Measurements

Once the chips were diced and wire bonded to the package, they were ready to be tested. Prior to carrying out heating experiments, resistance measurements were taken on all circuits to verify that the proper connections were in place after dicing was completed. Table B.2 through B.4 provides all the measured values for the individual chips. The pin numbers in column 1 correspond to the pin connections outlined in Figure B.34. Upon testing, it was noticed that the RTD circuit was not complete. Specifically, the RTD $Power_{in}$ and RTD $Power_{out}$ addition to RTD $Sense_{in}$ and RTD $Sense_{out}$ were open circuits (see Figure B.34). Based on these results, it was determined that disconnects were present in the RTD serpentine unit. Upon further investigation, it was discovered that the heater region was not flat enough based on the deposition thicknesses for Si_xN_y and the nickel heater; disconnects were occurring at the edges.

Table. B.2. Resistivity measurements for all Chip 1 after dicing and testing. In the table, the pin number corresponds to the pins outlines in Figure B.34 for the wire bonding. An **X** under the resistance reading designates that an open circuit existed.

Chip 1				
Sensor	**Bonding Pad Pin Pairing**		**Resistance Reading (Ω)**	**Circuit**
Reference	61	62	1.1	Heater
Reference	3	4	54.9	Heater
Reference	3	61	107.2	Heater
Reference	4	62	121.1	Heater
Reference	4	61	121	Heater
Reference	3	62	107	Heater
Reference	2	63	**X**	RTD
Reference	1	64	**X**	RTD
Reference	63	64	53.4	RTD
Reference	1	2	66	RTD
Sensor 1	7	15	144.5	Heater
Sensor 1	8	14	117.2	Heater
Sensor 1	7	14	131	Heater
Sensor 1	8	15	131	Heater
Sensor 1	7	8	55.6	Heater
Sensor 1	9	10	48.8	Heater
Sensor 1	12	13	150.4	RTD
Sensor 1	14	15	55.8	RTD
Sensor 1	9	13	**X**	RTD
Sensor 1	10	12	**X**	RTD
Sensor 2	18	25	132	Heater
Sensor 2	19	26	**X**	Heater
Sensor 2	19	25	132	Heater
Sensor 2	18	19	56	Heater
Sensor 2	18	26	**X**	Heater
Sensor 2	20	21	**X**	RTD
Sensor 2	23	24	58.1	RTD
Sensor 2	25	26	**X**	RTD
Sensor 2	20	24	**X**	RTD
Sensor 2	21	23	**X**	RTD
Sensor 3	36	29	149	Heater
Sensor 3	35	30	121	Heater

Table. B.2. Continued

Sensor 3	29	30	58.3	Heater
Sensor 3	29	35	135.2	Heater
Sensor 3	30	36	136	Heater
Sensor 3	35	36	59	Heater
Sensor 3	31	32	150.7	RTD
Sensor 3	34	31	**X**	RTD
Sensor 3	33	32	**X**	RTD
Sensor 3	33	34	185	RTD

Table. B.3. Resistivity measurements for all Chip 2 after dicing and testing. In the table, the pin number corresponds to the pins outlines in Figure B.34 for the wire bonding. An **X** under the resistance reading designates that an open circuit existed.

Chip 2				
Sensor	**Bonding Pad Pin Pairing**		**Resistance Reading (Ω)**	**Circuit**
Reference	4	61	133	Heater
Reference	3	62	109	Heater
Reference	3	4	49.4	Heater
Reference	61	62	49.6	Heater
Reference	3	61	121	Heater
Reference	4	62	120	Heater
Reference	2	63	**X**	RTD
Reference	1	64	**X**	RTD
Reference	1	2	37.9	RTD
Reference	63	64	**X**	RTD
Sensor 1	7	15	136	Heater
Sensor 1	8	14	111	Heater
Sensor 1	7	8	52.2	Heater
Sensor 1	15	8	124	Heater
Sensor 1	15	14	51	Heater
Sensor 1	7	14	123.3	Heater
Sensor 1	9	13	**X**	RTD
Sensor 1	10	12	**X**	RTD
Sensor 1	9	10	**X**	RTD
Sensor 1	12	13	**X**	RTD
Sensor 2	18	26	138	Heater
Sensor 2	19	25	111	Heater
Sensor 2	18	19	64	Heater
Sensor 2	18	25	125	Heater
Sensor 2	18	19	52	Heater
Sensor 2	19	26	126	Heater
Sensor 2	20	24	**X**	RTD
Sensor 2	21	23	**X**	RTD
Sensor 2	20	21	52	RTD
Sensor 2	23	24	62.1	RTD
Sensor 3	29	36	**X**	Heater
Sensor 3	30	35	**X**	Heater
Sensor 3	30	29	58.6	Heater
Sensor 3	31	32	50	Heater

Table. B.3. Continued

Sensor 3	29	35	**X**	Heater
Sensor 3	30	36	**X**	Heater
Sensor 3	31	34	**X**	RTD
Sensor 3	32	33	**X**	RTD
Sensor 3	33	34	**X**	RTD
Sensor 3	35	36	**X**	RTD

Table. B.4. Resistivity measurements for all Chip 3 after dicing and testing. In the table, the pin number corresponds to the pins outlines in Figure B.34 for the wire bonding. An **X** under the resistance reading designates that an open circuit existed.

Chip 3				
Sensor	**Bonding Pad Pin Pairing**		**Resistance Reading (Ω)**	**Circuit**
Reference	4	61	**X**	Heater
Reference	3	62	**X**	Heater
Reference	3	4	49	Heater
Reference	61	62	**X**	Heater
Reference	3	61	**X**	Heater
Reference	4	62	**X**	Heater
Reference	2	63	**X**	RTD
Reference	1	64	**X**	RTD
Reference	1	2	**X**	RTD
Reference	63	64	**X**	RTD
Sensor 1	7	15	133.2	Heater
Sensor 1	8	14	114.2	Heater
Sensor 1	7	8	50.4	Heater
Sensor 1	15	8	121.3	Heater
Sensor 1	15	14	56	Heater
Sensor 1	7	14	126	Heater
Sensor 1	10	12	**X**	RTD
Sensor 1	9	10	**X**	RTD
Sensor 1	12	13	**X**	RTD
Sensor 2	18	26	**X**	Heater
Sensor 2	19	25	109.4	Heater
Sensor 2	18	19	**X**	Heater
Sensor 2	18	25	**X**	Heater
Sensor 2	18	19	**X**	Heater
Sensor 2	19	26	123.5	Heater
Sensor 2	20	24	**X**	RTD
Sensor 2	21	23	**X**	RTD
Sensor 2	20	21	**X**	RTD
Sensor 2	23	24	**X**	RTD
Sensor 2	25	26	52.4	Heater
Sensor 3	29	36	**X**	Heater
Sensor 3	30	35	**X**	Heater
Sensor 3	30	29	52	Heater
Sensor 3	31	32	73.3	Heater

Table. B.4. Continued

Sensor 3	29	35	**X**	Heater
Sensor 3	30	36	**X**	Heater
Sensor 3	31	34	1.3	RTD
Sensor 3	32	33	68	RTD
Sensor 3	33	34	**X**	RTD
Sensor 3	35	36	53.3	RTD

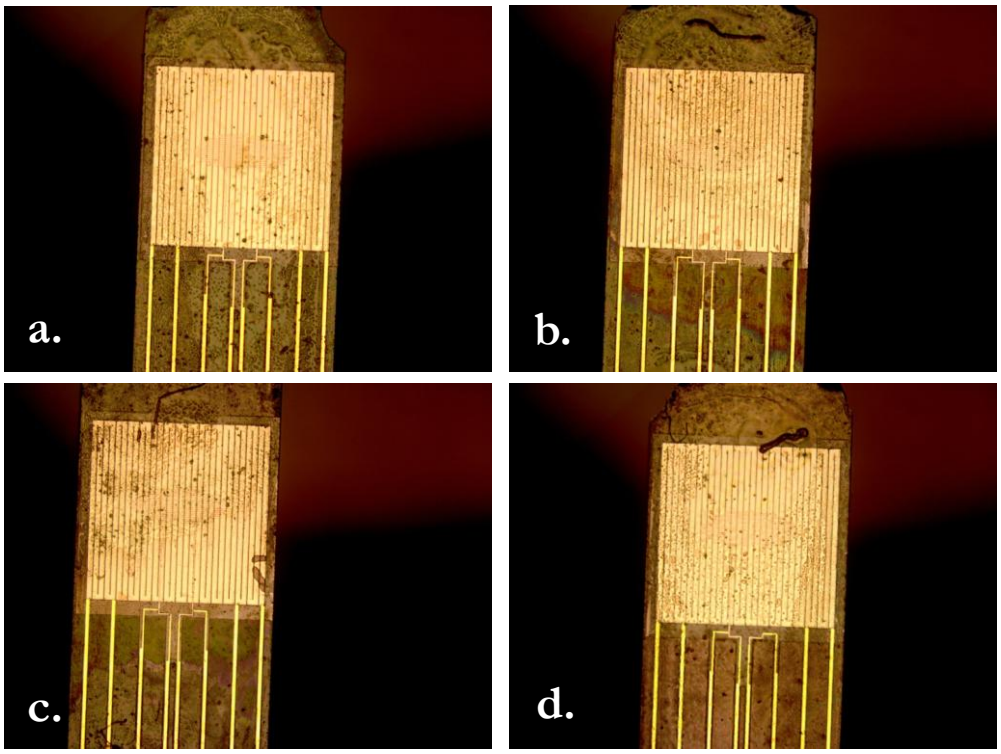

Figure B.32. All four heating units on one chip following dicing of the wafer. a.) reference sensor where no catalyst was deposited. No catalyst appears to be present. b, c, d.) Sensors where catalyst was deposited prior to dicing. No catalyst appears to remain (see Figure 9 for an optical micrograph of the catalyst following deposition).

B.6. Wiring

B.6.1. Wire Bonding

A total of 3 chips were successfully diced from one wafer. Each diced chip was fixed to a 64 pin side braze package (part # CSB06401) purchased from Spectrum Semiconductor Materials, Inc (San Jose, CA) using a high temperature ceramic epoxy (product # 940HT-1) purchased from Cotronics Corporation (Brooklyn, NY). The epoxy was prepared according to the suppliers instructions. Figure B.33 presents photographs of one diced chip attached to the package. The chip was wire bonded to the package using an MEI mode 1204-W hybrid wedge bonder (Marpet Enterprises, Inc) at a temperature of 150 °C using a controlled heat stage purchased from JM Industries (Worcester, MA). Gold wire, with a thickness of 1.5 mil, was used as received from Sigmond Cohn Corporation (Mt Vernon, NY). The heater regions for all sensors were designed to hang over the edge of the package to aid in gas flow during future testing. Figure B.34 presents the wiring diagram for a full chip containing a reference sensor and 3 sensors with catalyst. Included on the diagram is also the function of each connection on the device. A more detailed description and schematic is provided in Figure B.35 for a single sensor.

After wire bonding was completed, optical images were acquired for all bonding pads. Figure B.36 presents an optical micrograph of the eight bonding pads on one of the sensors. It is representative of all four sensors on each chip. Also presented is an optical micrograph of the bonding pads on the package and the gold wire connections.

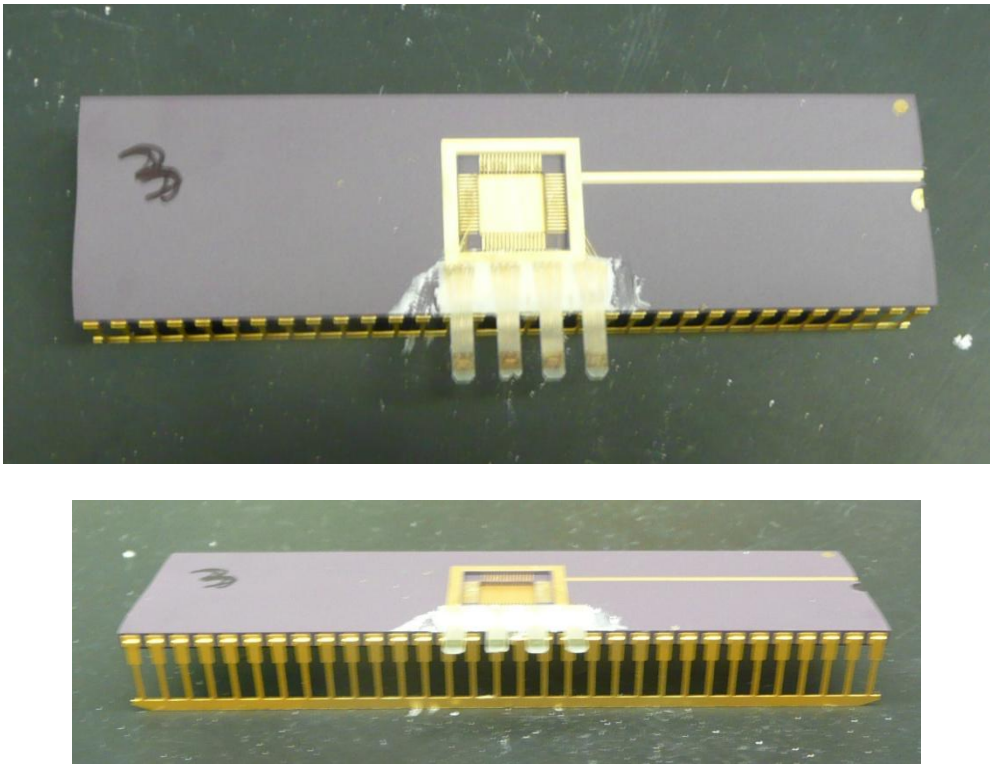

Figure B.33. Photographs of a diced chip fixed to the package post wire-bonding. Gold wire was using to bond the pads on the device to the pads on the package. Both a top (upper) and side (lower) view image are provided. The heater regions are hanging off the edge of the package to aid in gas flow during testing. The wiring diagram followed for the bonding is presented in Figure B.22.

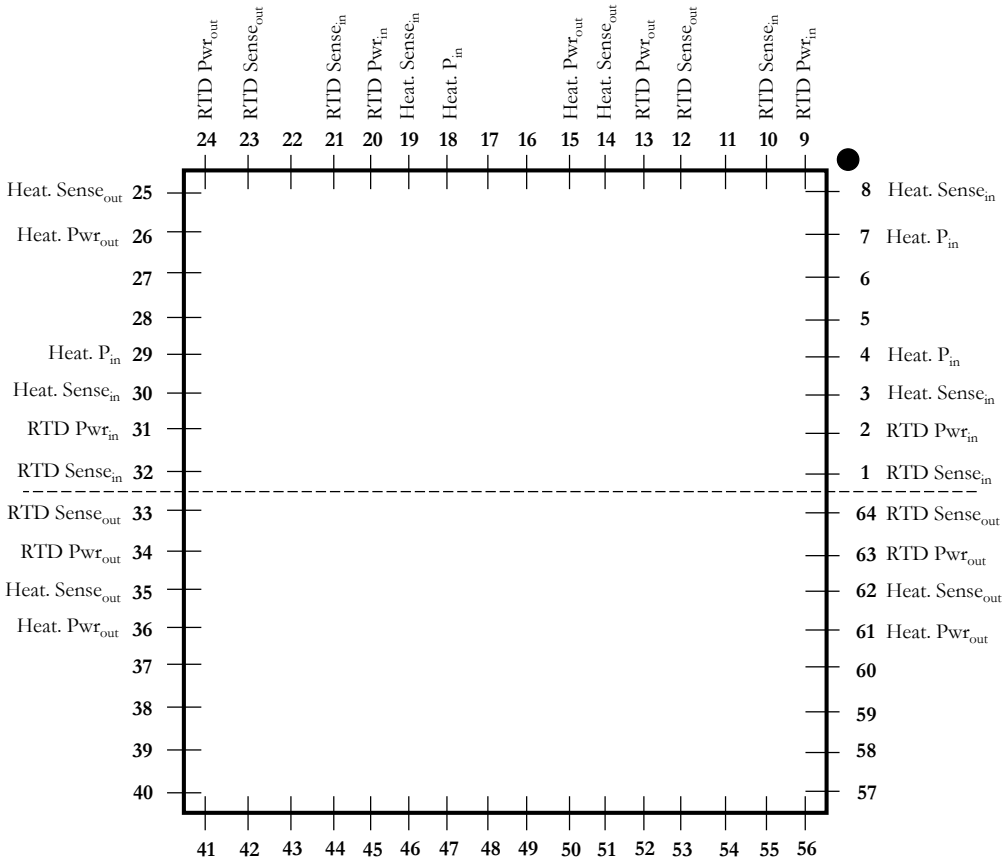

Figure B.34. Wiring diagram used for bonding. Bonding pins with a label next to them were used. All others were not connected. Pins 64-4 were connected to the reference sensor, pins 7-10 and 12-15 were connected to sensor #1, pins 18-21 and 23-26 were connected to sensor #2, and pins 29-36 were connected to sensor #3. The labels at the pins are representative of the function of that bonding pin on the device. A more detailed image is presented in Figure B.33.

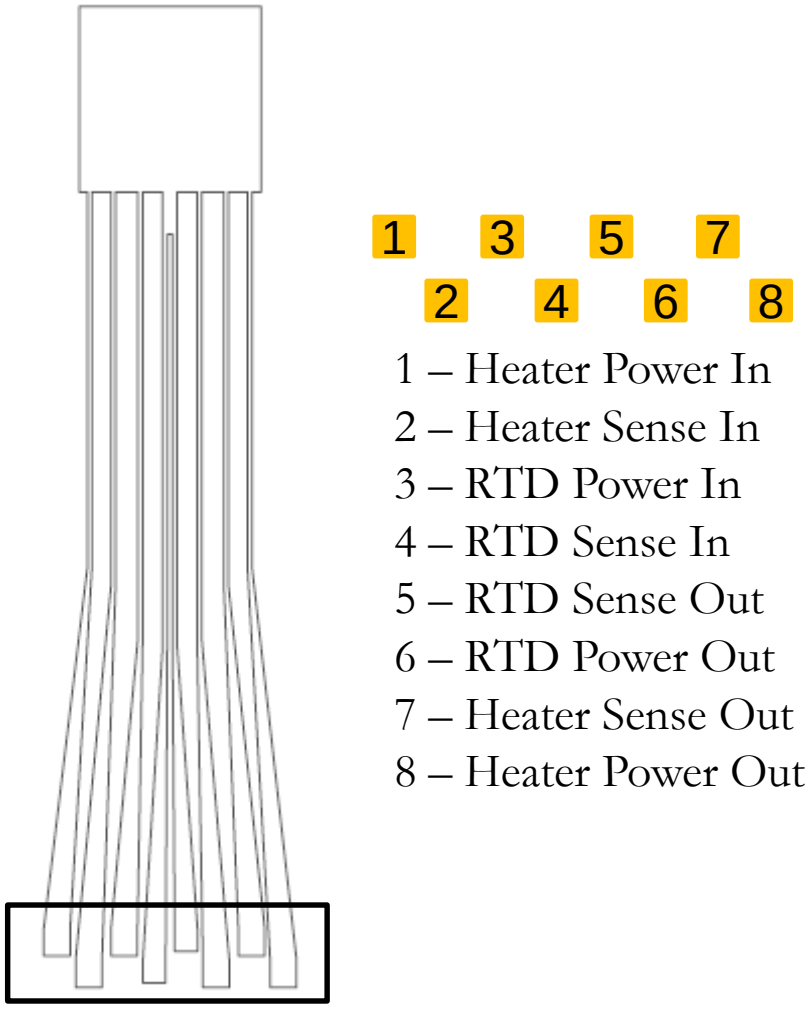

Figure B.35. Schematic of one sensor on a chip. Rectangle depicts the region shown in detail on the right. Bonding pads 1-8 are labeled and the corresponding function on the chip is provided. Pads 1, 2, 7, and 8 correspond to the heating unit circuit and pads 3 - 6 correspond to the RTD circuit.

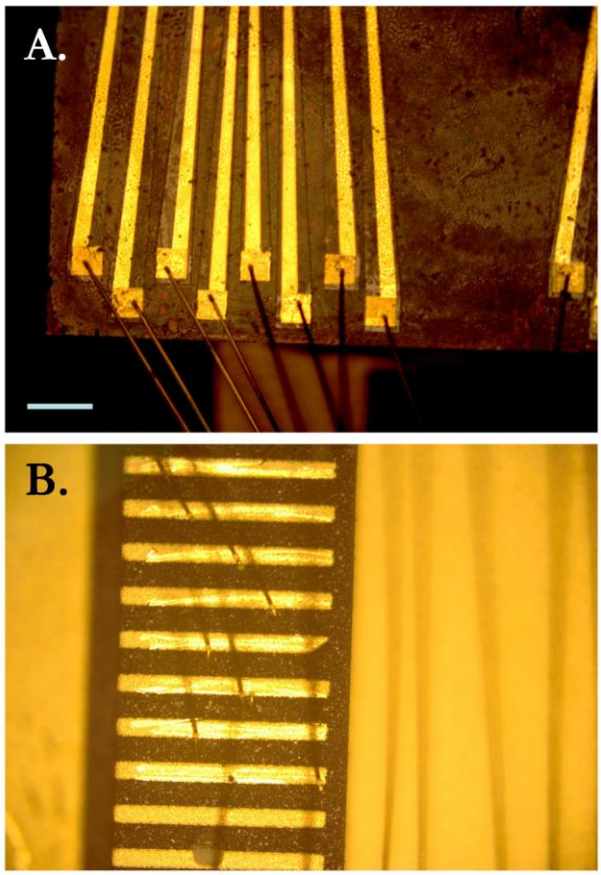

Figure B.36. A presents the eight gold bonding pads for the reference sensor on Chip 1. Also presented in B are the bonding pads on the package. Scratches on the bonding pads were to roughen the surface to help make a better wire connection. The scale bar denotes 500 µm for both images.

A.6.2. Creation of the Wiring Board

Upon completion of functional sensors, the chip will be ready for gas testing. In preparation for this, a board was wired to connect 4 RJ-45's (one corresponding to each sensor on the chip) to the 64 pin package. RJ-45's were purchased from Winford Engineering (product #PBC8P8C) and were fixed to breadboard adaptors. Each RJ-45 was then connected to a detector for monitoring the changes in resistance with heating over the heater and RTD units. For ease of use, a ZIF DIP socket was purchased from Linear Sales (part #264-4493-00-0602J) and wired to the board so that the same set-up could be used with multiple devices. Figures A.37 as well as A.38 present photographs of the completed board. Specifically, Figure B.37 presents a top view showing the DIP socket and the RJ-45's lined up and Figure B.38 presents the bottom view of the twisted pair wiring from the socket pins to the RJ-45's pins.

A.6.3. Creation of a Test Circuit

To assess the wiring of the circuit board prior to device testing, a test circuit was created to verify that the correct connections were made. The circuit consisted of a series of resistors (10 Ω) and light bulbs (MB-1829) to test the heating and the RTD units, respectively. These were soldered in pairs, corresponding to the functions outlined in Figure B.35. The wiring diagram for the test circuit is provided in Figure B.37. Due to space limitations during creation of the test circuit, pins used are not all in a row. Spaces needed to be included between resistor and light bulb pairs. This can be seen in the side

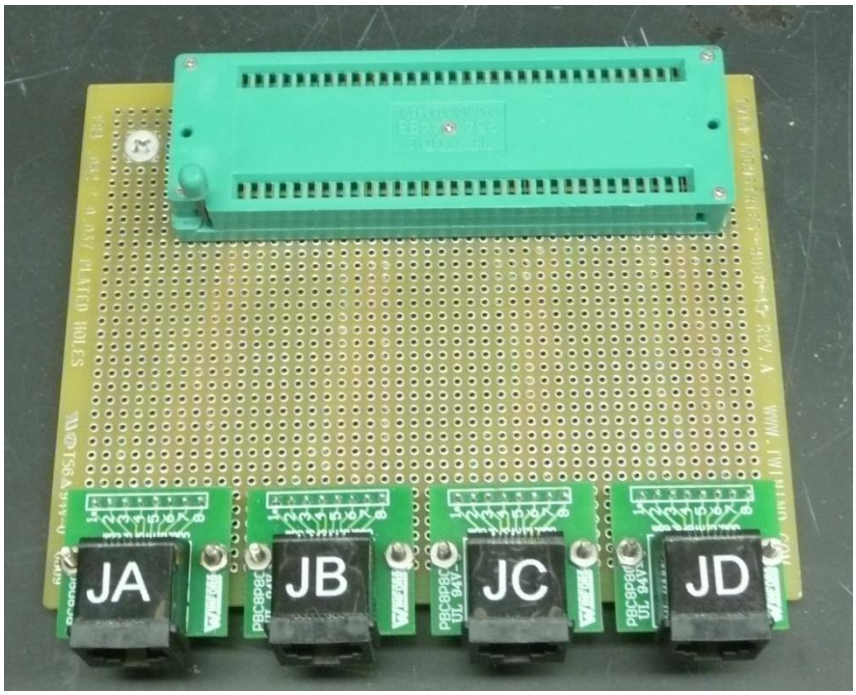

Figure B.37. Photograph showing the 4 RJ-45's as well as the 64 pin ZIF DIP socket. Each RJ-45 is connected to a specially designed box changes in resistance are measured. The socket was implemented to allow for multiple chips to be tested without creating a board for each. The wiring from the socket to the RJ-45's is presented in Figure B.40.

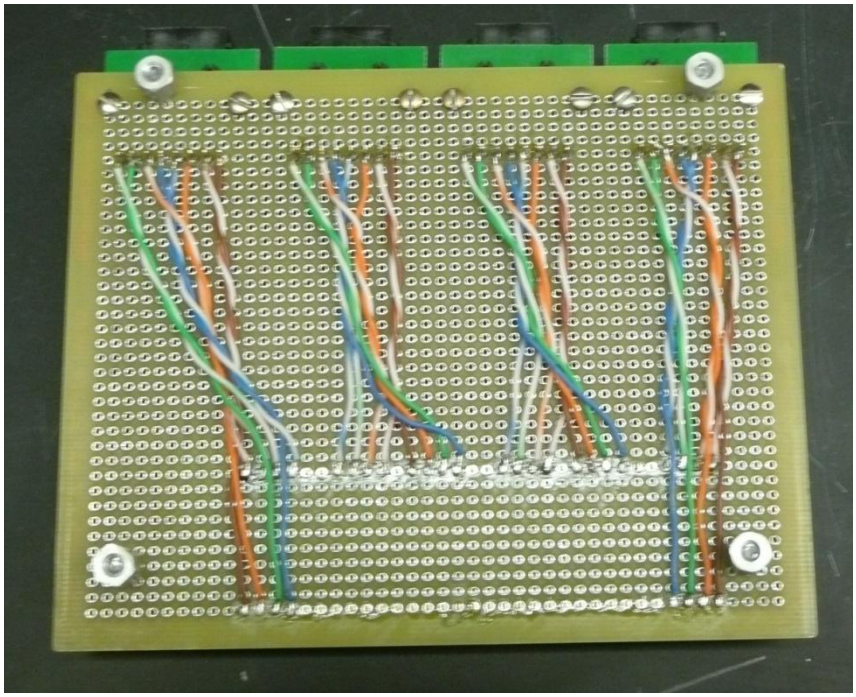

Figure B.38. A photograph showing the wiring from the socket (bottom of the image) to the RJ'45's (top of the image). Each RJ-45 corresponds to a different sensor on the fabricated ships. The packages pin assignments by sensor are depicted in Figure B.32 and the socket pin assignments are designated in Figure B. 37.

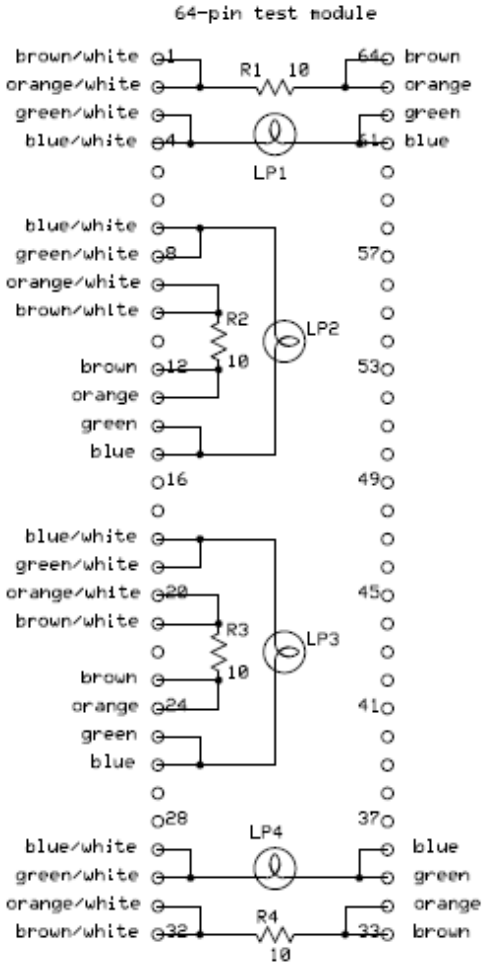

Figure B.39. Schematic showing the pin layout for the test circuit and where resistors and light bulbs were positioned. Also shown is the spacing required due to the space limitations of the package. Each pin on this image corresponds to the wiring diagram presented in Figure B.34.

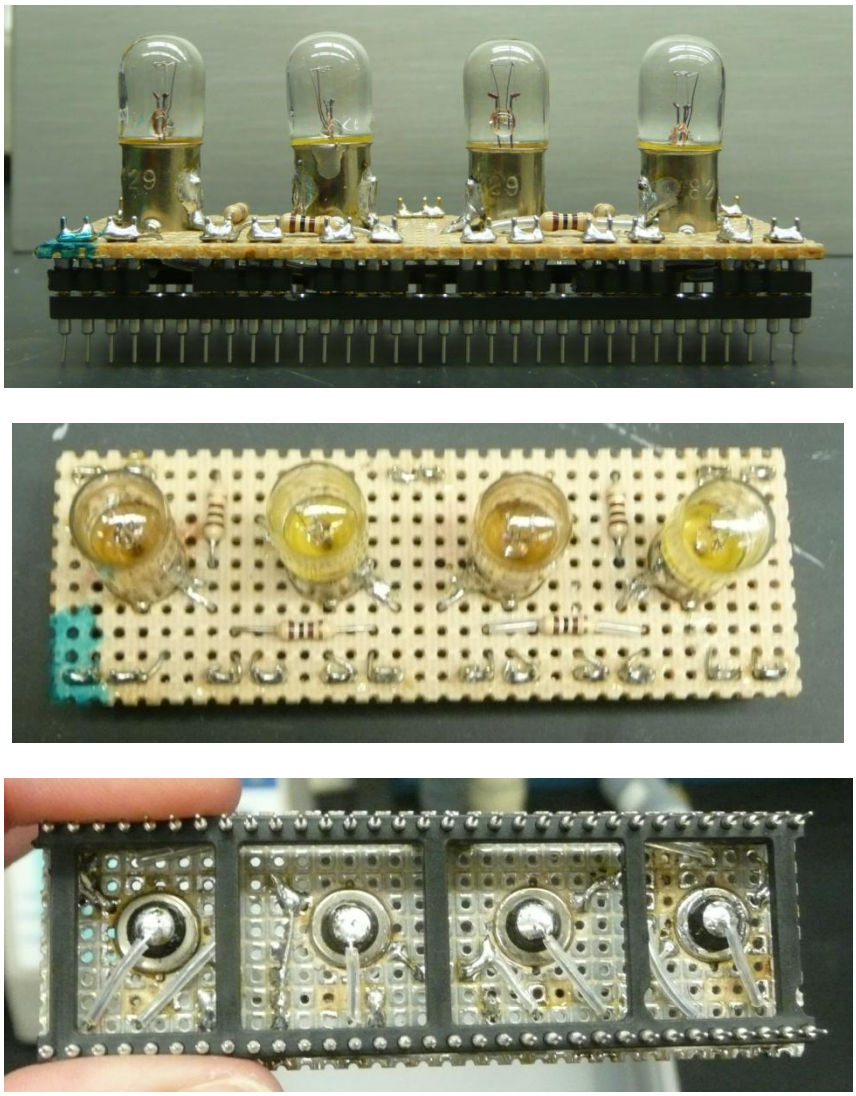

Figure B.40. Photographs of the test circuit created to test the connections on the board prior to experimentation with the sensor chips. The side view shows the resistors and light bulbs as well as the spacing created on the 64 pin socket. The middle and bottom image show additional details including the soldered connections (bottom image).

view of the test circuit provided in Figure B.38. Also presented in Figure B.38 are the top and bottom views showing the soldering in more detail.

B.7. Prototype #2 Initial Process Flow

Upon careful consideration of the issues and results obtained using sapphire as the base substrate for the sensor, a decision was made to move to a silicon wafer in hopes of creating a functional sensor. In doing so, a few design changes were made. The process flow for prototype #2 is provided below.

B.7.1. Deposition of Silicon Nitride Mesas for micro-Heater

Deposition and etching of the Si_xN_y mesa will be performed in the same manner as prototype #1. Photolithography patterning step #1 will be completed using the same parameters described in section B.4.1 in this appendix (see Figure B.14 for the mask pattern used).

B.7.2. Creation of Wiring for micro-Heater

Photolithography patterning step #2 will be completed using the same process parameters described in section B.4.2 of this appendix (see Figure B.16 for the mask pattern used).

B.7.3. Deposition of Nickel micro-Heater

Photolithography patterning step #3 will be completed using the process parameters described in section B.4.3 in this appendix (see Figure B.18 for the mask pattern used).

B.7.4. Deposition of Silicon Nitride Barrier Layer #1

The same low stress recipe previously described in this appendix will be used to deposit Si_xN_y over the entire wafer. The barrier layer mask was altered to add additional

alignment marks for the final process step, a silicon wafer etch. Figure B.40 presents the new mask pattern for a single chip. The silicon wafer etch is to be carried out using a Bosch process in an ICP where metal may not be exposed during the process. For this reason, the alignment mark had to be created using Si_xN_y. Photolithography patterning step #4 will be completed using the process parameters described in the section B.4.4.

B.7.5. Creation of Wiring for RTD

Photolithography patterning step #5 will be completed using the process parameters described in section B.4.5 of this appendix (see Figure B.22 for the mask pattern used).

B.7.6. Deposition of Nickel RTD

To correct for the disconnects in the RTD described in section B.5.1 of this appendix, nickel deposition for prototype #2 will be sputtered onto the entire wafer surface and etched back using 30% Ferric (III) Chloride. In doing so, the metal will coat all areas of the uneven surface, eliminating disconnects. A new schematic for the RTD deposition process is presented in Figure B.42. This will be the new photolithography step #6. The same mask presented in Figure B.24 will be used.

B.7.7. Deposition of Silicon Nitride Barrier Layer #2

The same low stress recipe previously described in this appendix will be used to deposit Si_xN_y over the entire wafer. Photolithography patterning step #7 will be completed using the same process parameters described in section B.4.7 of this appendix. Figure B.41 presents the new mask pattern for a single chip. It should be noted that this mask photolithography steps #4 and #7 will still use the same mask.

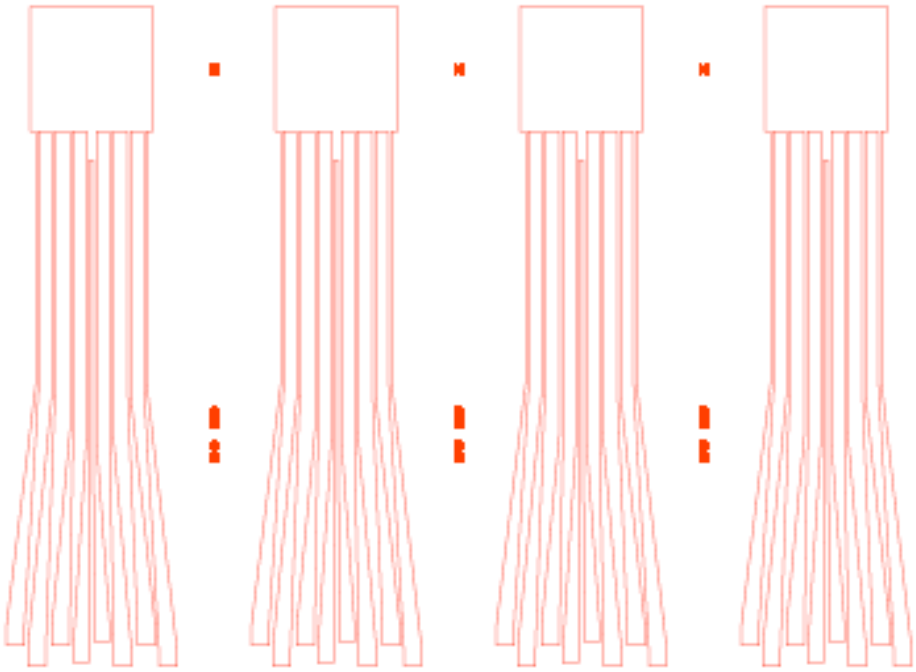

Figure B.41. Feature details for a single chip, representative of the new mask made to be used during photolithography patterning step #4 and #7. Alignment marks now exist for the final processing step, a silicon etch.

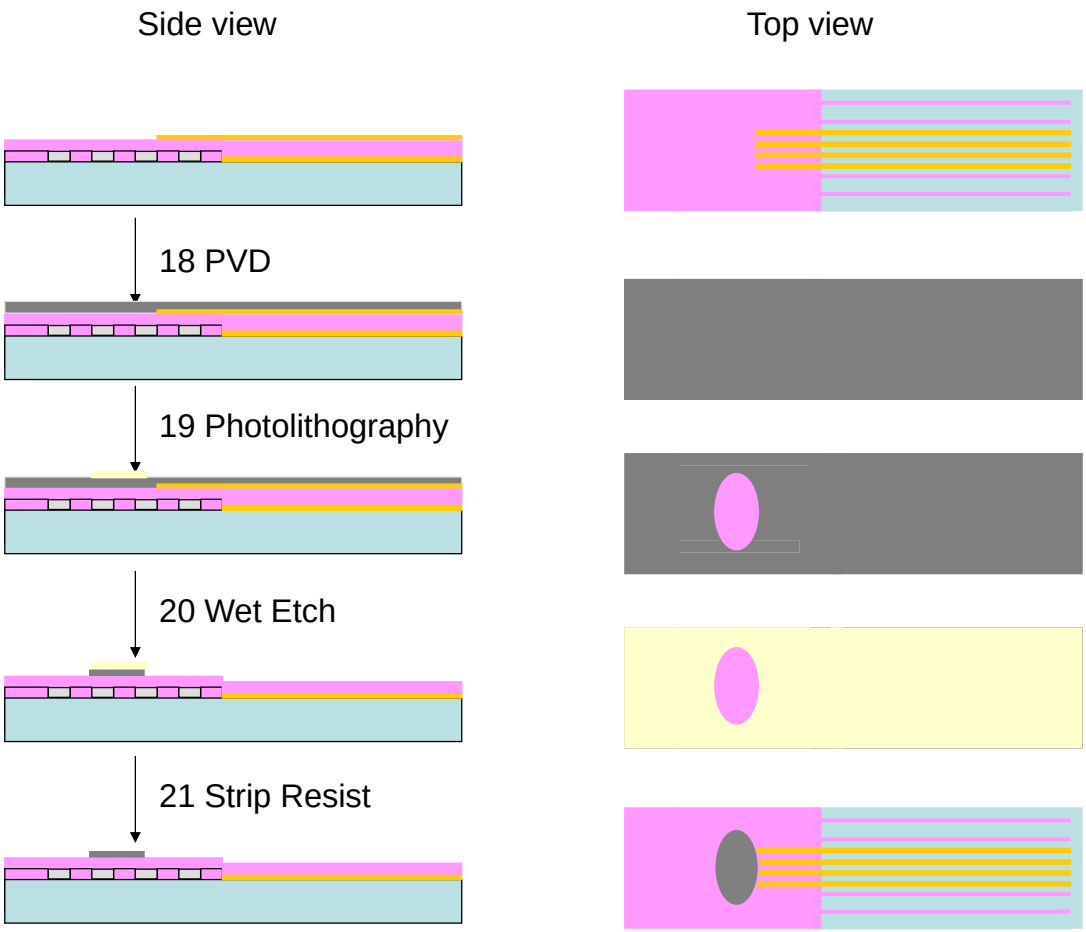

Figure B.42. Schematic of the process flow for creation of the RTD sensing element for prototype #2. Both a side and top view is provided.

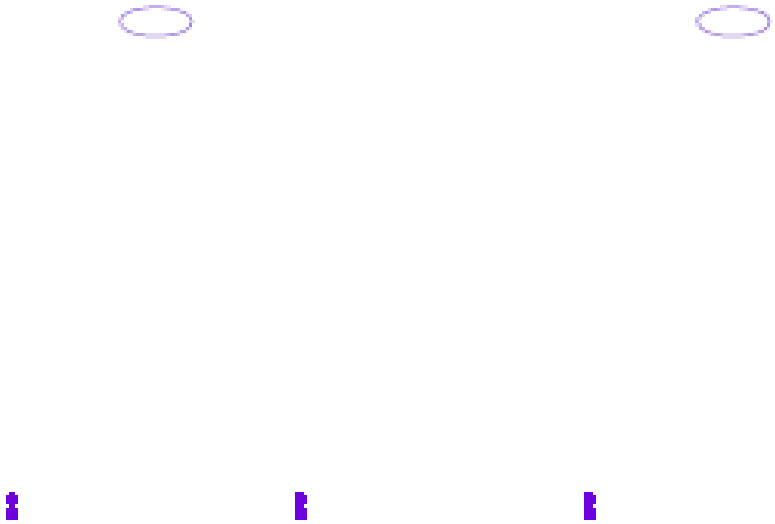

Figure B.43. Feature details for a single chip, representative of the new mask made to be used during photolithography patterning step #9. Two reference and 2 catalyst sensors now exist on each fabricated chip.

B.7.8. Deposition of Gold bonding Pads

Photolithography patterning step #8 will be completed using the process steps described in section B.4.8 of this appendix. See Figure B.27 for the mask pattern used.

B.7.9. Deposition of Metal Oxide Active Catalyst - Copper, Nickel and Titanium

Photolithography patterning step #9 will be completed using a new mask, presented in Figure B.43. The metal catalyst deposition was re-designed to account for the possibility that some sensors on a chip may not be fully functional. Instead of a single reference and 3 active catalyst sensors, there will be two of each in an alternating pattern. The process steps described in section B.4.9 of this appendix will remain the same for photolithography step #9. For the first prototype, a metal oxide catalyst of copper was chosen. This metal will be used again in addition to nickel and titanium, all on separate wafers.

B.7.10. Silicon Wafer Etch

An additional process step has been added for prototype #2 for release of the parts from the wafer. Due to the issues encountered with dicing the wafer, an etch will be employed through the entire silicon wafer. The silicon wafer etch is to be carried out using a Bosch process in the PECVD-ICP. The shape and design of the chip will remain the same as the diced sapphire chip for prototype #1; however the finger region will be slightly shorter to account for the inability of the silicon etch to thin the end of the fingers. The mask features for a single chip is presented in Figure B.44. All other steps post fabrication such as device testing and wiring will remain the same. Presented in Figure B.45 is a schematic for a single chip post etching with the features included. The blue ovals represent the metal oxide atop the heater region represented by a grey square. The

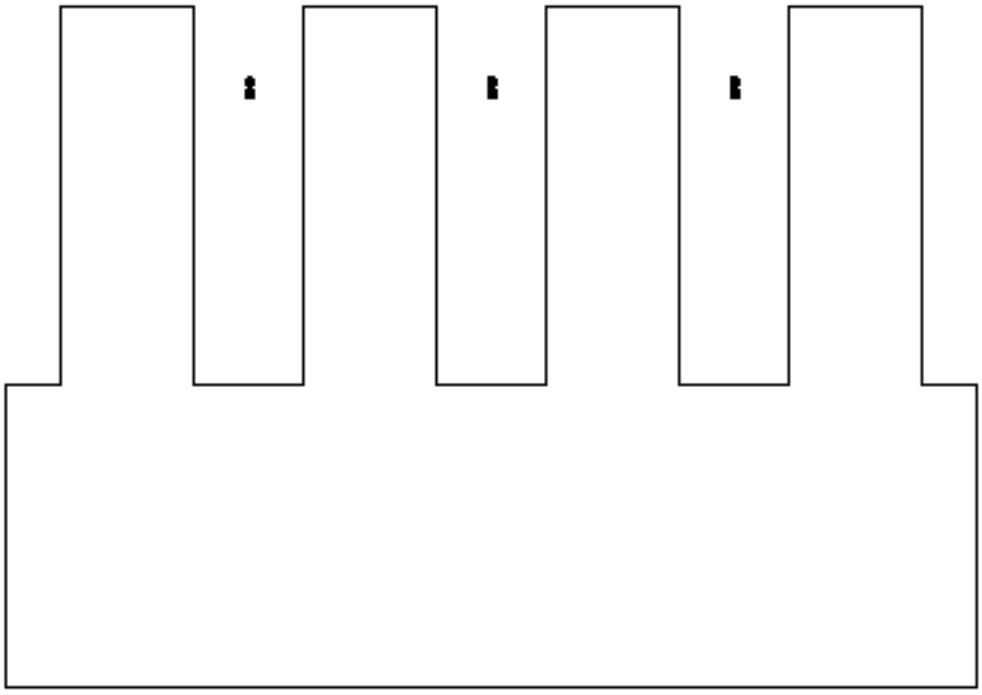

Figure B.44. Feature details for a single chip, representative of the new mask made to be used during photolithography patterning step #10. A complete etch of the silicon wafer is to be performed to create the chips instead of having them diced.

black lines represent the gold lead connections for both the heater and RTD sensing unit. It should be noted that the spacing is not drawn to scale. Also included are the gold bonding pads at the base of the gold leads in a staggered patter, represented by the green squares.

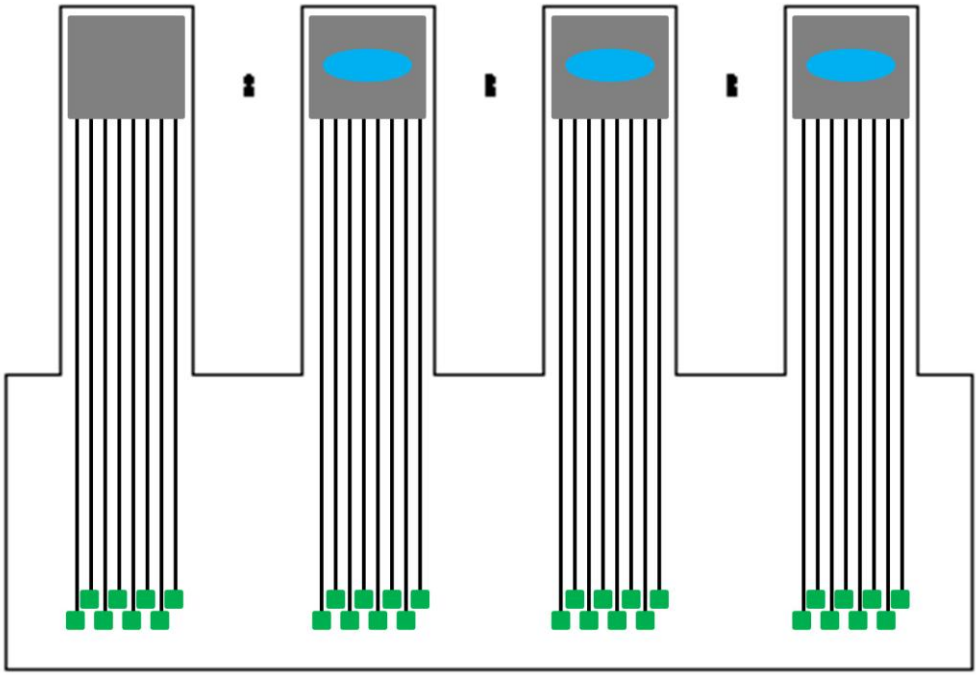

Figure B.45. Schematic of a completed chip with three sensing units and one reference. The grey boxes represent the heater nit, the blue ovals represent the metal oxide catalyst atop the RTD sending unit, the black lines represent the gold lead connections for the heater and RTD, and the green squares represent the gold bonding pads.

REFERENCES

VITA

NICOLE E. MAROTTA

MAROTTA was born in Niskayuna, New York where she attended elementary, middle, and high school. While in Niskayuna, she was actively involved in musical theatre, dance, and various sports. After graduating from high school in 2002, she moved to Buffalo NY where she received her bachelors degree in Chemistry from The State University of New York at Buffalo in 2006. During her four years in Buffalo she was a member of the UB Field Hockey Team. She was also a founding sister of the Delta Delta chapter of Delta Phi Epsilon sorority. Marotta moved to Atlanta in August of 2006 to pursue her doctorate in Biochemistry at Georgia Tech.

"Patterned Silver Nanorod Array Substrates for Surface Enhanced Raman Scattering," Marotta, N. E.; Barber, J. R.; Dluhy, P. R.; Bottomley, L. A. *Applied Spectroscopy* **2009**, *63*, 1101.

"Thermal Stability of Silver Nanorod Arrays," Beavers, K. R.; Marotta, N. E.; Bottomley, L. A. *Chemistry of Materials*, **2010**, *22*.

"Surface Enhanced Raman Scattering of Bacterial Cell Culture Media," Marotta, N. E.; Bottomley, L. A. *Applied Spectroscopy*, **2010** 4(6):601-6.

"Removal of Surface Contamination and Self-Assembled Monolayers from Ag Nanorod Substrates by Plasma Cleaning with Argon" Negri, P.; Marotta, N. E.; Bottomley, L. A.; Dluhy, R. A. *Applied Spectroscopy*, under review.

"Polystyrene beads as Probes of the SERS response Characteristics of Silver Nanorod Arrays" Marotta, N. E.; Bottomley, L.A. *Applied Spectroscopy,* under final review.

"Limitations of SERS-based assay of DNA hybridization" Marotta, N. E.; Bottomley, L. A. *JACS,* in preparation.

REFERENCES

1. Barhoumi, A., et al., *Surface-Enhanced Raman Spectroscopy of DNA.* Journal of the American Chemical Society, 2008. **130**(16): p. 5523-5529.

2. Cao, Y.-W.C., R. Jin, and C.A. Mirkin, *Nanoparticles with Raman Spectroscopic Fingerprints for DNA and RNA Detection.* Science, 2002. **297** p. 1536-1539.

3. Faulds, K., et al., *A new approach for DNA detection by SERRS.* Faraday Discussions, 2005. **132**: p. 261-268.

4. Graham, D. and K. Faulds, *Quantitative SERRS for DNA sequence analysis.* Chemical Society Reviews, 2008. **37**: p. 1042-1051.

5. Graham, D., et al., *Functionalized nanoparticles for bioanalysis by SERRS.* Bionanotechnology II: from Biomolecular Assembly to Applications, 2009. **37**.

6. Green, M., et al., *SERS platforms for high density DNA arrays.* Faraday Discussions, 2006. **132**: p. 269-280.

7. Mirkin, C.A., et al., *A DNA-based method for rationally assembling nanoparticles into macroscopic materials.* Nature, 1996. **382**.

8. Otto, C., et al., *Surface-Enhanced Raman-Spectroscopy of DNA Bases.* Journal of Raman Spectroscopy, 1986. **17**(3): p. 289-298.

9. Campion, A. and P. Kambhampati, *Surface-enhanced Raman scattering.* Chemical Society Reviews, 1998. **27**(4): p. 241-250.

10. McCreery, R.L., *Raman Spectroscopy for Chemical Analysis*. 2000, New York.

11. Schatz, G.C., *Theoretical-Studies of Surface Enhanced Raman-Scattering.* Accounts of Chemical Research, 1984. **17**(10): p. 370-376.

12. ; Available from: acs.org.

13. Ingle, J., J. D. and S.R. Crouch, *Spectrochemical Analysis*. 1988, Englewood Cliffs, New Jersey: Prentice Hall.

14. Movchan, B.A. and A.V. Demchish, *The Study of Structure and Properties of Thick Vacuum Condensates of Nickel, Titanium, Tungsten, Aluminum Oxide and Zirconium dioxide.* Physics od Metals and Metallography - USSR, 1969. **28**(4): p. 83.

15. Powell, A., et al., *Mathematical modeling of vapor-plume focusing in electron-beam evaporation.* Metallurgical and Materials Transactions a-Physical Metallurgy and Materials Science, 2001. **32**(8): p. 1959-1966.

16. Robbie, K., et al., *Inhomogeneous thin film optical filters fabricated using glancing angle deposition.* Electronics Letters, 1997. **33**(14): p. 1213-1214.

17. Robbie, K., J.C. Sit, and M.J. Brett, *Advanced techniques for glancing angle deposition.* Journal of Vacuum Science & Technology, B, 1998. **16**(3): p. 1115-1122.

18. Thornton, J.A., SAE Transactions, 1974. **82**: p. 1787-1805.

19. Thornton, J.A., *High Rate Thick Film Growth.* Annual Review of Materials Science, 1977. **7**: p. 239-260.

20. Tait, R.N., T. Smy, and M.J. Brett, *Modeling and Characterization of Columnar Growth in Evaporated Films.* Thin Solid Films, 1993. **226**(2): p. 196-201.

21. *Nobel Lectures*. Physics 1922 - 1941. 1956, Amsterdam: Elsevier Publishing Compnay.

22. Lewis, I.R., *Handbook of Raman Spectroscopy: From the Research Laboratory to the Process Line* Practical Spectroscopy ed. H.G.M. Edwards. 2001 Ann Arbor, Michigan.

23. Schatz, G.C. and R.P.V. Duyne, *Handbook of Vibrational Spectroscopy*, ed. J.M.C.a.P.R. Griffiths. Vol. 1. 2002, New York: Wiley.

24. Murphy, C.J., et al., *Chemical sensing and imaging with metallic nanorods.* Chemical Communications, 2008: p. 544-557.

25. Brodersen, S. and E.H. Richardson, *The Raman Spectrum of Gaseous Allene.* Journal of Molecular Spectroscopy, 1960. **4**(5): p. 439-445.

26. Claassen, H.H., *Raman Spectra of Chlorofluoromethanes in the Gaseous State.* Journal of Chemical Physics, 1954. **22**(1): p. 50-52.

27. Gullikson, C.W. and J.R. Nielsen, *Raman Spectrum of Gaseous Trifluoroacetonitrile.* Journal of Molecular Spectroscopy, 1957. **1**(2): p. 155-157.

28. Gullikson, C.W., J.R. Nielsen, and A.T. Stair, *Raman Spectrum of Sulfur Hexafluoride in the Gaseous and Solid States.* Journal of Molecular Spectroscopy, 1957. **1**(2): p. 151-154.

29. Matterson, A.H.S. and L.A. Woodward, *Relative Intensities of Totally Symmetrical Vibrations in the Raman Spectrum of Gaseous Neopentane.* Proceedings of the Royal Society of London Series a-Mathematical and Physical Sciences, 1955. **231**(1187): p. 514-521.

30. Nakagawa, I. and S.I. Mizushima, *The Assignments of the Raman and Infrared Frequencies of 1,2-Dichloroethane Observed in the Gaseous, Liquid, and Solid States.* Journal of Chemical Physics, 1953. **21**(12): p. 2195-2198.

31. Nielsen, J.R. and J.C. Albright, *Raman Spectrum of Gaseous 1-Fluoro-1-Chloroethylene.* Journal of Chemical Physics, 1957. **26**(6): p. 1566-1567.

32. Richards, C.M. and J.R. Nielsen, *Raman Spectra of Cis-2 and Trans-2-Butene and 1,3-Butadiene in the Gaseous and Liquid States.* Journal of the Optical Society of America, 1950. **40**(4): p. 255-255.

33. Taylor, R.C. and G.L. Vidale, *Raman Spectrum and Vibrational Assignments of Gaseous Dimethyl Ether.* Journal of Chemical Physics, 1957. **26**(1): p. 122-123.

34. Biswas, S.C., *Raman spectra an liquid and gaseous CH4.* Philosophical Magazine, 1932. **13**(84): p. 455-458.

35. Braune, H. and G. Engelbrecht, *On the Raman-effect of some inorganic halogenides in the liquid and gaseous state.* Zeitschrift Fur Physikalische Chemie-Abteilung B-Chemie Der Elementarprozesse Aufbau Der Materie, 1932. **19**(5): p. 303-313.

36. Weber, A. and E.A. McGinnis, *The Raman Spectrum of Gaseous Oxygen.* Journal of Molecular Spectroscopy, 1960. **4**(3): p. 195-200.

37. Imanishi, S., *Raman spectrum of gaseous carbon disulphide.* Nature, 1935. **135**: p. 396-396.

38. Adel, A., *The Raman spectrum of gaseous carbon dioxide.* Physical Review, 1933. **44**(8): p. 0691-0691.

39. Smith, J.S.K. and L.G. Bonner, *The Raman spectra of gaseous substances I apparatus and the spectrum of methylamme.* Journal of Chemical Physics, 1939. **7**(10): p. 880-883.

40. Wartell, R.M. and J.T. Harrell, *Characteristics and Variations of B-Type DNA Conformations in Solution - a Quantitative-Analysis of Raman Band Intensities of 8 Dnas.* Biochemistry, 1986. **25**(9): p. 2664-2671.

41. Wartell, R.M. and J.T. Harrell, *Characteristics of B-Type DNA Conformations in Solution - Analysis of Raman Band Intensities of 8-Dnas.* Biophysical Journal, 1986. **49**(2): p. A129-A129.

42. Biscar, J.P., R.F. Burczyk, and N. Kollias, *Emer-Raman Analysis of DNA Base Conformation.* Bulletin of the American Physical Society, 1974. **19**(3): p. 264-264.

43. Erfurth, S.C., E.J. Kiser, and Peticola.Wl, *Determination of Backbone Structure of Nucleic-Acids and Nucleic-Acid Oligomers by Laser Raman Scattering.* Proceedings of the National Academy of Sciences of the United States of America, 1972. **69**(4): p. 938-&.

44. Small, E.W. and Peticola.Wl, *Conformational Dependence of Raman Scattering Intensities from Polynucleotides .3. Order-Disorder Changes in Helical Structures.* Biopolymers, 1971. **10**(8): p. 1377-&.

45. Lu, K.C., E.W. Prohofsky, and L.L. Vanzandt, *Vibrational Modes of a-DNA, B-DNA, and a-Rna Backbones - Application of a Green-Function Refinement Procedure.* Biopolymers, 1977. **16**(11): p. 2491-2506.

46. Thomas, G.A. and W.L. Peticolas, *Fluctuations in Nucleic-Acid Conformations .2. Raman-Spectroscopic Evidence of Varying Ring Pucker in a-T Polynucleotides.* Journal of the American Chemical Society, 1983. **105**(4): p. 993-996.

47. Wartell, R.M., et al., *Raman-Spectroscopy Study of the B-Z Transition in (Dg-Dc)N.(Dg-Dc)N and a DNA Restriction Fragment.* Journal of Biomolecular Structure & Dynamics, 1983. **1**(1): p. 83-96.

48. Degrazia, H., et al., *Solution Conformations of Dnas Containing Binding-Sites of the Catabolite Gene Activator Protein and Lac Repressor Protein - Characterization by Raman-Spectroscopy.* Biochemistry, 1988. **27**(17): p. 6359-6365.

49. Degrazia, H., J. Harman, and R.M. Wartell, *Investigation of Camp Receptor Protein Secondary Structure by Raman-Spectroscopy.* Biophysical Journal, 1990. **57**(2): p. A67-A67.

50. Tan, G.S., et al., *Comparison of Camp Receptor Protein (Crp) and a Camp-Independent Form of Crp by Raman-Spectroscopy and DNA-Binding.* Biochemistry, 1991. **30**(20): p. 5076-5080.

51. Zuo, E.T., et al., *Effect of Base-Pair Sequence on the Conformations and Thermally Induced Transitions in Oligodeoxyribonucleotides Containing Only at Base-Pairs.* Biochemistry, 1990. **29**(18): p. 4446-4456.

52. Mansy, S., S.K. Engstrom, and W.L. Peticolas, *Laser Raman Identification of an Interaction Site on DNA for Arginine Containing Histones in Chromatin.* Biochemical and Biophysical Research Communications, 1976. **68**(4): p. 1242-1247.

53. Goodwin, D.C. and J. Brahms, *Form of DNA and Nature of Interactions with Proteins in Chromatin.* Nucleic Acids Research, 1978. **5**(3): p. 835-850.

54. Martin, J.C., R.M. Wartell, and D.C. Oshea, *Conformational Features of Distamycin-DNA and Netropsin-DNA Complexes by Raman-Spectroscopy.*

Proceedings of the National Academy of Sciences of the United States of America, 1978. **75**(11): p. 5483-5487.

55. Fleischmann, M., P.J. Hendra, and M.A. J., *Raman-Spectra of Pyridine Adsorbed at a Silver Electrode.* Chemical Physics Letters, 1974. **26**(2): p. 163-166.

56. Hendra, P.J., J.R. Horder, and E.J. Loader, *Laser-Raman Spectrum of Pyridine Adsorbed on Oxide Surfaces.* Journal of the Chemical Society a -Inorganic Physical Theoretical, 1971(11): p. 1766-&.

57. Hendra, P.J., et al., *Laser Raman-Spectra of Species Adsorbed on Oxide Surfaces .2.* Journal of Physical Chemistry, 1974. **78**(3): p. 300-304.

58. Albrecht, M.G. and J.A. Creighton, *Anomalously Intense Raman-Spectra of Pyridine at a Silver Electrode.* Journal of the American Chemical Society, 1977. **99**(15): p. 5215-5217.

59. Jeanmaire, D.L. and R.P. Vanduyne, *Surface Raman Spectroelectrochemistry .1. Heterocyclic, Aromatic, and Aliphatic-Amines Adsorbed on Anodized Silver Electrode.* Journal of Electroanalytical Chemistry, 1977. **84**(1): p. 1-20.

60. Katan, T., S. Szpak, and D.N. Bennion, *Silver-Silver Chloride Electrodes - Surface Morphology on Charging and Discharging.* Journal of the Electrochemical Society, 1974. **121**(6): p. 757-764.

61. Haarer, D., M.R. Philpott, and H. Morawitz, *Field-Induced Charge-Transfer Exciton-Transitions.* Journal of Chemical Physics, 1975. **63**(12): p. 5238-5245.

62. Fleischmann, M., et al., *Raman-Spectroscopy at Electrode-Electrolyte Interfaces.* Journal of Raman Spectroscopy, 1976. **4**(3): p. 269-274.

63. Paul, R.L., et al., *Laser Raman-Spectroscopy at Surface of a Copper Electrode.* Journal of Electroanalytical Chemistry, 1975. **66**(3): p. 248-249.

64. McQuillan, A.J., P.J. Hendra, and M. Fleischmann, *Raman Spectroscopic Investigation of Silver Electrodes.* Journal of Electroanalytical Chemistry, 1975. **65**(2): p. 933-944.

65. Barradas, R.G. and P.G. Hamilton, *Chemical structure and adsorption of organic molecules at the polarized mercury-electrolyte interface.* Canadian Journal of Chemistry, 1965. **43**: p. 2468-2485.

66. Van Duyne, R.P., *Chemical and Biochemical Applications of Lasers*, ed. C.B. Moore. Vol. 4. 1979, New York: Academic Press.

67. Furtak, T.E. and J. Reyes, *A Critical Analysis of Theoretical-Models for the Giant Raman Effect from Adsorbed Molecules.* Surface Science, 1980. **93**(2-3): p. 351-382.

68. Otto, A., *Surface Enhanced Raman-Scattering (Sers), What Do We Know.* Applied Surface Science, 1980. **6**(3-4): p. 309-355.

69. Chang, R.K. and T.E. Furtak, *Surface Enahnced Raman Scattering*, ed. R.K. Chang and T.E. Furtak. 1982, New York: Plenum Press.

70. King, F.W., R.P. Vanduyne, and G.C. Schatz, *Theory of Raman-Scattering by Molecules Adsorbed on Electrode Surfaces.* Journal of Chemical Physics, 1978. **69**(10): p. 4472-4481.

71. Ford, G.W. and W.H. Weber, *Electromagnetic Effects on a Molecule at a Metal-Surface .1. Effects of Nonlocality and Finite Molecular-Size.* Surface Science, 1981. **109**(2): p. 451-481.

72. Ford, G.W. and W.H. Weber, *Electromagnetic Effects in the Surface Enhanced Raman-Scattering from a Molecule at a Liquid Hg Surface.* Surface Science, 1981. **110**(1): p. L587-L592.

73. Weber, W.H. and G.W. Ford, *Enhanced Raman-Scattering by Adsorbates Including the Nonlocal Response of the Metal and the Excitation of Nonradiative Modes.* Physical Review Letters, 1980. **44**(26): p. 1774-1777.

74. Kliewer, K.L. and R. Fuchs, *Anomalous Skin Effect for Specular Electron Scattering and Optical Experiments at Non-Normal Angles of Incidence.* Physical Review, 1968. **172**(3): p. 607-&.

75. Moskovits, M., *Surface-Enhanced Spectroscopy.* Reviews of Modern Physics, 1985. **57**(3): p. 783-826.

76. Aroca, R., *Surface Enhanced Vibrational Spectroscopy*. 2006, New York.

77. Wetzel, H., H. Gerischer, and B. Pettinger, *Surface-Enhanced Raman-Scattering from Silver-Cyanide and Silver-Thiocyanate Vibrations and the Importance of Adatoms.* Chemical Physics Letters, 1981. **80**(1): p. 159-162.

78. Allen, C.S., G.C. Schatz, and R.P. Vanduyne, *Tunable Laser Excitation Profile of Surface Enhanced Raman-Scattering from Pyridine Adsorbed on a Copper Electrode Surface.* Chemical Physics Letters, 1980. **75**(2): p. 201-205.

79. Le Ru, E.C., E. Blackie, and P.G. Etchegoin, *Surface enhanced Raman Scattering Enhancement factors: A Comprehensive study.* Journal of Physical Chemistry C, 2007. **111**: p. 13794-13803.

80. Kneipp, K., et al., *Single molecule detection using surface-enhanced Raman scattering (SERS).* Physical Review Letters, 1997. **78**(9): p. 1667-1670.

81. Nie, S.M. and S.R. Emery, *Probing single molecules and single nanoparticles by surface-enhanced Raman scattering.* Science, 1997. **275**(5303): p. 1102-1106.

82. Dieringer, J.A., et al., *Surface enhanced Raman spectroscopy: new materials, concepts, characterization tools, and applications.* Faraday Discussions, 2005. **132**: p. 9-26.

83. Gersten, J. and A. Nitzan, *Electromagnetic Theory of Enhanced Raman-Scattering by Molecules Adsorbed on Rough Surfaces.* Journal of Chemical Physics, 1980. **73**(7): p. 3023-3037.

84. Whitney, A.V., et al., *Localized surface plasmon resonance nanosensor: A high-resolution distance-dependence study using atomic layer deposition.* Journal of Physical Chemistry B, 2005. **109**(43): p. 20522-20528.

85. Elam, J.W., M.D. Groner, and S.M. George, *Viscous flow reactor with quartz crystal microbalance for thin film growth by atomic layer deposition.* Review of Scientific Instruments, 2002. **73**.

86. Kennedy, B.J., et al., *Determination of the distance dependence and experimental effects for modified SERS substrates based on self-assembled monolayers formed*

using alkanethiols. Journal of Physical Chemistry B, 1999. **103**(18): p. 3640-3646.

87. Haes, A.J., et al., *Nanoscale optical biosensor: Short range distance dependence of the localized surface plasmon resonance of noble metal nanoparticles.* Journal of Physical Chemistry B, 2004. **108**(22): p. 6961-6968.

88. Angel, S.M., et al., *Near-Infrared Surface-Enhanced Raman-Spectroscopy .1. Copper and Gold Electrodes.* Applied Spectroscopy, 1988. **42**(8): p. 1327-1331.

89. Otto, A., et al., *Surface-Enhanced Raman-Scattering.* Journal of Physics-Condensed Matter, 1992. **4**(5): p. 1143-1212.

90. Zhao, L.L., L. Jensen, and G.C. Schatz, *Pyridine-Ag-20 cluster: A model system for studying surface-enhanced Raman scattering.* Journal of the American Chemical Society, 2006. **128**: p. 2911-2919.

91. Wang, D.S. and M. Kerker, *Enhanced Raman-Scattering by Molecules Adsorbed at the Surface of Colloidal Spheroids.* Physical Review B, 1981. **24**(4): p. 1777-1790.

92. Murphy, C.J., et al., *Anisotropic metal nanoparticles: Synthesis, assembly, and optical applications.* Journal of Physical Chemistry B, 2005. **109**(29): p. 13857-13870.

93. Haynes, C.L., A.D. McFarland, and R.P. Van Duyne, *Surface-Enhanced Raman Spectroscopy.* Analytical Chemistry (Washington, DC, United States), 2005. **77**: p. 338 A-346 A.

94. Haes, A.J. and R.P. Van Duyne, *A Nanoscale Optical Biosensor: Sensitivity and Selectivity of an Approach Based on the Localized Surface Plasmon Resonance Spectroscopy of Triangular Silver Nanoparticles.* J. Am. Chem. Soc. FIELD Full Journal Title:Journal of the American Chemical Society, 2002. **124**: p. 10596.

95. Kneipp, K., et al., *Ultrasensitive Chemical Analysis by Raman spectroscopy.* Chemical Reviews, 1999. **99**.

96. Dieringer, J.A., et al., *Surface enhanced Raman spectroscopy: new materials, concepts, characterization tools, and applications.* Faraday Discussions, 2006. **132**: p. 9-26.

97. Natan, M.J., *Concluding Remarks - Surface enhanced Raman scattering.* Faraday Discussions, 2006. **132**.

98. Moskovits, M., *Surface-enhanced Raman spectroscopy: A brief retrospective.* Journal of Raman Spectroscopy, 2005. **36**.

99. Aroca, R.F., et al., *Surface-enhanced Raman scattering on colloidal nanostructures.* Advances in Colloid and Interface Science, 2005. **116**.

100. De Jesus, M.A., G.K. S., and M.J. Sepaniak, *Use of a Sample Translation Technique to Minimize Adverse Effects of Laser Irradiation in Surface-Enhanced Raman Spectrometry.* Applied Spectroscopy, 2003. **57**.

101. Cermakova, K., et al., *Surface-enhanced raman-scattering (sers) spectroscopy with borohydride-reduced silver colloids - controlling adsorption of the scattering species by surface-potential of silver colloid.* Chemical Communications (Cambridge, United Kingdom), 1993. **58**.

102. Munro, C.H., et al., *Characterization of the surface of a citrate-reduced colloid optimized for use as a substrate for surface-enhanced resonance raman scattering.* Langmuir, 1995. **11**.

103. Turkevich, J., P.C. Stevenson, and J. Hillier, *A study of the nucleation and growth processes in the synthesis of colloidal gold.* Discussions of the Faraday Society, 1951. **11**: p. 55-75.

104. Brust, M., et al., *Synthesis of Thiol-derivatised Gold Nanoparticles in a Two-phase Liquid-Liquid System.* Chemical Communications (Cambridge, United Kingdom), 1994.

105. Perrault, S.D. and W.C.W. Chan, *Synthesis and Surface Modification of Highly Monodispersed, Spherical Gold Nanoparticles of 50-200 nm.* Journal of the American Chemical Society, 2009. **131**.

106. Kelly, K.L., et al., *The optical properties of metal nanoparticles : the influence of size, shape, and dielectric environment.* Journal of Physical Chemistry B, 2003. **107**.

107. GarciaVidal, F.J. and J.B. Pendry, *Collective theory for surface enhanced Raman scattering.* Physical Review Letters, 1996. **77**(6): p. 1163-1166.

108. Zou, S.L. and G.C. Schatz, *Silver nanoparticle array structures that produce giant enhancements in electromagnetic fields.* Chemical Physics Letters, 2005. **403**: p. 62-67.

109. Braun, G., et al., *Surface-Enhanced Raman Spectroscopy for DNA Detection by Nanoparticle Assembly onto Smooth Metal Films.* Journal of the American Chemical Society Communications, 2007. **129** p. 6378-6379.

110. Braun, G., et al., *Generalized Approach to SERS-Active Nanomaterials via Controlled Nanoparticle Linking, Polymer Encapsulation, and Small-Molecule Infusion.* Journal of Physical Chemistry C, 2009. **113**: p. 13622-13629.

111. Averitt, R.D., D. Sarkar, and N.J. Halas, *Plasmon resonance shifts of Au-coated Au2S nanoshells: Insight into multicomponent nanoparticle growth.* Physical Review Letters, 1997. **78**(22): p. 4217-4220.

112. Westcott, S.L., et al., *Formation and adsorption of clusters of gold nanoparticles onto functionalized silica nanoparticle surfaces.* Langmuir, 1998. **14**(19): p. 5396-5401.

113. Oldenburg, S.J., et al., *Nanoengineering of optical resonances.* Chemical Physics Letters, 1998. **288**(2-4): p. 243-247.

114. Oldenburg, S.J., et al., *Surface enhanced Raman scattering in the near infrared using metal nanoshell substrates.* Journal of Chemical Physics, 1999. **111**(10): p. 4729-4735.

115. Barhoumi, A., D. Zhang, and N.J. Halas, *Correlation of Molecular Orientation and Packing Density in a dsDNA Self-Assembled Monolayer Observable with Surface-Enhanced Raman Spectroscopy.* Journal of the American Chemical Society, 2008. **130**(43): p. 14040-14041.

116. Bardhan, R., et al., *Nanoshells with Targeted Simultaneous Enhancement of Magnetic and Optical Imaging and Photothermal Therapeutic Response.* Advanced Functional Materials, 2009. **19**(24): p. 3901-3909.

117. Choi, M.R., et al., *Delivery of Therapeutic Nanoshells to Hypoxic Areas of Tumors Using a Cellular Trojan Horse.* Cancer Research, 2009. **69**(24): p. 860S-861S.

118. Haynes, C.L. and R.P. Van Duyne, *Nanosphere lithography: A versatile nanofabrication tool for studies of size-dependent nanoparticle optics.* Journal of Physical Chemistry B, 2001. **105**(24): p. 5599-5611.

119. Jensen, T.R., et al., *Nanosphere lithography: Tunable localized surface plasmon resonance spectra of silver nanoparticles.* Journal of Physical Chemistry B, 2000. **104**(45): p. 10549-10556.

120. Litorja, M., et al., *Surface-enhanced Raman scattering detected temperature programmed desorption: Optical properties, nanostructure, and stability of silver film over SiO2 nanosphere surfaces.* Journal of Physical Chemistry B, 2001. **105**(29): p. 6907-6915.

121. Haes, A.J., et al., *A nanoscale optical biosensor: The long range distance dependence of the localized surface plasmon resonance of noble metal nanoparticles.* Journal of Physical Chemistry B, 2004. **108**(1): p. 109-116.

122. Willets, K.A. and R.P. Van Duyne, *Localized Surface Plasmon Resonance Spectroscopy and Sensing.* Annu. Rev. Phys. Chem., 2007. **58**: p. 267-97.

123. Dieringer, J.A., et al., *Surface-Enhanced Raman Excitation Spectroscopy of a Single Rhodamine 6G Molecule.* Journal of the American Chemical Society, 2009. **131**(2): p. 849-854.

124. Camden, J.P., et al., *Probing the Structure of Single-Molecule Surface-Enhanced Raman Scattering Hot Spots.* Journal of the American Chemical Society, 2008. **130**(38): p. 12616-12617.

125. Anker, J.N., et al., *Biosensing with plasmonic nanosensors.* Nature Materials, 2008. **7**(6): p. 442-453.

126. Camden, J.P., et al., *Controlled Plasmonic Nanostructures for Surface-Enhanced Spectroscopy and Sensing.* Accounts of Chemical Research, 2008. **41**(12): p. 1653-1661.

127. Haynes, C.L., et al., *Surface-enhanced Raman sensors: early history and the development of sensors for quantitative biowarfare agent and glucose detection.* Journal of Raman Spectroscopy, 2005. **36**: p. 471-484.

128. Yonzon, C.R., et al., *A comparative analysis of localized and propagating surface plasmon resonance sensors: The binding of concanavalin a to a monosaccharide functionalized self-assembled monolayer.* Journal of the American Chemical Society, 2004. **126**(39): p. 12669-12676.

129. Zhao, J., et al., *Localized surface plamson resonance biosensors.* Nanomedicine, 2006. **1**(2): p. 219-228.

130. El-Sayed, M.A., *Some interesting properties of metals confined in time and nanometer space of different shapes.* Accounts of Chemical Research, 2001. **34**(4): p. 257-64.

131. Murphy, C.J., et al., *One-Dimensional Colloidal Gold and Silver Nanostructures.* Inorganic Chemistry, 2006. **45**(19): p. 7544-7554.

132. Dluhy, R.A., *Nanostructure Arrays for Virus Detection*. 2004, NIH: University of Georgia, Georgia Institute of Technology. p. 38.

133. Driskell, J.D., et al., *Rapid microRNA (miRNA) detection and classification via surface-enhanced Raman spectroscopy (SERS).* Biosensors & Bioelectronics, 2008. **24**(4): p. 917-922.

134. Driskell, J.D., et al., *The Use of Aligned Silver Nanorod Arrays Prepared by Oblique Angle Deposition as Surface Enhanced Raman Scattering Substrates.* Journal of Physical Chemistry C, 2008. **112**(4): p. 895-901.

135. Driskell, J.D., et al., *Infectious agent detection with SERS-active silver nanorod arrays prepared by oblique angle deposition.* IEEE Sensors Journal, 2008. **8**(5-6): p. 863-870.

136. Zhao, Y.P., S.B. Chaney, and Z.Y. Zhang, *Absorbance spectra of aligned Ag nanorod arrays prepared by oblique angle deposition.* Journal of Applied Physics, 2006. **100**(6): p. 063527/1-063527/8.

137. Zhao, Y.P., et al., *Designing nanostructures for sensor applications.* Journal of Electronic Materials, 2006. **35**(5): p. 846-851.

138. Zhao, Y.P., et al., *Silver nanorod arrays as highly sensitive SERS substrates for viral detection.* Proceedings of the SPIE-The International Society for Optical Engineering, 2006. **6324**(Plasmonics: Nanoimaging, Nanofabrication, and Their Applications II): p. 63240M/1-63240M/9.

139. Shanmukh, S., et al., *Rapid and sensitive detection of respiratory virus molecular signatures using a silver nanorod array SERS substrate.* Nano Letters, 2006. **6**(11): p. 2630-2636.

140. Shanmukh, S., et al., *Identification and classification of respiratory syncytial virus (RSV) strains by surface-enhanced Raman spectroscopy and multivariate statistical techniques.* Anal. Bioanal. Chem., 2008. **390**: p. 1551–1555.

141. Liu, Y., et al., *Angle dependent surface enhanced Raman scattering obtained from a Ag nanorod array substrate.* Applied Physics Letters, 2006. **89**(17): p. 173134/1-173134/3.

142. Murphy, C.J., et al., *Surfactant-directed synthesis and optical properties of one-dimensional plasmonic metallic nanostructures.* Mrs Bulletin, 2005. **30**(5): p. 349-355.

143. Chaney, S.B., et al., *Aligned silver nanorod arrays produce high sensitivity surface-enhanced Raman spectroscopy substrates.* Applied Physics Letters, 2005. **87**(3): p. 031908/1-031908/3.

144. Leverette, C.L. and R.A. Dluhy, *Vibrational characterization of a planar-supported model bilayer system utilizing surface-enhanced Raman scattering (SERS) and infrared reflection-absorption spectroscopy (IRRAS).* Colloids and Surfaces A: Physicochemical and Engineering Aspects, 2004. **243**(1-3): p. 157-167.

145. Leverette, C.L., et al., *Aligned silver nanorod arrays as substrates for surface-enhanced infrared absorption spectroscopy.* Applied Spectroscopy, 2006. **60**(8): p. 906-913.

146. Leverette, C.L., et al., *Development of A Novel Dual-Layer Thick Ag Substrate for Surface-Enhanced Raman Scattering (SERS) of Self-Assembled Monolayers.* Journal of Physical Chemistry B, 2002. **106**(34): p. 8747-8755.

147. Tripp, R.A., R. Dluhy, and Y.-P. Zhao, *Novel nanostructures for SERS biosensing.* NanoToday, 2008. **8**(3-4): p. 31-37.

148. Zhao, Y.P., et al., *Polarized Surface Enhanced Raman and Absorbance Spectra of Aligned Silver Nanorod Arrays.* Journal of Physical Chemistry B, 2006. **110**(7): p. 3153-3157.

149. Dhawan, A., et al., *Nano-engineered surface-enhanced Raman scattering (SERS) substrates with patterned structures on the distal end of optical fibers.* Proceedings of the SPIE, 2008. **6869**(Plasmonics in Biology and Medicine V): p. 68690G/1-68690G/10.

150. Qian, X.M. and S.M. Nie, *Single-molecule and single-nanoparticle SERS: from fundamental mechanisms to biomedical applications.* Chemical Society Reviews, 2008. **37**(5): p. 912-920.

151. Scaffidi, J.P., et al., *SERS-based plasmonic nanobiosensing in single living cells.* Analytical and Bioanalytical Chemistry, 2009. **393**(4): p. 1135-1141.

152. Vo-Dinh, T., *Nanobiosensing using plasmonic nanoprobes.* IEEE Journal of Selected Topics in Quantum Electronics, 2008. **14**(1): p. 198-205.

153. Gish, D.A., et al., *Localized Surface Plasmon Resonance Biosensor Using Silver Nanostructures Fabricated by Glancing Angle Deposition.* Analytical Chemistry (Washington, DC, United States), 2007. **79**(11): p. 4228-4232.

154. Qian, X., X. Zhou, and S. Nie, *Surface-Enhanced Raman Nanoparticle Beacons Based on Bioconjugated Gold Nanocrystals and Long Range Plasmonic Coupling.* Journal of the American Chemical Society, 2008. **130**(45): p. 14934-14935.

155. Thanh, N.T.K. and Z. Rosenzweig, *Development of an aggregation-base immunoassay for anti-protein A using gold nanoparticles.* Analytical Chemistry (Washington, DC, United States), 2002. **74**.

156. Wei, F., et al., *Aromatic Amino Acids Providing Characteristic Motifs in the Raman and SERS Spectroscopy of Peptides.* Journal of Physical Chemistry B, 2008. **112**(30): p. 9158-9164.

157. Nithipatikom, K., et al., *Characterization and application of Raman labels for confocal Raman microspectroscopic detection of cellular proteins in single cells.* Analytical Biochemistry, 2003. **322**(2): p. 198-207.

158. Huang, W.E., et al., *Raman Microscopic Analysis of Single Microbial Cells.* Analytical Chemistry, 2004. **76**(15): p. 4452-4458.

159. Krafft, C., et al., *Mapping of single cells by near infrared Raman microspectroscopy* Vibrational Spectroscopy, 2003. **32**: p. 75-83.

160. Sujuth, A., et al., *Imaging the cell wall of living single yeast cells using surface-enhanced Raman spectroscopy.* Analytical and Bionalytical Chemistry, 2009. **394**: p. 1803-1809.

161. Alexander, T.A., P.M. Pellegrino, and J.B. Gillespie, *Near-Infrared Surface-Enhanced-Raman-Scatterinf-Mediated Detection of Single Optically Trapped Bacterial Spores.* Applied Spectroscopy, 2003. **57**(11).

162. Chu, H., Y. Huang, and Y. Zhao, *Silver Nanorod Arrays as a Surface-Enhanced Raman Scattering Substrate for Foodborne Pathogenic Bacteria Detection.* Applied Spectroscopy, 2008. **62**(8): p. 922-931.

163. Culha, M., et al., *Characterization of Thermophillic Bacteria Using Surface-Enhanced Raman Scattering.* Applied Spectroscopy, 2008. **62**(11): p. 1226-1232.

164. de Gelder, J., et al., *Raman spectroscopic study of bacterial endospores.* Analytical and Bionalytical Chemistry, 2007. **389**: p. 2143-2151.

165. Efirma, S. and B.V. Bronk, *Silver Colloids Impregnating or Coating Bacteria.* Journal of Physical Chemistry B, 1998. **102**(31): p. 5947-5950.

166. Efirma, S. and I. Zeiri, *Understanding SERS of bacteria.* Journal of Raman Spectroscopy, 2009. **40**: p. 277-288.

167. Goeller, L.J. and M.R. Riley, *Discrimination of Bacteria and Bacteriophages by Raman Spectroscopy and Surface-enhanced Raman Spectroscopy.* Applied Spectroscopy, 2007. **61**(7): p. 679-685.

168. Jarvis, R.M., A. Brooker, and R. Goodacre, *Surface-enhanced Raman scattering for the rapid discrimination of bacteria.* Faraday Discussions, 2005. **132**: p. 281-292.

169. Jarvis, R.M. and R. Goodacre, *Discrimination of Bacteria Using Surface-Enhanced Raman Spectroscopy.* Analytical Chemistry, 2008. **76**(1): p. 40-47.

170. Jarvis, R.M., et al., *Surface-Enhanced Raman Scattering from Intracellular and Extracellular Bacterial Locations.* Analytical Chemistry, 2008. **80**: p. 6741-6746.

171. Kahraman, M., et al., *Reproducible Surface-Enhanced Raman Scattering Spectra of Bacteria on Aggregated Silver Nanoparticles.* Applied Spectroscopy, 2007. **61**(5): p. 479-485.

172. Kahraman, M., et al., *Experimental parameters influencing surfafe-enhanced Raman scattering of bacteria* Journal of Biomedical Optics, 2007. **12**(5): p. 054015-1-6.

173. Kahraman, M., et al., *Convective assembly of Bacteria for Surface-Enhanced Raman Scattering.* Langmuir, 2008. **24**(894-901).

174. Laucks, M.L., et al., *Comparison of Psychro-active Arctic Marine Bacteria and Common Mesophillic Bacteria Using Surface-Enhanced Raman Spectroscopy.* Applied Spectroscopy, 2005. **59**(10): p. 1222-1228.

175. Liu, Y., et al., *Label-Free SERS for Rapid Species Identification of Escherichia coli, Listeria monocytogenes, and Salmonella typhimurium Bacteria.* Spectroscopy Online, 2008. **32**(2): p. 48-54.

176. Marotta, N.E. and L.A. Bottomley, *Surface Enhanced Raman Scattering of Bacterial Cell Culture Growth Media.* Applied Spectroscopy, 2010. **64**: p. in press.

177. Patel, I.S., et al., *Barcoding bacterial cells: a SERS-based methodology for pathogen identification.* Journal of Raman Spectroscopy, 2008. **39**: p. 1660-1672.

178. Schuster, K.C., E. Urlaub, and J.R. Gapes, *Single-cell analysis of bacteria by Raman microscopy: spectral information on the chemical composition of cells and on the heterogeneity in a culture.* Journal of Microbiological Methods, 2000. **42**: p. 29-38.

179. Sengupta, A., M.L. Laucks, and E.J. Davis, *Surface-Enhanced Raman Spectroscopy of Bacteria and Pollen.* Applied Spectroscopy, 2005. **59**(8): p. 1016-1023.

180. Sengupta, A., M. Mujacic, and E.J. Davis, *Detection of bacteria by surface-enhanced Raman spectroscopy.* Analytical and Bioanalytical Chemistry, 2006. **386**: p. 1379-1386.

181. Zeiri, I., et al., *Silver metal induced surface enhance Raman of bacteria.* Colloids and Surfaces A: Physicochemical and Engineering Aspects, 2002. **208**: p. 357-362.

182. Zeiri, I., et al., *Surface-Enhanced Raman Spectroscopy as a Tool for Probing Biochemical Components in Bacteria.* Applied Spectroscopy, 2004. **58**(1): p. 33-40.

183. Zeiri, I. and S. Efirma, *Surface-enhanced Raman spectroscopy of bacteria: the effect of excitation wavelength and chemical modification of the colloidal milieu.* Journal of Raman Spectroscopy, 2005. **36**: p. 667-675.

184. Faulds, K., W. Smith, and D. Graham, *DNA detection by surface enhanced resonance Raman scattering (SERRS).* The Analyst, 2005. **130**: p. 1125-1131.

185. Liu, J. and Y. Lu, *Design of asymmetric DNAzymes for dynamic control of nanoparticle aggregation states in response to chemical stimuli.* Organic & Biomolecular Chemistry, 2006. **4**.

186. Park, T., et al., *Highly sensitive signal detection of duplex dye-labelled DNA oligonucleotides in a PDMS microfluidic chip: confocal surface-enhanced Raman spectroscopic study.* Lab on a Chip, 2005. **5**(4): p. 437-442.

187. Rosi, N.L. and C.A. Mirkin, *Nanostructures in biodiagnostics.* Chemical Reviews, 2005. **105**.

188. Porter, M.D., et al., *SERS as a bioassay platform: fundamentals, design, and applications.* Chemical Society Reviews, 2008. **37**: p. 1001-1011.

189. Sastry, M., et al., *Optical Absorption Study of the Biotin−Avidin Interaction on Colloidal Silver and Gold Particles.* Langmuir, 1998. **14**.

190. Fullam, S., N. Rao, and D. Fitzmaurice, *Noncovalent self- assembly of silver nanocrystal aggregates in solution.* Journal of Physical Chemistry B, 2000. **104**.

191. Liu, J. and Y. Lu, *Adenosine-dependent assembly of aptazyme-functionalized gold nanoparticles and its application as a colorimetric biosensor.* Analytical Chemistry (Washington, DC, United States), 2004. **76**: p. 1627-1632.

192. Aslan, K., et al., *Saccharide Sensing Using Gold and Silver Nanoparticles.* Journal of Fluorecence, 2004. **14**.

193. Kim, Y., R.C. Johnson, and J.T. Hupp, *Gold Nanoparticle Based Sensing of "Spectroscopically Silent" Heavy Metal Ions.* Nano Letters, 2001. **1**.

194. Demirel, M.C., et al., *Bio-organism sensing via surface enhanced Raman spectroscopy on controlled metal/polymer nanostructured substrates.* Biointerphases, 2009. **4**(2): p. 35-41.

195. Driskell, J.D., et al., *Rapid and Sensitive Detection of Rotavirus Molecular Signatures Using Surface Enhanced Raman Spectroscopy.* PLoS One, 2010. **5**(4).

196. Alexander, T.A., *Development of methodology based on commercialized SERS-active substrates for rapid discrimination of Poxviridae virions.* Analytical Chemistry, 2008. **80**(8): p. 2817-2825.

197. Bao, P.D., et al., *Surface-enhanced Raman spectroscopy of insect nuclear polyhedrosis virus.* Journal of Raman Spectroscopy, 2001. **32**(4): p. 227-230.

198. Driskell, J.D., et al., *Low-level detection of viral pathogens by a surface-enhanced Raman scattering based immunoassay.* Analytical Chemistry, 2005. **77**(19): p. 6147-6154.

199. Harpster, M.H., et al., *SERS detection of indirect viral DNA capture using colloidal gold and methylene blue as a Raman label.* Biosensors & Bioelectronics, 2009. **25**(4): p. 674-681.

200. Liang, Y., et al., *Biocompatible core-shell nanoparticle-based surface-enhanced Raman scattering probes for detection of DNA related to HIV gene using silica-coated magnetic nanoparticles as separation tools.* Talanta, 2007. **72**(2): p. 443-449.

201. Luna-Pineda, T., et al., *Spectroscopic Characterization of Biological Agents Using FTIR, Normal Raman and Surface Enhanced Raman Scattering.* Proceedings of SPIE, 2007. **6554**: p. 65540K-1-11.

202. Naja, G., et al., *Raman-based detection of bacteria using silver nanoparticles conjugated with antibodies.* Analyst, 2007. **132**: p. 679-686.

203. Ivleve, N.P., et al., *In Situ Surface-Enhanced Raman Scattering Analysis of Biofilm.* Analytical Chemistry, 2008. **80**(22): p. 8538-8544.

204. Xie, C., et al., *Identification of Single Bacterial Cells in Aqueous Solution Using Confocal Laser Tweezers Raman Spectroscopy.* Analytical Chemistry, 2005. **77**(14): p. 4390-4397.

205. Schuster, K.C., et al., *Multidimensional Information on the Chemical Composition of Single Bacterial Cells by Confocal Raman Microspectroscopy.* Analytical Chemistry, 2000. **72**(22): p. 5529-5534.

206. Storhoff, J.J., et al., *One-Pot Colorimetric Differentiation of Polynucleotides with Single Base Imperfections Using Gold Nanoparticle Probes.* Journal of the American Chemical Society, 1998. **120**.

207. Halas, N., *Playing with plasmons. Tuning the optical resonant properties of metallic nanoshells.* M.R.S. Bulletin, 2005. **30**(5): p. 362-367.

208. Heck, K.N., et al., *Observing Metal-Catalyzed Chemical Reactions in Situ Using Surface-Enhanced Raman Spectroscopy on Pd-Au Nanoshells.* Journal of the American Chemical Society, 2008. **130**(49): p. 16592-16600.

209. Lal, S., et al., *Tailoring plasmonic substrates for surface enhanced spectroscopies.* Chemical Society Reviews, 2008. **37**(5): p. 898-911.

210. Lassiter, J.B., et al., *Reshaping the Plasmonic Properties of an Individual Nanoparticle.* Nano Letters, 2009. **9**(12): p. 4326-4332.

211. Graham, D., K. Faulds, and W.E. Smith, *Biosensing using silver nanoparticles and surface enhanced resonance Raman scattering.* Chemical Communications (Cambridge, United Kingdom), 2006: p. 4363-4371.

212. Graham, D., et al., *Control of enhanced Raman scattering using a DNA-based assembly process of dye-coded nanoparticles.* Nature Nanotechnology, 2008. **3**.

213. Herne, T.M. and M.J. Tarlov, *Characterization of DNA probes immobilized on gold surfaces.* Journal of the American Chemical Society, 1997. **119**(38): p. 8916-8920.

214. Herne, T.M. and M.J. Tarlov, *Structural characterization and hybridization reactions of surface bound, single-stranded DNA.* Abstracts of Papers of the American Chemical Society, 1997. **214**: p. 62-MTLS.

215. Tarlov, M., et al., *DNA-Probe Modified Alkanethiol Monolayers.* Abstracts of Papers of the American Chemical Society, 1995. **209**: p. 160-COLL.

216. Steel, A.B., T.M. Herne, and M.J. Tarlov, *Electrochemical quantitation of DNA immobilized on gold.* Analytical Chemistry, 1998. **70**(22): p. 4670-4677.

217. Olsen, K.G., A.B. Steel, and M.J. Tarlov, *Immobilized DNA electrodes: The effect of target length on DNA hybridization.* Abstracts of Papers of the American Chemical Society, 2000. **220**: p. 310-COLL.

218. Villanueva, M., et al., *DNA hybridization on electrode surfaces.* Abstracts of Papers of the American Chemical Society, 2000. **220**: p. 132-CHED.

219. Petrovykh, D.Y., et al., *Quantitative analysis and characterization of DNA immobilized on gold.* Journal of the American Chemical Society, 2003. **125**(17): p. 5219-5226.

220. Bunshah, R.F., ed. *Handbook of Deposition Technologies for Films and Coatings*. second ed. Science, Technology, and Applications. 1974, Noyes Publictions: Westwood, NJ.

221. Mahan, J.E., *Physical Vapor Deposition of Thin Films*. 2000, New York, NY: John Wiley and Sons. 340.

222. Ohring, M., *Materials Science og Thin Film*. 2002, San Diego: Academic Press.

223. Thornton, J.A., *Semiconductor Materials and Process Technology Handbook for Very Large Sclae Integration (VLSI) and Ulta Large Scale Integration (ULSI)*, ed. G.F. McGuire. 1988, Park Ridge, N.J.: Noyes Publications.

224. Maissel, L. and R. Glang, eds. *Handbook of Thin Film Technology*. 1970, McGraw-Hill: New York. 1216.

225. Mucha, J.A., D.W. Hess, and E.S. Aydil, *Plasma Etching*, in *Introduction to Microlithography*, W. Thompson, Bowden, Editor. 1994, American Chemical Society. p. 377-507.

226. Hawkeye, M.M. and M.J. Brett, *Glancing angle deposition: Fabrication, properties, and applications of micro- and nanostructured thin films.* Journal of Vacuum Science & Technology, A: Vacuum, Surfaces, and Films, 2007. **25**(5): p. 1317-1335.

227. Kundt, A., *On the Double Refraction of Light in Metal Layers Which have been Prepared by Kathode Sputtering.* Ann. Phys., 1886. **27**(59).

228. Holland, L., *The Effect of Vapor Incidence on the Structure of Evaporated Aluminum Films.* Journal of the Optical Society of America A: Optics and Image Science, 1953. **43**: p. 376-380.

229. Holland, L., *Vapor Deposition of Thin Films*. 1956, New York: Wiley.

230. Smith, D.O., *Anisotropy in Permalloy Films.* Journal of Applied Physics, 1959. **30**: p. 264S.

231. Knorr, T.G. and R.W. Hoffman, *Dependence of Geometric Magnetic Anisotropy in Thin Iron Films.* Physical Review 1959. **113**: p. 1039-1046

232. Nieuwenhuizen, J.M. and H.B. Haanstra, Philips Technical Review, 1966. **27**: p. 87.

233. Konig, H. and G. Helwig, **Uber Die Struktur Schrag Aufgedampfter Schichten Und Ihr Einfluss Auf Die Entwicklung Submikroskopischer Oberflachenrauhigkeiten.* Optik, 1950. **6**(2): p. 111-124.

234. Brett, M.J. and M.M. Hawkeye, *New materials at a glance.* Science (Washington, DC, United States), 2008. **319**: p. 1192-1193.

235. Brett, M.J. and M.J. Colgan, *Field emission from carbon and silicon films with pillar microstructure* Thin Solid Films, 2001. **389**(1): p. 1-4.

236. Brett, M.J. and J.N. Broughton, *Electrochemical capacitance in manganese thin films with chevron microstructure* ELECTROCHEMICAL AND SOLID STATE LETTERS, 2002. **5**: p. A279.

237. Kiema, G.K., M.J. Colgan, and M.J. Brett, *Dye sensitized solar cells incorporating obliquely deposited titanium oxide layers* SOLAR ENERGY MATERIALS AND SOLAR CELLS 2005. **85**(3): p. 321-331.

238. Bauer, E. and J.H. van der Merwe, *Structure and growth of crystalline superlattices: From monolayer to superlattice.* Physical Review B, 1986. **33**: p. 3657-3671.

239. Koch, R., *The intrinsic stress of polycrystalline and epitaxial thin metal films.* Journal of Physics - Condensed Matter, 1994. **6**: p. 9519-9550.

240. Vook, R.W., *THEORIES OF NUCLEATION AND GROWTH OF THIN-FILMS* PROCEEDINGS OF THE SOCIETY OF PHOTO-OPTICAL INSTRUMENTATION ENGINEERS, 1982. **346** p. 2-8.

241. Reichelt, K., *NUCLEATION AND GROWTH OF THIN-FILMS* Vacuum, 1988. **38**(12): p. 1083-1099.

242. Abelmann, L. and C. Lodder, *Oblique evaporation and surface diffusion.* Thin Solid Films, 1997. **305**(1-2): p. 1-21.

243. Vick, D., et al., *Production of porous carbon thin films by pulsed laser deposition.* Thin Solid Films, 1999. **350**(1,2): p. 49-52.

244. Hrudey, P.C.P., K.L. Westra, and M.J. Brett, *Highly ordered organic Alq3 chiral luminescent thin films fabricated by glancing-angle deposition* Advanced Materials 2006. **18** (2): p. 224.

245. Smith, D.O., M.S. Cohen, and G.P. Weiss, *OBLIQUE-INCIDENCE ANISOTROPY IN EVAPORATED PERMALLOY FILMS* JOURNAL OF APPLIED PHYSICS 1960. **31** (10): p. 1755-1762.

246. Barabasi, A.-L. and H.E. Stanley, *Fractal Comcepts in Surface Growth*. 1995, Cambridge: Cambridge University Press.

247. Kaminska, K., et al., *Growth of vacuum evaporated ultraporous silicon studied with spectroscopic ellipsometry and scanning electron microscopy.* Journal of Applied Physics, 2005. **97**(1): p. 013511/1-013511/8.

248. Karabacak, T., G.C. Wang, and T.M. Lu, *Quasi-periodic nanostructures grown by oblique angle deposition.* Journal of Applied Physics, 2003. **94**(12): p. 7723-7728

249. Elias, A.L., K.D. Harris, and M.J. Brett, *Fabrication of helically perforated nickel, gold, and polystyrene thin films.* Journal of Microelectromechanical Systems, 2004. **13**: p. 808-813.

250. Harris, K.D., A. Huizinga, and M.J. Brett, *High-Speed Porous Thin Film Humidity Sensors.* Electrochem. Solid-St. Lett., 2002. **5**.

251. Harris, K.D., et al., *Fabrication of porous platinum thin films for hydrocarbon sensor applications.* Sensors and Materials, 2001. **13**(4): p. 225-234.

252. Harris, K.D., et al., *Porous thin films for thermal barrier coatings.* Surface and Coatings Technology, 2001. **138**(2-3): p. 185-191.

253. Harris, K.D., K.L. Westra, and M.J. Brett, *Fabrication of perforated thin films with helical and chevron pore shapes.* Electrochemical and Solid-State Letters, 2001. **4**(6): p. C39-C42.

254. Harris, K.D., K.L. Westra, and M.J. Brett, *Fabrication of helically perforated thin films.* Materials Research Society Symposium Proceedings, 2001. **636**(Nonlithographic and Lithographic Methods of Nanofabrication: From Ultralarge-Scale Integration to Photonics to Molecular Electronics): p. D9 37/1-D9 37/6.

255. Jensen, L. and M.J. Brett, *Periodically structured glancing angle deposition thin films.* IEEE Transactions on Nanotechnology, 2005. **4**: p. 269.

256. Malac, M., et al., *Fabrication of submicrometer regular arrays of pillars and helices.* Journal of Vacuum Science & Technology, B: Microelectronics and Nanometer Structures, 1999. **17**(6): p. 2671-2674.

257. Dick, B., et al., *Periodic magnetic microstructures by glancing angle deposition.* Journal of Vacuum Science & Technology, A: Vacuum, Surfaces, and Films, 2000. **18**(4, Pt. 2): p. 1838-1844.

258. Malac, M. and R.F. Egerton, *Observations of the microscopic growth mechanism of pillars and helices formed by glancing-angle thin-film deposition.* Journal of Vacuum Science & Technology A, 2001. **19**: p. 158.

259. Horn, M.W., et al., *Selective growth of sculptured nanowires on microlithographic lattices.* Journal of Vacuum Science & Technology B, 2004. **22**: p. 3426.

260. Malac, M. and R.F. Egerton, *Thin-film regular-array structures with 10-100 nm repeat distance* Nanotechnology, 2001. **12**: p. 11.

261. Dick, B., et al., *Embossed Polymeric Relief Structures as a Template for the Growth of Periodic Inorganic Microstructures.* Nano Letters, 2001. **1**(2): p. 71-73.

262. Ye, D.X., et al., *Growth of uniformly aligned nanorod arrays by oblique angle deposition with two-phase substrate rotation.* Nanotechnology, 2004. **15**(7): p. 817-821.

263. Horn, M.W., et al., *Blending of nanoscale and microscale in uniform large-area sculptured thin-film architectures* Nanotechnology, 2004. **15**.

264. Ye, D.X., et al., *Uniform Si nanostructures grown by oblique angle deposition with substrate swing rotation* Nanotechnology, 2005. **16**.

265. Jensen, M.O. and M.J. Brett, *Functional pattern engineering in glancing angle deposition thin films.* Journal of Nanoscience and Nanotechnology, 2005. **5**(5): p. 723-728.

266. Kesapragada, S.V. and D. Gall, *Anisotropic broadening of Cu nanorods during glancing angle deposition.* Applied Physics Letters, 2006. **89**(20).

267. Zhou, C.M. and D. Gall, *The structure of Ta nanopillars grown by glancing angle deposition.* Thin Solid Films, 2006. **515**(3): p. 1223-1227.

268. Robbie, K. and M.J. Brett, *Sculptured thin films and glancing angle deposition: growth mechanics and applications.* Journal of Vacuum Science & Technology, A: Vacuum, Surfaces, and Films, 1997. **15**(3, Pt. 2): p. 1460-1465.

269. Jensen, M.O. and M.J. Brett, *Porosity engineering in glancing angle deposition thin films.* Applied Physics A: Materials Science & Processing, 2005. **80**(4): p. 763-768.

270. Gish, D.A., M.A. Summers, and M.J. Brett, *Morphology of periodic nanostructures for photonic crystals grown by glancing angle deposition.* Photonics and Nanostructures - Fundamentals and Applications, 2006. **4**(1): p. 23-29.

271. Robbie, K., et al., *Fabrication of Thin Films with Highly Porous Microstructures.* Journal of Vacuum Science and Technology A, 1995. **13**(3): p. 1032-1035.

272. Hodgkinson, I., et al., *Vacuum Deposition of Biaxial Films with Surface-Alligned Principle Axes and Large Bifringence*. OSA Technical Digest Series Vol. 9. 1998, Washington DC: Optical Society of America.

273. Macleod, H.A., *Thin-Film Optical Filters*. 1986, New York: McGraw-Hill.

274. Steele, J.J. and M.J. Brett, *Nanostructure engineering in porous columnar thin films. Recent advances.* Journal of Materials Science: Materials in Electronics, 2007. **18**(4): p. 367-379.

275. Motohiro, T. and Y. Taga, *Thin film retardation plate by oblique deposition.* Applied Optics, 1989. **28**: p. 2466–2482.

276. Robbie, K., M.J. Brett, and A. Lakhtakia, *Chiral sculptured thin film.* Nature (London), 1996. **384**: p. 616.

277. Kaminska, K., et al., *Vacuum evaporated porous silicon photonic interference filters.* Applied Optics, 2003. **42**(20): p. 4212-4219.

278. Kaminska, K. and K. Robbie, *Birefringent omnidirectional reflector.* Applied Optics, 2004. **43**(7): p. 1570-1576.

279. Kennedy, S.R. and M.J. Brett, *Porous Broadband Antireflection Coating by Glancing Angle Deposition.* Applied Optics, 2003. **42**(22): p. 4573-4579.

280. Steele, J.J., et al., *Nanostructured gradient index optical filter for high-speed humidity sensing.* Sensors and Actuators, B: Chemical, 2006. **B120**(1): p. 213-219.

281. van Popta, A.C., et al., *Porous nanostructured optical filters rendered insensitive to humidity by vapor-phase functionalization.* Advanced Functional Materials, 2006. **16**(10): p. 1331-1336.

282. Suzuki, M. and Y. Taga, *Numerical study of the effective surface area of obliquely deposited thin films.* Journal of Applied Physics, 2001. **90**.

283. O'Regan, B. and M. Grätzel, *A low-cost, high-efficiency solar cell based on dye-sensitized colloidal TiO2 films.* Nature (London), 1991. **353**: p. 737.

284. Saraf, L., et al., *Ceria Incorporation into YSZ Columnar Nanostructures.* Electrochem. Solid-St. Lett., 2005. **8**.

285. Steele, J.J., et al., *Impact of morphology on high-speed humidity sensor performance* IEEE SENSORS JOURNAL, 2006. **6** (1): p. 24-27.

286. Suzuki, M., T. Ito, and Y. Taga, *Photocatalysis of sculptured thin films of TiO2* Applied Physics Letters, 2001. **78**.

287. Tsoi, S., et al., *Superhydrophobic, High Surface Area, 3-D SiO2 Nanostructures through Siloxane-Based Surface Functionalization.* Langmuir, 2004. **20**: p. 10771-10773.

288. Tsoi, S., et al., *Surface Functionalization of Porous Nanostructured Metal Oxide Thin Films Fabricated by Glancing Angle Deposition.* Chemistry of Materials, 2006. **18**: p. 5260-5266.

289. Pawar, A.B. and I. Kretzschmar, *Multifunctional Patchy Particles by Glancing Angle Deposition.* Langmuir, 2009. **25**(9057): p. 9057–9063.

290. Pawar, A.B. and I. Kretzschmar, *Patchy Particles by Glancing Angle Deposition".* Langmuir, 2008. **24**: p. 355-358.

291. McDermott, J.J. and D. Velegol, *Simple Fabrication of Metallic Colloidal Doublets Having Electrical Connectivity.* Langmuir, 2008. **24**: p. 4335-4339.

292. Marotta, N.E., et al., *Patterned Silver Nanorod Array Substrates for Surface-Enhanced Raman Scattering.* Applied Spectroscopy, 2009. **63**(10): p. 1101-1106.

293. Jensen, M.O. and M.J. Brett, *Embedded air and solid defects in periodically structured porous thin films.* Nanotechnology, 2005. **16**(11): p. 2639-2646.

294. Balakrishnan, J., I.D. Boyd, and D.G. Braun, *Monte Carlo simulation of vapor transport in physical vapor deposition of titanium.* Journal of Vacuum Science & Technology, A: Vacuum, Surfaces, and Films, 2000. **18**(3): p. 907-916.

295. Ellegaard, O., J. Schou, and H.M. Urbassek, *Monte Carlo description of gas flow from laser-evaporated silver.* Applied Physics A: Materials Science & Processing, 1999. **69**(Suppl.): p. S577-S581.

296. Fan, J., I.D. Boyd, and C. Shelton, *Monte Carlo modeling of electron beam physical vapor deposition of yttrium.* Journal of Vacuum Science & Technology, A: Vacuum, Surfaces, and Films, 2000. **18**(6): p. 2937-2945.

297. Liu, H.W., et al., *Monte Carlo simulations of gas flow and heat transfer in vacuum packaged MEMS devices.* Applied Thermal Engineering, 2007. **27**(2-3): p. 323-329.

298. Minson, P., A. Powell, and G. Trapaga, *Theory of vapor plume focusing in electron beam evaporation by the direct simulation Monte-Carlo method.* Proceedings of the Conference on Electron Beam Melting and Refining--State of the Art, 1996. **1996**: p. 126-137.

299. Liu, Y.C., C.C. Yu, and S.F. Sheu, *Low concentration rhodamine 6G observed by surface-enhanced Raman scattering on optimally electrochemically roughened silver substrates.* Journal of Materials Chemistry, 2006. **16**(35): p. 3546-3551.

300. Pristinski, D., et al., *In situ SERS study of Rhodamine 6G adsorbed on individually immobilized Ag nanoparticles.* Journal of Raman Spectroscopy, 2006. **37**(7): p. 762-770.

301. Morgenstern, K., G. Rosenfeld, and G. Comsa, *Local correlation during Ostwald ripening of two-dimensional islands on Ag(111).* Surface Science, 1999. **441**(2-3): p. 289-300.

302. Pedemonte, L., R. Tatarek, and G. Bracco, *Surface self-diffusion at intermediate temperature: The Ag(110) case.* Physical Review B, 2002. **66**(4): p. 5.

303. Liu, Y.J., et al., *Surface Enhanced Raman Scattering from an Ag Nanorod Array Substrate: The Site Dependent Enhancement and Layer Absorbance Effect.* Journal of Physical Chemistry C, 2009. **113**(22): p. 9664-9669.

304. Whitney, A.V., et al., *Toward A Thermally Robust Operando Surface-Enhanced Raman Spectroscopy (SERS) Substrate.* Journal of Physical Chemistry C, 2007. **111**(45): p. 16827-16832.

305. Morgenstern, K., K.-H. Rieder, and G.A. Fiete, *Disorder-induced local-density-of-states oscillations on narrow Ag(111) terraces.* Phys. Rev. B: Condens. Matter Mater. Phys. , 2005. **71**(15): p. 155413/1-155413/12.

306. Esser, M., et al., *Dynamics of vacancy island coalescence on Ag(111).* Surface Science, 1998. **402-404**: p. 341-345.

307. Kaganer, V.M., K.H. Ploog, and K.K. Sabelfeld, *Coarsening of facetted two-dimensional islands by dynamic coalescence.* Physical Review B, 2006. **73**(11): p. -.

308. Layson, A.R., et al., *The effect of common gases on nucleation of metal islands: The role of oxygen in Ag(100) homoepitaxy.* Journal of Chemical Physics, 2003. **118**(14): p. 6467-6472.

309. Layson, A.R., J.W. Evans, and P.A. Thiel, *Additive-enhanced coarsening and smoothening of metal films: Complex mass-flow dynamics underlying nanostructure evolution.* Phys. Rev. B: Condens. Matter Mater. Phys. , 2002. **65**(19): p. 193409/1-193409/4.

310. Layson, A.R. and P.A. Thiel, *Testing realistic environments for metal film growth and aging: chemical insights into the effect of oxygen on Ag/Ag(100).* Surface Science Letters, 2001. **472** p. L151-L156.

311. Morgenstern, K., *Fast scanning tunnelling microscopy as a tool to understand changes on metal surfaces. From nanostructures to single atoms.* Physica Status Solidi B: Basic Solid State Physics, 2005. **242**(4): p. 773-796.

312. Morgenstern, K., K.-F. Braun, and K.-H. Rieder, *Surface-state depopulation on small Ag(111) terraces.* Physical Review Letters, 2002. **89**(22): p. 226801/1-226801/4.

313. Morgenstern, K., E. Laegsgaard, and F. Besenbacher, *Island decay on the anisotropic Ag(110) surface.* Mater. Res. Soc. Symp. Proc. , 2001. **648**(Growth, Evolution and Properties of Surfaces, Thin Films and Self-Organized Structures): p. P1 5/1-P1 5/11.

314. Morgenstern, K., E. Laegsgaard, and F. Besenbacher, *Decay of two-dimensional islands on Ag(110).* NATO Science Series, II: Mathematics, Physics and Chemistry, 2001. **29**(Collective Diffusion on Surfaces: Correlation Effects and Adatom Interactions): p. 201-212.

315. Morgenstern, K., E. Laegsgaard, and F. Besenbacher, *Brownian motion of 2D vacancy islands by adatom terrace diffusion.* Physical Review Letters, 2001. **86**(25): p. 5739-5742.

316. Morgenstern, K., E. Laegsgaard, and F. Besenbacher, *Quantum Size Effects in Adatom Island Decay.* Physical Review Letters, 2005. **94**(16): p. 166104/1-166104/4.

317. Morgenstern, K., G. Rosenfeld, and G. Comsa, *Decay of two-dimensional Ag islands on Ag(111).* Physical Review Letters, 1996. **76**(12): p. 2113-16.

318. Morgenstern, K., et al., *Kinetics of fast island decay on Ag(111).* Phys. Rev. B: Condens. Matter Mater. Phys. , 2001. **63**(4): p. 045412/1-045412/5.

319. Morgenstern, K., et al., *Brownian motion of vacancy islands on Ag(111).* Physical Review Letters, 1995. **74**(11): p. 2058-61.

320. Semin, D.J., et al., *Time-dependent morphology changes in thin silver films on mica: A scaling analysis of atomic force microscopy results.* Journal of Chemical Physics, 1996. **105**(13): p. 5542-5551.

321. Stoldt, C.R., et al., *Kinetic roughening of multilayer Ag/Ag(100) films. Complex temperature-dependence in a simple system.* Mater. Res. Soc. Symp. Proc., 2000. **619**(Recent Developments in Oxide and Metal Epitaxy: Theory and Experiment): p. 15-25.

322. Stoldt, C.R., et al., *Smoluchowski ripening of Ag islands on Ag(100).* Journal of Chemical Physics, 1999. **111**(11): p. 5157-5166.

323. Thiel, P.A. and J.W. Evans, *Cluster diffusion, coalescence, and coarsening in metal(100) homoepitaxial systems.* Ser. Dir. Condens. Matter Phys., 1998. **14**(Morphological Organization in Epitaxial Growth and Removal): p. 384-402.

324. Thiel, P.A. and J.W. Evans, *Nucleation, growth, and relaxation of thin films. Metal(100) homoepitaxial systems.* Journal of Physical Chemistry B, 2000. **104**(8): p. 1663-1676.

325. Thiel, P.A., et al., *Coarsening of Two-Dimensional Nanoclusters on Metal Surfaces.* Journal of Physical Chemistry C, 2009. **113**(13): p. 5047-5067.

326. Ferrando, R. and G. Treglia, *Anisotropy of Diffusion Along Steps on the (111)Faces of Gold and Silver.* Physical Review B, 1994. **50**(16): p. 12104-12117.

327. Winegard, W.C., *Anisotropy of Surface Self-Diffusion of Silver.* Acta Metallurgica, 1953. **1**(2): p. 230.

328. Yu, B.D. and M. Scheffler, *Anisotropy of growth of the close-packed surfaces of silver.* Physical Review Letters, 1996. **77**(6): p. 1095-1098.

329. Wen, J.M., et al., *Coarsening mechanisms in a metal film: from cluster diffusion to vacancy ripening.* Physical Review Letters, 1996. **76**(4): p. 652-5.

330. Kizuka, T., H. Ichinose, and Y. Ishida, *Atomic-Structure and Thermal-Stability of Nanocrystalline Silver.* Journal of the Japan Institute of Metals, 1991. **55**(3): p. 233-240.

331. Mougin, K., et al., *Thermal stability and reconstruction of nanoparticulate Au film on model molecular surfaces.* Journal of Colloid and Interface Science, 2009. **333**(2): p. 719-724.

332. Nandipati, G., et al., *Parallel kinetic Monte Carlo simulations of Ag(111) island coarsening using a large database.* Journal of Physics: Condensed Matter, 2009. **21**(8): p. 084214.

333. Rorak, S.E., et al., *Changes in thin-metal-film nanostructure at near-ambient temperatures.* Nanostructured Materials, 1997. **679**: p. 152-168.

334. Franchy, R., et al., *Negative ion resonances of O-2 adsorbed on Ag surfaces.* Journal of Physics: Condensed Matter, 2000. **12**(6): p. R53-R82.

335. Ma, W.Q. and Y. Fang, *Experimental (SERS) and theoretical (DFT) studies on the adsorption of p-, m-, and o-nitroaniline on gold nanoparticles.* Journal of Colloid and Interface Science, 2006. **303**(1): p. 1-8.

336. Menzel, E. and C. Menzel-Kopp, *Surface migration of oxygen and metal atoms during the oxidation of copper and silver.* Surface Science, 1964. **2**: p. 376-80.

337. Messerli, S., et al., *Oxygen molecules on Ag(0 0 1). Superstructure, binding site and molecular orientation.* Chemical Physics Letters, 2000. **328**(4,5,6): p. 330-336.

338. Savio, L., L. Vattuone, and M. Rocca, *Surface plasmon dispersion on sputtered and nanostructured Ag(001).* Physical Review B, 2003. **67**(4): p. 045406(5).

339. Savio, L., L. Vattuone, and M. Rocca, *From adsorption at the surface to incorporation into subsurface sites: the role of steps for O/Ag.* Applied Physics a-Materials Science & Processing, 2007. **87**(3): p. 399-404.

340. Savio, L., et al., *Substrate reconstruction and electronic surface states: Ag(001).* Surface Science, 2001. **486**(1-2): p. 65-72.

341. Vattuone, L., et al. *HREELS study of O-2 molecular chemisorption on Ag(001)*. 1997: Elsevier Science Bv.

342. Weaver, J.F. and G.B. Hoflund, *Surface Characterization Study of the Thermal-Decomposition of Ag2o.* Chemistry of Materials, 1994. **6**(10): p. 1693-1699.

343. Caspersen, K.J., et al., *Nanostructure formation and relaxation in metal(100) homoepitaxial thin films: Atomistic and continuum modeling.* Comput. Mater. Chem., 2004: p. 91-124.

344. Loffreda, D., et al., *Oxygen vibrations in O-Ag(001).* Surface Science, 2003. **530**(1-2): p. 26-36.

345. Valbusa, U., et al., *Adsorption and desorption of O-2 on Ag surfaces.* Vacuum, 1998. **50**(3-4): p. 445-450.

346. Savio, L., et al. *Oxygen interaction at Ag(511): from chemisorption to the initial stages of oxide formation*. 2008: Iop Publishing Ltd.

347. Vattuone, L., et al., *Collision induced desorption and dissociation of O-2 chemisorbed on Ag(001).* Journal of Chemical Physics, 1998. **109**(6): p. 2490-2502.

348. Shen, M.M., et al., *Accelerated coarsening of Ag adatom islands on Ag(111) due to trace amounts of S: Mass-transport mediated by Ag-S complexes.* Journal of Chemical Physics, 2009. **130**(9): p. 094701(13).

349. Beavers, K.R., N.E. Marotta, and L.A. Bottomley, *Thermal Stability of Silver Nanorod Arrays.* Chemistry of Materials, 2010. **22**: p. 2184-2189.

350. Vo-Dinh, T., et al., *Surface-enhanced Raman scattering (SERS) method and instrumentation for genomics and biomedical analysis.* Journal of Raman Spectroscopy, 1999. **30**(9): p. 785-793.

351. Lochte, T., *Ph.D. Thesis*. 1997, University of Essen.

352. Premasiri, W.R., et al., *Characterization of the Surface Enhanced Raman Scattering (SERS) of Bacteria.* Journal of Physical Chemistry B, 2005. **109**(1): p. 312-320.

353. Liu, Y., et al., *Potential of Surface-Enhanced Raman Spectroscopy for the Rapid Identification of Escherichia coli and Listeria monocytogenes Cultures on Silver Colloidal Nanoparticles.* Applied Spectroscopy, 2007. **61**(8): p. 824-831.

354. Demiril, M.c., et al., *Bio-organism sensing via surface enhanced Raman spectroscopy on controlled metal/polymer nanostructured substrates.* Biointer*phases* 2009. **4**(2).

355. Yan, B., et al., *Multiscale Signal Enhancement: Nanoparticle Cluster Arrays.* ACS Nano, 2009. **3**(5).

356. Lodish, H., et al., *Molecular Cell Biology*. Fifth ed. 1986, New York, NY: W. H. Freeman and Company.

357. Janeway, C.A., *Imunnobiology: The Immune System in Health and Disease*. 6th ed. 2004, New York: Garland Science Publishing.

358. Voet, D. and J. Voet, *Biochemistry*. Third ed. Biomolecules, Mechanisms of Enzyme Action, and Metabolism. Vol. 1. 2004, Hoboken, NJ: John Wiley & Sons, Inc.

359. Kotiranta, A., et al., *Surface Stucture, Hydrophobicity, Phagocytosis, and Adherence to Matrix Proteins of Bacillus cerus Cells with and without the Crystallin Surface Protein Layer.* Infection and Immunity, 1998. **66**(10): p. 4895-4902.

360. Kotiranta, A., K. Lounatmaa, and M. Haapasalo, *Epidemiology and pathogenesis of Bacillus cerueus infections.* Microbes and Infection, 2000. **2**: p. 189-198.

361. Sanchez, B., S. Arias, and S. Chaignepain, *Identification of surface proteins involved in the adhesion of a probiotic Bacillus cereus strain to mucin and fibronectin* Microbiology - SGM, 2009. **155**: p. 1708-1716.

362. Li, J., et al., *Species-Specific Cell Wall Binding Affinity of the S-Layer Proteins of Mosquitocidal Bacterium Bacillus sphaericus C3-41.* Applied and Environmental Microbiology, 2009. **75**(12): p. 3891-3895.

363. Valasquez, L. and J. Dussen, *Biosorption and bioaccumulation of heavy metals on dead and living biomass of Bacillus sphaericus.* Journal of Hazardous Materials, 2009. **167**(1-3): p. 713-716.

364. Kalmokoff, M.L., J.W. Austin, and T.D. Cyr, *Physical and genetic characterization of an outer-membrane protein (OmpM1) containing an N-terminal S-layer-like homology domain from the phylogenetically Gram-positive gut anaerobe Mitsuokella multacida.* Anaerobe, 2009. **15**(3): p. 74-81.

365. Mobili, P., M.D. Serradell, and S.A. Trejo, *Heterogeneity of S-layer proteins from aggregating and non-aggregating Lactobacillus kefir strains* Antonie Van Leeuwehnhoek International Journal of General and Molecular Microbiology, 2009. **95**(4): p. 363-372.

366. Fagan, R.P., D. Albesa-Jove, and Q. O., *Structural insights into the molecular organization of the S-layer from Clostridium difficile* Molecular Microbiology, 2009. **71**(5): p. 1308-1322.

367. Matias, V.R.F. and T.J. Beveridge, *Cry-electron microscopy reveals native polymeric cell wall structure in Bacillus subtilis 168 and the existence f a periplasmic space.* Molecular Microbiology, 2005. **56**: p. 240-251.

368. Matias, V.R.F. and T.J. Beveridge, *Native cell wall organiation shown by cryo-electron microscopy confirms the existence of a periplasmic space in Staphylococcus aureus.* Journal of Bacteriology, 2006. **188**(1011-1021).

369. Wang, L., et al., *Cell wall structure of a mutant of Mycbacterium smegmatis defective in the biosynthesis of mycolic acids.* Journal of Biological Chemistry, 2000. **275**: p. 7224-7229.

370. Zhao, G., et al., *Binding of S-layer homology modules from Closteridium thermocellum SdbA to peptidoglycans.* Applied Microbiology, 2006. **70**: p. 464-469.

371. Chauvaux, S., M. Matuschek, and P. Beguin, *Distinct affinity of binding sites for S-layer homologous domains in Clostridium thermolcellum and Bacillus anthracis cell envelopes.* Journal of Bacteriology, 1999. **181**: p. 2455-2458.

372. Engelhardt, H. and J. Peters, *Structural research on surface layers - A focus on stability, surfacel layer homology domains, and surface layer-cell wall interactions.* Journal of Structural Biology, 1998. **124**: p. 276-302.

373. Ilk, N., et al., *Structural and functional analysis of secondary cell wall polymer of Bacillus spaericus CCM 2177 that serves as an S-layer-specific anchor.* Journal of Bacteriology, 1999. **181**(7643-7646).

374. Mesnage, S., et al., *Bacterial SLH domain proteins are non-covalently anchored to the celle surface via a conserved mechanism involoving polysaccharide pyruvylation.* EMBO J., 2000. **19**: p. 4473-4484.

375. Schaffer, C. and P. Messner, *The sructure of secondary cell wall polymers: hoe Gram-positive bacteria stick their cell walls together.* Microbiology, 2005. **151**: p. 643-651.

376. Ford, M.J., J.F. Nomellini, and J. Smit, *S-layer anchoring and localization of an S-layer-associated protease in Caulobacter crescentus.* Journal of Bacteriology, 2007. **189** p. 2226-2237.

377. Garduno, R.A., et al., *Novel structural patterns in divalent cation-depleted surface layers of Aeromonas salmonicida.* Journal of Structural Biology, 1992. **109**: p. 184-195.

378. Nomellini, J.F., et al., *Factors controlling in vitro recrystalliation of the Caulobacter crescentus paracrystalline S-layer.* Journal of Bacteriology, 1997. **179**(6349-6354).

379. Walker, S.G., et al., *Characterization of mutants of Caulobacter crescetus defective in surface attachment of the paracrystalline surface layer.* Journal of Bacteriology, 1994. **176**: p. 6321-6323.

380. Notingher, I., et al., *In situ monitoring of cell death using Raman microspectroscopy* Biopolymers, 2004. **72**: p. 230-240.

381. Nijssen, A., et al., *Discriminating basal cell carcinoma from its surrounding tissue by Raman spectroscopy* Journal of Investigative Dermatology, 2003. **119**: p. 64-69.

382. BD, *BD Bionutrients™ Technical Manual; Advanced Bioprocessing.* BD Bionutrients™ Technical Manual; Advanced Bioprocessing, 2006: p. 1-68.

383. Kao, P.K., et al., *Surface-Enhanced Raman Detection on Metalized Nanostructured Poly(p-xylylene) Films.* Advanced Materials, 2008. **20**: p. 3562-3565.

384. Maquelin, K., et al., *Raman Spectroscopic Method for Identification of Clinically Relevant Microorganisms Growing on Solid Culture Medium.* Analytical Chemistry, 2000. **72**(1): p. 12-19.

385. Luo, B.S. and M. Lin, *A Portable Raman System for the Identification of Foodborne Pathogenic Bacteria.* Journal of Rapid Methods and Automation in Microbiology, 2008. **16**: p. 238-255.

386. Susi, H., et al., *LASER-RAMAN INVESTIGATION OF PHOSPHOLIPID-POLYPEPTIDE INTERACTIONS IN MODEL MEMBRANES.* Biochemistry, 1979. **18**(2): p. 297-301.

387. Pearman, W.F. and A.W. Fountain III, *Classification of Chemical and Biological Warfare Agent Simulants by Surface-Enhanced Raman Spectroscopy and Multivariate Statistical Techniques.* Applied Spectroscopy, 2006. **60**(4): p. 356-265.

388. Rosch, P., et al., *Fast and reliable identification of microorgnisms by means of Raman spectroscopy.* SPIE-OSA, 2007. **6633**: p. 66331A-1-9.

389. Guicheteau, J.A., et al., *Bacillus Spore Classification via Surface-Enhanced Raman Spectroscopy and Principal Component Analysis.* Applied Spectroscopy, 2008. **62**(3): p. 267-272.

390. Guicheteau, J.A. and S.D. Christesen, *Principal Component Analysis of Bacteria Using Surface-Enhanced Raman Spectroscopy.* Proceedings of SPIE, 2006. **6218**: p. 1-8.

391. Dluhy, R.A., *Nanostructure Arrays for Virus Detection*. 2004, NIH: University of Georgia, Georgia Institute of Technology. p. 38.

392. Ieven, M., *Currently used nucleic acid amplification tests for the detection of viruses and atypicals in acute respiratory infections.* Journal of Clinical Virology, 2007. **40**(4): p. 259-276.

393. Vernet, G., *Use of molecular assays for the diagnosis of influenza.* Expert Review of Anti-Infective Therapy, 2007. **5**(1): p. 89-104.

394. Ellis, J. and M. Zambon, *Molecular diagnosis of influenza.* Reviews in Medical Virology, 2002. **12**: p. 375-389.

395. Sigurs, N., et al., *Severe respiratory syncytial virus bronchiolitis in infancy and asthma and allergy at age 13.* American Journal of Respiratory and Critical Care Medicine, 2005. **171**(2): p. 137-141.

396. Shay, D.K., et al., *Bronchiolitis-associated hospitalizations among US children, 1980-1996.* Jama-Journal of the American Medical Association, 1999. **282**(15): p. 1440-1446.

397. Shay, D.K., et al., *Bronchiolitis-associated mortality and estimates of respiratory syncytial virus-associated deaths among US children, 1979-1997.* Journal of Infectious Diseases, 2001. **183**(1): p. 16-22.

398. Holman, R.C., et al., *Risk factors for bronchiolitis-associated deaths among infants in the United States.* Pediatric Infectious Disease Journal, 2003. **22**(6): p. 483-489.

399. Lee, P.C. and D. Meisel, *Adsorption and Surface-Enhanced Raman of Dyes on Silver and Gold Sols.* Journal of Physical Chemistry, 1982. **86**(17): p. 3391-3395.

400. Vo-Dinh, T., F. Yan, and M.B. Wabuyele, *Surface-enhanced Raman scattering for biomedical diagnostics and molecular imaging.* Top. Appl. Phys., 2006. **103**(Surface-Enhanced Raman Scattering): p. 409-426.

401. Wynveen, A. and C.N. Likos, *Interactions between planar stiff polyelectrolyte brushes.* Physical Review E, 2009. **80**(1).

402. Markov, V.A., et al., *Conformational properties of rigid-chain amphiphilic macromolecules: The phase diagram.* Polymer Science Series A, 2008. **50**(6): p. 621-629.

403. Sil, D., et al., *Trivalent ligands with rigid DNA spacers reveal structural requirements for IgE receptor signaling in RBL mast cells.* ACS Chemical Biology, 2007. **2**(10): p. 674-684.

404. Campos, J.L., et al., *DNA coiled coils.* Proceedings of the National Academy of Sciences of the United States of America, 2005. **102**(10): p. 3663-3666.

405. Goodman, R.P., et al., *Rapid chiral assembly of rigid DNA building blocks for molecular nanofabrication.* Science, 2005. **310**(5754): p. 1661-1665.

406. Marotta, N.E. and L.A. Bottomley, *Polystyrene beads as probes of the SERS response characteristics of silver nanorod arrays.* Applied Spectroscopy, 2010. **under final review**.

407. Steel, A.B., et al., *Immobilization of Nucleic Acids at Solid Surfaces: Effect of Oligonucleotide Length on Layer Assembly.* Biophysical Journal, 2000. **79**: p. 975-981.

408. Steel, A.B., T.M. Herne, and M.J. Tarlov, *Electrochemical Quantitation of DNA Immobilized on Gold.* Analytical Chemistry (Washington, DC, United States), 1998. **70**: p. 4670-4677.

409. Love, J.C., et al., *Self-assembled monolayers of thiolates on metals as a form of nanotechnology.* Chemical Reviews, 2005. **105**: p. 1103-1169.

410. de Gennes, P.G., *Polymers at an Interface; A Simplified View.* Advanced Colloid Interface Science, 1987. **27**: p. 189-209.

411. de Gennes, P.G., *Polymer solutions near an interface. Adsorption and depletion layers.* Macromolecules (Washington, DC, United States), 1981. **14**: p. 1637-1644.

412. de Gennes, P.G., *Polymers at an interface. 2. Interaction between two plates carrying adsorbed polymer layers.* Macromolecules (Washington, DC, United States), 1982. **15**: p. 492-500.

413. O'Shaughnessy, B. and D. Vavylonis, *Kinetic regimes and cross-over times in many-particle reacting systems.* Europhysical Letters, 1999. **45**: p. 653-658.

414. O'Shaughnessy, B. and D. Vavylonis, *Reactive polymer interfaces: How reaction kinetics depend on reactivity and density of chemical groups.* Macromolecules (Washington, DC, United States), 1999. **32**: p. 1785-1796.

415. O'Shaughnessy, B. and D. Vavylonis, *Theoretical and Mathematical Models in Polymer Science.* Academic, 1998.

416. O'Shaughnessy, B. and D. Vavylonis, *Irreversible adsorption from dilute polymer solutions.* European Physical Journal E: Soft Matter, 2003. **11**: p. 213-230.

417. O'Shaughnessy, B. and D. Vavylonis, *Non-equilibrium in adsorbed polymer layers.* Journal of Physics - Condensed Matter, 2005. **17**: p. R63-R99.

418. Fleer, G.J., et al., *Polymers at Interfaces*. 1993: Chapman and Hall.

419. Brotherson, B., et al., *Salt Effect on Cationic Polyacrylamide Conformation on Mica Studied by Single Molecule "Pulling" with Scanning Probe Microscopy.* Journal of Physical Chemistry C, 2008. **112**(40): p. 12686-12691.

420. Brotherson, B., et al., *Cationic Polyacrylamide Conformation on Mica Studied by Single Molecule "Pulling" with Scanning Probe Microscopy.* Macromolecules (Washington, DC, United States), 2007. **40**: p. 4561-4567.

421. Al-Maawali, S., et al., *Single-molecule AFM study of polystyrene grafted at gold surfaces.* Journal of Adhesion Science and Technology, 2005. **81**: p. 999-1016.

422. Hugel, T., et al., *Elasticity of Single Polyelectrolyte Chains and Their Desorption From Solid Supports Studied by AFM Based Single Molecule Force Spectroscopy.* Macromolecules (Washington, DC, United States), 2001. **34**: p. 1039-1047.

423. Li, H., et al., *Single-molecule force spectroscopy on xanthan by AFM.* Advanced Materials & Processes, 1998. **3**: p. 316-319.

424. Brogly, M., et al., *A nanoscale study of the adhesive contact.* Comptes rendus Chimie, 2006. **9**(1): p. 99-110.

425. Cappella, B., S.K. Kaliappan, and H. Sturm, *Using AFM force-distance curves to study the glass-to-rubber transition of amorphous polymers and their elastic-plastic properties as a function of temperature.* Macromolecules (Washington, DC, United States), 2005. **83**(5): p. 1874-1881.

426. Hugel, T. and M. Seitz, *The study of molecular interactions by AFM force spectroscopy.* Macromolecular Rapid Communications, 2001. **22**(13): p. 989-1016.

427. Okajima, T., et al., *Force spectroscopy on single polymer incorporated into polymer gels.* Journal of Nanoscience and Nanotechnology, 2007. **7**(3): p. 790-795.

428. Burnham, N.A., R.J. Colton, and H.M. Pollock, *Interpretation of force curves in force microscopy.* Nanotechnology, 1993. **4**: p. 64-80.

429. Evans, E. and K. Ritchie, *Dynamic strength of molecular adhesion bonds.* Biophysical Journal, 1997. **72**(4): p. 1541-1555.

430. Evans, E. and K. Ritchie, *Strength of a Weak Bond Connecting Flexible Polymer Chains.* Biophysical Journal, 1999. **76**(5): p. 2439-2447.

431. Aime, J.P., et al., *Comments on the use of the force mode in atomic force microscopy for polymer films.* Journal of Applied Physics, 1994. **76**(2): p. 754-762.

432. Brogly, M., et al., *On the use of SPM to probe the interplay between polymer surface chemistry and polymer surface mechanics.* Journal of Physics - Conferance Series, 2007. **61**(135-139).

433. Brogly, M., et al., *Adhesion at the nanoscale: an approach by AFM.* Adhesion 2005: p. 33-45.

434. Clausen-Schaumann, H., et al., *Force spectroscopy with single bio-molecules.* Current Opinion in Chemical Biology, 2000. **4**: p. 524-530.

435. Haverkamp, R.G., A.T. Marshall, and M.A.K. Williams, *Model for stretching elastic biopolymers which exhibit conformational transformations.* Statistical, Nonlinear, Soft Matter Physics, 2007. **75**(2-1): p. 021907/1-021907/7.

436. Israelachvili, J.N., *Intermolecular & Surface Forces*. 1992: Academic Press.

437. Jarkova, E., N.-K. Lee, and S. Obukhov, *Extracting Structural Information of a Heteropolymer from Force-Extension Curves.* Macromolecules (Washington, DC, United States), 2005. **38**(6): p. 2469-2474.

438. Jarkova, E., T.J.H. Vlugt, and N.-K. Lee, *Stretching a heteropolymer.* Journal of Chemical Physics, 2005. **122**(11): p. 114904/1-114904/9.

439. Levy, R. and M. Maaloum, *New Tools for Force Spectroscopy.* Ultramicroscopy, 2005. **102**: p. 311-315.

440. Ray, C., J.R. Brown, and B.B. Akhremitchev, *Correction of systematic errors in single-molecule force spectroscopy with polymeric tethers by atomic force microscopy.* Journal of Physical Chemistry B, 2007. **111**: p. 1963-1974.

441. Senden, T.J., *Force microscopy and surface interactions.* Current Opinion in Colloid & Interface Science, 2001. **6**: p. 95-101.

442. Ray, C., J.R. Brown, and B.B. Akhremitchev, *Rupture force analysis and the associated systematic errors in force spectroscopy by AFM.* Langmuir, 2007. **23**(11): p. 6076-6083.

443. Pierce, *Instructions*, *BS(PEG)$_n$*, in *www.thermo.com/pierce*, P. Biotechnology, Editor. 2010, Thermo Scientific: Rockford, IL. p. 1-3.